



# Development of electrode architectures for miniaturized biofuel cells

Aleksandar Karajić

## ► To cite this version:

Aleksandar Karajić. Development of electrode architectures for miniaturized biofuel cells. Chemical Physics [physics.chem-ph]. Université de Bordeaux, 2015. English. NNT : 2015BORD0305 . tel-01424143

**HAL Id: tel-01424143**

**<https://theses.hal.science/tel-01424143>**

Submitted on 2 Jan 2017

**HAL** is a multi-disciplinary open access archive for the deposit and dissemination of scientific research documents, whether they are published or not. The documents may come from teaching and research institutions in France or abroad, or from public or private research centers.

L'archive ouverte pluridisciplinaire **HAL**, est destinée au dépôt et à la diffusion de documents scientifiques de niveau recherche, publiés ou non, émanant des établissements d'enseignement et de recherche français ou étrangers, des laboratoires publics ou privés.



# THÈSE

PRÉSENTÉE A

**L'UNIVERSITÉ DE BORDEAUX**

ÉCOLE DOCTORALE DES SCIENCES CHIMIQUES

Par Aleksandar Karajić

POUR OBTENIR LE GRADE DE

DOCTEUR

SPÉCIALITÉ : Chimie-Physique

## **Development of electrode architectures for miniaturized biofuel cells**

Directeurs de thèse : Prof. Alexander Kuhn et Dr. Nicolas Mano

Soutenue le : 15.12.2015.

Devant la commission d'examen formée de :

M. BARTLETT N. Philip	Professeur, Université de Southampton	Rapporteur
M. WALCARIUS Alain	Directeur de recherche, CNRS, Nancy	Rapporteur
M. MIHI Agustín	Chercheur, Université de Rovira i Virgili Tarragona	Examineur
M. RAVAINÉ Serge	Professeur, Université de Bordeaux	Examineur
M. KUHN Alexander	Professeur, INP - Bordeaux	Directeur de thèse
M. MANO Nicolas	Directeur de recherche, CNRS, Bordeaux	Co- directeur de thèse

## Acknowledgements

This work has been done in the laboratories of Institute of Molecular Sciences (ISM) and Research Center Paule Pascal (CRPP) at the University of Bordeaux.

First of all I would like to take this opportunity to acknowledge all members of the jury for their acceptance to evaluate my thesis and for their useful comments and suggestions, particularly to Prof. Philip Bartlett from the University of Southampton and Dr. Alan Walcarius from CNRS/University of Lorraine for accepting the invitation as reviewers of this manuscript and for their useful comments and corrections.

I would like to express my big gratitude to both of my supervisors, Prof. Alexander Kuhn (ISM) and Dr. Nicolas Mano (CRPP) for guiding me during the last three years through complex fields of electrochemistry, material science and bioelectrochemistry and for sharing their great experience and knowledge with me. Thank you for providing me guidance at key moments in my work while also allowing me to work independently. Merci beaucoup et/und Danke schön!

This work has been financially supported by AMADEus-LabEx project (University of Bordeaux) on what I am very grateful. Also, I would like to acknowledge the Institute of molecular sciences (ISM/Bordeaux) and National Polytechnic Institute of Bordeaux (INP/Bordeaux). Thank you all!

I am very grateful to my colleagues from NSYSA group for their support and a lot of nice moments that we spent together. Many thanks to Dr. Suresh Vajrala, Dr. Léa Messenger, Dr. Aileen Justies, Dr. Salem Ben Amor, Dr. Florent Pinaut, Dr. Catherine Adam, Dr. Jérôme Roche, Hannah Nas, Antoine Richieu, Alessandra Zanut, Dr. Sudarat Yadnum, Dr. Churalat Wattanakit, Oranit Phuakkong, Supakit Tiewchareon, Thittaya Yutthalekham, Dr. Damien Quinton, Dr. Pascal Massé, Dr. Vasilica Lates, Dr. Marlène Rouhet, Beatriz Diez Buitrago, Saioa Basauri Cadarso, Eugenio Gianessi, Li Haidong, Iuliia Malytska, Hélène Labie, Pauline Lefrancois, Gibran Hernandez Moreno, Dr. Milena Milutinovic-Dumont, Dr. Zahra Fatah Ali, Pierre Bouillac, Jovana Jovanovic, Damla Keskin and Dr. Habatmu Henock.

However, I would like to express my special gratitude to Dr. Anne de Poulpiquet, Dr. Stéphane Reculosa and Dr. Emmanuel Suraniti for everything that they have done for me. Thank you for the honest friendship, your support and professional help. I will always remember it. Merci a tous!

Many thanks to Prof. Jochen Lang and Dr. Eileen Pedraza from the Institute of Chemistry and Biology of Membranes and Nano-objects (University of Bordeaux) for the collaboration in the field of coupling electrochemistry with electrophysiology of pancreatic beta cells. Thank you Eileen for plenty of nice conversations that we had during the experiments and for helping me to improve my English skills.

Also, I would like to knowledge Prof. Philippe Barthélémy and Dr. Deepak Jain from the Institute of Health and Medical Care (INSERM) from the University of Bordeaux for their collaboration on the project about low molecular weight hydrogel for bio-electrode interfaces.

I would especially like to acknowledge permanent members of NSYSA group for the fruitful academic discussions that we had during the lab seminars. Thank you Dr. Bertrand Goudeau, Dr. Dodzi Zigah, Dr. Laurent Bouffier, Dr. Neso Sojic, Dr. Stéphane Arbault, Dr. Valérie Ravaine, Dr. Adeline Perro-Marre, Patrick Garrigue and Véronique Lapeyre. For the administrative support, I would like to acknowledge to our secretary Aline Simon-Lalande.

I would like to thank the CRPP team for the collaboration in the area of biofuel cells and for a great time that we have spent together, especially during the last few months of my PhD project. Many thanks to Dr. Marine Cadet, Magdalena Murawska, Dr. Jad Rouhana, Dr. Lise Edembe and Sébastien Gounel.

Najiskrenije se zahvaljujem svojoj porodici na razumevanju, ljubavi i podršci koju su mi pružili ne samo tokom izrade i pisanja ove teze vec tokom celokupnog dosadašnjeg života. Hvala!

Posebnu zahvalnost dugujem profesoru Draganu Manojloviću i svojoj bivoj mentorki profesorki Snežani Nikolić-Mandić sa Hemijskog fakulteta na Univerzitetu u Beogradu na znanju i iskustvu koje su mi preneli tokom osnovnih i master studija kao i na nesebičnoj podršci.

Zahvaljujem koleginici dr Milica Sentić na iskrenom prijateljstvu, podršci i nesvakidašnjim situacijama kroz koje smo zajedno prošli tokom prethodne četiri godine. Veliko ti hvala na svemu!!!

Posebno se zahvaljujem Siniši Mitroviću, Stefanu Mijatoviću, Diane Michalon i Mariam Hovhannisyan na iskrenom prijateljstvu i mnoštvu lepih trenutaka koje smo zajedno proveli. Hvala vam!



## Abstract

The increasing demand for miniaturized and eventually implantable electrochemical tools such as biosensors, biofuel cells and batteries has led to the development of new technologies to overcome existing problems related to large dimensions, low current densities, and insufficient power output of such devices. In the present work we describe new approaches for the fabrication of miniaturized, macroporous and coaxial electrode architectures that could find their practical application for the fabrication of the systems mentioned above. Furthermore, we have demonstrated the functionality of macroporous electrodes with respect to the design of miniaturized glucose/oxygen biofuel cells. Preliminary results regarding the design of a new type of whole-cell based glucose biosensors are also presented.

The first part of this work is focusing on different strategies for the fabrication of colloidal crystals (Chapter 1) that can be used for the synthesis of macroporous electrodes (Chapter 2) by following the so-called hard template approach. The synthesis of macroporous electrodes is based on the potentiostatic electrodeposition of conductive materials (such as metals in the present work) into a silica based colloidal template that has been synthesized by the Langmuir-Blodgett procedure. This method has been used for the design and fabrication of miniaturized coaxial and macroporous two electrode-electrochemical cells by following two different and complementary procedures: 1. The first fabrication procedure is based on the electrodeposition of alternating gold-nickel-gold metal layers, subsequent etching of the intermediate nickel layer and a structural stabilization; 2. The second alternative and complementary strategy for the fabrication of coaxial and macroporous double electrochemical cells relies on assembling the final architecture from two independently prepared and electrochemically addressable cylindrical macroporous electrodes. The main difference between these two approaches is the range of inter-electrode distances (from tens of micrometers (first approach) to hundreds of micrometers that can be achieved by second fabrication procedure). Also, we demonstrate the electrochemical functionality of both electrode architectures by cyclo-voltammetric investigation of the oxygen reduction reaction that takes place at the surface of both electrodes.

The biggest advantage of the presented strategies is the possibility to fine tune the electrode thickness (and therefore active surface areas), the spatial separation between inner and outer electrode (the volume of electrolyte that can be stored between them) and the pore size (by changing the diameter of silica colloidal particles).

In the following segment (Chapter 3), we demonstrate the possibility to use macroporous electrodes for the fabrication of an enzymatic biocathode. The macroporous gold substrates were chosen as promising candidates to improve the electrochemical performances (current and power output) of an enzymatic glucose/oxygen biofuel cells due to their high active surface

area. Cyclic-voltammetry has been used for electrodeposition of Os-redox polymer and a Bilirubin oxidase (BOD)/Os-redox polymer adduct in the macroporous structure. We have also studied the bioelectrocatalytic oxygen reduction at the surface of BOD/Os-redox polymer modified electrodes, as well as the stability of the so obtained bioelectrocatalytic film.

Finally, our contribution to the development of a new type of whole cell based biosensor is described in Chapter 4. We have used electrochemistry as a tool to guide glucose sensitive pancreatic insulinoma cells (INS832/13) and dissociated Langerhans islets towards microelectrodes. This has been achieved by means of a pattern of optimized electrode potentials that were generated in a micro-electrode array device. The main purpose of using electrophoresis for the immobilization of pancreatic cells on the surface of microelectrodes is the improvement of the quality of the measured glucose-dependent extracellular signal, which leads to the increase in overall performances of the final biosensor (*e.g.* sensitivity).

**Key words:** Langmuir – Blodgett; colloidal crystals; template materials; electrodeposition; electrochemical devices; macroporous electrodes; biofuel cells; biocathode; Bilirubin oxidase; Os-redox polymer; beta cells.

## Résumé

La demande croissante de systèmes électrochimiques miniaturisés et potentiellement implantables tels que les biocapteurs, les biopiles à combustible et les batteries a conduit à l'émergence de nouvelles technologies pour surmonter les problèmes expérimentaux liés aux grandes dimensions, aux faibles densités de courant, et à la puissance de sortie insuffisante de ces dispositifs. Dans ce travail de thèse, nous présentons de nouvelles approches pour la fabrication d'électrodes miniaturisées avec des architectures macroporeuses et coaxiales dont les applications pourraient être dans les domaines cités plus haut. De plus, nous avons démontré l'utilisation de telles électrodes macroporeuses pour la conception de biopiles fonctionnant à base de glucose et d'oxygène. Les résultats préliminaires concernant la conception d'un nouveau type de biocapteurs de glucose à base de cellules vivantes sont également présentés.

La première partie de ce travail se concentre sur différentes stratégies pour la fabrication de cristaux colloïdaux (chapitre 1) qui peuvent être utilisés pour la préparation d'électrodes macroporeuses (chapitre 2) en suivant l'approche dite de matrice sacrificielle dure. La synthèse d'électrodes macroporeuses est basée sur l'électrodéposition potentiostatique de matériaux conducteurs (tels que les métaux dans le contexte de ce travail) dans une matrice colloïdale à base de silice qui a été synthétisée par le procédé de Langmuir-Blodgett. Cette méthode a été utilisée pour la conception et la fabrication de cellules électrochimiques à deux électrodes macroporeuses coaxiales et miniaturisées en suivant deux procédures différentes et complémentaires: 1. La première procédure de fabrication est basée sur l'électrodéposition de couches de métaux alternées or-nickel-or, avant la dissolution de la couche de nickel intermédiaire puis une stabilisation mécanique de la structure; 2. La seconde stratégie alternative et complémentaire pour la fabrication de cellules électrochimiques coaxiales et macroporeuses repose sur l'assemblage de l'architecture finale à partir de deux électrodes cylindriques macroporeuses préparées indépendamment et adressables par voie électrochimique. La principale différence entre ces deux approches est la gamme de l'espacement inter-électrode (de quelques dizaines de micromètres (première approche) à des centaines de micromètres qui peut être obtenu par le second procédé de fabrication). En outre, nous avons démontré le fonctionnement électrochimique des deux architectures d'électrodes par l'évaluation en voltampérométrie cyclique à balayage de la réaction de réduction de l'oxygène qui a lieu à la surface des deux électrodes.

Le plus grand avantage des stratégies présentées est la possibilité de contrôler finement l'épaisseur de l'électrode (et donc des surfaces actives), la séparation spatiale entre l'électrode interne et externe (c'est-à-dire le volume d'électrolyte qui peut être stocké dans l'interstice) et la taille des pores (en changeant le diamètre des particules colloïdales de silice).

Dans la partie suivante (chapitre 3), nous démontrons la possibilité d'utiliser des électrodes macroporeuses pour la fabrication d'une biocathode enzymatique. Les substrats d'or macroporeux ont été choisis comme candidats prometteurs pour améliorer les performances électrochimiques (courant et puissance de sortie) d'une biopile enzymatique à glucose/oxygène en raison de leur surface active élevée.

La voltampérométrie cyclique a été utilisée pour l'électrodéposition d'un polymère rédox d'osmium et d'un adduit avec une bilirubine oxydase (BOD)/polymère-Os dans la structure macroporeuse. Nous avons également étudié la réduction bioélectrocatalytique d'oxygène à la surface des électrodes modifiées correspondantes, ainsi que la stabilité du film bioélectrocatalytique ainsi obtenu.

Enfin, notre contribution au développement d'un nouveau type de biocapteur à base de cellules entières est décrite dans le chapitre 4. Nous avons utilisé l'électrochimie comme outil pour guider les cellules d'insulinome pancréatique sensibles au glucose (INS832/13) et les îlots de Langerhans dissociés vers des microélectrodes. Ceci a été réalisé au moyen d'une séquence de sauts de potentiels optimisée qui a été générée au niveau d'un ensemble de microélectrodes. Le but principal de l'utilisation du phénomène d'électrophorèse pour l'immobilisation des cellules pancréatiques sur la surface de microélectrodes est l'amélioration de la qualité du signal extracellulaire de mesure dépendant du glucose, ce qui conduit à l'augmentation des performances globales du biocapteur correspondant (par exemple en obtenant une meilleure sensibilité).

**Mots clés :** Langmuir – Blodgett; cristaux colloïdaux; matrice sacrificielle de matériaux; électrodéposition; dispositifs électrochimiques; électrodes macroporeuses; biopiles; biocathode; Bilirubin oxydase; polymère-rédox d'osmium; cellules bêta.

# CONTENTS

<b>Introduction .....</b>	<b>1</b>
 <b>1. Colloidal crystals : Assembly and characterisation.....</b>	<b>4</b>
1.1. A self-assembly of colloidal particles: Mechanism and driving forces .....	4
1.2. An overview of the most utilized methods for the synthesis of colloidal-crystals .....	9
1.2.1. Sedimentation and vertical deposition .....	9
1.2.2. Electrophoretic and dielectrophoretic synthesis of colloidal crystals.....	13
1.2.3. Langmuir – Blodgett technique for the synthesis of colloidal crystals.....	16
Literature.....	21
 <b>2. Development of coaxial macroporous electrode architectures by infiltration of colloidal crystals .....</b>	<b>23</b>
2.1. Overview of common methods for the infiltration of colloidal crystals.....	24
2.1.1. Chemical vapor and atomic layer deposition .....	24
2.1.2. Techniques for the fabrication of macroporous materials via infiltration of liquid precursors .....	28
2.1.3. Electrodeposition for the synthesis of (macro)porous materials .....	32
2.2. Synthesis of macroporous gold and nickel electrodes .....	34
2.3. Electrochemical characterization of macroporous gold electrodes .....	41
2.4. Bottom-up generation of miniaturized coaxial and macroporous double electrodes with tunable porosity .....	45
2.5. Alternative design of a coaxial macroporous two-electrode electrochemical cell .....	51
2.6. Conclusion.....	55
Literature .....	57
 <b>3. Macroporous electrodes for the fabrication of a biocathode .....</b>	<b>61</b>
3.1. (Bio)fuel cells: Basic principles and key performance characteristics .....	61
3.2. Electron transfer mechanisms: Direct and mediated electron transfer.....	68
3.3. The enzymes for biocathodes: Multicopper oxidases (MCOs).....	79
3.4. Cylindrical macroporous electrodes for a BOD (fung. <i>Magnaporthe oryzae</i> ) based biocathode.....	81
3.5. Conclusions and perspectives .....	92
Literature .....	93

<b>4. Guiding pancreatic <math>\beta</math>-cells to target electrodes: towards a whole-cell biosensor for diabetes</b>	<b>97</b>
4.1. Electrical activity of pancreatic $\beta$ -cells	99
4.2. Directed motion of charged objects in electric fields	104
4.3. Guiding pancreatic $\beta$ -cells to target electrodes	107
Literature	116
<b>5. Experimental section</b>	<b>117</b>
<b>1. Synthesis and covalent modification of silica particles</b>	<b>117</b>
1.1. Synthesis of silica nanoparticles	117
1.2. Covalent functionalization of silica nanoparticles	119
1.3. Purification of covalently modified silica nanoparticles	120
<b>Fabrication of colloidal-crystal template</b>	<b>120</b>
1.4. Cleaning of silica nanoparticles	120
1.5. Resuspension of silica nanoparticles	121
1.6. Preparation of Langmuir- Blodgett (LB) films	121
<b>2. Preparation of inner electrode and outer electrodes (procedure based on the glass capillary approach)</b>	<b>122</b>
2.1. Preparation of the samples	122
2.1.1. Cleaning and hydrophilisation of the samples	122
2.2. Electroless metallization of glass capillaries	123
2.3. Preparation of the inner electrode	124
2.3.1. Electrical addressing of the inner electrode	124
2.4. Preparation of the outer electrode	124
2.4.1. Electrical addressing of the outer electrode	125
2.5. Etching of silver and nickel layers	125
2.6. Sealing of the assembled structure	125
2.7. Etching of silica nanoparticles and glass capillary	125
2.8. Preparation of coaxial and macroporous two-electrode electrochemical cell	125
2.8.1 Electrodeposition of alternating metal layers	126
2.8.2 Etching of the nickel layer	126
2.8.3 Stabilisation of the coaxial structure	127
2.8.4 Dissolution of silica nanobeads	127
2.9. Electrochemical characterization	127
<b>3. Macroporous electrodes for the fabrication of a biocathode</b>	<b>128</b>
3.1. Cleaning of the bare and macroporous gold electrodes prior to the electrochemical characterization	128
3.2. Electrochemical determination of the electroactive surface area	128
3.3. Preparation of BOD and polymer solutions and (co)electrodeposition	129
3.3.1 Preparation of Os-polymer solution and electrodeposition of the polymer	129
3.3.2. Preparation of the BOD/Os-polymer mixture and their coelectrodeposition	129

3.3.3. Testing of the Os-polymer and BOD/Os-polymer modified electrodes .....	130
3.4. Stability test of BOD/Os-polymer modified electrodes .....	130
<b>4. Guiding pancreatic <math>\beta</math>-cells to target electrodes in a whole-cell biosensor for diabetes .....</b>	<b>130</b>
4.1. Preparation of low-conductivity buffer .....	130
4.2. Micro-electrode arrays (MEAs) .....	131
4.3. Spatial manipulation by electrophoresis .....	131
<b>Conclusions and perspectives .....</b>	<b>133</b>
<b>Résumé.....</b>	<b>138</b>

## LIST OF ABBREVIATIONS

Abbreviation	Meaning
AC	Alternating current
ADP	Adenosine-diphosphate
Adr	Adrenaline
ALD	Atomic layer deposition
AIDH	Alcohol dehydrogenase
ATP	Adenosine triphosphate
AuNP	Gold nanoparticles
BOD	Bilirubin oxidase
BV	Benzyl viologen
C.E.	Counter electrode
ccd	Catalytic current decrease
CM	Clausius – Mossoti
CNP	Carbon nanopowder
CRE	Carbon rod electrode
CVD	Chemical vapor deposition
DC	Direct current
DEP effect/method	Dielectrophoretic effect/method
DET	Direct electron transfer
DLVO theory	Derjaguin-Landau-Verwey-Overbeek theory
DMSO	Dimethyl sulfoxide
DySA	Dynamic self-assembly
EBFC	Enzyme based biofuel cell
EHDF	Electrohydrodynamic flow
EMF	Electromotive force
ESA	Equilibrium self-assembly
ET	Electron transfer
f.c.c.	Face-centered-cubic
FAD	Flavine adenine dinucleotide
fd	Filamentous bacteriophage
GC	Glassy-carbon
Gli	Glibenclamide
GLUT2	Glucose transporters
GOx	Glucose-oxidase
Hase	Hydrogenase
HF	Hydrofluoric acid
HRP	Horseradish peroxidase



<b>IHEISA</b>	Isothermal heating evaporation-induced self-assembly
<b>INS cells</b>	Insulinoma cells
<b>ITO</b>	Indium Tin oxide
<b>IUPAC</b>	International Union of Pure and Applied Chemistry
<b>K<sub>ATP</sub>-channels</b>	Adenosine triphosphate - dependent potassium channels
<b>K-Ca channels</b>	Calcium - dependent potassium-channels
<b>K-DR channels</b>	Delayed rectifying potassium-ion channels
<b>Lac</b>	Laccase
<b>MBFC</b>	Microbial biofuel cell
<b>MCOs</b>	Multicopper oxidases
<b>MEA*</b>	Metal/electrode assembly
<b>MEA**</b>	Microelectrode arrays
<b>MET</b>	Mediated electron transfer
<b>MP8</b>	Microperoxidase
<b>MWCNT</b>	Multiwall carbon nanotubes
<b>NADH</b>	Nicotinamide adenine dinucleotide
<b>NCDs</b>	Noncommunicable diseases
<b>NP</b>	Nanoparticles
<b>OCV</b>	Open circuit voltage
<b>PANI</b>	Polyaniline
<b>PB</b>	Phosphate buffer solution
<b>PEM</b>	Proton-exchange membrane
<b>PMMA</b>	Polymethylmethacrylate
<b>PPy</b>	Polypyrrole
<b>PQQ</b>	Pyrroloquinoline quinone
<b>PS</b>	Polystyrene
<b>PZC</b>	Point of zero charge
<b>R.E.</b>	Reference electrode
<b>SAM</b>	Self-assembled monolayers
<b>SBP</b>	Soybean peroxidase
<b>SEM</b>	Scanning electron microscopy
<b>SGE</b>	Spectrographic graphite electrode
<b>TCA cycle</b>	Tricarboxylic acid (Krebs) cycle
<b>TMA</b>	3-methylaluminium
<b>UV</b>	Ultraviolet
<b>vdW</b>	van der Waals
<b>W.E.</b>	Working electrode
<b>WHO</b>	World Health Organization

---

## INTRODUCTION

### **Introduction**

The demand for miniaturized and eventually implantable electrochemical tools such as biosensors, biofuel cells and batteries has led to the development of new technologies to overcome existing problems related to large dimensions, low current densities, and insufficient power output of such devices. The improvement of their electrochemical performance can be partially addressed by the choice of appropriate electrode materials, architectures and surface properties. The synergy that exists between these three structural characteristics can be exploited in the field of the fabrication of miniaturized electrochemical platforms. Since the limits for scaling down electrochemical devices is determined by the possibility to decrease the geometric dimensions of their corresponding electrodes (or alternatively to remove some of their bulky elements), the right choice of electrode material is of essential importance. However decreasing the size of electrodes intrinsically leads to a loss of current or power, which can be in many cases compensated, at least partially, by increasing artificially their active surface area. This can be achieved either by using surfaces with a high roughness factor, or by employing porous electrode materials. We have, in the present work, focused our efforts on this latter aspect.

Since the concept of porous electrodes was introduced one century ago, many efforts have been made in designing new synthetic procedures for their fabrication. Furthermore, the variety of existing techniques, as well as the diversity of macroporous materials, allows tailoring of electrode surfaces in order to obtain an optimal electrochemical response for a given electrochemical system. In general, (macro)porous materials can be synthesized through the filling of a temporary template with the desired material. Depending on the type of materials that are used as a template, these approaches can be classified as: 1. hard (e.g. track etched membranes) and 2. soft template (e.g. mesoporous structure obtained by electrodeposition of metals through the water domains of a lyotropic liquid crystalline phase) routes. Another way that follows the hard template route is based on the infiltration of nanoparticle templates by electroconductive materials (e.g. metals or electron-conductive polymer).

In the present work, and as discussed in the first chapter, highly organized macroporous electrodes are prepared by the infiltration of silica based nanoparticle templates (colloidal crystals) with solid and electro-conductive materials. For this purpose, the silica colloidal crystals were synthesized by the Langmuir-Blodgett (LB) technique, which has been selected as the best option among other existing methods. The main advantage of the LB procedure is a

perfect control of the number of silica nanoparticle layers, absence of cracks (one of the most important prerequisites for the fabrication of high quality macroporous electrodes) in the synthesized colloidal crystals and the possibility to fabricate ordered hierarchical structures by depositing layers of beads with different diameters.

The next chapter will mainly focus on the fabrication of miniaturized coaxial double electrodes based on macroporous gold as a structural material. Due to their high active surface areas, (macro)porous materials are perfect candidates for the design of miniaturized electrochemical devices. The increase in the electrode's specific surface area allows a significant decrease of the footprint of the final device. The fabrication of double-electrode structures can be carried out by following two different procedures. The first one is based on electrodeposition of alternating gold-nickel-gold metal layers through a pre-synthesized cylindrical colloidal crystal template ( $\emptyset_{(\text{silica beads})} = 600 \text{ nm}$ ). This step is followed by consecutive etching of the "sacrificial" nickel layer, structural stabilization and etching of the silica beads from remaining gold/silica composite. The presented strategy introduces a new, straight-forward way to fabricate miniaturized cylindrical double-electrode electrochemical cells (with an electro-active volume in the range of  $0.1 \mu\text{l}$ ) with tunable active surface area (by changing the thickness of the porous gold layers), inter-electrode distance (by controlling the thickness of nickel layer) and cell volume. Another strategy that is described in the same chapter relies on the assembly of two independently prepared cylindrical macroporous electrodes. It also presents a new way to elaborate macroporous electrodes by electrodeposition of gold through the silica-bead template that has been generated on the surface of a metalized glass capillary. As will be discussed, both architectures show good structural stability (the lack of intrinsic short-circuit is confirmed by cyclic voltammetry) and an electrochemical functionality which is demonstrated by the electroreduction of oxygen at each of two independent electrodes.

The possibility to utilize cylindrical macroporous electrodes for the fabrication of a biocathode (and eventually a biofuel cell) is the focus of Chapter 3. The four-electron oxygen reduction is a challenging reaction since the power output of most of fuel/oxygen biofuel cells is limited by the activity of the biocathode. This is especially pronounced in environments where the oxygen concentration is very small (e.g. the subcutaneous oxygen concentration is only  $0.2 \text{ mM}$ ). An improvement of the performance of biofuel cells can be expected by increasing the active surface area of the biocathode or by enhancing the efficiency of the wiring of enzymes with the electrode surface. The present strategy for the fabrication of a macroporous biocathode relies on electrochemically assisted codeposition of Bilirubin oxidase (BOD, obtained from the fungal source - *Magnaporthe oryzae*) as a biocatalyst for oxygen-reduction and an osmium based

redox polymer which serves as a redox mediator. Coelectrodeposition of enzymes and Os-redox polymers is based on the simultaneous chemical cross-linking (between enzyme molecules and the reduced form of the Os-redox polymer) and precipitation of the BOD/Os-polymer adduct. The bioelectrocatalytic film formed that way shows activity with respect to oxygen reduction, and an enhanced structural stability in comparison with non-porous electrodes. Coelectrodeposition of enzymes and Os-based polymers is a convenient way to immobilize bioelectrocatalytic films. It can be easily implemented in the fabrication of a miniaturized macroporous and coaxial glucose/oxygen biofuel cell since it allows selective modification of each coaxial macroporous electrodes (with the corresponding bioelectrocatalytic film) independently.

In the last chapter we discuss the development of a whole cell-based bioelectronic glucose sensor that exploits the multi-parametric sensing ability of pancreatic islet cells for the treatment of diabetes. Pancreatic beta cells are known as one kind of electrogenic cells (along with neurons and cardiac muscle cells) whose electric activity relies on the concentration of glucose and some other nutrients (certain amino acids and fatty acids). Therefore, they are excellent candidates for a whole-cell based glucose biosensor since they were shaped during the evolution for this purpose. The sensitivity to changes in glucose level distinguishes them from other recognition elements that are exploited in glucose biosensors. The electrical signal generated by the activity of beta cells can be recorded using micro-electrode arrays (MEA). However, the quality of the signal and the overall sensor performance relies on a close cell-electrode interaction. In order to improve this interaction and minimize the distance between the electrode and the immobilized cells, a non-invasive electrophoretic method that exploits the intrinsic electrical properties (negative charge of cell membrane) of these types of cells to guide them toward targeted electrodes (by moving the cells in the applied electric field) is the focus of this chapter. It will be shown that the cells are able to retain their viability after the electrophoretic treatment.

In conclusion this thesis should demonstrate that by controlling the nature and the use of appropriate electrochemical tools new application perspectives can be opened in the broad field of bioelectrochemistry.

---

*CHAPTER 1*

COLLOIDAL CRYSTALS: ASSEMBLY AND  
CHARACTERIZATION

### 1.1. A Self-assembly of colloidal particles: Mechanism and driving forces

Mimicking of complex natural structures has become one of the commonly used tools in the field of nano-structuration of materials. Some complex structures that can be found in Nature are so complex in their architecture that we cannot simply copy them. Others, less demanding structures, can be efficiently replicated by nowadays existing engineering methods. This is facilitated by a variety of different synthetic materials. The main benefit of such an approach allows us to adapt and to exploit the different physical properties that such kind of materials offer [1].

Self-assembly is a process by which the discrete components (such as atoms and molecules) spontaneously organize into a two or three-dimensional geometry due to various specific interactions. A broader definition of self-assembly allows to include also spontaneous organization of much bigger building units such as spherical colloidal particles with various diameters [2,3] and morphology. If the particles are arranged in a highly ordered manner, the so obtained structure can show optical properties (e.g. diffraction of light) just like real crystals [4]. This regularity arises from the long range of order of the building units which are preferentially forming a face-center-cubic (f.c.c.) crystal lattice with hexagonal arrangement [5]. This kind of materials are often named synthetic opals due to their similarity to natural gem opals (**Figures 1.1a and b**). They show the same optical properties which are originating from the diffraction of visible light at a periodically repeated crystal unit. The crystalline structure of gemstone opals consists of an ordered assembly of silica nanoparticles, which are regularly packed during the years of geological maturing (sedimentation and compression) [6].

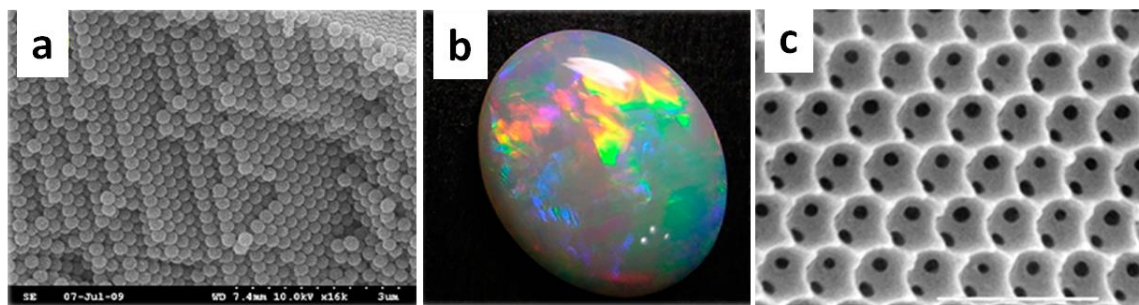


**Figure 1.1.** (a) SEM image of an artificial silica colloidal crystal (artificial opal) and (b) natural gemstone opal [6]. SEM image of an inverse opal structure obtained after infiltration of a silica-based colloidal crystal by a phenolic resin and its subsequent etching (c) [7].

Another interesting feature of artificial opals is the tuneability of their photonic properties. Photonic crystals are a group of materials that could be used for light manipulation due to their photonic band-gap which allows the propagation of certain wave-lengths while others are prohibited.

This feature derives from the periodic modulation of the refractive index within the colloidal-crystal, due to the periodic modulation in the composition of material which is building up the structure (*i.e.* silica/air) [6].

Assuming a f.c.c. crystal unit cell, based on geometrical considerations it can be theoretically calculated that the free space within colloidal-crystals occupies 24% of the total crystal volume. This space can be easily filled-up with different materials that are remaining after removing of the colloidal template. The so-obtained highly porous material, resembling a honeycomb structure is called an “inverse opal” (**Figure 1.1c**) since it presents the replica of the starting template [4,7,8]. As will be described in more detail in **Chapter 3**, those materials already found applications in the field of electrochemistry.

From the thermodynamic point of view, self-assembly processes can be divided into two groups:

1. Static (equilibrium self-assembly, ESA) where the system resides in its local minimum. During its formation the system may adsorb energy from the environment (*e.g.* stirring, heating *etc.*) but once it is formed it resides in its stable state [9].

ESA can be driven either by energetic or entropic aspects, or both of them at the same time.

- 1.1. An example for the energetically driven self-assembly is the formation of sphalerite - (ZnS) and diamond-like crystals consisted of oppositely charged Au ( $\varnothing = 5.1$  nm) and Ag ( $\varnothing = 4.8$  nm) nanoparticles (NP). Since the metallic NPs are not charged by their nature, appropriate surface modification is required. This could be accomplished through the formation of self-assembled monolayers of carboxyl and amine based thiols that are known to exhibit high affinity for gold and silver surfaces. In this case, the formation of a “NP ion” based lattice arises from the electrostatic interaction in between oppositely charged particles. **Figure 1.2b** presents the morphology of crystals obtained by dissolution of a Au-Ag NP precipitate in H<sub>2</sub>O/DMSO (1:4 v/v), which is followed by slow ( $\approx 12$ h) evaporation of water. The quality and the amount of the crystals (**Figure 1.2**) obtained in this way was significantly increased when one of the components of the system (*e.g.* positively charged Ag NP obtained through chemical modification with HS(CH<sub>2</sub>)<sub>11</sub>NMe<sub>3</sub><sup>+</sup>Cl<sup>-</sup>) was polydisperse ( $\sigma$  (AgNP) = 45% where  $\sigma$  is a standard deviation of the nanoparticle diameter) and small Ag NP were present in the suspension along with negatively charged Au NP (obtained by chemical modification of Au NP ( $\sigma = 20\%$ ) with HS(CH<sub>2</sub>)<sub>10</sub>COOH). The role of the small Ag NP is to screen the effective charge (decrease effective screening length) of the bigger oppositely charged Au NP and in this way moderate the attraction forces between them. As a consequence of this effect, bigger NP do not randomly aggregate but rather form regular assemblies (crystals) due to the moderation of the electrostatic attraction potential [10].



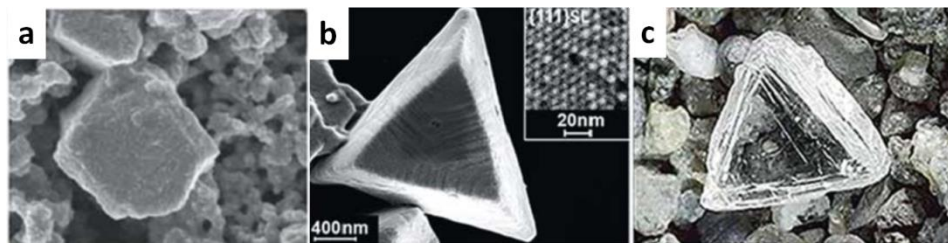


**Figure 1.2.** SEM images of the crystal morphologies obtained by self-assembly of functionalized Au and Ag NP. (a) Poorly defined crystalline morphology of a precipitate obtained by mixing oppositely charged and monodispersed Au NP. (b) The morphology of a truncated tetrahedron was obtained by mixing monodisperse negatively charged Au NP with polydisperse positively charged Ag NP. The so-obtained crystals possess a diamond-like crystal lattice, present in natural diamond c) [10].

- 1.2. Besides electrostatic interactions (as part of energetically driven self-assembly), self-assembly can be influenced by entropy. From thermodynamic considerations, the spontaneity of some processes (at constant P and T) is determined by a change of the Gibbs function ( $\Delta G < 0$  kJ – spontaneous process,  $\Delta G > 0$  kJ not likely to occur spontaneously) and can be expressed as  $\Delta G = \Delta H - T \cdot \Delta S$ , where:  $\Delta H$  – change of the systems enthalpy (kJ), T- temperature (K) and  $\Delta S$  – change in entropy (kJ). If the entropy of the system becomes dominant over the enthalpy term, then the self-assembly of building units can be entirely driven by entropy. An interesting example that illustrates this feature is the self-assembly of like-charged virus rods, where the electrostatic interactions are all repulsive. In disorganized states, the translational and rotational motions of virus nanorods are not free as one could expect since the virus particles are constantly bumping against each other. When the rods are organized in layers of a smectic phase, the degree of freedom increases due to the possibility to freely exchange their position with each other within the layer as a compensation of translational and rotational restrictions (**Figure 1.3**). This leads to an increase in entropy and therefore the decrease of the global energy of the system [11–13].

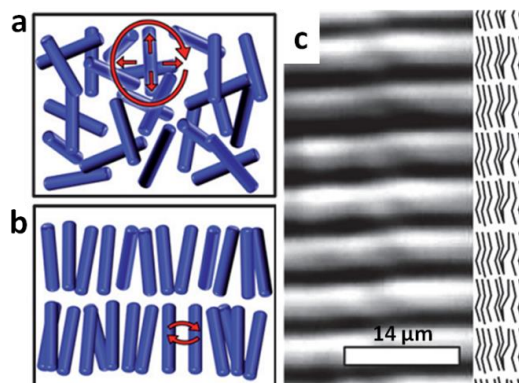


**Figure 1.3** (a) and (b) Schematic representation of self-assembly of the filamentous (rod-like) viruses influenced by entropy; (c) Images of the ordered (smectic) phase of filamentous bacteriophage (*fd*) (contour length = 1.2  $\mu\text{m}$ ) mutant viruses [11,12].

- 1.3. The most abundant mechanism of self-assembly is influenced by both, the enthalpy and the entropy. The example that illustrates the influence of those gathered parameters is the micellar self-assembly of surfactant molecules with different structures. Unlike the gemini cationic double-tail surfactant molecules  $[(C_mH_{2m+1}(CH_3)_2N-(CH_2)_k-N(CH_3)_2C_nH_{2n+1})Br_2]$ , monomer molecules  $[(CH_2)_3-NC_nH_{2n+1}]Br$  are forming micelles thanks to the predominant influence of entropy. This can be explained by from the exclusion of water that is surrounding surfactant molecules (due to unfavorable interactions between hydrophobic tails of surfactant molecules and water molecules). The calorimetric investigation of the formation of micelles shows that the involvement of entropy and enthalpy is dependent on chemical structure of the surfactant. It has been demonstrated that the change of the micellar enthalpy for  $[C_{12}H_{25}(CH_3)_2N-(CH_2)_6]Br$  contributes much less to the formation of the micelles then in the case of gemini molecules such as  $[C_{12}H_{25}(CH_3)_2N-(CH_2)_{12}-N(CH_3)_2C_{12}H_{25}]Br$  [11,14].
2. Dynamical self-assembly (DySA) is another way by which building units can organize themselves. In contrast to equilibrium self-assembly, the system is kept far from equilibrium through a constant input and dissipation of energy (**Figure 1.4a**) [11]. For example, the energy of a magnetic field can be used to direct the assembly of ferromagnetic doped polymer pallets towards an axis of rotation of an externally placed magnet. At the same time the rotation of the external magnet causes the consequent rotation of the magnetic polymer discs. This in turn causes a hydrodynamic flow of the surrounding liquid (ethylene-glycol/water) which results in repulsion of the discs. The obtained assembly is the result of the superposition of two differently directed forces; the attractive magnetic and the opposing hydrodynamic force (**Figure 1.4b and c**) [15].

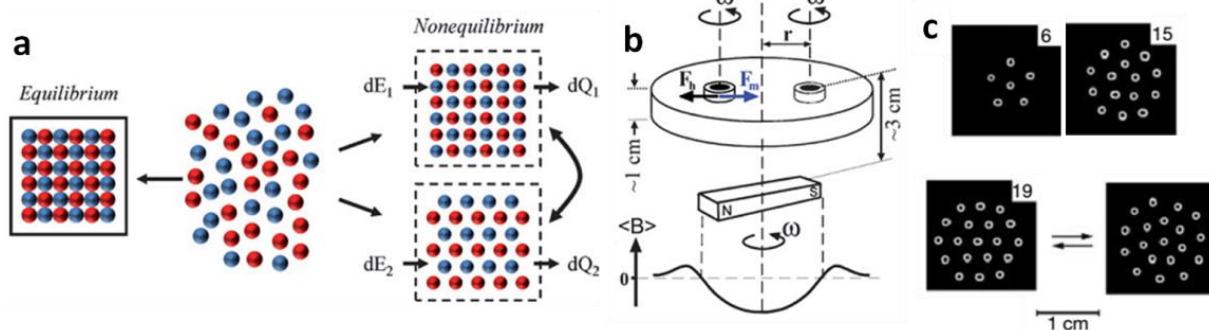


**Figure 1.4.** (a) Schematic representations of the difference between equilibrium (static) and DySA. In the first case, once the system is settled in its energy minimum, it is closed for the energy exchange with an environment. In DySA, the flux of delivered energy is used by the system to “self-assemble” (one portion is dissipated as a heat) and to reside in one of the several metastable states [11]. (b) Representation of the magnetohydrodynamic self-assembly guided by two opposing forces (attractive magnetic force  $F_m$  and repulsive hydrodynamic force  $F_h$ ) [11]. (c) An example of DySA of magnetic discs (the number of objects is indicated in corresponding insets). The example of the system with 19 discs illustrates a transition between two metastable states influenced by the rotational speed of an externally placed magnet [15].

As mentioned above, self-assembly can be extended over a big range of sizes of building units (atoms, molecules or colloidal particles). Besides the thermodynamic consideration, the self-assembly of colloidal particles can be described in the light of different forces that are acting upon a whole process and which can be ambivalent in their nature. The fine balance between attractive and repulsive interactions determines the possibility of aggregation of colloidal particles.

The first group of colloidal interactions is dominated by the balance between the attractive van der Waals (*abr.* vdW; dipole-dipole and dipole-induced dipole) and opposing electrostatic interactions. The second one is based on repulsion between electric-double layers of interacting particles. Those interactions present the basis of the Derjaguin-Landau-Verwey-Overbeek (DLVO) theory which explains the balance of forces that plays an important role in the self-assembly process. Regarding the DLVO theory, the total potential energy ( $U_{\text{total}}(x)$ ) of the assembly is given (**Equation 1**) as a contribution of repulsive ( $U_r(x)$ ), attractive ( $U_a(x)$ ) and external force ( $U_{\text{ext.}}(x)$ ). The latter one becomes an important constituent of the system (comparable to attractive vdW and electrostatic repulsion) whenever the building units are in the colloidal range.

$$U_{\text{total}}(x) = U_a(x) + U_r(x) + U_{\text{ext.}}(x) \quad \text{Equation 1.1}$$

Unlike the long-range vdW and electrostatic interactions, depletion, solvation, hydration and steric interactions are short range. Therefore, their influence has to be considered as the interparticle distance decreases.

A second group of forces are not arising from molecular interactions. They become an important part of the energetic landscape in colloidal systems since they originate from various colloidal phenomena. This group includes capillary forces, gravity, osmotic pressure, electrophoretic force, magnetophoretic force and force by flow. Since they have a similar length-scale as colloidal forces they have to be included into the description of self-assembly. Those forces can be attractive or repulsive just like in the case of the colloidal one. One general characteristic of colloidal forces is that they do not exhibit directionality but rather random behavior. This is the reason why colloidal self-assembly is a random process especially if no external influence is involved. Most of externally applied forces possess directionality, which can be exploited in colloidal systems. Due to the possibility to adjust their intensity, external forces can take control over the assembly process and in that way a unidirectional action can be implemented into a system (**Figure 1.5**). Typical examples of external forces are capillary forces, electric and magnetic fields, spatial confinement, mechanical forces, centrifugal forces *etc.* Since the colloidal crystals present highly organized structures, the directionality is of essential importance due to the ability to affect some of the structural parameters (*e.g.* number of layers, precise position of colloidal particles).

Some approaches, based on forces mentioned above, present popular ways to synthesize colloidal-crystals[3]. They will be in the focus of the following subchapters.

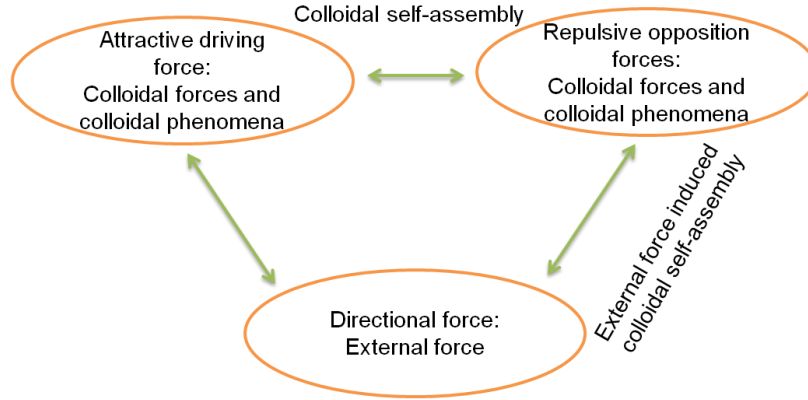


**Figure 1.5.** Principal scheme of the force balance and external force induced colloidal self-assembly (Adapted from [3]).

## 1.2. An overview of the most utilized methods for the synthesis of colloidal-crystals

### 1.2.1. Sedimentation and vertical deposition

The sedimentation technique presents one of the simplest and most straightforward methods for the fabrication of colloidal crystals. Based on sedimentation, the self-assembly process relies on the precipitation of colloidal particles in ordered arrays under the action of the gravitational force that is known to have an impact on every object within its field. This presents an excellent example of directionality that can be easily imposed on the system. The motion of colloidal particles in the gravitational field depends on their diameter and can be described by the well-known Stokes equation for spherical objects (**Equation 1.2**) [16,17]:

$$v = d^2(\rho_p - \rho_l)g/18\eta_l \quad \text{Equation 1.2.}$$

where:  $v$  is the speed of sedimentation,  $d$  is the diameter of colloidal particles,  $\rho_p$  and  $\rho_l$  are the corresponding densities of the colloidal particles and the liquid medium, respectively,  $g$  is the gravitational acceleration and  $\eta_l$  is the viscosity of the liquid medium. Besides the diameter, sedimentation of colloidal particles is dependent on their volume fraction in the suspension [18].

It can be concluded from the equation above that bigger particles will precipitate much faster than smaller ones.

As expected, if the particle size is too small ( $d < 100$  nm) the sedimentation process under normal gravity is too slow to be useful [18].

Theoretical calculations have shown that nanoparticles are preferably self-assembling in fcc crystalline arrangement due to the lower energy requirement compared to the hexagonal close packing (hcp), although this difference is very small ( $\Delta F \equiv (F_{\text{hcp}} - F_{\text{fcc}})/RT = 0.005$ , where  $\Delta F$  is a difference in the Helmholtz's free energy) [19,20]. This result has been confirmed experimentally as shown for silica-based colloidal-crystals (**Figure 1.6a and b**) with different lattice parameters which are varied by the sphere diameter [21].

The influence of gravity is comparable with the kinetic (thermal) energy ( $\propto kT$ ,  $k$  is the Boltzmann constant) of the particles which impose the conclusion that the system is close to thermodynamic equilibrium. Due to the long time required for the sedimentation, the rearrangement of colloidal particles which are not positioned in a local energy minimum takes place and in that way an ordered close packing of the spheres can be accomplished [22].

Due to the fact that normal gravity requires a long time (weeks or even few months) to influence colloidal crystal growth, centrifugal forces can be exploited in a colloidal systems to accelerate the self-assembly (**Figure 1.6c**) [23].

Despite their simplicity, sedimentation and centrifugation have certain drawbacks concerning the quality of the obtained colloidal-crystals. It has been observed that the structures synthesized in this way possess defects and polycrystalline domains of different sizes, while their thickness is not easy to control.

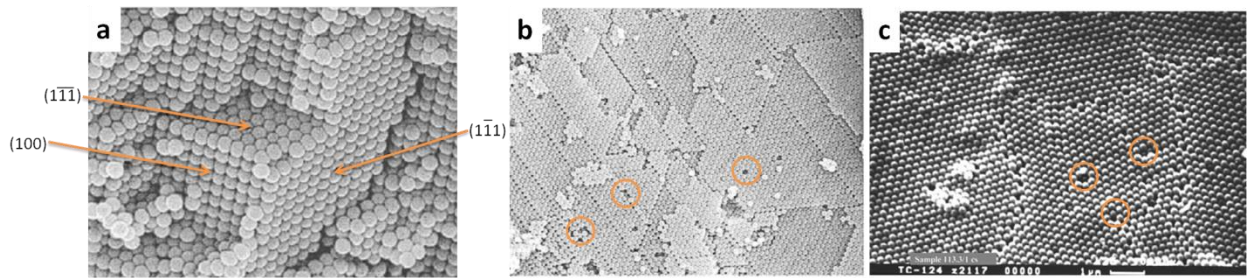


**Figure 1.6.** SEM images of the cleaved edge (a) and large internal (111) domain (b) of an fcc structure obtained by sedimentation of 415 nm silica nanoparticles onto a polymethylmethacrylate (PMMA) surface. The experimental observation indicates that all arrangements are compatible with the fcc crystalline structure [21]; c) An example of silica based colloidal crystal synthesized by means of centrifugal forces assisted sedimentation with an acceleration of  $8750 \text{ m/s}^2$ . Both structures present in this figure exhibit numerous vacancies (marked on the images with orange circles) and distinctly separate monocrystalline domains (present on figure (c) with apparent grain boundaries) [23].



Another way to synthesize colloidal crystals is based on the evaporation of a solvent from the suspension of colloidal particles.

This process, known as the evaporation assembly, can be summarized in a few steps (**Figure 1.7**): 1. **Nucleation** – the process that refers to the formation of colloidal-crystal nuclei due to the initial assembly of colloidal particles. This is governed by attractive lateral capillary forces whose intensity rise (compared to the thermal energy of the colloidal particles) as solvent thickness decreases within the wetting film; 2. **Convective** delivery of nanoparticles from the bulk to the wetting film. The flow of particles is driven by solvent flux ( $J_w$ ) induced by its evaporation ( $J_e$ ). The flow of solvent imposes hydrodynamic pressure onto the wetting film and in that way directs the nanoparticles towards the formed nuclei; 3. **Capturing** of incoming particles within an array by action of attractive capillary forces [24,25].

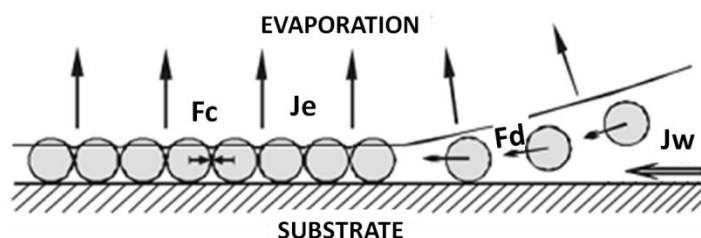


**Figure 1.7.** The schematic of colloidal self-assembly driven by evaporation of water from a suspension of colloidal particles ( $F_c$ – capillary force,  $F_d$ – hydrodynamic force,  $J_e$  – evaporation flux,  $J_w$  – incoming water flux) (adopted and modified from [25]).

The method that presents an extension of the evaporation technique is the evaporation induced vertical deposition. The only difference here is the vertical [26,27] or slightly tilted [28] position of the substrate within the colloidal suspension. As the solvent evaporates a regular array of colloidal particles is formed within the wetting film. The main advantage of vertical deposition comparing to simple evaporation technique is a better quality of the colloidal deposit in terms of size of crystalline domains and a reduced number of defects (*i.e.* vacancies and dislocations) present in the film due to the directional “crystallization” in the meniscus [26]. To control those parameters, temperature and polydispersity (it should be less than 8%) of the system seems to be the most important variables [26,29]. The thickness of the deposit can be varied by multiple coatings and the volume fraction of the spheres [29].

The first prerequisite for the successful vertical deposition of particles is that the speed of their sedimentation is lower than the growth rate of the crystal. Therefore, the utilization of vertical deposition for the synthesis of colloidal crystals mainly depends on the density and size of the colloidal particles and the evaporation rate of the solvent. [26].

Convection induced by thermal gradients (CITG) [30] in an ethanol suspension of silica particles and mechanical agitation [31] (slight stirring) can be used to avoid precipitation. The obtained array of colloidal particles shows good quality (**Figure 1.8 a and b**).

Another approach based on convective agitation of the suspension is isothermal heating evaporation-induced self-assembly (IHEISA). The principle of HEISA is similar to the CITG method with the only difference that the system is isothermally heated close to the boiling point of the solvent (i.e. methanol, ethanol). Besides the uniformity of the film and an increased rate of formation of the colloidal crystal (1cm/h), using this technique allows preparing “sandwich” structures made of particles with very different diameters (**Figure 1.8c**) [26].

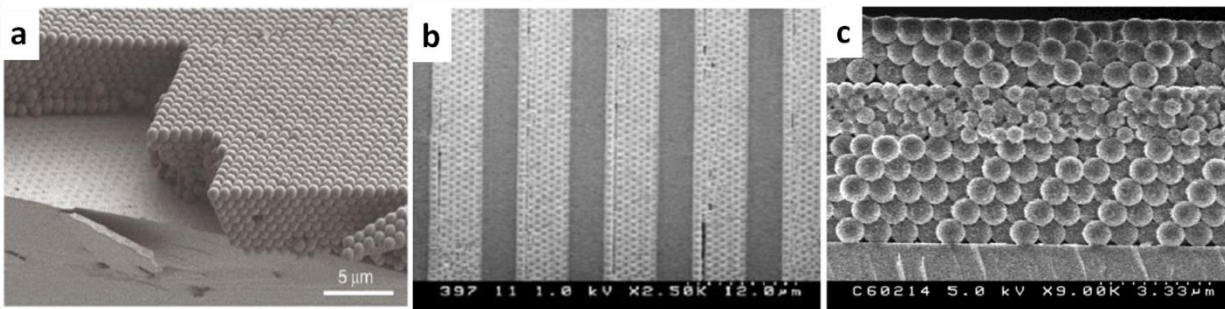


**Figure 1.8.** (a) SEM image of a colloidal crystal obtained by vertical deposition of silica particles ( $\varnothing = 855$  nm) onto the surface of a silicon wafer by means of vertical deposition enhanced by thermal gradient convection [30]; (b) Global view of a silica ( $\varnothing = 850$  nm) opal structure within rectangular shaped polyurethane microchannels. During the assembly of the structure, the colloidal suspension in ethanol was slightly stirred [31]; (c) An example of an ABA (each letter denotes a different diameter of silica nanoparticles) sandwich structure obtained by alternating deposition of 850 nm and 250 nm silica nanoparticles by IHEISA [26].

As mentioned before, colloidal films prepared by vertical deposition methods show less defects, cracks and polycrystallinity in comparison with samples prepared by sedimentation as depicted in **Figure 1.9a** and **b**. For instance, dislocations are the consequence of polydispersity and the presence of colloidal particles with significantly different diameters (usually smaller) than the original one. This causes the formation of grain boundaries in the structure. Another type of defects are micro-cracks whose mechanism of formation is related to drying of the adsorbed solvent layer on the surface of the colloidal particles. This results in the shrinkage of the self-assembled structure (the inset in the **Figure 1.9b**).

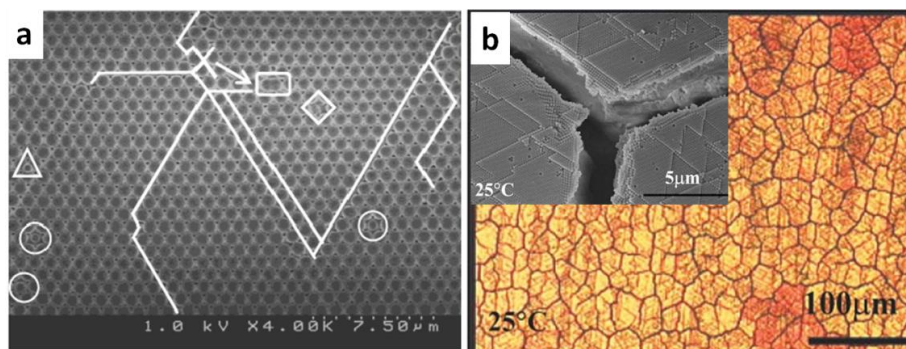


**Figure 1.9.** (a) Top-view SEM image of a silica colloidal crystal obtained by IHEISA. Different kinds of defect are depicted as follows: the white triangles – small spheres occupying an interstitial sites; the circles - space occupied by spheres with a smaller diameter than the original one; the rhomboid – place of a missing sphere in the lattice, the rectangle – doublet of colloidal particles within the colloidal crystal (doublet particles are the result of sphere adhesion during the silica regrowth step in the synthesis); the white lines – denotes the dislocations and their long-range spreading [26]; (b) Optical micrograph with the SEM inset showing multiple cracks formed during the water evaporation from the freshly synthesized colloidal crystal [32].

### **1.2.2. Electrophoretic and Dielectrophoretic synthesis of colloidal crystals**

Another strategy to impose directionality in a colloidal system, and in that way to synthesize colloidal crystals, is to use electric fields. There is the possibility to use both direct (DC) and alternating current (AC). Depending on the mechanism through which particles are assembled one can distinguish electrophoretic (based on DC) or dielectrophoretic (the electric field is usually generated by AC) self-assembly [33] (described in more detail in **Chapter 4**).

While the utilization of a DC electric field acts on charged particles, AC can be used to induce the polarization of dielectric colloids for further manipulation. Besides the motion of nanoparticles, an electric field has a significant influence on the surrounding liquid in the colloidal suspension. Two types of electric field induced motion of liquid medium have been observed: **1.** DC electroosmotic flow induced by the migration of a counter ion layer adsorbed along the wall of the chamber between two electrodes. This can disturb the assembly process due to the random orientation of the moving liquid [33]; **2.** The electrohydrodynamic flow (EHDF) phenomenon due to the flux of incoming colloidal particles towards the electrode surface. This leads to perturbation of the lateral homogeneity of the concentration polarization near the electrode surface. As a consequence, a lateral flow of liquid medium brings colloidal particles closer together, which finally results in the formation of ordered 2D colloidal assemblies [34,35].

Electrophoretic deposition presents a method for the fast synthesis of colloidal crystals. It is based on the application of a DC electric field through a suspension of colloidal particles that is confined in between two electrodes (see **Chapter 4, Figure 4.9a**) [33,36].



Colloidal crystals assembled from different kinds of nanoparticles (e.g. silica[16] and polystyrene [37] based nanoparticles) can be synthesized using this method. The main drawback of DC field induced self assembly in aqueous solutions is the water electrolysis that can take place upon applying the electrode potential [33,38]. The formation of oxygen and hydrogen bubbles at the electrode surface can prevent formation of colloidal crystals. In order to avoid undesired water electrolysis, while still retaining a sufficient intensity of applied electric field, the distance in between two electrodes can be decreased (in millimeter range) [37,39] and suitable solvents (e.g. ethanol [40], acetylacetone [41], water-dimethylsulfoxide mixture [42] etc.) can be used.

It has been shown that the deposition rate of silica nanoparticles increases when the pH is differing from their point of zero charge (PZC) and the electric field intensity is increasing. Compared to sedimentation methods, electrophoretic synthesis of colloidal crystals is much faster which is an important issue especially in the case of nanoparticles with small diameters (e.g. < 300 nm) [16], where the sedimentation assembly could take even a few weeks.

Electrophoretic deposition can be used together with other techniques in order to fabricate high quality ordered colloidal assemblies. For example, colloidal crystals with different lattice structures (face centered cubic (fcc) and body centered cubic (bcc)) can be easily synthesized by means of electrophoretic deposition of polystyrene beads onto lithographically (e.g. the “lift-off” method) patterned surfaces of indium-tin oxide (ITO) electrodes (**Figure 1.10a and b**). In this case, the thickness of the colloidal crystal depends on time and the volume fraction of colloidal particles in the suspension [43]. This is the general characteristics of systems for electrophoretic synthesis of colloidal crystals.

Another way to fabricate patterned assemblies of negatively charged polystyrene particles is based on the synergetic action between electrophoretically induced assembly and UV light. During the patterned illumination of the surface of an ITO electrode, by means of a photolithographic mask, an induced slight increase in current densities can selectively guide incoming particles to the illuminated areas and in that way multi-domain 2D colloidal assemblies can be reversibly synthesized. Further stabilization of the system through the permanent attachment of the colloidal particles can be accomplished by increasing the applied electrode potential for a short time interval (**Figure 1.10c**) [44].

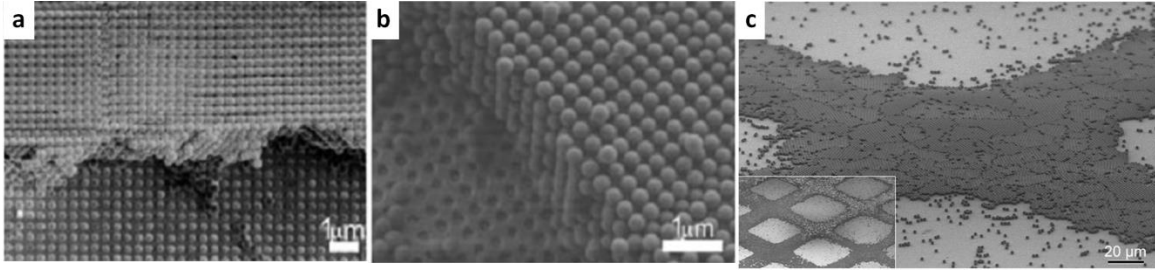


**Figure 1.10.** Cross-sectional SEM images of: (a) polystyrene ( $\varnothing = 310$  nm) based fcc colloidal crystal with the (111) plane oriented towards the surface of the pattern, (b) bcc colloidal crystal with (100) crystal plane. The colloidal crystal has been assembled by applying a DC electric field of  $200 \text{ V cm}^{-1}$  to the ethanol-water suspension of polystyrene beads [43]; (c) Top-view SEM image of the colloidal pattern synthesized by UV light supported assembly of polystyrene particles ( $\varnothing = 2 \text{ } \mu\text{m}$ ) on the surface of an ITO electrode. A DC electric field of  $6500 \text{ V m}^{-1}$  has been applied [44].

The problems related to the water electrolysis and electroosmotic flow which is anticipated for a DC field can be largely eliminated if an AC field is used. Furthermore, the utilization of AC allows much higher electric field strength and the possibility to manipulate and assemble dielectric nanoparticles into ordered arrays [33]. Upon the application of an AC electric field to the suspension of colloidal particles a dielectrophoretic effect (DEP) can be induced (more detailed explanation of dielectrophoretic phenomenon can be found in **Chapter 4**) [33,45]. As the polarization of the electrodes is constantly changing during time, the particle migration and attraction is not directly induced by the Columbic action but rather through the induced polarization of the colloidal particles. The dipoles induced that way are capable of interacting with the gradient of an inhomogeneous electric field. This can result in the migration of the particles down the gradient and *vice versa* [33,46].

An interesting example that demonstrated the DEP synthesis of 2D colloidal crystals is shown in **Figure 1.11**. In the present case, DEP induced dipoles of polystyrene beads are interacting not only with the AC electric field but also among each other. The latter interaction results in the alignment of induced dipoles into chains (**Figure 1.11a** and **c**). In the second step, so formed chains are attracted by DEP towards the glass surface between two planar ITO electrodes (**Figure 1.11b** and **d**). The intensity of the chaining force ( $F_{chain}$ ) is given as:  $F_{chain} = -C\pi\epsilon r^2 K^2 E^2$ , where:  $C$  is coefficient that scales from 3 to  $> 1000$ . Coefficient  $C$  depends on the distance between particles in the chain and the length of the chain;  $\epsilon$  is the dielectric constant of the material of which colloidal particles are made;  $r$  is the diameter of the colloidal particles,  $K$  is the Clausius – Massoti function (**Chapter 4**) and  $E$  is the intensity of the applied electric field [46,47].

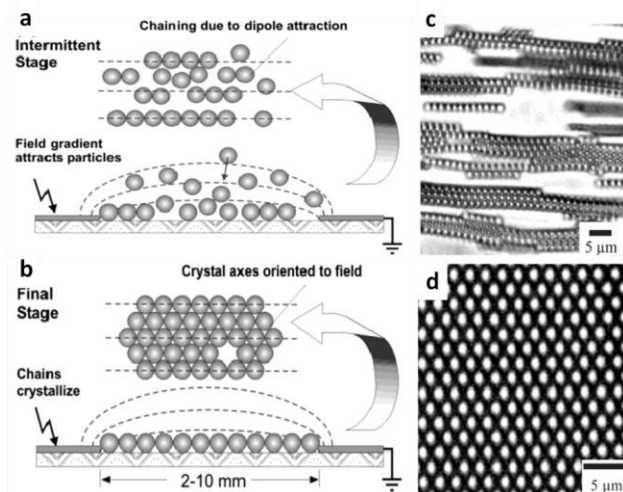


**Figure 1.11.** Schematic representation (a) and (b) and SEM images (c) and (d) of the two stages during the formation of ordered 2D arrays of latex particles ( $\phi = 1.4 \mu\text{m}$ ). In the first stage (a), latex particles are assembled into chains (c) (after the 2 s) due to the induced dipole-induced dipole attractive force. Once the chains are formed, the 2D assembly (d) is formed between the two electrodes (during the 15 s) by DEP induced motion of chains down the gradient of the applied electric field [46].

The AC driven self-assembly process seems to be dependent on the temperature of the system, the field intensity [48] and the AC frequency [49]. Besides polystyrene, other types of nanoparticles (*e.g.* silica and gold) have been manipulated and assembled in AC electric fields.

### 1.2.3. Langmuir – Blodgett technique for the synthesis of colloidal crystals

The Langmuir-Blodgett technique presents one of the best ways to control the assembling process and to introduce directionality into colloidal systems by means of an externally applied lateral mechanical force [3]. Originally, it has been developed to allow transfer of monomolecular films (Langmuir films) of amphiphilic molecules from the water-air interface onto the surface of solid substrates [50,51]. **Figure 1.12.b** and **c** [52] depicts the basic principle of the deposition of an amphiphilic molecular film onto a hydrophobic surface. Prior to the deposition step, a monomolecular film has to be formed at the water-air interface where the non-polar (hydrophobic) hydrocarbon tails are oriented towards the air, while the hydrophilic head is immersed into the water subphase. Once the compact film is formed the transfer of the monolayer can be accomplished by simple dipping and withdrawing of the sample.

The mechanism of the deposition depends on the hydrophilic-hydrophobic properties of the substrate [53]. When a hydrophobic sample is dipped into the water subphase, the molecules in the first deposited monolayer are preferentially oriented with their hydrophobic part towards the hydrophobic surface. In a second step, when the substrate is lifted-up, another layer of molecules are deposited. During the withdrawing step, molecules in the second layer orientate themselves towards the previously deposited layer with their hydrophilic heads.

The deposition cycles can be repeated until the desired number of layers is deposited [54].

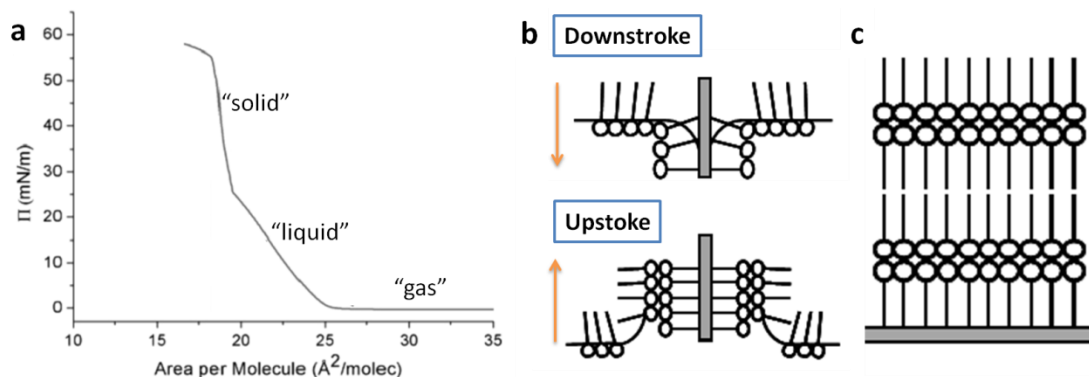


**Figure 1.12.** (a) An example of a compression isotherm recorded during the preparation of Langmuir film of arachidic acid at the water/air interface (adapted and modified from [55]). The three domains, referred to as pseudo “solid”, “liquid” and “gaseous” state respectively, are clearly visible. The transfer of a monolayer of amphiphilic molecules and the final stacking within the structure are schematically presented in figures b) and c) [52].

Prior to the deposition onto a substrate, a densely packed monolayer has to be formed at the interface. This can be achieved by spreading the molecules onto the water surface and their subsequent compression by means of moveable barriers until a compact film is formed. The compression process can be followed by measuring the surface pressure as a function of area per molecule or film area. Once the optimized degree of compression is achieved, the transfer can start. The whole process of formation of the Langmuir film can be summarized in three steps: **1.** at low surface pressure molecules are far away from each other and thus no significant interaction occurs between them. This large degree of freedom corresponds to a pseudo gaseous state in two dimensions; **2.** Further compression leads to an increase of surface pressure which indicates the phase change from gaseous to liquid state; **3.** Upon further compression, the pressure raises steeply (**Figure 1.12a**). This point presents the liquid - solid transition at which a dense and well-organized film exists. Further compression of the Langmuir monolayer leads to the collapse of the film where the film breaks and the molecules are either depositing on top of each other or transferred to the water subphase [56].

Besides amphiphilic molecules, much larger building units from the colloidal domain can serve for the synthesis of an ordered 2D array of colloidal particles. Due to their facile fabrication, silica beads are one of the most utilized colloidal particles that have been employed for the synthesis of colloidal crystals by the Langmuir-Blodgett procedure. Proper surface modification of silica beads allows them to float at the water surface and to be assembled similar to molecular monolayers.

The balance of hydrophilic/hydrophobic properties of modified nanoparticles controls their behavior at the interface [57]. If the particles are too hydrophilic (silica beads without surface functionalization) aggregation and sinking in the water subphase will occur. On the opposite the aggregation will happen at the interface if the particles are too hydrophobic [58]. The proper choice of modifying reagent is one of the crucial issues that has to be well addressed in order to obtain a dense and well-organized colloidal film. The silanization of silica nanoparticles [57,59] seems to be a very convenient method for addressing this problem. Alternatively, functionalized silica beads can be suspended in a solution of surfactant and used right away in the Langmuir-Blodgett experiment [60]. The appropriate surface modification is an unavoidable step when it comes to compression of the Langmuir film of particles with larger diameters ( $\varnothing > 400$  nm) while for smaller silica beads ( $\varnothing = 180 - 360$  nm) chemical modification is not absolutely necessary [61]. Here, just like in the case of amphiphilic molecules, silica beads have to be suspended in a water immiscible and highly volatile solvent (*i.e.* chloroform or chloroform/ethanol mixture). This allows efficient spreading of the beads at the interface without sinking in the water subphase.

Upon the formation of the silica bead monolayer by closing the moveable barriers (**Figure 1.13a**), the compression is followed by measuring the surface pressure as a function of film area (**Figure 1.13b**). In this case the absence of the pseudo-liquid phase in the compression isotherm is notable compared to molecular Langmuir films. At the beginning, when the barriers are completely open the surface pressure is at its zero value. The system resides in this state until the interaction between spheres becomes significant due to the decrease of the interparticle distance. The point at which the colloidal particles are in close contact leads to a steep increase in surface pressure and a highly compressed state (“solid state”) is achieved. This indicates a low compressibility of the system due to the presence of hard silica spheres [59].

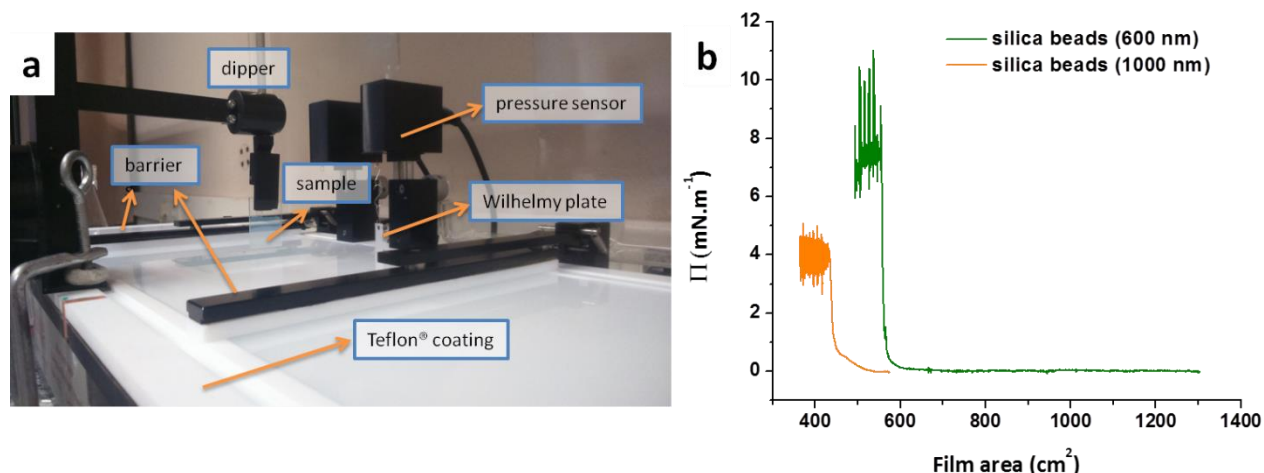


**Figure 1.13** (a) Photograph of Langmuir-Blodgett trough (NIMA Technology 622, Coventry, England) during the synthesis of silica ( $\varnothing = 600\text{nm}$ ) based colloidal crystal at the surface of glass slide. (b) The examples of experimental compression isotherms recorded during the compression of Langmuir film made of 1000 nm (orange curve) and 600 nm (green curve) silica beads.

Once the film is synthesized, the 2D silica bead monolayers can be transferred onto the surface of any hydrophilic substrate and in that way a 3D colloidal crystal can be synthesized.

In this case, the deposition of colloidal particles takes place exclusively during the upstroke of the substrate. **Figures 1.14a** and **b** present the cross-sectional and top SEM views of a silica bead based colloidal crystal. By taking a close look on the top SEM view, one can clearly see certain defects in the form of vacancies and grain boundaries as well as crystalline domains.

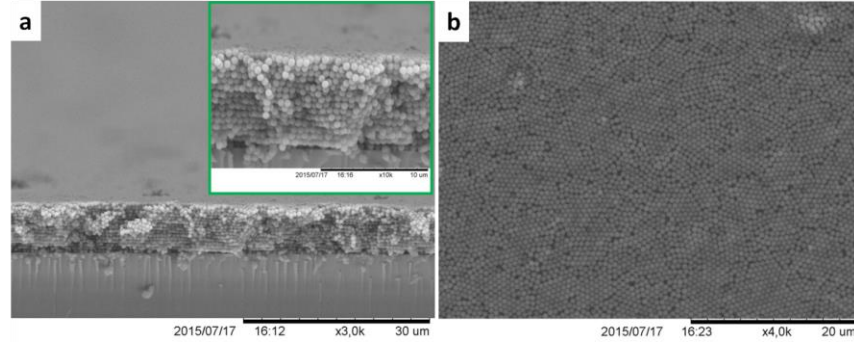


**Figure 1.14** Cross-sectional (a) and top view (b) SEM images of 600nm silica beads. From the cross-sectional SEM image one can see that 15 layers of silica colloidal particles have been deposited onto the surface of a microscopic glass slide. The synthesis was accomplished by slowly withdrawing (at  $1 \text{ mm min}^{-1}$ ) and fast dipping (at  $63 \text{ mm min}^{-1}$ ) of the substrate.

Nevertheless, the crystal obtained is crack free, which is a crucial point with respect to the following electrodeposition step (see **Chapter 2**).

The compression process can be easily followed by means of thin chromatographic paper or a platinum plate (known as Wilhelmy plates) which is partially immersed in the water subphase and directly connected to a sensitive balance. The determination of the surface pressure ( $\Pi$ ) is based on measuring the intensity of force ( $F$ ) which acts on the Wilhelmy plates during the compression of the monolayer. The surface pressure is given as:

$$\Pi = -\Delta\gamma \Rightarrow \Pi = -\left[\frac{\Delta F}{2(t_p + w_p)}\right] \Rightarrow \Pi = \frac{\Delta F}{2w_p} \text{ if } w_p \gg t_p$$

with  $\Delta\gamma$  being the change in surface tension,  $t_p$  and  $w_p$  are the thickness and the width of the Wilhelmy plate, respectively [62]. The spikes that appear at the top of the compression isotherm during the transfer of monolayers are related to the penetration of the substrate through the Langmuir film (**Figure 1.13 b**).

The Langmuir-Blodgett technique allows precise control over the number of deposited colloidal monolayers and a high quality of the synthesized colloidal crystal. This already presents, together with the possibility to synthesize heterogeneous alternating structures (*e.g.* by using beads with different size [63] or by alternating colloidal and molecular layers [64]), the most important advantage of the Langmuir-Blodgett technique in comparison with other techniques



that have been described before.

As has been mentioned earlier, colloidal crystals can be considered as artificial opals due to their good structural organization and therefore intensive coloration when illuminated with visible light. This feature depends on the angle of the incident light for the same size and type of colloidal particles as depicted in the **Figure 1.15**. Observed brilliant colors are the consequence of Bragg diffraction. This can be expressed as:  $m\lambda_m = \lambda_b = 2n_e d_{hkl} \sin \alpha_b$ , where  $m$  is integer,  $\lambda_b$  is the Bragg diffraction wavelength,  $d_{hkl}$  is the distance between two consecutive lattice planes with Miller indices  $hkl$  (for fcc (111) plane it can be calculated as  $d_{hkl} = 0.82 \cdot d$ ,  $d$  is the diameter of the silica particles),  $\alpha_b$  is the Bragg angle and  $n_e$  is the effective refractive index ( $n_e = \sqrt{\phi n_s^2 + (1 - \phi)n_a^2}$ , where  $\phi$  is the volume fraction of the colloidal crystal occupied by hard spheres, which for a fcc system has a value of 0.74,  $n_s$  and  $n_a$  are the refractive indices of silica and air respectively [58]).



**Figure 1.15.** Optical photographs of monolayers of silica beads ( $\varnothing = 600$  nm) at a glass substrate taken at different angles relative to the source of the incidence white light.

This macroscopic observation can serve as a first proof of the quality of the Langmuir-Blodgett films and translate the successful transfer of the colloidal particles onto the surface of a solid substrate.

## **Literature**

- [1] A.R. Parker, H.E. Townley, *Nat. Nanotechnol.* 2 (2007) 347.
- [2] M. Grzelczak, J. Vermant, E.M. Furst, L.M. Liz-Marzán, *ACS Nano* 4 (2010) 3591.
- [3] Y.S. Lee, *Self-Assembly and Nanotechnology: A Force Balance Approach*, New Jersey (published simultaneously in Canada), John Wiley & Sons, Inc., 2008.[4]H. Fudouzi, Y. Xia, *Langmuir* 19 (2003) 9653.
- [5] A. Stein, *Microporous Mesoporous Mater.* 44–45 (2001) 227.
- [6] Y. Zhao, L. Shang, Y. Cheng, Z. Gu, *Acc. Chem. Res.* 47 (2014) 3632.
- [7] O.D. Velev, A.M. Lenhoff, *Curr. Opin. Colloid Interface Sci.* 5 (2000) 56.
- [8] A. Stein, *Microporous Mesoporous Mater.* 44–45 (2001) 227.
- [9] G.M. Whitesides, B. Grzybowski, *Science*. 295 (2002) 2418.
- [10] A.M. Kalsin, M. Fialkowski, M. Paszewski, S.K. Smoukov, K.J.M. Bishop, B. A. Grzybowski, *Science* 312 (2006) 420.
- [11] B. A. Grzybowski, C.E. Wilmer, J. Kim, K.P. Browne, K.J.M. Bishop, *Soft Matter* 5 (2009) 1110.
- [12] Z. Dogic, S. Fraden, C.F. Group, *1 Phase Behavior of Virus / Sphere Mixtures and Entropy Driven Ordering within the Second Virial Approximation*, Wiley-VCH Verlag GmbH & Co. KGaA, Weinheim, 2006.
- [13] K.R. Purdy, S. Fraden, *Phys. Rev. E - Stat. Nonlinear, Soft Matter Phys.* 70 (2004) 1.
- [14] G. Bai, J. Wang, H. Yan, Z. Li, R.K. Thomas, *J. Phys. Chem. B* 105 (2001) 3105.
- [15] B. A. Grzybowski, H. a Stone, G.M. Whitesides, *Nature* 405 (2000) 1033.
- [16] M. Holgado, F. García-Santamaría, A. Blanco, M. Ibisate, A. Cintas, H. Míguez, C.J. Serna, C. Molpeceres, J. Requena, A. Mifsud, F. Meseguer, C. López, *Langmuir* 15 (1999) 4701.
- [17] R. Mayoral, J. Requena, J. Moya, *Adv. Mater.* 9 (1997) 257.
- [18] K.E. Davis, W.B. Russel, W.J. Glantschnig, *J. Chem. Soc. Faraday Trans.* 87 (1991) 411.
- [19] L. V. Woodcock, *Nature* 385 (1997) 141.
- [20] P.G. Bolhuis, D. Frenkel, S. C. Mau, D.A. Huse, *Nature* 388 (1997) 235.
- [21] A. Mifsud, J.S. Moya, L. Va, *Langmuir* 13 (1997) 6009.
- [22] R. Salvarezza, L. Vázquez, H. Míguez, R. Mayoral, C. López, F. Meseguer, *Phys. Rev. Lett.* 77 (1996) 4572.
- [23] V.M. Shelekhina, O. A. Prokhorov, P. A. Vityaz, a. P. Stupak, S.V. Gaponenko, N.V. Gaponenko, *Synth. Met.* 124 (2001) 137.
- [24] N.D. Denkov, O.D. Velev, P. A. Kralchevsky, I.B. Ivanov, H. Yoshimura, K. Nagayama, *Nature* 361 (1993) 26.
- [25] P. A. Kralchevsky, N.D. Denkov, *Curr. Opin. Colloid Interface Sci.* 6 (2001) 383.
- [26] S. Wong, V. Kitaev, G. A. Ozin, *J. Am. Chem. Soc.* 125 (2003) 15589.
- [27] A.S. Dimitrov, K. Nagayama, *Langmuir* 12 (1996) 1303.
- [28] S.H. Im, M.H. Kim, O.O. Park, *Chem. Mater.* 15 (2003) 1797.
- [29] P. Jiang, J. Bertone, *Chem. Mater.* 11 (1999) 2132.
- [30] Y. A. Vlasov, X.Z. Bo, J.C. Sturm, D.J. Norris, *Nature* 414 (2001) 289.



- [31] S.M. Yang, H. Míguez, G. A. Ozin, *Adv. Funct. Mater.* 12 (2002) 425.
- [32] M. McLachlan, N. Johnson, R. De La Rue, D. McComb, *J. Mater. Chem.* (2010) 144.
- [33] O.D. Velev, K.H. Bhatt, *Soft Matter* 2 (2006) 738.
- [34] M. Trau, D. A. Saville, I. A. Aksay, *Langmuir* 13 (1997) 6375.
- [35] W.D. Ristenpart, I. A. Aksay, D. A. Saville, *Phys. Rev. E - Stat. Nonlinear, Soft Matter Phys.* 69 (2004) 1.
- [36] G. Cao, *J. Phys. Chem. B* 108 (2004) 19921.
- [37] A.L. Rogach, N.A. Kotov, D.S. Koktysh, J.W. Ostrander, G.A. Ragoisha, *Chem. Mater.* 12 (2000) 2721.
- [38] M. Ammam, *Biosens. Bioelectron.* 58 (2014) 121.
- [39] R.C. Hayward, D. A. Saville, I. A. Aksay, *Nature* 404 (2000) 56.
- [40] Y.J. Huang, C.H. Lai, P.W. Wu, *Electrochem. Solid-State Lett.* 11 (2008) P20.
- [41] L. Besra, C. Compson, M. Liu, *J. Am. Ceram. Soc.* 89 (2006) 3003.
- [42] A. Yethiraj, J.H.J. Thijssen, A. Wouterse, A. van Blaaderen, *Adv. Mater.* 16 (2004) 596.
- [43] N. V. Dziomkina, M. A. Hempenius, G.J. Vancso, *Adv. Mater.* 17 (2005) 237.
- [44] R.C. Hayward, D.A. Saville, I.A. Aksay, *Nature* 404 (2000) 56.
- [45] J. Voldman, *Annu. Rev. Biomed. Eng.* 8 (2006) 425.
- [46] S.O. Lumsdon, E.W. Kaler, J.P. Williams, O.D. Velev, *Appl. Phys. Lett.* 82 (2003) 949.
- [47] S.O. Lumsdon, E.W. Kaler, O.D. Velev, *Langmuir* 20 (2004) 2108.
- [48] Y. Liu, R.G. Xie, X.Y. Liu, *Appl. Phys. Lett.* 91 (2007) 20.
- [49] A.S. Negi, K. Sengupta, A. K. Sood, *Langmuir* 21 (2005) 11623.
- [50] K.B. Blodgett, *J. Am. Chem. Soc.* 57 (1935) 1007.
- [51] K.B. Blodgett, *J. Langmuir, Phys. Rev.* 51 (1937) 964.
- [52] D.R. Talham, T. Yamamoto, M.W. Meisel, *J. Phys. Condens. Matter* 20 (2008) 184006.
- [53] H. Motschmann, M. Helmuth, *Handb. Appl. Surf. Colloid Chem.* (2001) 629.
- [54] M.K. P. Martin, M. Szablewski, *Langmuir-Blodgett Troughs (Operating Manual)*, 6th edition, Nima Technology Ltd, Coventry CV4 7EZ. England, 2002.
- [55] G. Oncins, J. Torrent-Burgués, F. Sanz, *J. Phys. Chem. C* 112 (2008) 1967.
- [56] C. Zoski, *Handbook of Electrochemistry*, Elsevier, Amsterdam, 2007.
- [57] M. Bardosova, P. Hodge, V. Smatko, R.H. Tredgold, D. Whitehead, *Acta Phys. Slovaca*, 54 (2004) 409.
- [58] S. Reculosa, S. Ravaine, *Chem. Mater.* 15 (2003) 598.
- [59] S. Reculosa, P. Massé, S. Ravaine, *J. Colloid Interface Sci.* 279 (2004) 471.
- [60] B. Van Duffel, R.H. A. Ras, F.C. De Schryver, R. A. Schoonheydt, *J. Mater. Chem.* 11 (2001) 3333.
- [61] M. Bardosova, F.C. Dillon, M.E. Pemble, I.M. Povey, R.H. Tredgold, *J. Colloid Interface Sci.* 333 (2009) 816.
- [62] KSV Nima, *Software Manual Langmuir and Langmuir-Blodgett Devices*, Espoo, Finland, n.d.
- [63] M. Heim, S. Reculosa, S. Ravaine, A. Kuhn, *Adv. Funct. Mater.* 22 (2012) 538.
- [64] P. Massé, S. Reculosa, K. Clays, S. Ravaine, *Chem. Phys. Lett.* 422 (2006) 251.

---

*CHAPTER 2*

DEVELOPMENT OF COAXIAL MACROPOROUS ELECTRODE  
ARCHITECTURE BY INFILTRATION OF COLLOIDAL CRYSTALS

## **2. Development of coaxial macroporous electrode architectures by infiltration of colloidal crystals**

Taking advantage of long-range ordering of nano- and sub-micrometric particles, colloidal crystals have found their application as templates for the synthesis of highly ordered porous electrodes. Void space in between particles occupy on average 26 % v/v of the total template volume and can be filled with a wide spectrum of different electro-active materials, which opens the possibility of various applications in different fields ranging from electroanalysis [1–5] and electrocatalysis [6–11] to batteries [12–17] and biofuel cells [18].

The basic route for the synthesis of porous electrodes can be summarized in a few steps (**Figure 2.1**):

1. Infiltration of different materials into the void space of the colloidal crystal, 2. Solidification of the material by means of different strategies based on induced polymerization, sol-gel method, electrodeposition etc., 3. Removal of the colloidal template by dissolution or a calcination process [19]. Using this, so called “hard template” approach, different macroporous materials have been synthesized, including macroporous metals [6,20–24], electroconductive and nonconductive organic polymers [25–28], semiconductors [29–33] and metal-oxides [14,34,35].

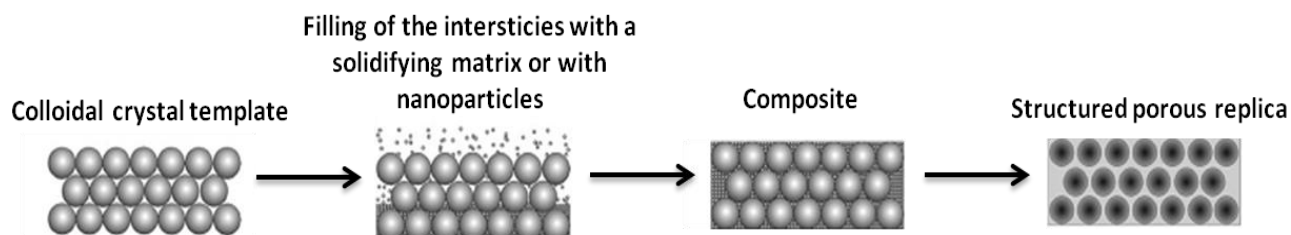


**Figure 2.1** Schematic representation of the procedure for the synthesis of macroporous materials [36].

Following the described procedure, macroporous electrodes represent negative replica of the colloidal crystal, comprising 74 % v/v (equivalent to atomic packing factor of fcc crystalline system) of free space [35] homogeneously distributed inside the porous structure. Therefore, those materials are known as “inverse opals”.

This results in high volume-to-surface ratio materials, which allows their utilization in the different fields of electrochemistry.

## **2 – Development of coaxial macroporous electrode architectures by infiltration of colloidal crystals**

---

As previously discussed in **Chapter 1**, different types of nano- and sub-micrometric particles (e.g. silica, polymethylmetacrylate (PMMA), polystyrene (PS), latex, PS-polyacrylic acid copolymer) can be used to synthesize the template. In order to ensure the mechanical stability of the template, colloidal silica crystals can be heated, prior to the infiltration, which results in the formation of a “neck” between the neighboring spheres. This intermediate step enhances the robustness of the template and it allows complete removal of silica spheres with hydrofluoric acid (HF) afterwards. In the case of polymeric particles, calcination or common solvents (tetrahydrofuran, toluene and dichloromethane) can be used to remove the template. A requirement for facile and complete removal of particles from the composite material is the incomplete filling of the template to avoid closing the whole structure and difficult penetration of solvent or hydrofluoric acid [19,37,38].

Using different approaches e.g. templates made of nanoparticles, or obtained by spontaneous or electro-assisted assembly of surfactant molecules [7,39], porous electrodes with different pore diameters and uniformly or hierarchically structured organization can be prepared [38].

Regarding the pore diameter the International Union of Pure and Applied Chemistry (*IUPAC*) classified porous materials into three groups: 1. **Nanoporous** ( $\varnothing < 2$  nm), 2. **Mesoporous** ( $2$  nm  $< \varnothing < 50$  nm) and 3. **Macroporous materials** ( $\varnothing > 50$  nm) [33].

During the last decade, different infiltration techniques of materials into a pre-synthesized template have been developed. This includes 1. **Chemical vapor and atomic layer deposition** (CVD, ALD), 2. **Sol-gel method**, 3. **Precipitation and electroless deposition**, 4. **Electrodeposition**.

### **2.1. Overview of common methods for the infiltration of colloidal crystals**

#### **2.1.1. Chemical vapor and atomic layer deposition**

Chemical vapor deposition (CVD) is a technique that is widely used for the fabrication of different coatings and films on the surface of a substrate. Briefly, the method is based on the dissociation or chemical reaction of one or more gaseous precursors induced by means of heat, light or plasma, to form a stable solid product that precipitates at the surface of the solid

## 2 – Development of coaxial macroporous electrode architectures by infiltration of colloidal crystals

substrate.

The deposition step includes a homogeneous chemical reaction in the gas phase or a heterogeneous reaction at the gas-substrate interface where the precursor is homogeneously distributed in the high purity reactive (e.g.  $H_2$ ) or inert gas-carrier stream (nitrogen, argon etc.) (**Figure 2.2**) [40].

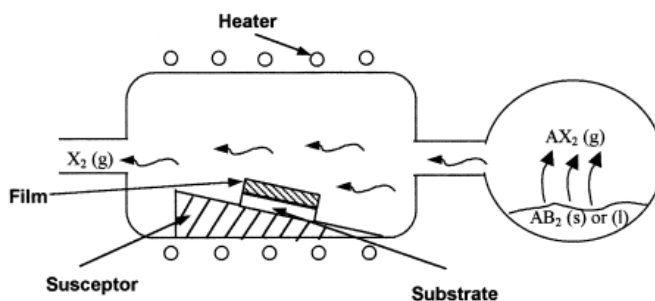


**Figure 2.2** Schematic representation of CVD technique [40].

Beside substrates with a flat surface, CVD can be a useful tool for the infiltration of different materials into the volume of colloidal crystals. The gaseous precursors can easily diffuse and precipitate within the template, thus building-up the composite that can be easily transformed into a porous material.

Depending on the infiltration step, the resulting structure (after the template is dissolved), is either surface or volume templated. The surface templated structure is the result of the predominant coating of the colloidal spheres without complete filling of the interstitial space between particles, while the volume templated material is the result of a complete infiltration of the material through the volume of the colloidal crystal [41]. The latter shows better mechanical stability than the surface templated one.

**Figure 2.3** represents macroporous graphitic and diamond based inverse opals fabricated by thermal and plasma enhanced CVD respectively. The structures are obtained by deposition of carbon material into a colloidal silica crystal template with a notable structural difference between them. Macroporous graphitic material (**Figure 2.3a**) is an example of a surface template structure, with a vacant space between neighboring spheres, while this volume is completely filled with material in the case of macroporous diamond (**Figure 2.3b**). In both cases, the macroporous structure consists of an interconnected pore network [42].

## 2 – Development of coaxial macroporous electrode architectures by infiltration of colloidal crystals

---

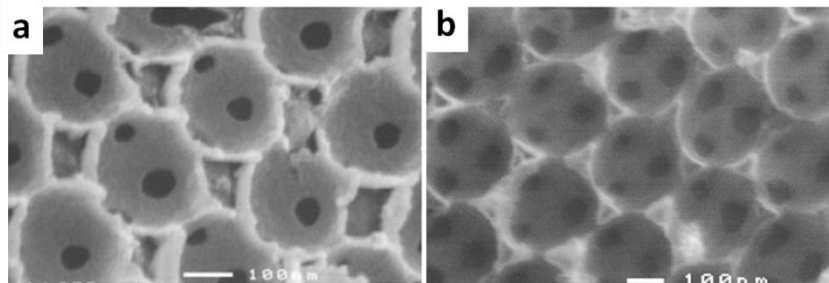


**Figure 2.3** Cross-sectional SEM image of (a) surface templated macroporous graphite ( $\phi_{\text{pores}}=250$  nm synthesized by thermal CVD of a propylene – nitrogen mixture at 800 °C and  $p=1$  atm. Volume template structure of macroporous diamond (b) synthesized by plasma enhanced CVD of a hydrogen-methane mixture onto pre-infiltrated diamond seeds ( $\phi=2-5$  nm) [42].

The main drawback of the CVD method for the fabrication of porous materials is the fact that this technique is not a bottom-up approach, since the building material is equally and simultaneously deposited throughout the whole template. As a consequence, the resulting structure is closed by a thin overlayer of material (**Figure 2.4a** and **b**) [43,44], which doesn't allow the efficient penetration of a solvent that is needed to remove the template from the composite. This limits the utilization of CVD as a method for the synthesis of macroporous materials with a controllable thickness.

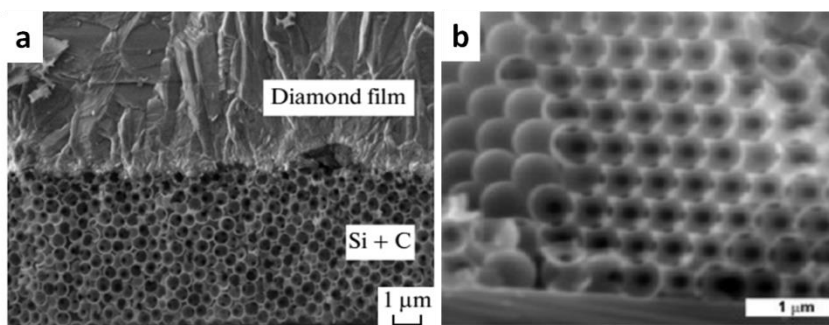


**Figure 2.4** SEM images of macroporous diamond (a) [43] and zinc-oxide (b) [44] produced by microwave plasma CVD from a methane-hydrogen mixture (diamond) at 780-830 °C and metal-organic CVD of zinc-oxide from the hydrolytic decomposition of dimethylzinc at 90 °C.

Nevertheless, in the light of material synthesis, CVD still presents a powerful tool for the deposition of different materials, including macroporous metals (Au [20], Pt and Pt-Pd alloys [21], W [45]), carbon-based materials (graphite, diamond, tiled-graphite) [42,46] and

## 2 – Development of coaxial macroporous electrode architectures by infiltration of colloidal crystals

---

semiconductors (Si[15], Ge [31]) etc.

Another technique, which presents an improvement of CVD, is atomic layer deposition (ALD). Compared to CVD, atomic layer deposition represents a layer-by-layer approach, where the material is growing during the deposition cycles in a monolayer fashion allowing precise control in the Ångstrom range over the deposition process. The method is based on a sequential, self-limiting reaction where the reactants are introduced in the reaction chamber separately. In other words, the surface of the substrate is exposed only to the one reactant a time. Each injection of the precursor is followed by a purging step (e.g. high purity N<sub>2</sub> or Ar etc.), which ensures that only a chemisorbed monolayer, that can react with an second precursor, stays onto the surface of the substrate [47]. One example is ALD of alumina into a colloidal crystal template. The deposition is based on an alternating pulsed injection of 3-methylaluminium (TMA) and water carried by a nitrogen stream, into the chamber that contains the substrate. The reaction mechanism includes the chemisorption of TMA through the hydroxyl-methyl substitution (cycle A) followed by the injection of water to complete the hydrolysis (cycle B) (**Figure 2.5**) [48].

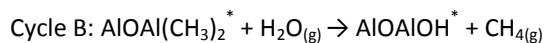
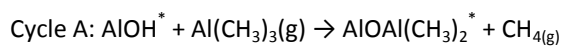


**Figure 2.5** Reaction mechanism for the ALD deposition of alumina into a silica colloidal crystal template [48].

**Figure 2.6a** presents an example of ALD infiltration of titanium-dioxide into a silica nanoparticle template, obtained by alternating injection of TiCl<sub>4</sub> and H<sub>2</sub>O at 100 °C into the nitrogen stream. The SEM image shows that the structure is a surface template. Geometrical considerations indicate that the void space in between spheres will get closed when the thickness of the coating reaches 7.75% of the pore diameter, which would finally lead to a volume template structure [49]. The ALD method allows not only deposition of a metal oxides but also of mixed salts [50] (**Figure 2.6b**) in order to synthesize inverse opals or multi-component macroporous TiO<sub>2</sub>/ZnS:MnS layers [51].

## 2 – Development of coaxial macroporous electrode architectures by infiltration of colloidal crystals

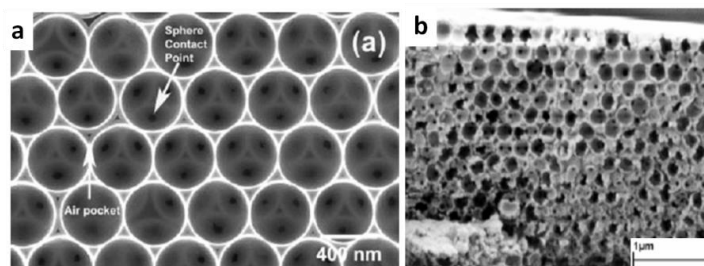


**Figure 2.6** SEM images of ion-milled TiO<sub>2</sub> [49] (a) and a cross-section of ZnS/MnS (b) [52] inverse opals synthesized by the ALD method.

In comparison to CVD, ALD has several advantages: a) precise thickness control in the Ångstrom range, b) good and uniform coverage of a 3D substrate, c) possibility of industrial production [53].

### 2.1.2. Techniques for the fabrication of macroporous materials via infiltration of liquid precursors

Besides the infiltration of gaseous precursors by CVD or ALD, as previously described, it is also possible to infiltrate different liquid precursors in the volume of a colloidal crystal template. There are plenty of examples based on the infiltration of liquid precursors which are additionally broadening the spectrum of materials that can be used for making macroporous materials.

The nature of the template used for the preparation of porous materials allows dividing those techniques into the 1. **Hard template route** (e.g. colloidal crystal template) and 2. **Soft template route** (e.g. lyotropic crystalline phase) [54].

The hard template route includes infiltration of different liquid precursors that can be solidified in a subsequent step in the template. Besides solutions, the free volume of a colloidal crystal structure (26%) can also be infiltrated with a suspension of e.g. gold nanoparticles ( $\phi$ : 15-25nm) [22]. Once the gold nanoparticles are densely packed within the structure, calcinations of the latex-gold composite, to remove the latex spheres and sinter the gold NP, results in a self-supported macroporous structure (**Figure 2.7 a and b.**) [23]. It is also possible to fix gold nanoparticles ( $\phi$  = 5 nm) chemically onto the surface of a thiol-modified silica template and to use them as a nucleation sites during the following electroless deposition of gold or other metals (Ni, Cu, Ag, Pt) (**Figure 2.7c**) [55].



## 2 – Development of coaxial macroporous electrode architectures by infiltration of colloidal crystals

Macroporous gold structures formed in that way can serve as a support for the catalytic electroless deposition of copper. This proves that the gold NP keep their integrity and still can serve as crystallization centers for the deposition of other metals [22]. Beside macroporous gold, nanocrystals of silver could be directly synthesized within an opal that has been pre-impregnated with a diamminesilver(I) complex and subsequently reduced with formaldehyde to form a nanocrystal-based macroporous network [56].

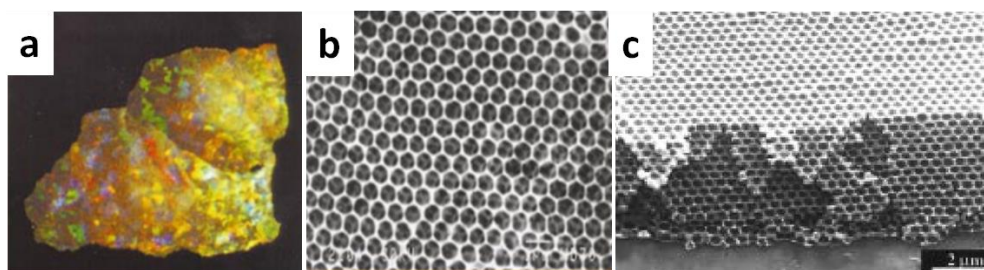


**Figure 2.7** Optical micrograph (a) and top-view SEM image (b) [23] of composite material formed by infiltration of gold nanoparticles into the latex based ( $\phi=630$  nm) colloidal crystal. (c) A macroporous nickel film obtained from a thiol-modified silica ( $\phi = 353$  nm) opal [55] .

Another example of hard template synthesis of macroporous materials is the sol-gel approach. The method is based on the infiltration of solutions of metal alkoxides [4,57] which are dissolved in appropriate alcohol or water suspensions of colloidal particles (sol) [58]. The formation of a macroporous network is induced either by the polymerization of the sol and formation of the gel or in the case of metal alkoxides by the hydrolysis once when the substrate is exposed to humid atmosphere [59]. The latter synthesis can be repeated in several impregnation-hydrolysis cycles until the colloidal template is fully filled with the material [4]. In some cases, polycondensation of the silica sol is induced electrochemically due to the local increase of a pH during the water reduction, which leads to gel formation [60].

Silica sol can also be polymerized on cationic surfactant modified latex spheres [61] (**Figure 2.8a**). The metal alkoxide route is used for the synthesis of macroporous  $V_2O_5$  [34],  $TiO_2$  (**Figure 2.8b**) [62], composite materials such as  $Li_{1.5}Al_{0.5}Ti_{1.5}(PO_4)_3$  (LATP) [63] , doped macroporous  $ZrO_2:Eu^{3+}$  (**Figure 2.8c**) film [64] etc.

## 2 – Development of coaxial macroporous electrode architectures by infiltration of colloidal crystals

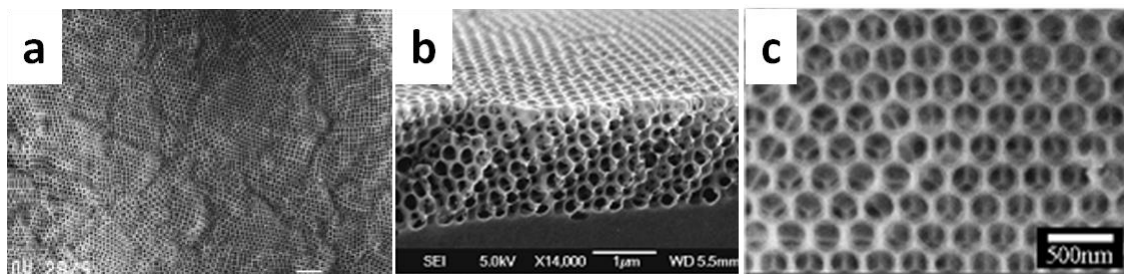


**Figure 2.8** SEM images of the inverse opal structure of silica (a) [61], titania (b) [62] and doped Zr:Eu<sup>3+</sup> (c) [64]. All structures were produced by the sol-gel procedure.

The final macroporous structure is obtained by removal of the polymer spheres through a calcination process, which results in a significant shrinkage of the structures by 15-30 % due to the evaporation of the solvents that have been used [59]. This can be seen by simple comparison of the center-to-center distance between the nanoparticles and the final pores (**Figure 2.9**) [65]. If the precursor is a suspension of metal nanoparticles, then the shrinkage of the porous structure during the calcinations is in the range of 5-10 % since the infiltrated material is already in its final form [59].

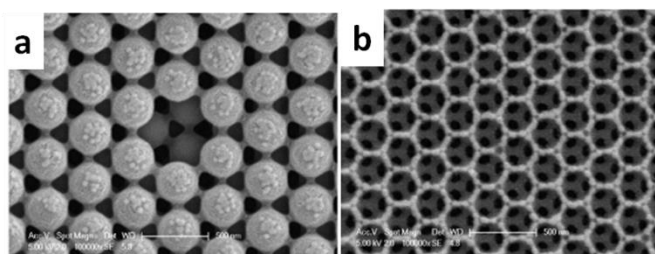


**Figure 2.9** Top-view SEM images of the polymethylmetacrylate (PMMA) colloidal crystal template and its CeO<sub>2</sub> inverse opal. SEM of the macroporous structure depicts the significant shrinkage of the CeO<sub>2</sub> gel during the calcification process [65].

The described alkoxide based sol-gel procedure can be used for the fabrication of macroporous electrodes only if the metal alkoxide is moderately active. An alternative approach based on the impregnation of opals with a metal salts (acetates, nitrates, oxalates, glyoxalates ect.) can be more convenient in some cases. Taking advantage of the thermal instability of certain salts, it is possible to fabricate the macroporous material simultaneously with calcination of the colloidal template.

## 2 – Development of coaxial macroporous electrode architectures by infiltration of colloidal crystals

---

In the case of bivalent metallic oxalates, the final porous material (pure metal, carbonate or oxide can be made by thermal degradation of corresponding oxalates in the temperature range from 235 to 418 °C) seems to be dependent on radii of the metal ions. One of the main prerequisites for this, as well as for the sol-gel procedure, is that the glass transition temperature of the polymeric colloidal crystal template is higher than the temperature at which the metal salts are decomposing. This is necessary in order to maintain the 3D framework shape. Based on this route macroporous  $\text{Al}_2\text{O}_3$ ,  $\text{Fe}_2\text{O}_3$ ,  $\text{Cr}_2\text{O}_3$ ,  $\text{Co}_3\text{O}_4$ ,  $\text{CaCO}_3$ ,  $\text{ZnO}$ ,  $\text{ZnAl}_2\text{O}_4$ ,  $\text{LaAlO}_3$ ,  $\text{ZnCr}_2\text{O}_4$ ,  $\text{LaMnO}_3$  etc. have been prepared [35,66].

Colloidal crystals can serve as “nanoreactors” for the synthesis of various organic polymers. In this case infiltration of monomers is followed by a polymerization step initiated by heat, UV light or catalyst [67].

This approach is convenient for the synthesis of a macroporous polymeric network of styrene/p-methylstyrene copolymer [27], macroporous polyurethane, polystyrene, methylmetacrylate (**Figure 2.10a**) [25] and epoxy resin (**Figure 2.10b**) [68]. In contrast to the polymer synthesis within the opal structure, a more facile example is based on the infiltration of an organic solution of phenol resin into the template structure. The composite produced that way can be easily transformed into glassy carbon material by a temperature controlled calcinations process (**Figure 2.10c**) [42].

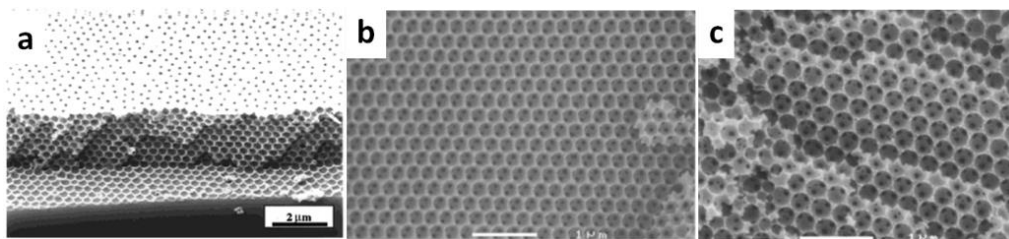


**Figure 2.10** SEM pictures denotes highly ordered structures of (a) PMA [25], (b) thermally cured phenol resin [42] and (c) macroporous glassy carbon inverse opal synthesized by pyrolyzing the resin [42].

Mesoporous materials with an extremely high surface area could be synthesized through the soft template route based on the self-assembly of surfactant molecules. The general principle of this strategy is based on a chemically or electrochemically induced hydrolysis of either metal alkoxides (sol-gel) or pH dependent precipitation of metal ions around the lyotropic crystalline phase formed through the assembly of surfactant molecules.

## 2 – Development of coaxial macroporous electrode architectures by infiltration of colloidal crystals

The kind of lyotropic crystalline phase that can be formed depends on the surfactant concentration as depicted in **Figure 2.11a** [54,69]. The assembly of surfactants is known to occur at the electrode surface under the influence of the applied electric field, even if the surfactant concentration is low (e.g. 1%). Some of the materials that can be synthesized following this route are metals [7,9] and metal oxides [39].

Infiltration of the liquid precursor could be used for the synthesis of hierarchical structures using three-modal composite films. To increase the active surface area, calcinations and sintering of a PS colloidal crystal ( $\phi = 465$  nm) that has been infused with PMMA ( $\phi = 84$  nm) and silica ( $\phi = 6$  nm) results in a hierarchical mixed macro-mesoporous silica (**Figure 2.11b**) [70].

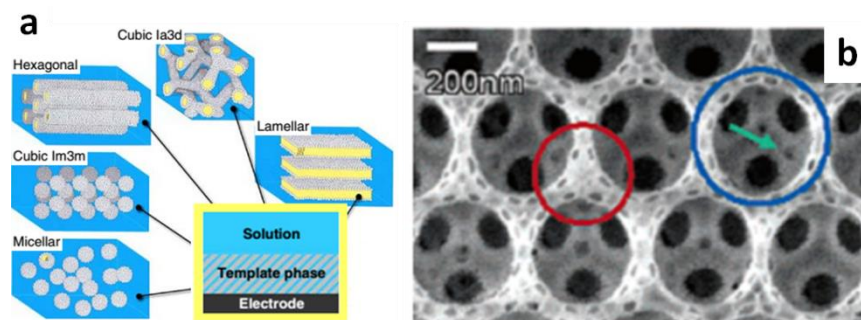


**Figure 2.11** Schematic representation of various spatial arrangements of the surfactant phase (a) [54] and SEM image of hierarchical trimodal meso-macroporous silica (blue ring denotes macropores, red ring- interconnected mesopores, green arrow – interstructural mesopores) [70].

### 2.1.3. Electrodeposition for the synthesis of (macro)porous materials

In contrast to other techniques that can be used for the synthesis of porous structures, as discussed before, infiltration of different materials into the colloidal crystals by means of electrodeposition seems to be the most promising approach for the synthesis of inverse opals with controllable thicknesses, wall thickness and interconnecting windows between the pores [59].

The main advantage of electrodeposition over other techniques that have been used for the synthesis of porous materials is the fact that electrodeposition presents a “bottom-up” approach. The infiltration of the materials starts from the bottom of the colloidal crystal and proceeds towards the top layer.

## 2 – Development of coaxial macroporous electrode architectures by infiltration of colloidal crystals

---

In other words, this way of synthesis of inverse opals provides a good control over the thickness of the electrodeposited material which is not possible by using other techniques (e.g. CVD, ALD, sol-gel etc.).

Commonly, electrodeposition is carried out in a three-electrode system that comprises: 1. **Working electrode (W.E.)**, 2. **Counter electrode (C.E.)** and 3. **Reference electrode (R.E.)**. The three electrode system is connected to the direct current power supply (galvanostat-potentiostat) (**Figure 2.12**) [71].

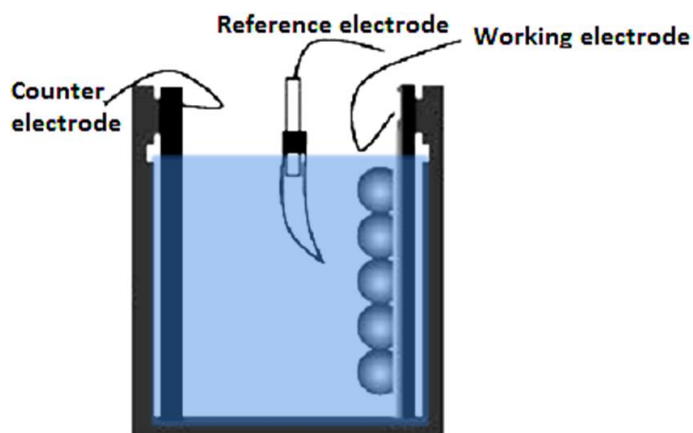


**Figure 2.12** Principal scheme of a three-electrode system consisting of a working, counter (auxiliary) and reference electrode (Adapted and modified from [71]).

The method is based on the electroreduction (e.g. metal ions) or electrooxydation (e.g. monomers) of an electroactive species, present in the bulk solution, at the surface of the working electrode under the conditions of constant electrode potential (potentiostatic deposition) or constant current (galvanostatic deposition) [72]. By polarizing the working electrode having the colloidal crystal at its surface at a sufficiently negative or positive (vs. RE) electrode potential, electrodeposition of the material takes place and empty void space in-between neighboring spheres gets filled up. Since the electrochemical synthesis of the material starts from the electrode surface, the electrodeposition can be stopped when the desired level of the colloidal template is infiltrated. That allows the controlled deposition of the material throughout the template which can be stopped before the material reaches the top layer of nanoparticles. This ensures that the resulting structure has an open pore mouth (**Figure 2.13**) in the terminal layer.

## 2 – Development of coaxial macroporous electrode architectures by infiltration of colloidal crystals

If the macroporous material is dedicated to electrochemical applications (e.g. macroporous electrode), an open porosity is of great importance with respect to the diffusion of electrolyte through the system of interconnected pores.

The main prerequisites that have to be fulfilled prior to the electrodeposition are that a colloidal crystal template has to be generated on the surface of an electro-conductive material (ITO, metallic plates, metal-coated glass etc.) and that the desired material can be electrodeposited from an electroactive precursor. The latter presents one of the limitations of this technique.

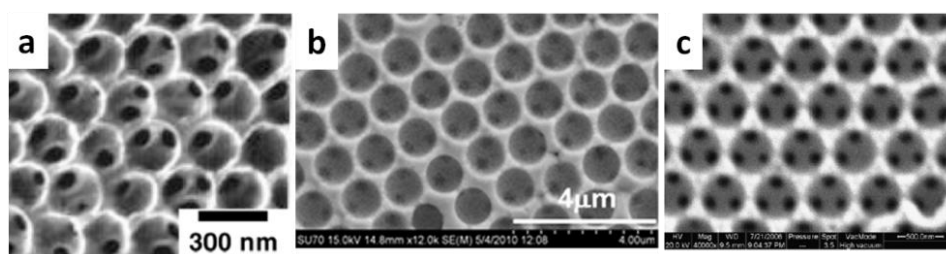


**Figure 2.13** Top view SEM images of volume templated macroporous polypyrrole (PPy) (a) [73] , gold (Au) [74] and Prussian blue (c) [5]. The figure presents the high quality porous structure with a system of interconnected pores and an open pore “mouth” regardless the material.

As in the case of the previously discussed nanocrystal deposition method for the synthesis of metallic materials, once the nanoparticles are removed from the composite with an appropriate solvent or HF, the shrinkage of the structure is negligible since the synthesized material is already in its final form and thus doesn't require any additional treatment (e.g. calcinations). Produced in this way, porous materials present an example of a volume templated structure based on the previously discussed mechanism of the infiltration.

The wide range of electro-active precursors provides a variety of porous materials that can be synthesized following the electrodeposition procedure. For example, there are plenty of examples for the electrodeposition of meso- or macroporous metals (gold [2,3,8,71,75–78], platinum [6,7,9], silver [10,79], cobalt [80], nickel [81], nickel-iron [80] and tin-cobalt [13] alloys, aluminum [12] etc.), semiconductors (germanium [30], cadmium-selenide [82], gallium-arsenide [83], copper(I) oxide [84], cadmium sulphide, zinc selenide, lead selenide [83], etc.), electroconductive polymers (polypyrrol (PPy) [73,85], polyaniline (PANI) [86], poly(bithiophene) [28] etc.), metal oxides [14,84,87], complex salts [5] etc.



## ***2 – Development of coaxial macroporous electrode architectures by infiltration of colloidal crystals***

---

Electrodeposition is also a convenient way to generate more complex hierarchical structures consisting of pores with different diameters which can belong to the same (multimacroporous structures) [74,76,88] or different (meso-macroporous) classes of porosity [9,89] .

### **2.2. Synthesis of macroporous gold and nickel electrodes**

Based on different approaches (vertical deposition, sedimentation, centrifugation, Langmuir-Blodgett method) colloidal crystal templates can be synthesized on various supporting materials. Depending on the electrochemical behavior of the selected material for infiltration of the opals, the final macroporous structures can find applications in many areas of electrochemistry.

Among all possible porous materials, meso- and macroporous metal films have been very frequently used as electrode material due to their good conductivity, mechanical stability, and in the case of macroporous gold, facile surface modification through the formation of self-assembled monolayers of various molecules.

The electrodeposition of metals into silica based colloidal crystal templates is schematically depicted in the **Figure 2.14**. In this study, colloidal crystals synthesized by the Langmuir-Blodgett technique served as a template for the electrodeposition (**Figure 2.14a**). In order to select the working (geometric) area of the electrode, a thin layer of an adhesive (nail varnish) was applied to the surface of the substrate. After the template is electrically connected by soldering a piece of wire (**Figure 2.14b**), electrodeposition can be performed in order to obtain a silica-metal composite structure (**Figure 2.14c**). Finally, after etching the composite structure in 5% hydro-fluoric acid, a macroporous metal electrode is obtained.

## 2 – Development of coaxial macroporous electrode architectures by infiltration of colloidal crystals

---

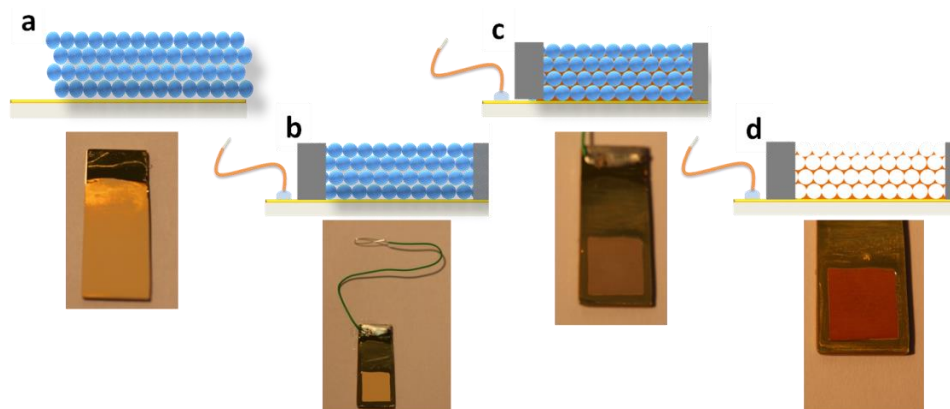


**Figure 2.14** Schematic representation of the procedure for the fabrication of macroporous electrodes by the electrodeposition of metallic materials into the opal structure based on a hard template route.

Depending on the geometry of the substrate that is used for the synthesis of the colloidal crystals, the fabrication of macroporous electrodes with various architectures is possible. For example, in this work precut gold coated glass slides and gold microwires have been used for the fabrication of macroporous gold and nickel electrodes with planar and cylindrical geometry, respectively.

The electrodeposition step was carried out in a three electrode system with a colloidal crystal template on a gold surface as working electrode (WE), silver/silver-chloride (3 M NaCl) as reference electrode (RE) and a platinum grid or hollow platinum cylinder as a counter electrode (CE). The surface of the counter electrode was at least two times bigger than the surface of the working electrode in order to ensure current flow through the system which is not limited by the CE.

In order to ensure a homogeneous electric field during the electrodeposition, the geometry of the counter electrode should be the same as the geometry of the working electrode. This is a very important prerequisite that has to be fulfilled in order to obtain a homogeneous growth of the metal deposit through the template and thus a homogeneous thickness of the resulting macroporous electrode.

For the electrodeposition of gold, commercially available ECF60 solution has been used (Metalor®) while the macroporous nickel was synthesized using a semi-bright nickel electroplating solution (AlfaAesar®).



## 2 – Development of coaxial macroporous electrode architectures by infiltration of colloidal crystals

Since electrodeposition is possible only if the working electrode is sufficiently polarized, cyclic voltammetry (CV) was used in order to estimate the optimal value of the electrode potential. **Figure 2.15** presents cyclic-voltammograms where the dashed lines indicate the onset potential for the reduction of gold and nickel. The determined optimal electrode potentials for the electrodeposition of gold and nickel were -0.66 V and -0.85 V, respectively. Those values differ significantly from the values of the standard electrode potentials for  $\text{Au}^+/\text{Au}$  ( $E_{\text{Au}^+/\text{Au}}^0 = 1.83 \text{ V}$ ) and  $\text{Ni}^{2+}/\text{Ni}$  ( $E_{\text{Ni}^{2+}/\text{Ni}}^0 = -0.26 \text{ V}$ ) [90] couples, due to the complex composition (metal salt, supporting electrolyte, complexing agents and surfactants) of the commercial electroplating bath solutions. The role of the additives and surfactants is to improve the smoothness of the deposit and the wettability of the substrate.

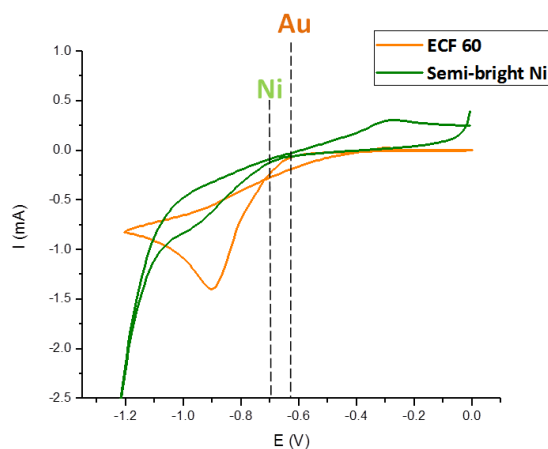


**Figure 2.15** Cyclic-voltammograms of a gold (orange) and nickel (green) commercial electroplating bath solution ECF60 (Metalor®) and Semi-bright Nickel (AlfaAesar®) recorded using a three electrode system consisting of counter (Pt), working (Au) (approximate area of working electrode was  $1\text{cm}^2$ ) and Ag/AgCl (3 M NaCl) reference electrodes. Onset potentials of -0.63 V for gold and -0.7 V, both vs. Ag/AgCl RE, for nickel are indicated with dashed lines.

The chronoamperometric curve for the electrodeposition of a gold (ECF 60) on a gold plate as WE is presented in **Figure 2.16**. By taking a close look it is possible to distinguish two different regions of the current intensity. After the charging of double layer, which typically takes a few milliseconds, a steep increase in reduction current can be noticed in Region I. This can be ascribed to the nucleation which takes place at the electrode surface. This step is followed by the continuous growth of a metal front (Region II).

[72].

## 2 – Development of coaxial macroporous electrode architectures by infiltration of colloidal crystals

---

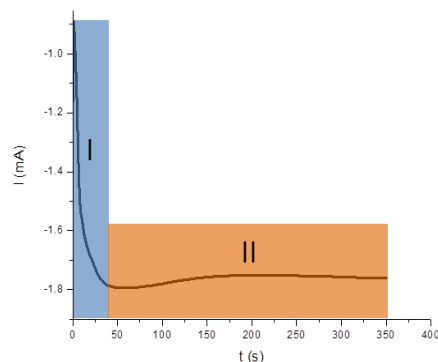


**Figure 2.16** Chronoamperometric curve for the electrodeposition of gold (ECF 60) onto a gold plate as a WE at -0.66 V vs. Ag/AgCl RE. Regions I, II and III, present the evolution of the current intensity during the initial stages of electrodeposition. The area of the working electrode was approximately 1 cm<sup>2</sup>.

In contrast to electrodes with a constant surface, chronoamperometric curves for the electrodeposition into colloidal crystal templated substrates show a very characteristic oscillation in the current intensity (**Figure 2.17**). The reason for this lies in the mechanism of the infiltration, based on the electrodeposition of the material into the void space between the neighboring silica spheres. At the beginning of the electrodeposition, the current has a local maximum on the absolute current scale, due to the maximal surface of the electrode available for the electrodeposition. As the metal deposit is growing further during the electrodeposition and infiltrates the first half-layer of silica beads, the absolute current intensity reaches the first local minimum. This is due to the fact that the volume of the void space available for infiltration decreases during the electrodeposition up to the half-height of the first bead layer, which causes a decrease of the reduction current. For every next half-layer, current passes through a series of local minima and maxima. This allows a extremely precise control of the growth of metal deposit, since the electrodeposition can be stopped when the desired half-layer of silica beads is infiltrated with material. The electrodeposition step is followed by acidic etching of the silica-metal composite structure, in order to obtain the final macroporous structure. Stopping the electrodeposition at the half-height of a given bead layer results in a macroporous structure with an open “pore mouth”. During the electrodeposition, the amplitude of the oscillations is damped due to the fact that the quality of the long-range organization of silica beads decreases throughout the template, when compared to the very first layer. Finally, this phenomenon leads to the total annihilation of the oscillations once a certain number of half-layers are infiltrated with the material.

## 2 – Development of coaxial macroporous electrode architectures by infiltration of colloidal crystals

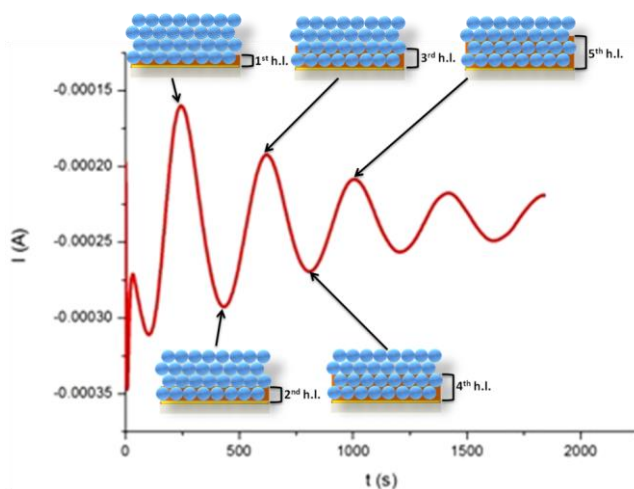


**Figure 2.17** Chronoamperometric curve for the electrodeposition of gold (ECF 60,  $E = -0.66$  V vs. Ag/AgCl (3 M NaCl)) into the first 9 half-layers of silica beads composing the colloidal crystal template ( $\phi = 1$   $\mu\text{m}$ ). Approximate geometric electrode area of a planar electrode was 1  $\text{cm}^2$ .

**Figure 2.18** presents SEM images of macroporous samples with planar and cylindrical geometry during their fabrication. **Figure 2.18 a** and **d** shows the cross section of the composite structure after the infiltration of planar (a) and cylindrical (d) multilayered Langmuir-Blodgett films with 15 and 29 half layers respectively. An excess of non-infiltrated silica beads can be noticed on the top of the structures. **Figures 2.18 b** and **e** illustrate macroporous planar and cylindrical structures obtained after the silica is removed from the composite by etching with hydrofluoric acid. It can be seen that the samples have a homogeneous thickness on a large scale. By taking a closer look on the inset of the image **b**, one can notice small dark spots within the macropores. Those spots present the interconnection windows between neighboring pores, created at the points where the silica nanoparticles used to be in the direct contact. The top view SEM (**Figures 2.18 c** and **f**) reveals the homogeneous surface distribution of the pores.

## 2 – Development of coaxial macroporous electrode architectures by infiltration of colloidal crystals

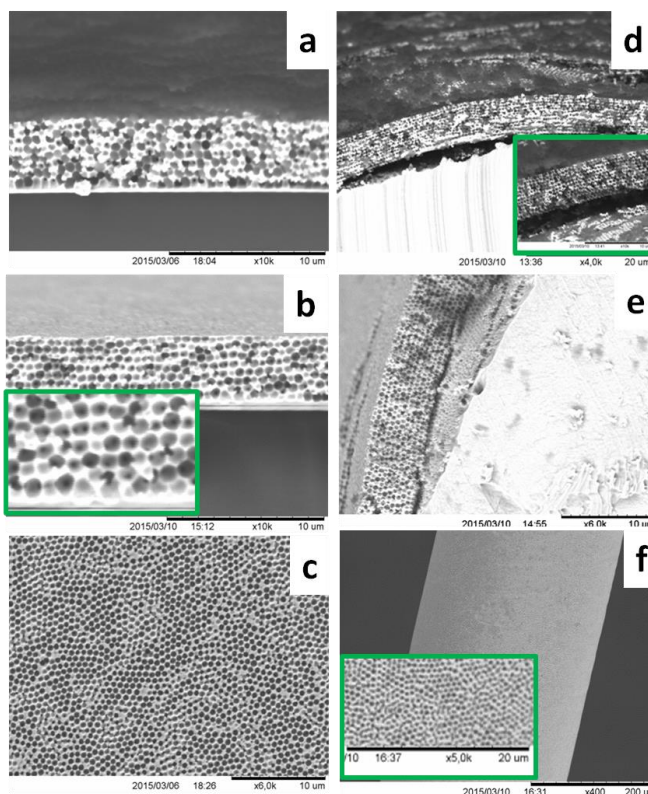


**Figure 2.18** SEM images of macroporous gold electrodes ( $\phi = 600$  nm): a,d - Cross sectional SEM of planar and cylindrical gold-silica composites, synthesized by electrodeposition of gold into a 15 h.l. (planar substrate) and 29 h.l. (cylindrical substrate) template; b ,e - SEM of macroporous structures obtained after the etching in 5% wt. HF; c,d - Top view SEM of planar and cylindrical macroporous samples, demonstrating the homogeneity of the pore distribution. It is also notable that the pores are open in the outermost pore layer.

The availability of various electroplating solutions opens the possibility for the electrodeposition of different metals. The SEM images and chronoamperometric curve for the electrodeposition of cylindrical macroporous nickel are depicted in **Figure 2.19**. As it can be seen, the absolute current intensities recorded during the electrodeposition of nickel are in average much higher compared to those for the electrodeposition of gold. This can be attributed to the higher throwing power of this bath, related to a higher concentration of nickel ions and the more negative electrode potential applied during the electrodeposition of nickel.

## 2 – Development of coaxial macroporous electrode architectures by infiltration of colloidal crystals

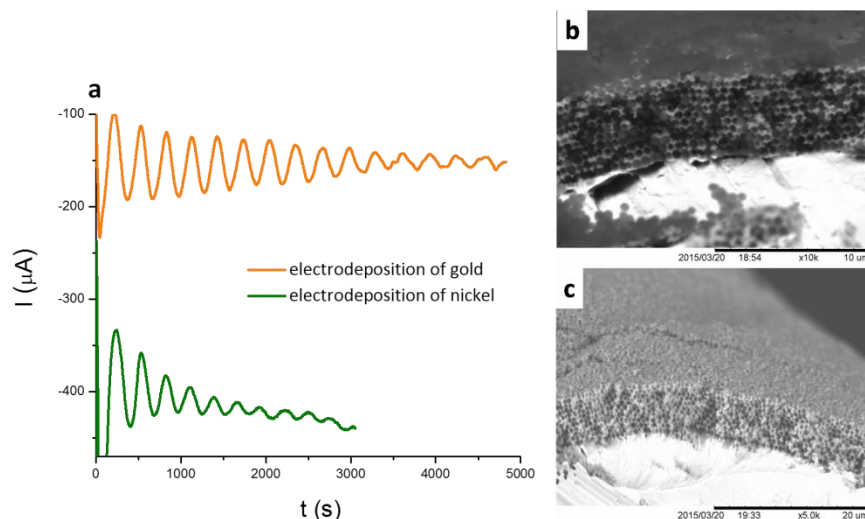


**Figure 2.19** a) Comparison of chronoamperometric curves for the electrodeposition of gold ( $E = -0.66$  V vs. Ag/AgCl (3 M NaCl)) and nickel ( $E = -0.85$  V vs. Ag/AgCl (3 M NaCl)) through a cylindrical silica based colloidal crystal template that has been synthesized on a gold microwire ( $l \approx 2$  cm,  $\varnothing = 250$   $\mu\text{m}$ ); b) Cross-sectional SEM images of a silica/nickel composite and a cylindrical macroporous nickel electrode obtained by potentiostatic electrodeposition of nickel (at  $E = -0.85$  V vs. Ag/AgCl (3 M NaCl)) through a 600 nm silica nanoparticle template.

### 2.3. Electrochemical characterization of macroporous gold electrodes

From a materials point of view, metallic macroporous electrodes can find applications in different fields of electrochemistry, as mentioned before. Taking the advantage of a high electroactive surface, macroporous electrodes could be used for the fabrication of electrochemical systems with improved performances such as biofuel cells, batteries and biosensors [69]. Thus, accurately measuring the active surface area of such electrodes is an important aspect. Depending on the electrode material, different approaches can be used for this measurement.

For example, the adsorption ( $H_{\text{ads.}}$ ) and desorption ( $H_{\text{des.}}$ ) of hydrogen atoms onto the surface of platinum electrodes (**Figure 2.20**) [7] can be used for the electrochemical determination of the real electrode surface. The charge related to the adsorption-desorption steps is directly proportional to the electrode surface after subtracting the charge related to the double-layer charging [91].

## 2 – Development of coaxial macroporous electrode architectures by infiltration of colloidal crystals

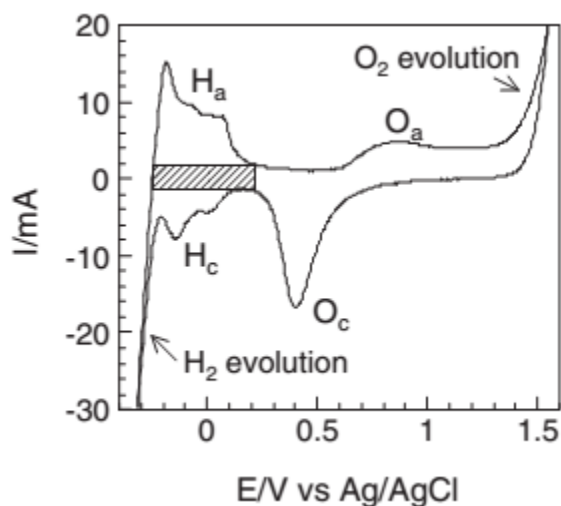


**Figure 2.20** Literature example of a cyclic voltammogram of a mesoporous platinum electrode recorded in 0.5 M sulfuric acid. H<sub>c</sub> - formation of adsorbed hydrogen, H<sub>a</sub> - oxidation of adsorbed hydrogen, O<sub>a</sub> - formation of adsorbed oxygen, O<sub>c</sub> – reduction of oxide layer [7].

In contrast to platinum, gold electrodes do not exhibit such a behavior regarding the hydrogen adsorption – desorption mechanism. The determination of the real electrode surface area for polycrystalline gold electrodes is based on the reductive stripping of an electrochemically synthesized thin layer of gold-oxide. **Figure 2.21** illustrates the cyclic voltammograms of a smooth wire and a set of macroporous gold electrodes recorded in 0.5 M sulfuric acid solution. During the anodic scan, in the range from 0 V to 1.6 V, the oxidation of the gold surface accompanied by the formation of a thin layer of gold oxide starts at 1.1 V.

The amount of gold-oxide formed in that way corresponds to the active surface area of a gold electrode. In the reverse (cathodic) scan, stripping of the previously formed gold-oxide layer occurs and a cathodic current peak appears at 0.9 V. Since the gold-oxide layer covers the entire surface of the gold electrode the charge related to the stripping step can be used for the direct calculation of the real electrode surface, based on a conversion factor of 390  $\mu\text{C}/\text{cm}^2$  which has been reported for these specific experimental conditions [91].

## 2 – Development of coaxial macroporous electrode architectures by infiltration of colloidal crystals

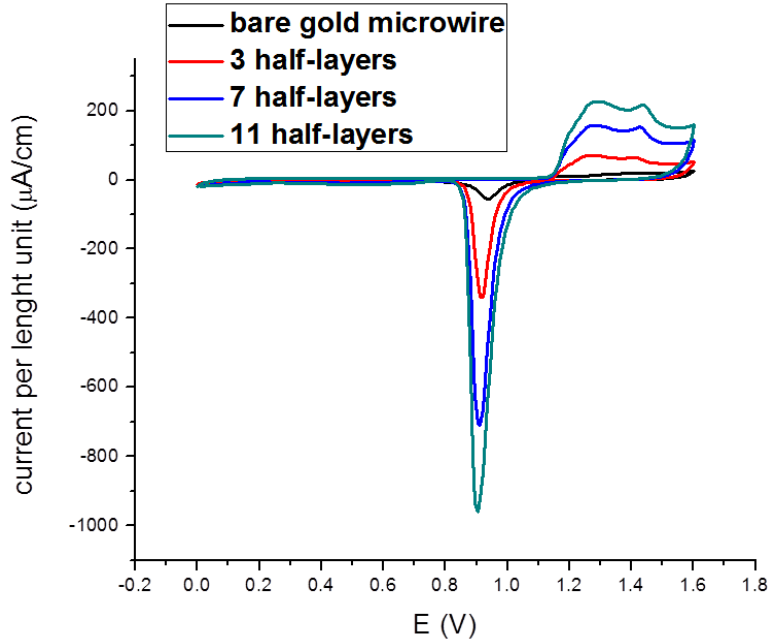


**Figure 2.21** Electrochemical characterization of cylindrical macroporous electrodes ( $\phi_{\text{pores}} = 600 \text{ nm}$ ,  $d_{\text{wire}} = 250 \text{ }\mu\text{m}$ ) in 0.5 M sulfuric acid, at a scan rate of 100 mV/s. All potentials are given *versus* Ag/AgCl (3 M NaCl).

Another parameter that is used to quantify the artificially increased electrode surface area is the roughness factor  $R$  (**Equation 2.1a**). It presents the ratio between the real electrode surface and the geometrical one [90]. The roughness factor is much higher for porous electrodes compared to the non-porous analogues. Based on fundamental geometrical considerations, the theoretical value for the roughness factor ( $R_t$ ) can be calculated according the **Equation 2.1b** [92]. This theoretical value depends exclusively on the number of complete pore layers ( $n$ ) without taking into account the diameter of the pores. The values obtained are in good correlation with the increase of active surface area calculated for the samples whose cyclic-voltammograms are shown in **Figure 2.21**.

$$R = \frac{S_{\text{active}}}{S_{\text{geometric}}} \quad (\text{a}) \quad ; \quad R_t = \sqrt{\frac{4}{3}} \times n \times \pi \quad (\text{b}) \quad (\text{Equation 2.1.})$$

**Table 2.1.** summarizes the quantitative characterization of the cylindrical macroporous electrodes. As can be seen, the values for  $R$  are always higher than  $R_t$ . This can be attributed to the additional internal surface roughness of the macroporous gold deposit.

## 2 – Development of coaxial macroporous electrode architectures by infiltration of colloidal crystals

The same phenomenon is observed for the bare gold wire, due to its intrinsic surface roughness, which is not included in the calculation of the theoretical roughness factor. Nevertheless, both roughness factors show a linear correlation with the number of pore layers (Figure 2.22).

Thickness of macroporous gold (layers)	Charge of the stripping peak ( $\mu\text{C}$ )	$S_{\text{active}}$ ( $\text{cm}^2$ )	$S_{\text{geometric}}$ ( $\text{cm}^2$ )	Roughness factor (R)	Theoretical roughness factor ( $R_t$ )
0	103	0.26	0.14	1.92	1.00
1.5	163	0.42	0.06	7.60	5.44
3.5	330	0.85	0.05	18.00	12.70
5.5	676	1.73	0.07	25.87	19.95

**Table 2.1.** Quantitative parameters for characterizing the active surface of cylindrical macroporous electrodes with the same pore ( $\phi = 600$  nm) and wire ( $\phi = 250$   $\mu\text{m}$ ) diameter but different thickness.

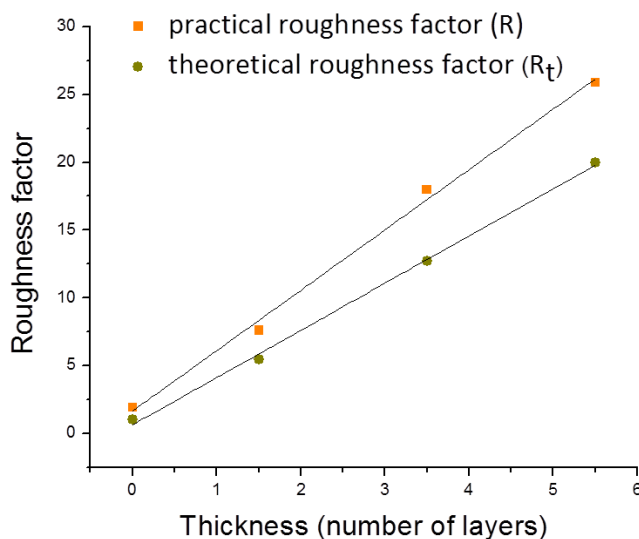


**Figure 2.22** Linear dependence of the practically determined (R) and theoretically calculated ( $R_t$ ) roughness factors for macroporous gold microwires with different thicknesses of the macroporous deposit.



#### **2.4. Bottom-up generation of miniaturized coaxial and macroporous double electrodes with tunable porosity**

The demand for miniaturized and potentially implantable electrochemical devices, such as biofuel cells, biosensors and batteries, led to the development of various technologies and strategies that can be used for their fabrication. The limits for the miniaturization of such electrochemical devices are mainly depending on the ability to decrease the dimensions or to eliminate some of their building elements, while maintaining good electrochemical properties of the device (current densities and power output).

The variety of materials as well as strategies that are used for the fabrication of electrode architectures opens the possibility for designing the electrochemical devices which are capable to operate under physiological conditions. Moreover, the ability to use the fuel and oxidizer, naturally present in the human body allowed the elimination of their most bulky elements (i.e. case, case seal, membrane, membrane seal etc.). Therefore designing appropriate electrode architectures is one of the key-challenges in the field of the fabrication of miniaturized and implantable devices. Macroporous electrodes are excellent candidates for the fabrication of miniaturized devices, due to their significantly increased active surface area, which allows the decrease of the overall geometrical dimensions of the device without decreasing the current. Moreover, by choosing a cylindrical geometry it should be possible to improve mass transport towards the electrode surfaces due to radial diffusion [93], which presents one of the most challenging problems in the elaboration of efficient electrochemical devices. This is of the outmost importance, especially when having in mind the fact that the concentration of some important electroactive species can be very low (e.g. subcutaneous concentration of oxygen is about 0.2 mM) [94].

A schematic representation of the procedure for the fabrication of miniaturized coaxial two-electrode electrochemical cells with tunable porosity is shown in **Figure 2.23**. The strategy is based on the potentiostatic electrodeposition of alternating gold-nickel-gold metal layers (**Figure 2.24**) through a cylindrical colloidal crystal template (**Figure 2.23a**). Switching between gold and nickel electroplating solutions and by applying sufficient cathodic potential in the consecutive steps, a three-layer silica/metal composite structure with controllable thickness can be obtained (**Figure 2.23b**). In this case, the nickel block plays the role of a sacrificial spacing element that separates two macroporous silica/gold composites.

## 2 – Development of coaxial macroporous electrode architectures by infiltration of colloidal crystals

After dissolving the nickel layer with nitric acid, a small amount of stabilizing element (diluted nail varnish) is incorporated at the extremities of the nickel-free structure (**Figure 2.23c**) to prevent structural collapse and the formation of a short circuit in the system. Both macroporous electrodes are electrically addressable in an independent way. The inner macroporous gold electrode is in direct contact with the initial gold microwire, while the outer one is addressed by a 50  $\mu\text{m}$  thick gold microwire using silver paint as a binding element. In the final step, silica beads are removed by etching the sample in 5% hydrofluoric acid (**Figure 2.23d**).

The space in between the two cylindrical macroporous electrodes can serve as an electrolyte container whose volume can be adjusted by varying the amount of electrodeposited nickel which allows changing the inter-electrode distance, typically in the range of tens of microns, in a very controlled way.

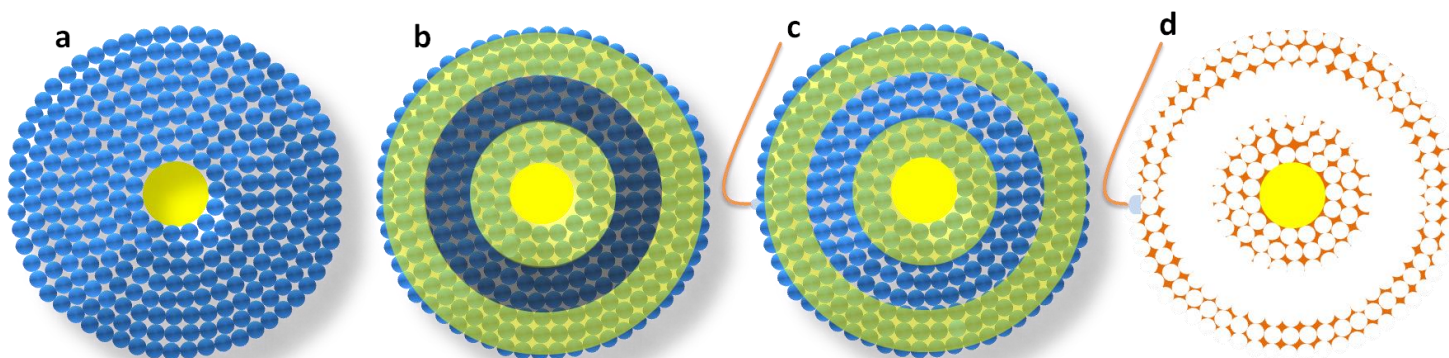


**Figure 2.23** Schematic representation showing the different steps of the fabrication of a cylindrical miniaturized two-electrode electrochemical cell.

As previously shown for the separate electrodeposition of gold and nickel through silica nanoparticle templates with planar and cylindrical geometry (**Figures 2.17 and 2.19a**) we observe again regular oscillations in the chronoamperometric curves during the electrodeposition of the alternating metal layers (**Figure 2.24**). The decrease in the current intensity during the electrodeposition of the second gold layer can be explained by the fact that the structural regularity decreases within the nanoparticle template.

## 2 – Development of coaxial macroporous electrode architectures by infiltration of colloidal crystals

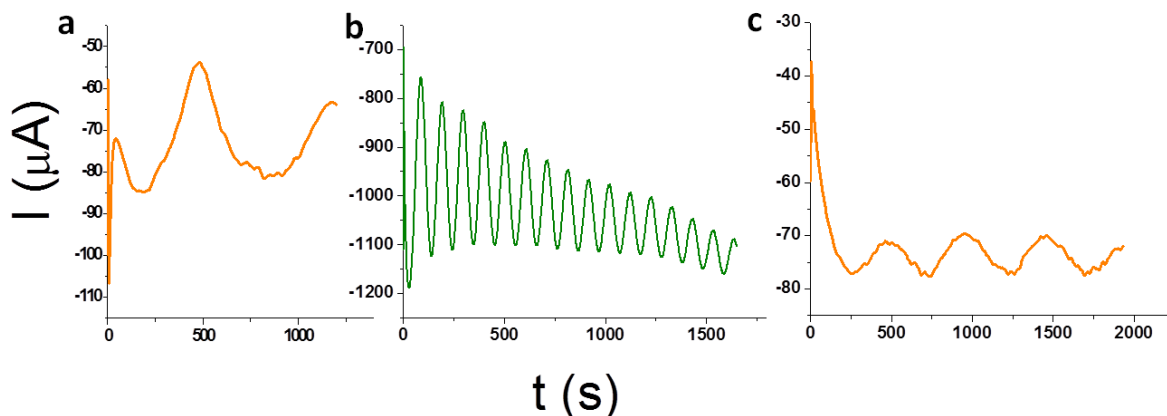


**Figure 2.24** Chronoamperometric curves for the electrodeposition of alternating gold (3 half layers), nickel (32 half-layers) and gold (8 half-layer) layers through the cylindrical colloidal crystal template. The length of the electrode that has been immersed in the electroplating solution during the electrodeposition of alternating Au-Ni-Au layers was reduced for each metal layer (in present case: 3cm (Au;  $E = -0.66$  V) – 2.5 cm (Ni;  $E = -0.85$  V) – 2 cm (Au;  $E = -0.75$  V)). Electrodepositions have been performed with a three-electrode system consisting of the templated Au microwire (working electrode), a hollow Pt cylinder (counter electrode) and a Ag/AgCl (3M NaCl) reference electrode.

**Figure 2.25** presents a SEM characterization of the miniaturized coaxial electrochemical cell obtained after the electrochemical etching of the intermediate nickel layer under acidic conditions. The structure shows the homogeneity of both macroporous gold electrodes and the very well defined gap between them.

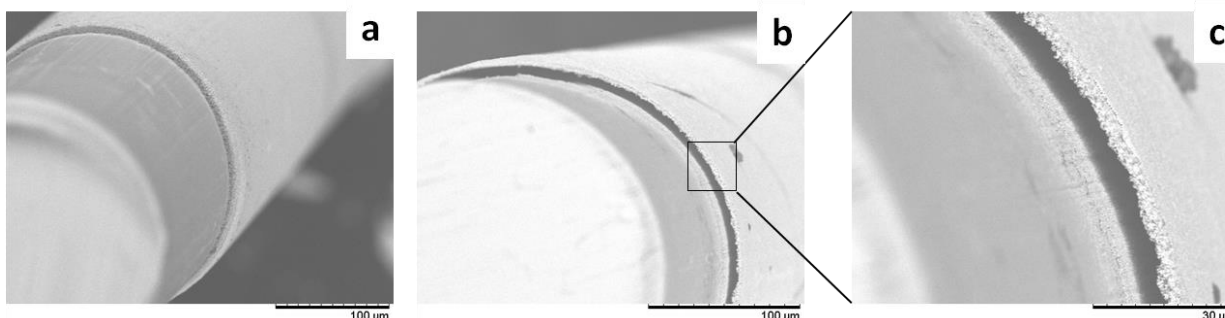


**Figure 2.25** SEM characterization of the coaxial two-electrode electrochemical cell before (a) and after (b,c) electrochemical etching carried out at 1.5 V in 30%  $H_2SO_4$  over 60 minutes.

Once the nickel spacing block is removed, the structural stability of the coaxial double-electrode architecture can be studied by cyclic voltammetry in 0.5 M sulfuric acid.

## 2 – Development of coaxial macroporous electrode architectures by infiltration of colloidal crystals

Prior to the last step where the silica beads are removed from the coaxial gold-silica composite, the silica containing structure was electrochemically characterized by connecting both (inner and outer) electrodes independently. In a control experiment, both electrodes were externally short-circuited and their common active surface area was determined. The different cyclic voltammograms recorded for each macroporous electrode confirmed the absence of intrinsic electrical short-circuit in the composite system that might be formed during the preparation procedure (infiltration of nail-varnish and external addressing of the outer electrode) as shown in **Figure 2.26a**. The active surface areas calculated from the stripping peak charges for the inner, outer and both composite electrodes were  $0.20\text{ cm}^2$ ,  $0.44\text{ cm}^2$  and  $0.62\text{ cm}^2$ , respectively. A device consisting of two electrodes with different active surface areas has been chosen on purpose, to make their cyclic-voltammograms easily distinguishable. Once the silica beads were removed from the composite, the structure was examined again since the silica particles served as a mechanical support to prevent structural collapse in the composite structure. Determined values for the active surface area of inner and outer cylindrical macroporous gold electrodes were  $0.21\text{ cm}^2$ ,  $0.58\text{ cm}^2$  respectively. The active surface area of both electrodes was  $0.80\text{ cm}^2$ , only 1.25% bigger than the sum of the individual surfaces (**Figure 2.26b**).

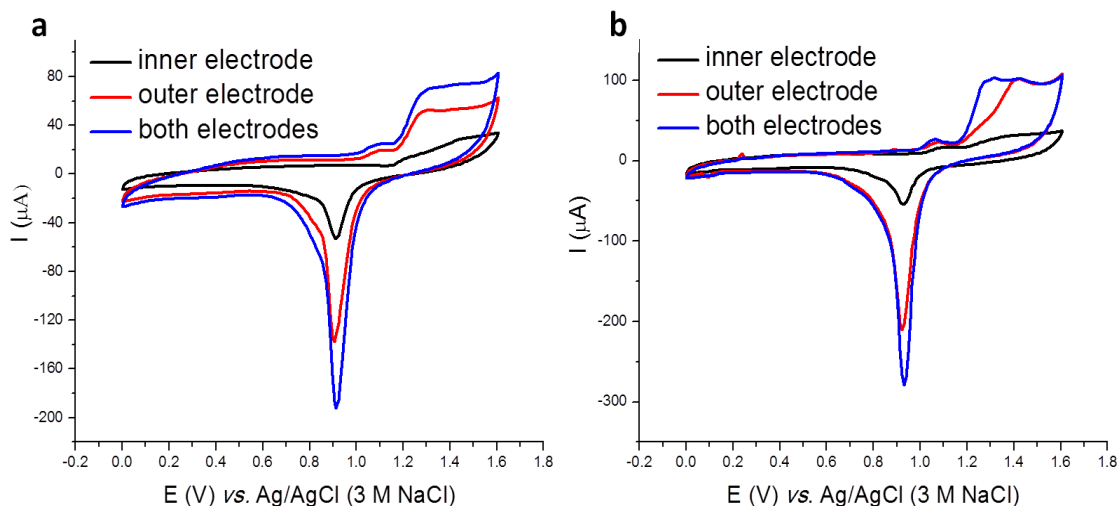


**Figure 2.26** Electrochemical characterization of structural stability and electrical independence of the coaxial electrodes before (a) and after the silica beads were removed from the composite. The coaxial sample is prepared by electrochemical deposition of gold (3 half-layers), nickel (23 half-layers) and gold (10 half-layers) into a silica based ( $\phi = 600\text{ nm}$ ) crystal template. Cyclic-voltammograms were recorded in deaerated  $0.5\text{ M}$  sulfuric acid, at  $100\text{ mV s}^{-1}$ .

## ***2 – Development of coaxial macroporous electrode architectures by infiltration of colloidal crystals***

---

It is worth mentioning that the experimentally determined active surface areas are not always in good correlation with the expected ones, due to the unequal surface coverage of both (inner and outer electrodes) with the nail varnish that has been used as a stabilizing element. This can be concluded from the values of the measured active surface areas of independent electrodes.

One would expect that the active surface of the outer electrode (10 half-layers) is about 3.33 times higher than the surface of the inner one (3 half-layers). However the experimental value of active surface area of outer electrode  $0.58 \text{ cm}^2$  is 1.2 times smaller than the expected  $0.70 \text{ cm}^2$  (calculated by multiplying the active surface area of inner electrode with factor 3.33).

It can be seen that the active surface area of the coaxial macroporous structure is 22.5% higher comparing to the surface area of the silica containing composite. This difference in active surface areas can be ascribed to the “hindering effect” of present beads which are limiting the penetration of electrolyte and the direct exposure of macroporous surface.

To investigate the electrochemical functionality of the macroporous coaxial architecture with respect to simple redox couples, cyclic-voltammetry experiments were performed in oxygen saturated sulfuric acid solution (**Figure 2.27a**). As it can be seen from the voltammograms, both macroporous electrodes gave independent signals when connected independently. For such a miniaturized electrochemical cell certain mass transport limitations could be expected. Keeping in mind the architecture of the cell, this should concern mostly the inner electrode surrounded by the outer one which might play the role of a protective shell. However, the outer electrode should not experience this phenomenon due to its direct contact with the bulk solution. Oxygen reduction has been chosen on purpose as a key test to validate the functionality of such an electrode architecture, having in mind the low solubility/diffusivity of oxygen in the solution and because of the importance of oxygen reduction in electrochemical devices such as bio(fuel) cells and biosensors. A slight shift in the onset potential (**inset at Figure 2.27a**) can be noticed, mostly due to the increase in active surface area and thus globally higher currents, which leads to a kind of magnifying effect.

For such a system one could expect the same values for the current densities once the current intensity is normalized by an active surface area of inner and outer electrode as well as for the short-circuited system (**Figure 2.27b**). However, it can be seen from the inset on **Figure 2.27b** that the plateau values for the inner electrode has a higher value than the outer electrode and their externally formed short-circuit.

## 2 – Development of coaxial macroporous electrode architectures by infiltration of colloidal crystals

The possible explanation of this behavior could be given under the assumption that the penetration of the electrolyte (0.5M sulfuric acid) is a time dependent process. The observed phenomenon indicates the increase in electro-available surface area for the inner electrode during the oxygen-reduction experiment (50 mM sulfuric acid at 5 mV/s) than during its quantification in 0.5M sulfuric acid at 100 mV/s. Due to the slow scan rate, the time scale for the oxygen-reduction experiment could be long enough to allow better penetration of the oxygen-saturated sulfuric acid which would result in a higher current values for the oxygen reduction and thus in a bigger current densities.

This is understandable especially if keeping in mind that the active surface area used for the calculation of current densities was determined under the different conditions (i.e. 20 times faster scan rate, as mentioned above). As a consequence, the determined active surface area for the inner was smaller than the one involved into the oxygen reduction process and thus the unexpected values of current densities were obtained.

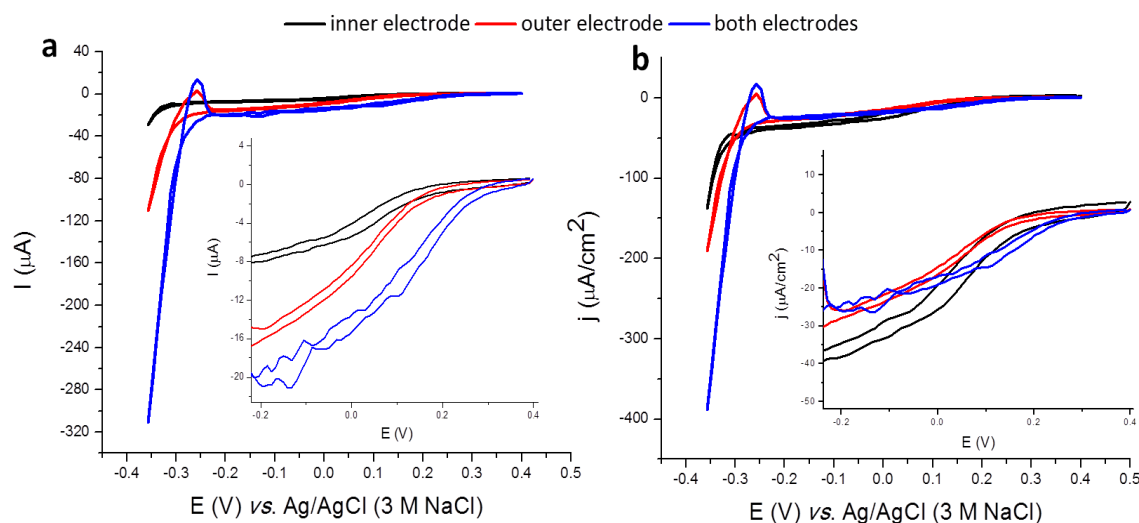


**Figure 2.27** a) Cyclic voltammograms of the oxygen reduction recorded in oxygen saturated 50 mM sulfuric acid at room temperature at a scan rate of 5 mVs<sup>-1</sup> (the measurements have been done in the following order: inner electrode - outer electrode - both of them). The coaxial electrodes were prepared by electrochemical deposition of gold (3 half layers - inner electrode, 10 half layers - outer electrode) into the silica based colloidal crystal template. The two electrodes are separated by a 14 μm wide gap. The set of the cyclic voltammograms present in figure b) were obtained by normalizing the values of the current intensity (present in the figure a)) with an electrode active surface area determined in 0.5 M sulfuric acid at scan rate of 100 mV/s. After stabilization of the structure with a nail varnish the electrochemically addressable length of the coaxial architecture was 3 mm.

## **2.5. Alternative design of a coaxial macroporous two-electrode electrochemical cell**

As previously discussed (**Subchapter 2.4.**), the bottom-up generation based on the electrodeposition of alternating metal layers presents an excellent strategy to generate coaxial macroporous two-electrode electrochemical cells with tunable properties. However, this approach is convenient only if the spatial separation between the inner and outer electrode is very small, typically not more than tens of micrometers. It is obvious that for making coaxial macroporous double electrodes with an inter-electrode distance of hundreds of microns would require a few hundred layers of silica nanoparticles.

Knowing the limits of the Langmuir-Blodgett technique in terms of template thickness it is therefore necessary to employ other strategies when bigger electrode separations are needed. An alternative and complementary approach that can be used to extend the range of inter-electrode distances is schematically illustrated in **Figure 2.28**. The strategy to fabricate such coaxial electrode architectures is based on the assembly of independently prepared inner and outer macroporous electrodes. In contrast to the preparation of the inner electrode where only the potentiostatic electrodeposition of gold through the cylindrical nanoparticle template is used, the procedure for the fabrication of the outer cylindrical macroporous electrode is based on multiple steps. Electroless deposition allows generating a very thin silver coating (**Figure 2.28b**) on the outer wall of a glass capillary (**Figure 2.28a**) through the chemical reduction of  $[\text{Ag}(\text{NH}_3)_2]^+$  (i.e. Tollens' reagent) ions by glucose. The formed "silver mirror" can be used in a straight-forward way as a substrate for the synthesis of cylindrical multilayered Langmuir-Blodgett films (**Figure 2.28c**) since the silver is hydrophilic and in contrast to gold it doesn't require any additional pretreatment. Prior to the subsequent electrodeposition of macroporous gold, a thin nickel layer was electrodeposited through the silica template for a short period of time in order to cover the existing silver coating (**Figure 2.28d**). This intermediate step allows a more homogeneous electrodeposition of gold through the nanoparticle template, since no notable oscillations of the current intensity were observed when the gold electrodeposition was carried out directly on the silver surface (**Figure 2.28e**).

Once the outer electrode is generated, the whole device is assembled by electrically connecting the outer electrode and incorporating the inner electrode into the cavity of the glass capillary (**Figure 2.28f**). The so-formed structure is sealed with epoxy glue (**Figure 2.28g**) on both sides of the glass capillary to ensure a good mechanical stability and the integrity of the device.



## 2 – Development of coaxial macroporous electrode architectures by infiltration of colloidal crystals

In the following the silver/nickel layer is removed with diluted nitric acid and then the capillary is dissolved with hydrofluoric acid. In this final step, the silica nanoparticles and glass capillary are etched away simultaneously with 30% hydrofluoric acid over 5-6 hours (**Figure 2.28h**). Despite these severe chemical conditions the epoxy seal remains intact, providing a good stability of the device.

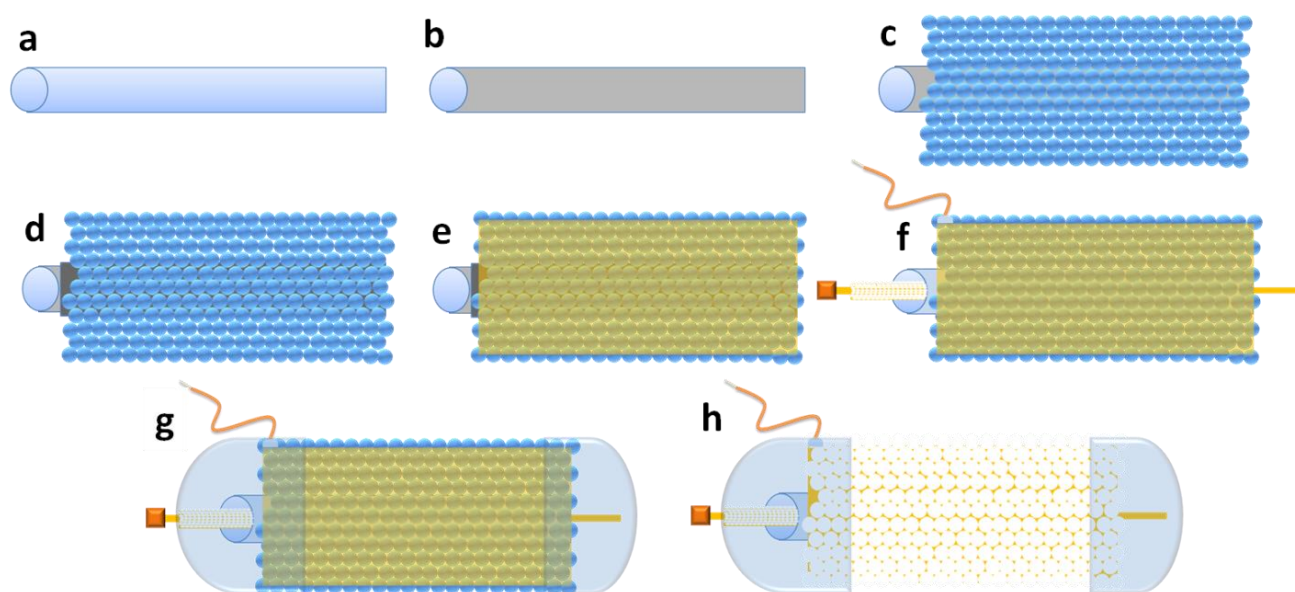


**Figure 2.28** Schematic representation of the procedure for fabricating the coaxial two-electrode electrochemical cell based on an alternative and complementary approach: a) pre-cleaned glass capillary, b) electroless silver coating, c) silica nanoparticle template synthesized by Langmuir-Blodgett technique, d) electrodeposition of a thin nickel layer over the silver coating, e) potentiostatic electrodeposition of gold through the nanoparticle template, f) assembly of the device, g) sealing of the structure with epoxy glue, h) final coaxial macroporous two-electrode electrochemical cell after the silica nanoparticles and the glass capillary have been etched with 30% HF.

Chronoamperometric curves recorded during the electrodeposition of gold show well pronounced oscillations (**Figure 2.29a**) which indicate the good quality of the colloidal crystal template and thus the homogeneity of the silver coating underneath. This is confirmed by SEM (**Figure 2.29b**) characterization where homogeneously distributed pores are observed, similarly to what has been observed in the case of the macroporous gold microwires. **Figures 2.29 c** and **d** present the topology of the macroporous cylinder (**c**) peeled off the glass capillary, after the dissolution of silver and nickel. (**d**) The assembled device with the macroporous outer and centrally positioned inner electrode. The possibility to peel the macroporous gold layer off the capillary opens also the possibility to fabricate transposable macroporous gold films.



## 2 – Development of coaxial macroporous electrode architectures by infiltration of colloidal crystals

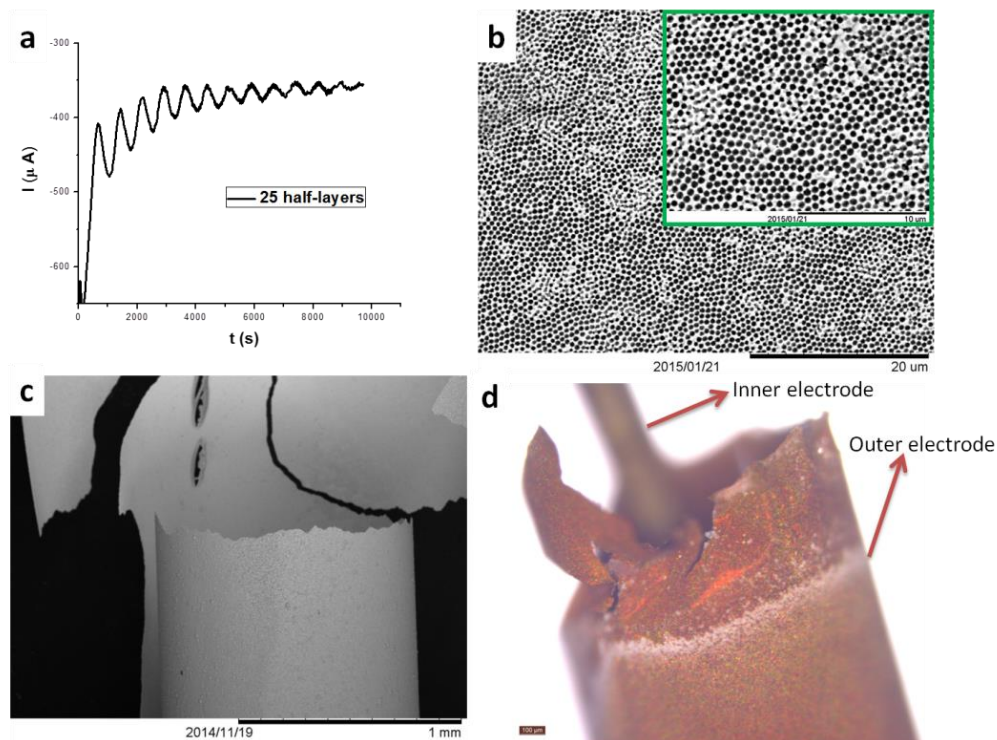


**Figure 2.29** a) Chronoamperometric curve for the electrodeposition of gold (ECF60,  $E = -0.66$  V) into a cylindrical colloidal template of 25 half-layers of silica nanoparticles (600 nm) that have been synthesized on a metalized glass capillary ( $\phi_{\text{inner cavity}} = 275$   $\mu\text{m}$ ;  $d_{\text{glass wall}} = 450$   $\mu\text{m}$ ) by the Langmuir-Blodgett technique, b) Top view SEM image shows the homogeneous surface distribution of the pores, c) SEM image of a macroporous cylinder peeled off the glass capillary after the nickel and silver layers have been dissolved with 24%  $\text{HNO}_3$ , d) Microscope image of the assembled device after dissolution of the glass capillary, where the centrally positioned macroporous gold wire ( $\phi = 250$   $\mu\text{m}$ ) was used as inner and the macroporous cylinder as the outer electrode. The inter-electrode distance was 450  $\mu\text{m}$ .

Once again, cyclic voltammetry was used to confirm the structural stability and the functionality of the device. Cyclic voltammograms recorded in 0.5 M sulfuric acid solution for both independently addressable electrodes (**Figure 2.30**) clearly demonstrate the absence of electrical short circuits in the system consisting of two distinct macroporous electrodes.

## 2 – Development of coaxial macroporous electrode architectures by infiltration of colloidal crystals

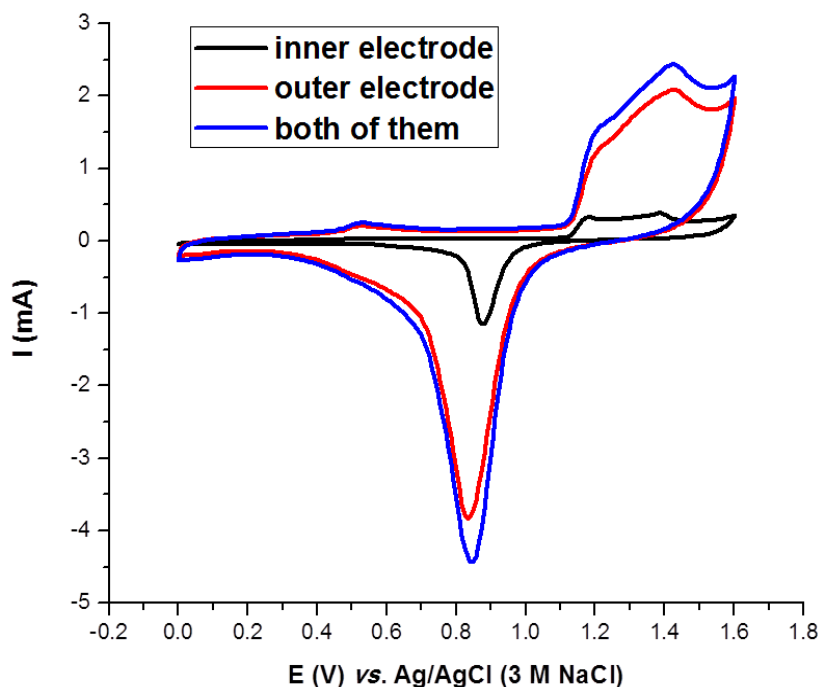


**Figure 2.30** Cyclic-voltammogram of independent coaxial and macroporous electrodes, recorded in 0.5 M  $\text{H}_2\text{SO}_4$  at a scan rate of  $100 \text{ mV s}^{-1}$ . Calculated active surface areas for inner and outer electrodes as well as for the short-circuited system were  $3.5 \text{ cm}^2$  (31 half-layer),  $20.8 \text{ cm}^2$  (25 half-layers) and  $24.6 \text{ cm}^2$  respectively

As in the first case of the miniaturized coaxial macroporous electrochemical cell, oxygen reduction was used as a key test to demonstrate the electrochemical functionality of such a system (**Figure 2.31a**). In general, the current intensities measured during the voltammetric records were higher in comparison with the first type of coaxial cell obtained by the alternating metal layer approach. This is due to the significant increase in active surface area. As a matter of fact the geometric surface of the outer electrode (determined by the dimensions of the glass capillary) is much higher than the one of the gold microwires. **Figure 2.31b** presents the cyclic-voltammograms obtained by normalizing current intensities with the active surface area of both, inner and outer electrodes. Regardless of the fabrication procedure, once again the mismatching between the determined active surface area and the surface which was electro-available for the oxygen reduction gave the similar result (**Figure 2.31b**) as had been observed for the samples prepared by the alternating metal approach (**pages 48. and 49.**).

## 2 – Development of coaxial macroporous electrode architectures by infiltration of colloidal crystals

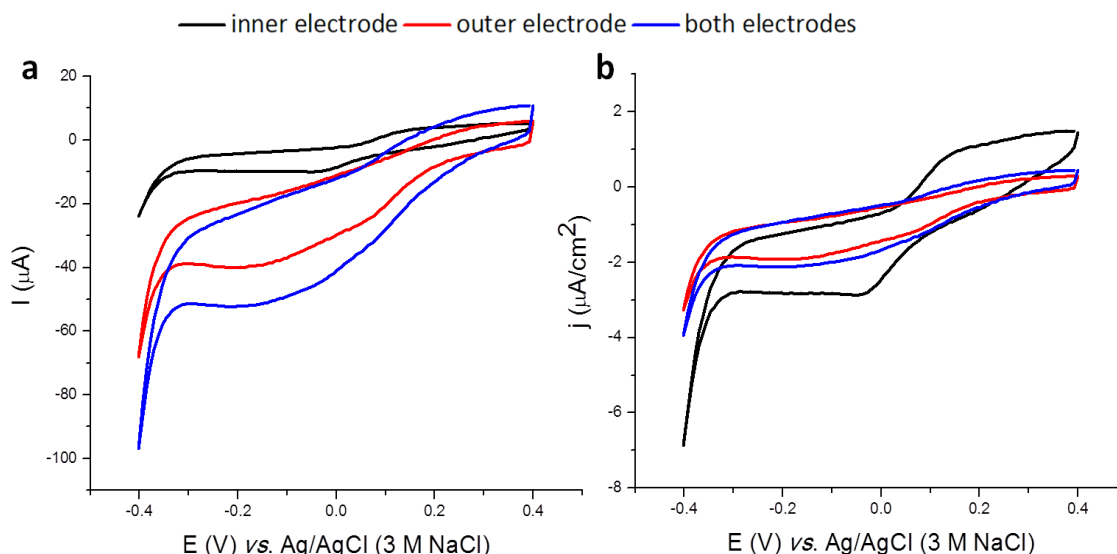


**Figure 2.31** a) Cyclic-voltammograms of the oxygen reduction recorded in oxygen saturated 50 mM sulfuric acid solution at  $5 \text{ mV s}^{-1}$ . The two coaxial electrodes are separated by a  $450 \text{ }\mu\text{m}$  gap while the total diameter of the device and its length were 1.2 mm and 5 mm respectively b) Cyclic voltammograms with the current intensities normalized by the active surface areas of inner ( $3.5 \text{ cm}^2$ ), outer ( $20.8 \text{ cm}^2$ ) electrode and the short-circuited system ( $24.6 \text{ cm}^2$ ).

### 2.6. Conclusion

Two different and complementary procedures for the fabrication of coaxial and macroporous two-electrode electrochemical cells have been present in this chapter. Both ways rely on the use of macroporous gold as a structural material that has been prepared via a so-called hard template approach. The first fabrication strategy is based on potentiostatic electrodeposition of alternating gold ( $E = -660 \text{ mV}$ ) - nickel ( $E = -850 \text{ mV}$ ) - gold ( $E = -750 \text{ mV}$ ) layers through a silica based ( $\phi_{\text{(silica particles)}} = 600 \text{ nm}$ ) colloidal template which has been prepared on the surface of a gold micro-wire ( $\phi = 250 \text{ }\mu\text{m}$ ) by the Langmuir-Blodgett procedure. This step was followed by selective etching of the nickel layer in nitric acid (30 % wt.) and the subsequent stabilization of the structure (using diluted nail varnish) and electrical addressing of both electrodes (the inner electrode is addressed by its direct contact with the supporting gold micro-wire while the outer one is addressed by means of a  $50 \text{ }\mu\text{m}$  gold micro-wire that is glued onto its surface by silver paint). In the last step, silica beads were removed by 5% HF and the final coaxial architecture is obtained.

## ***2 – Development of coaxial macroporous electrode architectures by infiltration of colloidal crystals***

---

Using this strategy, it is possible to fabricate a miniaturized double electrode electrochemical cell with a tunable porosity (by changing the diameter of silica beads), electrode active surface area (by changing the thickness of electrodeposited gold) and an inter electrode distance (in other words the volume of an electrolyte container) which lies in the range of tens of micrometers.

The second way to fabricate such kind of architectures with an inter-electrode distances in the range of hundreds of micrometers is based on the separate preparation of inner and outer macroporous gold electrodes and their assembly in the final device. Following this approach, the inner macroporous gold electrode is prepared separately by potentiostatic electrodeposition of gold (at  $E = -660$  mV) through-out a cylindrical silica colloidal template ( $\phi_{(\text{silica beads})} = 600$  nm,  $\phi_{(\text{gold micro-wire})} = 250$   $\mu\text{m}$ ). The fabrication procedure of the outer electrode can be summarized in few steps: 1. Cleaning of a TLC glass capillary with chloroform and “Piranha” solution respectively; 2. Electroless deposition of a thin silver layer (by chemical reduction of Tollens’ reagent with diluted glucose solution) onto the surface of the pre-cleaned glass substrate; 2. Synthesis of the colloidal crystal template ( $\phi_{(\text{silica beads})} = 600$  nm), 3. Short electrodeposition of a thin layer of nickel; 4. Subsequent electrodeposition of gold (ECF63, at  $E = -750$  mV) and 5. Chemical etching of the underlying silver and nickel layers by nitric acid. In the last step, the inner electrode is introduced into the cavity of the glass capillary, the outer electrode is electrically addressed by means of a gold micro-wire ( $\phi = 50$   $\mu\text{m}$ ) and the whole structure is sealed at both sides by an epoxy glue. Silica beads and glass capillary were simultaneously etched by concentrated HF.

Electrochemical characterization of these double electrode architectures prepared by using both strategies has been done by cyclic-voltammetry in deaerated 0.5 M sulfuric acid solution. The results presented in this chapter demonstrate excellent structural stability of the fabricated architectures. This can be seen from the difference in the charges related to the reduction of gold-oxide (this process takes place at approximately 0.9 V) at separately connected inner and outer electrodes (the electrodes are prepared with different active surface areas on purpose to make their cyclic-voltammograms easily distinguishable). Also, the electrochemical functionality has been demonstrated for both architectures. This has been done by investigating the oxygen reduction reaction at both (inner and outer) electrodes in oxygen saturated 50 mM sulfuric acid at a scan rate of 5 mVs<sup>-1</sup>. The results confirm that the oxygen reduction can take place at the surface of both macroporous electrodes proving that the inner electrode is electrochemically accessible although it is surrounded by the thicker outer one.

## ***2 – Development of coaxial macroporous electrode architectures by infiltration of colloidal crystals***

---

The current densities (obtained by normalizing current intensity with respect to the real electrode surface) for the oxygen reduction reaction were higher for the inner electrode than for the outer one suggesting that the surface of the inner electrode is under-estimated, possibly due to the slower penetration of the electrolyte during the determination of its electrode active surface area. Nevertheless, the two presented procedures for the fabrication of the two-electrode electrochemical cells present a novel approach to fabricate miniaturized electrochemical platforms that could find their application in the fields of miniaturized electrochemical devices such as biosensors, biofuel cells and batteries.

### **Literature**

- [1] V. Urbanová, K. Vytřas, A. Kuhn, *Electrochem. Commun.* 12 (2010) 114.
- [2] M. Gamero, M. Sosna, F. Pariente, E. Lorenzo, P.N. Bartlett, C. Alonso, *Talanta* 94 (2012) 328.
- [3] Y. Bai, W. Yang, Y. Sun, C. Sun, *Sensors Actuators B Chem.* 134 (2008) 471.
- [4] H. Cao, Y. Zhu, L. Tang, X. Yang, C. Li, *Electroanalysis* 20 (2008) 2223.
- [5] J.D. Qiu, H.Z. Peng, R.P. Liang, M. Xiong, *Electroanalysis* 19 (2007) 1201.
- [6] Y. Du, K. Lv, B. Su, N. Zhang, C. Wang, *J. Appl. Electrochem.* 39 (2009) 2409.
- [7] K.-S. Choi, E.W. McFarland, G.D. Stucky, *Adv. Mater.* 15 (2003) 2018.
- [8] S. Reculosa, M. Heim, F. Gao, N. Mano, S. Ravaine, A. Kuhn, *Adv. Funct. Mater.* 21 (2011) 691.
- [9] M. Heim, C. Wattanakit, S. Reculosa, C. Warakulwit, J. Limtrakul, S. Ravaine, A. Kuhn, *Electroanalysis* 25 (2013) 888.
- [10] M.-C. Tsai, D.-X. Zhuang, P.-Y. Chen, *Electrochim. Acta* 55 (2010) 1019.
- [11] J. Zhang, P. Liu, H. Ma, Y. Ding, *J. Phys. Chem. C* 111 (2007) 10382.
- [12] L.H.S. Gasparotto, A. Prowald, N. Borisenko, S.Z. El Abedin, A. Garsuch, F. Endres, *J. Power Sources* 196 (2011) 2879.
- [13] F.-S. Ke, L. Huang, H.-B. Wei, J.-S. Cai, X.-Y. Fan, F.-Z. Yang, S.-G. Sun, *J. Power Sources* 170 (2007) 450.
- [14] M.-S. Wu, Y.-P. Lin, *Electrochim. Acta* 56 (2011) 2068.
- [15] Z. Wang, F. Li, N.S. Ergang, A. Stein, *Carbon N. Y.* 46 (2008) 1702.
- [16] H. Sakai, T. Nakagawa, Y. Tokita, T. Hatazawa, T. Ikeda, S. Tsujimura, K. Kano, *Energy Environ. Sci.* 2 (2009) 133.
- [17] J.H. Pikul, H. Gang Zhang, J. Cho, P. V Braun, W.P. King, *Nat Commun* 4 (2013) 1732.
- [18] S. Boland, D. Leech, *Analyst* 137 (2012) 113.
- [19] M.L.K. Hoa, M. Lu, Y. Zhang, *Adv. Colloid Interface Sci.* 121 (2006) 9.
- [20] R.H.W. Au, R.J. Puddephatt, *Chem. Vap. Depos.* 13 (2007) 20.
- [21] M. Feng, R.J. Puddephatt, *Chem. Mater.* 15 (2003) 2696.
- [22] H. Cong, W. Cao, *J. Colloid Interface Sci.* 278 (2004) 423.
- [23] O.D. Velev, P.M. Tessier, A.M. Lenhoff, E.W. Kaler, *Nature* 401 (1999) 548.

## ***2 – Development of coaxial macroporous electrode architectures by infiltration of colloidal crystals***

---

- [24] P. Jiang, J. Cizeron, J.F. Bertone, V.L. Colvin, J. Am. Chem. Soc. 121 (1999) 7957.
- [25] P. Jiang, K.S. Hwang, D.M. Mittelman, J.F. Bertone, V.L. Colvin, J. Am. Chem. Soc. 121 (1999) 11630.
- [26] S.H. Park, Y. Xia, Adv. Mater. 10 (1998) 1045.
- [27] W. Yan, H. Li, X. Shen, Eur. Polym. J. 41 (2005) 992.
- [28] P.N. Bartlett, P.R. Birkin, M.A. Ghanem, C.-S. Toh, J. Mater. Chem. 11 (2001) 849.
- [29] A. Esmanski, G.A. Ozin, Adv. Funct. Mater. 19 (2009) 1999.
- [30] L.K. van Vugt, A.F. van Driel, R.W. Tjerkstra, L. Bechger, W.L. Vos, D. Vanmaekelbergh, J.J. Kelly, Chem. Commun. (2002) 2054.
- [31] H. Míguez, E. Chomski, F. García-Santamaría, M. Ibisate, S. John, C. López, F. Meseguer, J.P. Mondia, G.A. Ozin, O. Toader, H.M. van Driel, Adv. Mater. 13 (2001) 1634.
- [32] X. Meng, R. Al-Salman, J. Zhao, N. Borissenko, Y. Li, F. Endres, Angew. Chemie Int. Ed. 48 (2009) 2703.
- [33] H. Föll, M. Leisner, A. Cojocaru, J. Carstensen, Materials (Basel). 3 (2010) 3006.
- [34] J.S. Sakamoto, B. Dunn, J. Mater. Chem. 12 (2002) 2859.
- [35] M. Sadakane, T. Horiuchi, N. Kato, C. Takahashi, W. Ueda, Chem. Mater. 19 (2007) 5779.
- [36] O.D. Velev, A.M. Lenhoff, Curr. Opin. Colloid Interface Sci. 5 (2000) 56.
- [37] A. Stein, Microporous Mesoporous Mater. 44–45 (2001) 227.
- [38] O.D. Velev, E.W. Kaler, Adv. Mater. 12 (2000) 531.
- [39] K.S. Choi, H.C. Lichtenegger, G.D. Stucky, E.W. McFarland, J. Am. Chem. Soc. 124 (2002) 12402.
- [40] K. Choy, Prog. Mater. Sci. 48 (2003) 57.
- [41] A. Stein, F. Li, N.R. Denny, Chem. Mater. 20 (2008) 649.
- [42] A.A. Zakhidov, R.H. Baughman, Z. Iqbal, C. Cui, I. Khayrullin, S.O. Dantas, J. Marti, V.G. Ralchenko, Sci. 282 (1998) 897.
- [43] V.G. Ralchenko, D.N. Sovyk, A.P. Bolshakov, A.A. Homich, I.I. Vlasov, D.A. Kurdyukov, V.G. Golubev, A.A. Zakhidov, Phys. Solid State 53 (2011) 1131.
- [44] B.H. Juárez, P.D. García, D. Golmayo, A. Blanco, C. López, Adv. Mater. 17 (2005) 2761.
- [45] G. von Freymann, S. John, M. Schulz-Dobrick, E. Vekris, N. Tétreault, S. Wong, V. Kitaev, G.A. Ozin, Appl. Phys. Lett. 84 (2004).
- [46] S. Reculosa, B. Agricole, A. Derré, M. Couzi, E. Sellier, P. Delhaès, S. Ravaine, Electroanalysis 19 (2007) 379.
- [47] C. Marichy, M. Bechelany, N. Pinna, Adv. Mater. 24 (2012) 1017.
- [48] Z.A. Sechrist, B.T. Schwartz, J.H. Lee, J.A. McCormick, R. Piestun, W. Park, S.M. George, Chem. Mater. 18 (2006) 3562.
- [49] J.S. King, E. Graugnard, C.J. Summers, Adv. Mater. 17 (2005) 1010.
- [50] J.S. King, C.W. Neff, S. Blomquist, E. Forsythe, D. Morton, C.J. Summers, Phys. Status Solidi 241 (2004) 763.
- [51] J.S. King, E. Graugnard, C.J. Summers, Appl. Phys. Lett. 88 (2006) 86.
- [52] J.S. King, C.W. Neff, S. Blomquist, E. Forsythe, D. Morton, C.J. Summers, Phys. Status Solidi 241 (2004) 763.

## ***2 – Development of coaxial macroporous electrode architectures by infiltration of colloidal crystals***

---

- [53] C. Detavernier, J. Dendooven, S. Pulinthanathu Sree, K.F. Ludwig, J. A. Martens, *Chem. Soc. Rev.* 40 (2011) 5242.
- [54] A. Walcarius, *Anal. Bioanal. Chem.* 396 (2010) 261.
- [55] P. Jiang, J. Cizeron, J.F. Bertone, V.L. Colvin, *J. Am. Chem. Soc.* 121 (1999) 7957.
- [56] W. Quan-Zhou, Y. Qiang, L. Ju-Fang, D. Jing-Heng, L. Yu-Guang, *Chinese J. Chem.* 23 (2005) 689.
- [57] W. Dong, H.J. Bongard, F. Marlow, *Chem. Mater.* 15 (2003) 568.
- [58] F. Su, X.S. Zhao, Y. Wang, J. Zeng, Z. Zhou, J.Y. Lee, *J. Phys. Chem. B* 109 (2005) 20200.
- [59] A. Stein, R.C. Schroden, *Curr. Opin. Solid State Mater. Sci.* 5 (2001) 553.
- [60] Y. Bon Saint Côme, H. Lalo, Z. Wang, M. Etienne, J. Gajdzik, G.-W. Kohring, A. Walcarius, R. Hempelmann, A. Kuhn, *Langmuir* 27 (2011) 12737.
- [61] O.D. Velev, T.A. Jede, R.F. Lobo, A.M. Lenhoff, *Chem. Mater.* 10 (1998) 3597.
- [62] J.W. Galusha, C.-K. Tsung, G.D. Stucky, M.H. Bartl, *Chem. Mater.* 20 (2008) 4925.
- [63] M. Kotobuki, Y. Isshiki, H. Munakata, K. Kanamura, *Electrochim. Acta* 55 (2010) 6892.
- [64] X. Qu, H. Song, G. Pan, X. Bai, B. Dong, H. Zhao, Q. Dai, H. Zhang, R. Qin, S. Lu, *J. Phys. Chem. C* 113 (2009) 5906.
- [65] G.I.N. Waterhouse, J.B. Metson, H. Idriss, D. Sun-Waterhouse, *Chem. Mater.* 20 (2008) 1183.
- [66] H. Yan, C.F. Blanford, B.T. Holland, W.H. Smyrl, A. Stein, *Chem. Mater.* 12 (2000) 1134.
- [67] A. Stein, *Microporous Mesoporous Mater.* 44-45 (2001) 227.
- [68] H. Míguez, F. Meseguer, C. López, F. López-Tejiera, J. Sánchez-Dehesa, *Adv. Mater.* 13 (2001) 393.
- [69] A. Walcarius, A. Kuhn, *TrAC Trends Anal. Chem.* 27 (2008) 593.
- [70] J. Wang, Q. Li, W. Knoll, U. Jonas, *J. Am. Chem. Soc.* 128 (2006) 15606.
- [71] F. Sun, W.P. Cai, Y. Li, B. Cao, F. Lu, G. Duan, L. Zhang, *Adv. Mater.* 16 (2004) 1116.
- [72] S.S. V Tatiparti, F. Ebrahimi, *J. Solid State Electrochem.* 16 (2012) 1255.
- [73] T. Sumida, Y. Wada, T. Kitamura, S. Yanagida, *Chem. Commun.* (2000) 1613.
- [74] B. Zhao, M.M. Collinson, *J. Electroanal. Chem.* 684 (2012) 53.
- [75] M.E. Abdelsalam, P.N. Bartlett, T. Kelf, J. Baumberg, *Langmuir* 21 (2005) 1753.
- [76] M. Heim, S. Reculosa, S. Ravaine, A. Kuhn, *Adv. Funct. Mater.* 22 (2012) 538.
- [77] J.E.G.J. Wijnhoven, S.J.M. Zevenhuizen, M.A. Hendriks, D. Vanmaekelbergh, J.J. Kelly, W.L. Vos, *Adv. Mater.* 12 (2000) 888.
- [78] S. Ben-Ali, D.A. Cook, P.N. Bartlett, A. Kuhn, *J. Electroanal. Chem.* 579 (2005) 181.
- [79] S. Cherevko, X. Xing, C.-H. Chung, *Electrochem. Commun.* 12 (2010) 467.
- [80] P.N. Bartlett, M.A. Ghanem, I.S. El Hallag, P. de Groot, A. Zhukov, *J. Mater. Chem.* 13 (2003) 2596.
- [81] H. Zhang, X. Yu, P. V Braun, *Nat Nano* 6 (2011) 277.
- [82] P. V Braun, P. Wiltzius, *Nature* 402 (1999) 603.
- [83] Y.C. Lee, T.J. Kuo, C.J. Hsu, Y.W. Su, C.C. Chen, *Langmuir* 18 (2002) 9942.
- [84] X. Li, F. Tao, Y. Jiang, Z. Xu, *J. Colloid Interface Sci.* 308 (2007) 460.
- [85] M.A. Ghanem, P.N. Bartlett, P. de Groot, A. Zhukov, *Electrochem. Commun.* 6 (2004) 447.
- [86] X.H. Li, L. Dai, Y. Liu, X.J. Chen, W. Yan, L.P. Jiang, J.J. Zhu, *Adv. Funct. Mater.* 19 (2009) 3120.



## ***2 – Development of coaxial macroporous electrode architectures by infiltration of colloidal crystals***

---

- [87] J. Lenz, V. Trieu, A. Kuhn, R. Hempelmann, ECS Trans. 33 (2011) 19.
- [88] R. Szamocki, P. Masse, S. Ravaine, V. Ravaine, R. Hempelmann, A. Kuhn, J. Mater. Chem. 19 (2009) 409.
- [89] M. Heim, L. Rousseau, S. Reculosa, V. Urbanova, C. Mazzocco, S. Joucla, L. Bouffier, K. Vytras, P. Bartlett, A. Kuhn, B. Yvert, J. Neurophysiol. 108 (2012) 1793.
- [90] A.J. Bard, L.R. Faulkner, Electrochemical Methods - Fundamentals and Applications, Second Edition, John Wiley & Sons, Inc., New York - Chichester - Weinheim - Brisbane - Singapore - Toronto, 2001.
- [91] S. Trasatti, O.A. Petrii, Pure Appl. Chem. 63 (1991) 711.
- [92] R. Szamocki, A. Velichko, C. Holzapfel, F. Mücklich, S. Ravaine, P. Garrigue, N. Sojic, R. Hempelmann, A. Kuhn, Anal. Chem. 79 (2006) 533.
- [93] F. Gao, L. Viry, M. Maugey, P. Poulin, N. Mano, Nat Commun 1 (2010) 2.
- [94] A. Heller, Anal. Bioanal. Chem. 385 (2006) 469.



---

*CHAPTER 3*

MACROPOROUS ELECTRODES FOR THE FABRICATION OF A  
BIOCATHODE

Rising human population imposes higher demands for energy. The long-term use of fossil fuels leads to problems related to the emission of combustion products ( $\text{CO}_2$ ,  $\text{N}_x\text{O}_y$  and  $\text{SO}_x$  and airborne particles) which has a strong impact on the balance that exists in the environment (e.g. greenhouse effect, acid rain and some health issues closely connected to the pollutant concentration) [1]. Besides renewable energy sources (energy of wind, sun and water) the existing need for some secondary energy sources, such as bio mass, need to be considered. Thanks to the variety of different anaerobic microorganisms, capable of metabolizing biomass, other fuels (e.g. methane) can be produced and directly implemented into energy-conversion systems such as fuel cells known to possess high efficiency. For example, methane can be used directly as a fuel in high temperature fuel cells or it can be easily converted into hydrogen through the reformation process and then used as a secondary fuel. The latter strategy would present a better option from the environmental point of view since the only operational product is water and then these systems can partially contribute to the reduction of pollutant emission [1,2].

Besides fuel cells that rely on pure inorganic catalysis, biofuel cells are another type of energy-conversion devices which utilize catalysts of biological origin (e.g. enzymes, whole cells) [3]. Although, both types of devices (fuel and biofuel cells) are dedicated to the conversion of chemical energy into electric energy, biofuel cells are limited with respect to the power density that can be generated. One of the strategies through which those limitations can be partially addressed is based on the engineering and the implementation of new types of electrode materials.

This chapter will mainly focus on the possible application of macroporous electrodes (**see Chapter 2**) for increasing the electrochemical performance of enzymatic glucose/oxygen biofuel cells.

#### **3.1. (Bio)fuel cells: Basic principles and key performance characteristics**

Fuel-cells present one of the oldest energy conversion devices capable of transforming chemical energy into electricity [4,5]. They have been pioneered by Sir William Grove in 1839 [6]. In his original experiment, W. Grove demonstrated that electromotive force (EMF) can be developed and current can flow through the system once oxygen and hydrogen were supplied to two Pt electrodes (Pt strips) immersed in diluted sulfuric acid [7]. Since that period, fuel cells have passed through numerous modifications in order to further improve their electrochemical performances, miniaturize their dimensions and make them suitable for powering other devices [6].

### 3 – Macroporous electrodes for the fabrication of a biocathode

By definition, fuel cells (FCs) are electrochemical devices in which the chemical energy of the reactants (fuel and oxidant) is converted into electricity through the separate oxidation and reduction reactions occurring at an anode (oxidation of a fuel) and a cathode surface (reduction of an oxidant) (**Figure 3.1a**). The oxidation of a fuel releases electrons that are flowing through the external electrical circuit towards the cathode where the reduction of an oxidant takes place. The electrical circuit is completed by the flow of a compensating ionic charge (e.g. flux of hydronium ions) from the anodic compartment towards the cathodic one where they are finally consumed during the reduction of an oxidant (e.g. oxygen) [6,8].

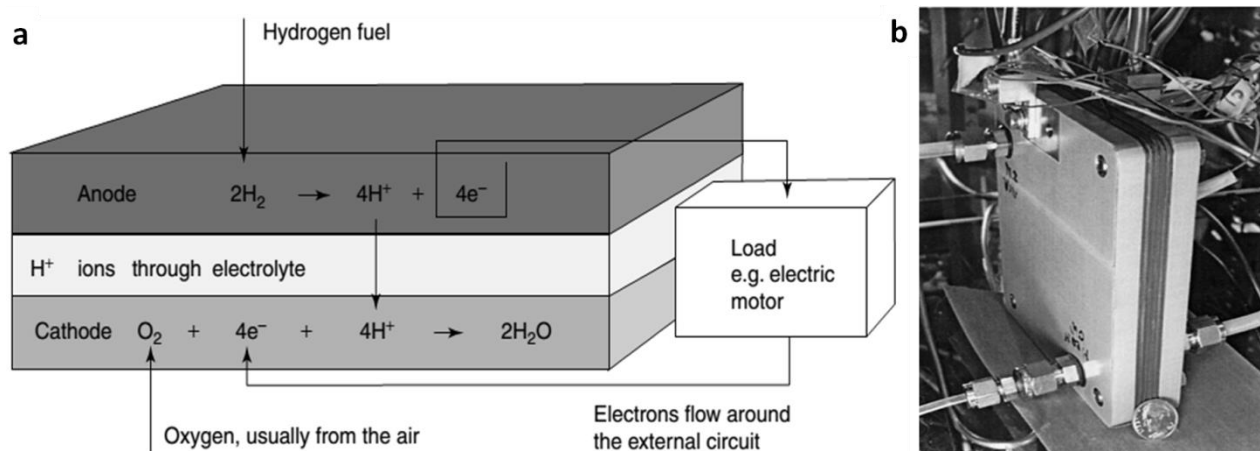


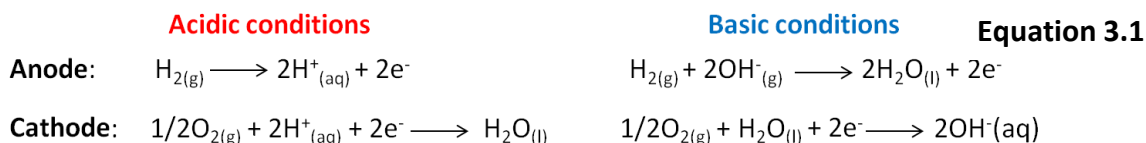
**Figure 3.1.** (a) Basic construction and principle of functioning of an acidic hydrogen-oxygen fuel cell [6]; (b) Photograph of a direct methanol/oxygen fuel cell (DMFC) stack (5 individual fuel cells were connected in a row) fabricated at Los Alamos National Laboratory (LANL), USA [9].

The flux of a compensating charge is made possible by a semi-permeable membrane (e.g. proton-exchange membrane (PEM)) whose major role in the system is to prevent the diffusion of reactants and their cross-over reactions at non-corresponding electrodes. This would significantly decrease the performance (power output) of the system [6,8]. Beside the prevention of cross-over reactions, semi-permeable membranes are designed to allow the conduction of protons (e.g. Nafion® membrane) and hydroxyl ions in between cathodic and anodic compartments [10,11]. This means that the ion-conductive polymeric membrane acts as a polymer electrolyte enabling the completion of an electric circuit (the flow of electrons is compensated by flow of ions in the solution) [10,11]. The examples where ion-conductive membranes have found their applications are membrane/electrode assemblies (MEAs). In MEAs, several ion-conductive membranes/electrode units are connected in a row, maximizing the final power output of a fuel cell [9]. In some cases, the use of membranes can be avoided by a constant flow of electrolyte between the two electrodes [12,13].

### 3 – Macroporous electrodes for the fabrication of a biocathode

The working principle of fuel cells depends on the operational conditions. For instance, hydrogen/oxygen is one of the oldest type of fuel cell which is able to operate under both, acidic [12] and basic [13] conditions (**Equations 3.1a and b** [1]).

The advantage of the latter is improved oxygen electro-reduction kinetics (in general that is the half-cell reaction that dominates the power generated by the system) as well as the possibility to use some other, less expensive, electro-catalysts (e.g. Ag/C instead of expensive Pt catalyst) [13].



For the best performance of fuel cells, high-purity gasses ( $\text{H}_2$  and  $\text{O}_2$ ) are required, because the smallest amount of impurities (e.g. CO and  $\text{CO}_2$ ) can poison the Pt catalyst [14]. Besides  $\text{H}_2$ , other fuels can be used such as methanol and also some hydrocarbons [8].

In biofuel cells, the choice of biocatalyst determines their final classification as either 1. Enzyme based biofuel cells (EBFC) [15] (**Figure 3.2a**) or 2. Microbial biofuel cells (MBFC) [16] (**Figure 3.2b**).

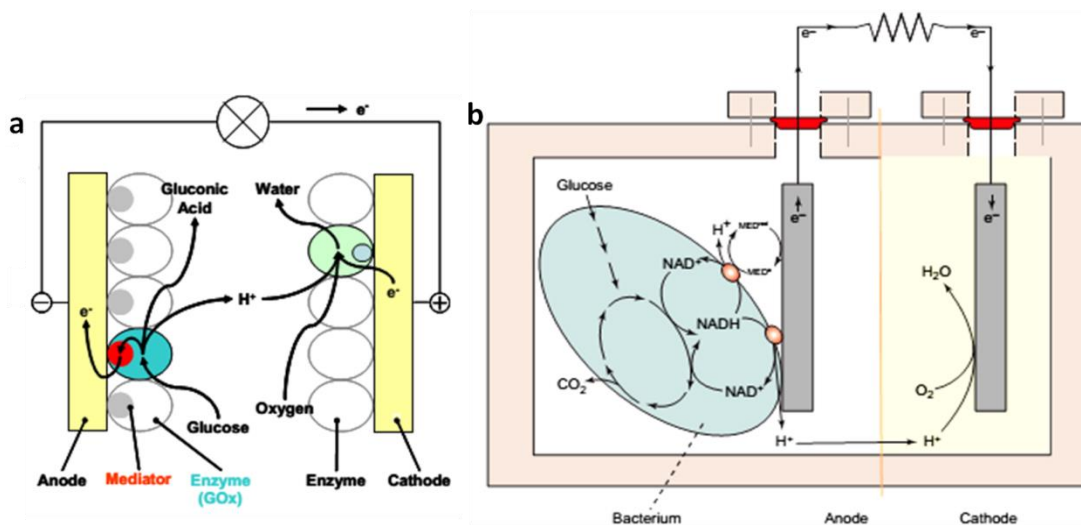


**Figure 3.2.** (a) Schematic of a glucose/oxygen BFC. Glucose oxidation at the anode is enzymatically catalyzed by glucose oxidase (GOx) while the oxygen is reduced to water in a reaction catalyzed by an oxygen reducing enzyme in the cathodic compartment. Flow of electrons through the externally placed load is compensated by proton flux in the solution [15]; (b) Schematic representation of a glucose/oxygen MBFC. Complete glucose oxidation to  $\text{CO}_2$  is accomplished by a full metabolic pathway within living bacteria while oxygen is electro-reduced at the cathode surface [16].

### 3 – Macroporous electrodes for the fabrication of a biocathode

From an electrochemical point of view, the essential difference between MBFCs and EBFCs (that comprise only one enzyme) is the efficiency of fuel oxidation. While MBFCs are able to completely oxidize fuels thanks to a cocktail of different enzymes that are involved in their natural metabolic pathways, single enzyme EBFCs are not able to accomplish this since the number of immobilized enzymes is a limiting factor [17,18]. Recently, an ethanol/oxygen biofuel cell based on the cascade of different enzymes (alcohol dehydrogenase (ADH), aldehyde dehydrogenase (ALDH) and the enzymes of Krebs cycle) has been designed for the full ethanol oxidation to  $\text{CO}_2$  in the anodic compartment while oxygen was reduced at a platinum based cathode [19]. Similar approaches of mimicking natural metabolic pathways, through the immobilization of enzymatic cascades, have been used for the fabrication of “total” glucose/oxygen EBFC [20]. While MBFCs dominate over EBFCs in terms of the efficiency of fuel oxidation, the problems related to mass transport limitations through the cell membrane are diminishing theoretical electrochemical performances of the device in comparison with EFCs [17]. Although the power density of EBFC is higher than for the microbial one, the limited lifetime of EBFCs (7-10 days) presents one of the issues that have to be improved [21].

The power that can be produced by biofuel cells is much less than the power that can be produced in fuel cells [17]. Another issue is the operating temperature of those devices. While fuel cells are operating at temperatures higher than  $50^\circ\text{C}$  (due to the significant amount of energy loss in the form of heat) (**Table 3.1.**) [8], the usual temperature at which enzymatic fuel cells are operating is in the  $20 - 40^\circ\text{C}$  range [3]. Furthermore, enzymes which are commonly used in BFC possess a narrow optimal range of pH values (*i.e.* near neutral) at which they exhibit their highest catalytic activity [17]. This value is far from the pH at which fuel cells are functioning (strongly acidic or basic condition). An important advantage of BFC over FC is the non-toxicity and biocompatibility of enzymes (especially the enzymes that are natural constituents of the human metabolism) and lower costs of the ingredients for their fabrication since FCs are usually based on platinum catalysts. With an appropriate design of the electrochemical platform [22] EBFCs can be miniaturized. All points mentioned above present some of the main advantages of biofuel cells over fuel cells which would allow the fabrication of devices that are able to operate under physiological conditions and eventually power small medical devices (e.g. pacemakers [23]) or to work as self-powered subcutaneous glucose sensor [24].

Type	Temperature $^\circ\text{C}$	Fuel	Electrolyte	Mobile ion
PEM : polymer electrolyte membrane	70–110	$\text{H}_2$ , $\text{CH}_3\text{OH}$	Sulfonated polymers (Nafion <sup>TM</sup> )	$(\text{H}_2\text{O})_n\text{H}^+$
AFC: alkali fuel cell	100–250	$\text{H}_2$	Aqueous KOH	$\text{OH}^-$
PAFC: phosphoric acid fuel cell	150–250	$\text{H}_2$	$\text{H}_3\text{PO}_4$	$\text{H}^+$
MCFC: molten carbonate fuel cell	500–700	hydrocarbons, CO	$(\text{Na,K})_2\text{CO}_3$	$\text{CO}_3^{2-}$
SOFC: solid oxide fuel cell	700–1000	hydrocarbons, CO	$(\text{Zr,Y})\text{O}_{2-\delta}$	$\text{O}^{2-}$

**Table 3.1.** Examples of different types of fuel cells with highlighted operating temperatures (adapted from [8]).

### 3 – Macroporous electrodes for the fabrication of a biocathode

With respect to thermodynamic aspects, biofuel cells present open systems in which the reactants and the energy can be exchanged with the environment and therefore can be described with classical approaches [5,6]. One of the key performance characteristics of a biofuel cells is their efficiency which can be calculated from:

1. Energy input through the reactants that are delivered to the electrodes. This is reflected in the change of enthalpy ( $\Delta H$ ) since it presents the total energy involved in a chemical reaction.
2. Energy loss in the form of heat ( $T \cdot \Delta S$ ;  $\Delta S$  – change of entropy) that is released into the environment.
3. Energy output as a change of Gibbs' free energy ( $\Delta G$ ). It can be calculated from the difference of the change of enthalpy and released heat :

$$\Delta G = \Delta H - T \cdot \Delta S$$

The value of  $\Delta G$  is equivalent to the useful work in an electrochemical system ( $\Delta G = W_{el}$ ) .

Knowing the thermodynamic quantities mentioned above, one can easily calculate the theoretical efficiency of a bio(fuel) cell as:

$$Efficiency = \frac{\Delta G}{\Delta H} = 1 - \frac{T\Delta S}{\Delta H} \quad \text{Equation 3.2.}$$

This is schematically presented in **Figure 3.3**.

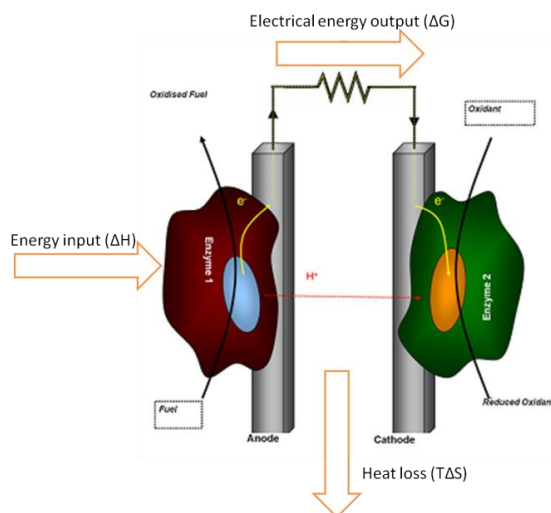


**Figure 3.3.** Schematic representation of a membraneless EBFC emphasizing the thermodynamic parameters of the system (modified and adapted from [25]).

### 3 – Macroporous electrodes for the fabrication of a biocathode

---

The energy output, that is produced by the electrochemical system can be calculated as  $\Delta G = W_{el.} = -zF\Delta E$ , where:  $z$  - number of electrons exchanged in the reaction,  $F$  – Faraday constant ( $F = 96485 \text{ Cmol}^{-1}$ ), (and therefore  $z \cdot F$  – transported charge),  $\Delta E$  – (theoretical) voltage of the (bio)fuel cell.

The thermodynamic (theoretical) open circuit voltage (OCV) developed within the electrochemical cell can be calculated as the difference of electrode potentials of the fuel/oxidized fuel and oxidant/reduced oxidant couples. It can be easily calculated for a reversible electrochemical system using the Nernst equation:  $E = E^0 - \frac{RT}{zF} \ln Q$ , where:  $E$  is the electrode potential,  $E^0$  - standard electrode potential,  $R$  – universal gas constant ( $R = 8.314 \text{ Jmol}^{-1}\text{K}^{-1}$ ),  $Q$  - reaction quotient.

Concerning the expression that connects  $\Delta G$  and OCV, another way to calculate the maximal efficiency of a (bio)fuel cell is:

$$\text{Efficiency} = \frac{-zF\Delta E}{\Delta H} \quad \text{Equation 3.3.}$$

Equation 3.3. presents the efficiency of the system when a certain amount of energy input is lost in the form of heat. If the system would work with a hypothetical efficiency of 100% (no heat losses and thus  $\Delta G = \Delta H$ ), the operating cell voltage would be:  $\Delta E = -\frac{\Delta H}{zF}$ . Regarding this relation, one can calculate the actual cell efficiency as:

$$\text{Efficiency} = \frac{V_c}{\Delta E} \cdot 100\% \quad \text{Equation 3.4.}$$

with  $V_c$  being the operating cell voltage.

From an electrochemical stand point, every biofuel cell is defined by the power output of the device which is determined by the current that flows through the system and the difference of electrode potentials (**Figure 3.4.**). As mentioned before, OCV is the maximal voltage of a biofuel cell at zero current (**Figure 3.4a**). As can be seen from the present voltammograms (**Figure 3.4a**) practically the OCV corresponds to the difference between the onset potentials of the cathodic and the anodic reactions. If the redox enzyme operates close to the thermodynamic potential of a substrate/product couple, then the OCV can be maximized due to the smaller activation overpotential required to keep the system running. In the opposite case (**Figure 3.4a**), one part of the cell voltage is lost due to the activation of an enzyme and therefore the OCV is becoming lower than its thermodynamic value [5,26]. In fuel cells this difference is due to crossover reactions that are taking place once the reactants diffuse across the semi-permeable membrane [8].

### 3 – Macroporous electrodes for the fabrication of a biocathode

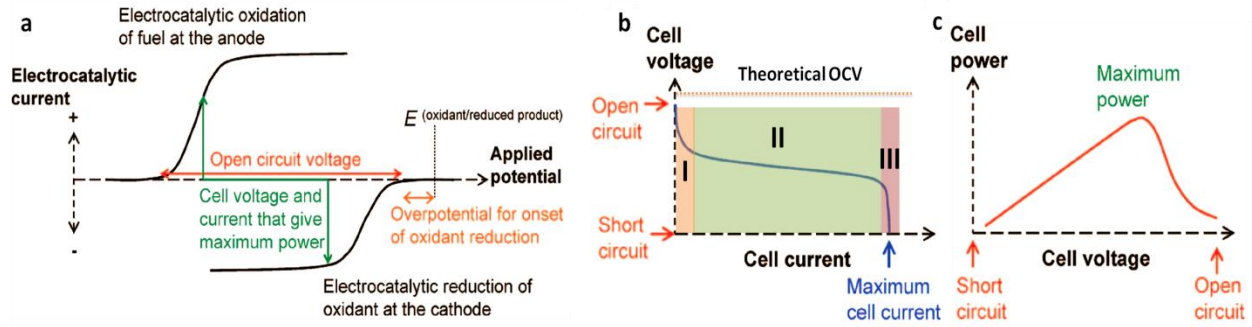


**Figure 3.4** (a) Polarization curves for a separate biocathode and bioanode; (b) Polarization curve of the biofuel cell; (c) Power curve indicating the maximum of power density (optimal conditions) (changed and adapted from [26]).

**Figure 3.4b** presents the polarization curve for a biofuel cell where two extremes can be seen. The first one corresponds to the OCV defined at zero current value. Another one corresponds to the situation of a short circuit between the two electrodes and therefore to the maximal current and minimal voltage. As it can be seen from **Figure 3.4b** the initial cell voltage (practical OCV) at zero current is smaller than its theoretical value (thermodynamic value). The cell polarization curve can be further divided into three distinct segments. In **Segment I**, the steep decrease of the cell voltage corresponds to kinetic losses, which are related to the slow rate of the electrode reaction due to e.g. slow electron-transfer kinetics. After this first decrease of the cell voltage, the polarization curve continues decreasing more linearly with a smaller slope over a wide range of current density values. This decrease, which can be seen in **Segment II**, corresponds to the Ohmic voltage drop originating from the system's intrinsic resistance and as well as from the resistance to the flow of ions within the electrolyte. Finally, (concentration polarization) losses related to mass transport limitations result in the final decrease of the potential until it reaches zero (**Segment III**) [5,8]. At that point, the current reaches its maximal value and the system behaves as if the electrodes were in a short circuit [26]. Each of the mentioned potential losses can be described with corresponding overpotentials. This allows calculating the cell voltage as:

$$E_{cell} = E_{thermodynamic} - \eta_{act} - \eta_{diff} - I \sum R \quad \text{Equation 3.5.}$$

where:  $E_{cell}$ ,  $E_{eq}$  are measured and theoretical (thermodynamic) voltages respectively,  $\eta_{act}$ ,  $\eta_{diff}$  are kinetic and mass transport based overpotentials respectively,  $I$  is the current that flows through the cell and  $\sum R$  is the sum of all resistances that are present in the system. The power curve (cell power as a function of a cell voltage) of the device is presented in **Figure 3.4c**. The power of a (bio)fuel cell, as one of the most important electrochemical key parameters, can be calculated as:  $P_{cell} = E_{cell} \cdot \int I dt$  if the current intensity is time dependent. In the case of a constant current the power calculation can be simplified:  $P_{cell} = E_{cell} \cdot I$ , where:  $P_{cell}$  is the cell power,  $E_{cell}$  and  $I$  are the cell voltage and the current intensity respectively [3].



Since the performances of the device is depending on its size (e.g. real electrode surface), another parameter has to be taken into consideration in order to make different biofuel cells comparable with each other. One of the best ways is to compare their power densities that can be calculated as given by **Equation 3.6** [3]:

$$P_{dens.} = \frac{P_{cell}}{A} \quad \text{Equation 3.6.}$$

## 3.2. Electron transfer mechanisms: Direct and Mediated electron transfer

The efficiency of biofuel cells is closely related to the electron transfer (ET) between enzymes and the electrode surface. Due to the fact that most redox enzymes have a redox unit deeply buried within a protein shell, electron-transfer is one of the most important issues that has to be addressed properly in order to extract the maximum performances of an actual device [17].

In general, there are two basic mechanisms through which ET can be accomplished: 1. **Direct Electron Transfer (Figure 3.5a)** and 2. **Mediated Electron Transfer (Figure 3.5b)**.

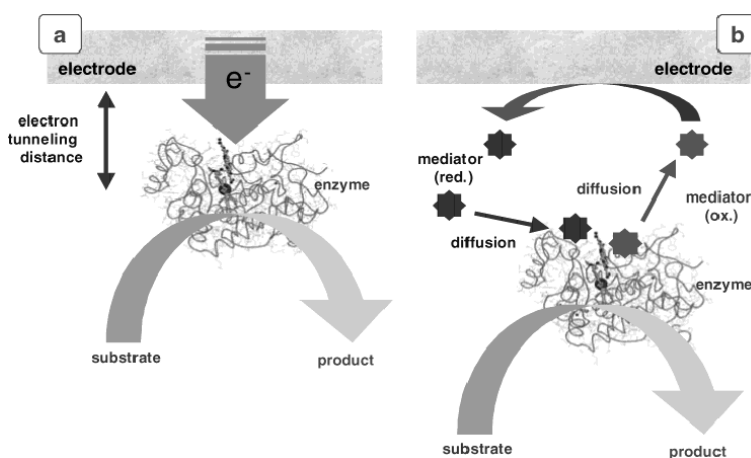


**Figure 3.5.** Schematic representation of two basic mechanisms of ET: (a) Direct electron transfer (DET); (b) Mediated electron transfer (MET) [17].

In direct electron transfer (DET), electrons are shuttled directly from the electrode surface to the substrate through the redox site of the enzyme and *vice versa* [17,18].

The first example of direct electron transfer of metalloproteins has been reported by Hill *et al.* [27] and Kuwana *et al.* [28] in 1977. In their independent researches, they have reported the reversible DET of cytochrome C (CytC) that was adsorbed at the surface of an indium-thin oxide (ITO) electrode and a gold disc electrode modified with 4,4'-bipyridyl.

### 3 – Macroporous electrodes for the fabrication of a biocathode

In the latter case, electrochemically inactive 4,4'-bipyridyl (in the operational potential window), served as an electron-transfer promoter (species that are redox inactive within the explored potential window and capable of promoting an interfacial electron-transfer between a redox-active protein and an electrode surface [27,29]).

The first theoretical study of electron transfer between small molecules (metal aquo complexes) in solution has been developed by Rudolph Marcus [30]. Latter, this theory has been extended to electron transfer at a protein-electrode interface.

Regarding the Marcus theory, the electron transfer kinetic can be described as:

$$k_{ET} = \frac{4\pi^2 H_{DA}^2}{h\sqrt{\pi\lambda k_B T}} e^{\left[\frac{-(\Delta G^0 + \lambda)^2}{4\lambda k_B T}\right]} \quad \text{Equation 3.7.}$$

where:  $k_{ET}$  is the electron transfer rate constant,  $H_{DA}$  is the constant that describes the strength of the electron coupling between the electron donor (D) and the electron acceptor (A),  $\Delta G^0$  is the change of the standard free energy (for one electron transfer it can be calculated as:  $\Delta G^0 = F(E_D^0 - E_A^0)$  [31])  $k_B$  and  $h$  are the Boltzmann and the Plank constants respectively,  $T$  is temperature and  $\lambda$  is the reorganization energy [5,32]. The reorganization energy is defined as the energy necessary to reorganize nuclear positions of the reactants and the solvent to those that correspond to the product state without electron-transfer occurring during that process [33].

Due to the fact that the active sites of enzymes are frequently positioned inside an insulating protein structure and that the average hydrodynamic diameter of redox enzymes is in the range of 50 to hundreds of Å [34], some of the most critical parameters that determines the possibility and the efficiency of an electron transfer between the adsorbed enzyme and an electrode surface are the electron-tunneling distance  $r$  and the tunneling parameter  $\beta$  (frequently called decaying parameter which ranges between 0.8 and 1.6 Å<sup>-1</sup> [35]). Concerning the importance of these two parameters, electron transfer rate constants can be further expressed in the light of Marcus theory as:

$$k(r) = k_0 e^{-\beta(r-r_0)} \quad \text{Equation 3.8.}$$

where:  $k(r)$  electron-transfer rate constant,  $k_0$  is an electron-transfer rate constant at the closest proximity between enzyme and electrode surface,  $r$  and  $r_0$  are actual and closest possible electron-transfer distances between electrode surface and the enzyme respectively [34].

### 3 – Macroporous electrodes for the fabrication of a biocathode

---

This dependence has been confirmed by the studies of DET of redox active proteins (cytochrome C [36–38] and azurin [39]) that have been attached to the electrode surface through self-assembled monolayers (SAM) of thiol-carboxylic acids [40] or alkanethiols at the surface of gold electrodes [39]. It has been shown that the electron-transfer rate decreases as the number of carbon atoms in the chain and therefore electron-transfer distance increases.

In this case, the change of electron transfer is correlated to the number of carbon atoms as:

$$k_1 = k_1^0 e(-\beta n) \quad \text{Equation 3.9.}$$

where  $n$  presents the number of methylene groups in the alkyl chain and  $k_1^0$  is an extrapolated value of the rate constant for  $n = 0$  [38].

The attachment of the proteins through SAMs can be accomplished either by formation of an electrostatic [37] or hydrophobic adduct [39] between the terminal SAM group and a protein. It has been shown for cyt C attached to the gold surface (*via* SAM of thiol carboxylic acid with different numbers of carbon atoms), that the value of the tunneling parameter  $\beta$  is  $1.09 \pm 0.02$  per methylene ( $-\text{CH}_2-$ ) group [37]. The value of the electron transfer constant decays exponentially for  $n > 8$ , while it reaches a plateau value for shorter lengths of protein binding molecules. This suggests a change in the electro transfer limiting step at the inflection point [31].

Besides the proteins that are unable to undergo DET, there are numerous enzymes that are able to directly exchange electrons with an electrode surface more or less efficiently. This has been demonstrated for different enzymes such as laccase (copper containing enzymes) [41,42], horse-radish peroxidase [43,44], p-cresolmethylhydroxylase [45], alcohol dehydrogenase (AIDH:PQQ-FAD dependent) [46], cellobiose dehydrogenase (CDH) [47,48] *etc.* Some of the enzymes that are capable of direct electric communication with an electrode surface often contain two closely positioned redox sites and therefore an efficient internal electron transfer can be established among them. Well known examples are enzymes from flavohemo proteins (*e.g.* CDH [47]) or the quinochemo protein family (pyrroloquinoline quinine – FAD dependent AIDH [46]) or copper-containing enzymes (*e.g.* laccase [41]). In the case of CDH, the electrons are transferred from the reduced form of a cofactor (*e.g.* flavine adenine dinucleotide ( $\text{FADH}_2$ )) to the electrode surface via a redox active heme prosthetic group, which is located close to the periphery of the protein shell as depicted in **Figure 3.6.** [48].

### 3 – Macroporous electrodes for the fabrication of a biocathode

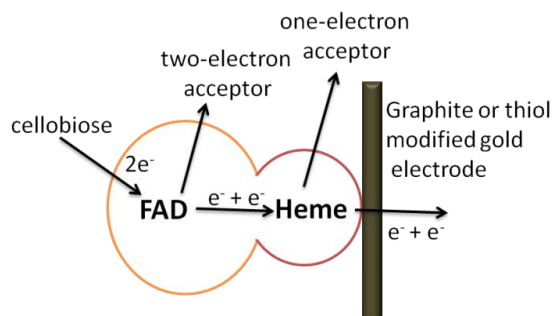


**Figure 3.6.** Schematic of coupled internal and interfacial electron transfer between CDH and an electrode surface (adapted and modified from [48]).

In the case of multicopper oxidases (e.g. laccase) the electrons are transferred from the  $T_1$  copper site to  $T_2/T_3$  catalytically active copper containing units [42].

Based on theoretical studies it has been shown that the electron transfer in multi-redox centers positioned within an enzyme structure is occurring at appreciable rates (in the range from  $10 - 10^4 \text{ s}^{-1}$ ) if the spatial separation between them is lower than 14-15 Å as shown in the **Figure 3.7a and b** [26,49].

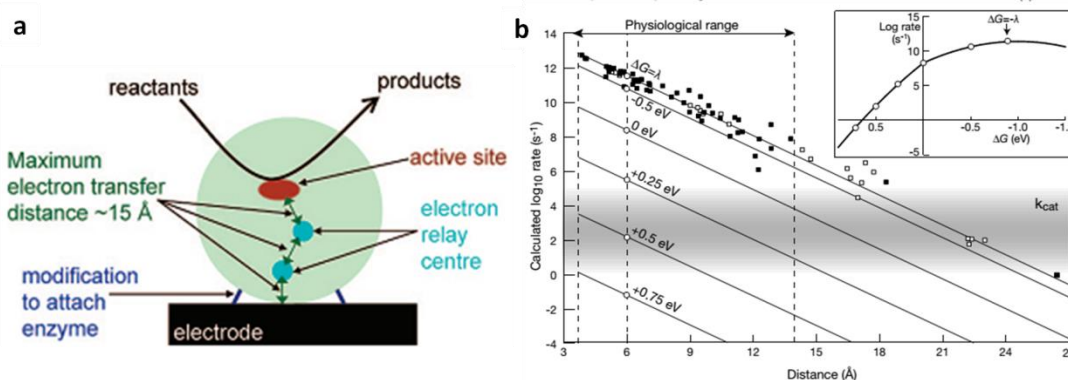


**Figure 3.7.** (a) Schematic representation of an internal electron transport path between redox active site units and an electrode surface *via* electron relay centers [26]. (b) The graph presents the dependence of the calculated  $\Delta G$  optimized electron transfer rate constants as a function of the distance between two redox sites buried inside the enzyme structure. It can be seen that the reactions which result in the biocatalytic transformation of the substrate under physiological conditions (denoted with solid bars) are occurring for a spatial separation below 14-15 Å (the electron-transfer is happening with appreciable rate) between redox active centers for the curve that corresponds to  $\Delta G = \lambda$ . In contrast to that, unproductive reactions are observed at distances bigger than 15 Å (empty squares) with two examples of enzymes whose redox center distance is higher than the optimal value, which can be explained by their possible physiologically inappropriate structures. The inset in the Figure (b) presents the dependence of the electron transfer rate constant on the  $\Delta G$  value for both, endergonic and exergonic tunneling reactions at 6 Å distance and same  $\lambda$ . The experimental spots are taken from the diagonal lines for different values of  $\Delta G$  at 6 Å [5,49].

### 3 – Macroporous electrodes for the fabrication of a biocathode

In contrast to enzymes with two redox centers, some enzymes who possess only one redox center buried deep in the protein structure cannot achieve appreciable rates of direct electron exchange with an electrode surface. This type of enzyme molecules can be efficiently “wired” to the electrode surface by means of various nano-elements due to their small dimensions which can efficiently shorten the electron-transfer distance (**Equation 3.7**) and increase interfacial electron-transfer rates in that way. For example, it has been reported that the cyclic voltammetry of adsorbed glucose oxidase (GOx) immobilized on the surface of glassy carbon electrode does not show any electrochemical response with respect to oxidation/reduction of the FAD cofactor. In comparison to that, a successful electron transfer (FAD<sub>(from adsorbed GOx)</sub>-electrode surface) of  $1.3 \text{ s}^{-1}$  at the surface of a Nafion/GOx-AuNP/GC electrode has been demonstrated [50]. Similar behavior was found for horseradish peroxidase (HRP) immobilized on the surface of an ITO electrode modified with chemically bonded AuNP (the average diameter was 15 nm) [51].

The ability of some enzymes to accomplish their electrical communication during the catalytic cycle via DET has been recognized in the field of biofuel cells. A few examples of biofuel cells based on DET are listed in **Table 3.2**.

Type	Enzymes	Electrode material	OCV (V)	Power density ( $\mu\text{W}\cdot\text{cm}^{-2}$ )	Reference
glucose/oxygen	CDH/BOx*	SGE	0.62 0.58*	3 4*	[55]
hydrogen/oxygen	Hase/BOx**	CNF@PG	1.06	1500	[56]
glucose/oxygen	GOx*/Lac	MWCNT	0.95	1.3	[57]
glucose/ethanol	GOx** -MP8/QH AIDH	CRE in Epoxy	0.27	n.r.	[58]

**Table 3.2.** Examples of biofuel cells that rely on DET where: CDH – cellobiose dehydrogenase (*Corynascus thermophilus*), BOx\* – Billirubin oxidase (*Myrothecium verrucaria*), Hase – Hydrogenase (*Aquifex aeolicus*), Box\*\* (*Bacillus pumilus*), GOx\*\*\* - glucose oxidase (*Aspergillus niger*), Lac- Laccase (*Trametes versicolor*), QH AIDH - hemecontaining pyrroloquinoline quinone-dependent alcohol dehydrogenase (*Gluconobacter sp. 33*), MP8 – microperoxidase (from horse heart); SGE – spectrographic graphite electrode, CNF – carbon nanofibre, PG – pyrolytic graphite, MWCNT – multiwall carbon nanotubes, CRE – carbon rode electrode. (n.r. – not reported)

The electron-transfer efficiency can be enhanced through the utilization of small molecular weight redox active molecules or redox-polymers, well-known as redox mediators. Although in the case of MET, current densities and power outputs are greater than in the case of DET, there are certain issues concerning stability, selectivity and cross-over reactions (in the case of diffusional redox mediators) at the counter electrode, which imposes the use of semipermeable membranes [17,18].

### 3 – Macroporous electrodes for the fabrication of a biocathode

The problem related to cross-over reactions can be avoided by redox mediators immobilized at the electrode surface (so called non-diffusional redox mediators) such as osmium-redox polymers [59] or electropolymerized films [60].

The mechanism of MET is given in **Figures 3.5** and **3.8a**. In general, upon a catalytic reaction (which involves the homogeneous electron transfer between an enzyme and a corresponding substrate), the redox mediator needs to be regenerated to its active form (re-oxidized or re-reduced) in order to involve an enzyme into a new catalytic cycle [17]. A general rule for selecting appropriate redox mediators is that their formal redox potential has to be slightly higher (or lower in case of cathodic enzymes) than the redox potential of the coenzyme that is supposed to be oxidized (reduced). The reduced (oxidized) mediators are getting oxidized (reduced) at the electrode surface that is polarized at a sufficiently positive/negative electrode potential and that way an electron flux from a redox enzyme towards the electrode surface (and *vice versa*) is established [59].

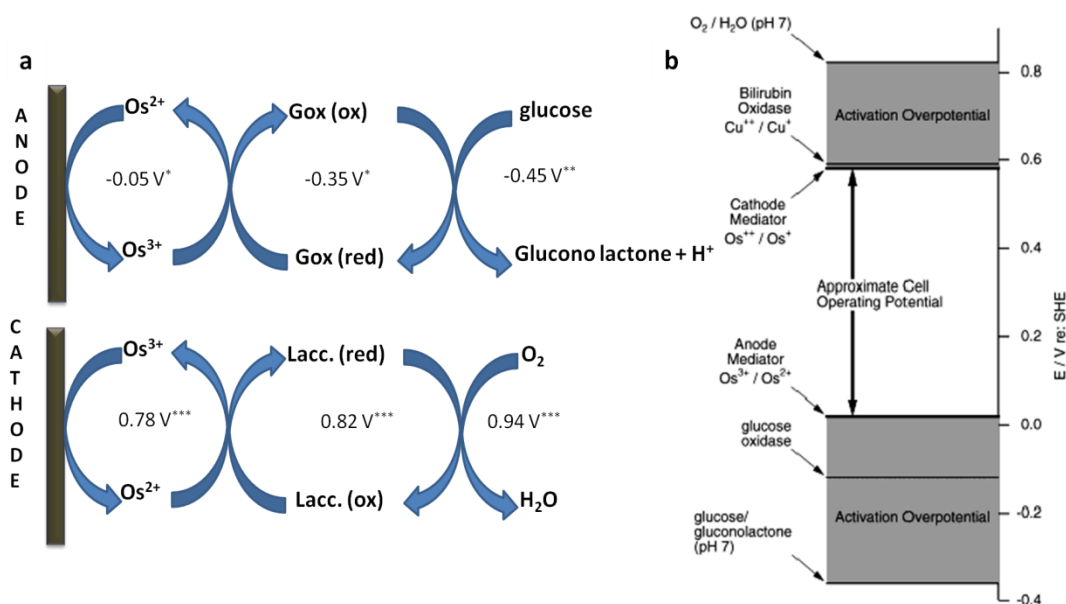


**Figure 3.8** (a) Schematic representation of the electron-transfer mechanism for an osmium based redox-polymer bioanode ( \* [61], \*\* [26]) and biocathode ( \*\*\* adapted and modified from [62]); (b) Graphical representation of the voltage loss in a biofuel cell due to the potential difference between consecutive steps in electron mediation [17].

This additional step (oxidation/reduction of redox mediator) decreases the open-circuit voltage of the system which is theoretically given as the formal potential difference between a fuel and an oxidant as depicted in **Figure 3.8b** [17].

Redox mediators can be immobilized at the electrode surface or be present in electrochemical systems as dissolved compounds that are transported *via* diffusion [3].

The utilization of redox mediators is of great importance in enzymatic systems that cannot efficiently undergo electron-transfer with electrode materials or for which the electron-transfer is accomplished at high electrode potentials. The latter case can be exemplified with  $\text{NAD}^+$  dependent enzymes such as glucose-dehydrogenase. The problem related to the electrochemical regeneration of  $\text{NAD}^+$  (catalytically active form of coenzyme) is the high overpotential ( $\approx 1\text{V}$ ; anodic peak observed at  $0.56\text{V}$  while  $E^{\circ'} = -0.56\text{V}$  vs. saturated calomel electrode (SCE)) required for its generation, that limits DET application in the case of  $\text{NAD}^+$  dependent enzymes [63]. This would reduce operational voltage of an actual biofuel cell due to the high activation losses. Another problem of NADH systems is electrode fouling (which shifts the formal electrode potential towards even more positive values) due to the adsorption of  $\text{NAD}^+$  at the electrode surface [64]. This can be avoided by choosing an appropriate electrode material [65].

In  $\text{NAD}^+$  dependent systems, an intermediate biocatalytic step is necessary in order to oxidize NADH at much lower over-potential. An example is the total methanol/oxygen biofuel cell whose activity relies on the cascade of methanol oxidation with three different enzymes (alcohol dehydrogenase (ADH), aldehyde dehydrogenase (AIDH) and formate dehydrogenase (FDH) respectively). Since NADH is formed in each of three consecutive oxidation steps, another enzyme (e.g. diaphorase) can be used to catalyze its oxidation. The catalytic activity of this latter enzyme can be further regenerated by benzyl viologen ( $\text{BV}^{2+/+}$ ) whose formal redox potential is  $-0.55\text{V}$ . The biofuel cell was able to generate  $0.68\text{ mWcm}^{-2}$  at  $0.49\text{V}$  [66].

Another important group of redox mediators that can be used for lowering the overpotential of NADH oxidation (due to their electrocatalytic properties) are azine mediators (their basic chemical structure is presented in Figure 3.9a). It has been shown that NADH can be efficiently oxidized at carbon-paste (CP) electrodes that have been chemically modified with methylene-green (phenothiazine type) at potentials of  $142\text{ mV}$  vs. SCE [67]. Besides their efficiency regarding NADH oxidation, chemical modification of azine mediators can be used in order to tune their electrocatalytic properties and therefore make them suitable mediators for other enzymes/molecules. Another advantage of azine mediators is the fact that they can be easily electro-polymerized. For instance, a methylene green film has been electrosynthesized (Figure 3.9b) at the surface of glassy-carbon electrodes. The oxidation of NADH at methylene-green@GC electrodes at  $+0.1\text{V}$  (vs. SCE at  $\text{pH} = 7.0$ ) has been accompanied with an increase in anodic current intensity [68]. Similarly, electrodeposition and electrocatalytic activity of other polyazine mediated NADH electro-oxidation reactions has been reported [69]. The utilization of polyazine mediator films has been exemplified for alcohol/oxygen biofuel cells based on a Pt cathode (20% Pt on Vulcan XC-2) and a poly(methylene-green) modified carbon felt anode with immobilized enzymes (ADH and ADH/AIDH mixture),  $\text{NAD}^+$  coenzyme and a tetrabutylammonium bromide/Nafion membrane/binder. As can be expected, the biofuel cell based on a mixture of two enzymes gave a higher power density:  $1.16 \pm 0.05\text{ mWcm}^{-2}$  (OCV =  $0.61\text{V}$ ) for an ADH based electrode and  $2.04\text{ mW/cm}^2$  (OCV =  $0.82\text{V}$ ) for an ADH/AIDH mixture, due to a more complete oxidation of the substrate [60].



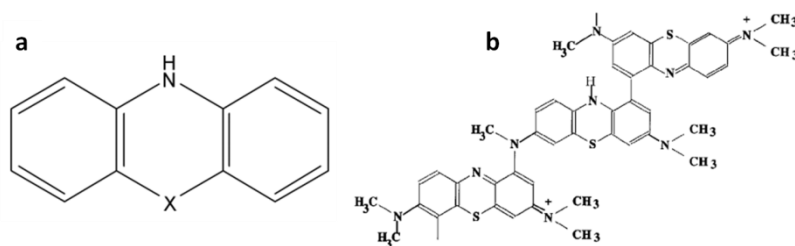


**Figure 3.9** (a) Simplified chemical structure of the azine redox mediators. The structure may contain different substituents at the aromatic rings [18]; (b) Hypothetic structure of electrochemically polymerized poly(methylene-green) film [73].

Besides  $\text{NAD}^+$  dependent enzymes, different redox mediators have been efficiently used in other enzymatic systems (e.g.  $\text{K}_3[\text{Fe}(\text{CN})_6]$  for BOD [70], PQQ@Au for GOx [71], CytC for CytC oxidase [71], methylene blue for hydrogenase [72]) to promote the electron-transfer and to increase the performances of the bioelectrodes .

Another group of very efficient redox mediators that have been used for many years are osmium based redox polymers. They are used in the form of a hydrogel, consisting of an enzyme, an Os based redox polymer and a cross linker [74–79]). The reticulated structure of the hydrogel allows permeation of solvent (e.g. water) molecules, diffusion of ions and non-charged species (e.g. oxygen, glucose *etc.*). The latter one can be substrates of corresponding enzymes that are contained in the hydrogel.

Moreover, unlike most hydrogels, osmium based redox polymers in their swollen state are also capable of conducting electrons. This makes them suitable for electrochemical purposes. The electron conduction mechanism is based on electron-transfer between neighboring oxidized and reduced osmium redox moieties through a self-collision phenomenon. The efficiency of electron-transfer depends on the displacement amplitude from the equilibrium positions of the redox active groups as denoted in **Figure 3.10a** [59,78].

The chemical structure of Os based redox polymers consists of an Os-redox complex that is directly or indirectly tethered to the polymer backbone (e.g. poly(N-vinylimidazole) or polyacrylimide/poly(N-vinylimidazole) copolymer) [75]. The flexibility of the osmium redox centers determines the “diffusivity” of electrons. For example, it has been shown that introduction of an eight atoms long tether in tris(bipyridine)Os based redox polymers (**Figure 3.10b**) increases the apparent diffusion coefficient (determined from the slope of the graph  $i = f(v^{\frac{1}{2}})$ ), given by the Randles-Sevčik equation [80]:  $i = 0.4463(nF)^{\frac{3}{2}}AD_{app}^{\frac{1}{2}}Cv^{\frac{1}{2}}/(RT)^{\frac{1}{2}}$ , where:  $n$  - number of exchanged electrons,  $F$  - Faraday constante,  $A$  - electrode surface area,  $D_{app}$  - apparent diffusion coefficient,  $C$  – concentration of redox species,  $v$  - scan rate) of tethered osmium centers, and thus resulted in  $D_{app}$  of  $(7.6 \pm 0.3) \cdot 10^{-7} \text{ cm}^2 \text{ s}^{-1}$ .



### 3 – Macroporous electrodes for the fabrication of a biocathode

This value is 100 times higher than the one reported for a non-tethered analogue ( $D_{app} = (6.2 \pm 0.8) \cdot 10^{-9} \text{ cm}^2 \text{ s}^{-1}$ ) [81]. The theoretical „bounded diffusion“ model (**Equation 3.10**) describes an extended electron-transfer in a system where no physical diffusion of redox species exists. In this model,  $D_{app}$  is directly proportional to the characteristic electron-hopping distance  $\delta$  in between neighbouring redox sites, the self-exchange rate constant  $k_{ex}$ , the distance across which osmium redox centers can move within the molecule  $\lambda$ , and a concentration of osmium redox sites ( $C_{RT}$ ) within the volume of a hydrogel [80,82].

$$D_{app} = \frac{1}{6} k_{ex} (3\lambda^2 + \delta^2) C_{RT} \quad \text{Equation 3.10}$$

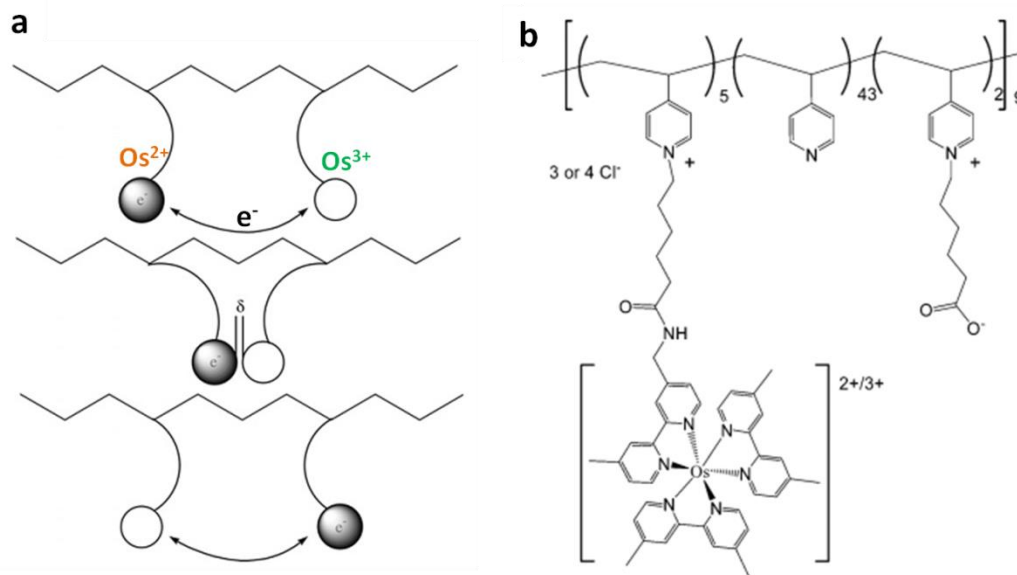


**Figure 3.10** (a) Schematic representation of electron conduction in an Os-based redox polymer. Electron transfer in between reduced and oxidized osmium centers is based on a self-collision phenomenon. Introducing a long tether increases electron “diffusivity” along the polymer “wire” (modified from [59]); (b) Chemical structure of a tris(4,4'-dimethyl-2,2'-bipyridil)osmium complex tethered to a partially quaternized polymer (poly(4-vinylpyridine)) backbone through an eight atoms long link [81].

It has also been shown that the  $D_{app}$  value increases upon quaternisation (alkylation of the pyridine ring in the polymer backbone which introduces extra positive charge due to the formation of pyridinium salt) of the structure which results in a better swelling of the polymer film. This intrinsic increase of the film volume decreases the concentration of osmium redox moieties but at the same time it increases the segmental motion within the film and therefore the effective collision frequencies. A similar effect was demonstrated by decreasing the pH of the system due to the protonation of the pyridine rings. This effect was significant for moderate degrees of quaternisation (for highly quaternized polymers pH has no significant effect on the value of  $D_{app}$ ).

### 3 – Macroporous electrodes for the fabrication of a biocathode

As expected, in contrast to quaternisation and protonation, the excessive amount of cross-linker (cross linker is added to increase mechanical stability of the films) restricts the electron diffusivity by limiting the segmental mobility [82].

The main advantage of this type of redox polymers is the possibility to finely tune their redox potential (as a function of the enzyme) by changing the structure of the ligands as depicted in **Table 3.3a** and **b**. This makes them suitable for biofuel cell applications since the redox polymer can be appropriately designed in order to diminish (as much as possible) the potential losses in biofuel cells. Although the half-cell potentials are dependent on pH, since protons are released at the anode and consumed at the cathode (**Equation 3.11**), the redox potential of the polymer “wires” are pH independent. As a consequence the difference between the redox potential of an enzyme and a redox polymer is pH sensitive. Therefore the polymer that has been designed to provide a certain potential difference at one pH will not be able to provide it at another one [59].

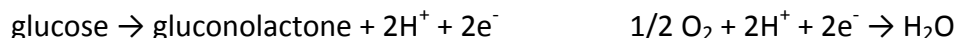
Compound	Structure	Redox potential/V	O <sub>2</sub> reduction rate/A cm <sup>-2</sup> <sup>a,b</sup>
4 Poly{ <i>N</i> -vinylimidazole[Os(4,4'-dimethyl-2,2'-bipyridine) <sub>2</sub> Cl] <sup>+2</sup> ·c0-acrylamide}		0.32, pH 5; 0.17, pH 7.2	2 × 10 <sup>-4</sup> (0.5 V, pH 5 citrate)
5 Poly{ <i>N</i> -vinylimidazole[Os(4,4'-dimethoxy-2,2'-bipyridine) <sub>2</sub> Cl] <sup>+2</sup> }		0.15, pH 7.4	6.5 × 10 <sup>-4</sup> (0.37 V, pH 7.4 PBS <sup>c</sup> )
6 Poly{ <i>N</i> -vinylimidazole[Os(4,4'-diamino-2,2'-bipyridine) <sub>2</sub> Cl] <sup>+2</sup> }		0.06, pH 7.4	1.7 × 10 <sup>-4</sup> (0.22 V, pH 7.4 PBS)
7 Poly{ <i>N</i> -vinylimidazole[Os( <i>N,N'</i> -dialkylated-2,2'-biimidazole) <sub>3</sub> ] <sup>+2</sup> }		0.02, pH 7.2	1.1 × 10 <sup>-3</sup> (0.22 V, pH 7.4 PBS); 3.2 × 10 <sup>-4</sup> (0.22 V, pH 5 citrate)

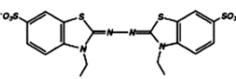
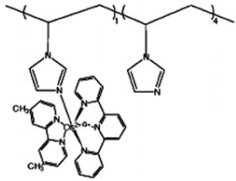
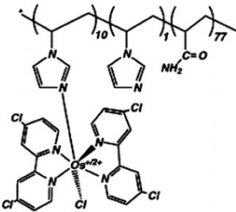
<sup>a</sup> Potential vs. SHE; <sup>b</sup> Glucose concentration 15 mM, 37 °C; <sup>c</sup> PBS = phosphate buffer solution, typically 20 mM phosphate buffer with 0.1 M NaCl.

**Table 3.3 (a)** List of anodic osmium-based redox mediators with their electrochemical characteristics [17,18].

### 3 – Macroporous electrodes for the fabrication of a biocathode

**Bioanode** (Gox/Os-polymer I)      **Biocathode**(BOD or Laccase/Os-polymer II)      Equation 3.11



Compound	Structure	Redox potential/V <sup>a</sup>	O <sub>2</sub> reduction rate/A cm <sup>-2</sup> <sup>a,b</sup>
1      2,2'-Azinobis(3-ethylbenzothiazoline-6-sulfonate) (ABTS)		0.66, pH 4; 0.72, pH 7	5 × 10 <sup>-4</sup> (0.43 V, pH 7 phosphate) <sup>c,e</sup>
2      Poly{N-vinylimidazole [Os(terpyridine) (4,4'-dimethyl-2,2'-bipyridine)] <sup>2+/3+</sup> }		0.79, pH 5	1 × 10 <sup>-2</sup> (0.62 V, pH 5 citrate) <sup>d,f</sup>
3      Poly{N-vinylimidazole[Os(4,4'-dichloro-2,2'-bipyridine) <sub>2</sub> Cl] <sup>2+/3+</sup> -co-acrylamide}		0.58, pH 7.4	9 × 10 <sup>-3</sup> (0.55 V, pH 7 phosphate) <sup>d,f</sup>

<sup>a</sup> Potential vs. SHE. <sup>b</sup> High-surface-area carbon supports in O<sub>2</sub>-saturated buffer. <sup>c</sup> Catalysed by bilirubin oxidase in the presence of chloride. <sup>d</sup> Catalysed by fungal laccase, chloride absent. <sup>e</sup> Moderate stirring by bubbled gas. <sup>f</sup> Strong stirring by rotating disk electrode at 4 krpm.

**Table 3.3** (a) List of cathodic redox mediators and their electrochemical characteristics [17,18].

There are many examples of biofuel cells (mostly glucose/oxygen) in which this kind of polymer is used [75,81,83]. One of the best examples that exemplifies the advantages of osmium containing hydrogels (cross linked mixture of anodic and cathodic polymer with GOx and BOD (from *Trachoderma tsunodae*) respectively) is a miniaturized glucose/oxygen biofuel cell made by coating 7 µm thick carbon fibers. In the present case, due to the fact that the system was based on hydrogel-film modified electrodes, the possibility to fabricate membraneless biofuel cells has been demonstrated. Such a system, operating under physiological conditions (pH= 7.2, at 37 °C in air saturated phosphate buffer saline (PBS, 20 mM PB + 0.14 M NaCl) solution) has developed 4.3 µW/cm<sup>2</sup> when operating at 0.52 V in a 15 mM glucose solution. Further, it has been shown that a biofuel cell is capable to operate *in vivo* once implanted in a grape (pH = 5.4, C<sub>glucose</sub> > 30 mM), with a final power output of 0.47 µW/cm<sup>2</sup> at 0.52 V [75].

Osmium redox polymers have been successively used for the fabrication of miniaturized self-powered amperometric glucose sensors [24]. In the present case, the biofuel cell/biosensor consisted of a glucose bioanode (GOx/Os complex tethered to a PVP backbone) and a Pt based cathode as presented in the **Figure 3.11**.

### 3 – Macroporous electrodes for the fabrication of a biocathode

The currents that have been measured upon glucose oxidation at the anode and oxygen reduction at the cathode showed a linear dependence with increasing glucose concentration in the range of 1 mM - 30 mM and it was independent of the applied resistance between 1 – 10 MΩ. The sensor showed remarkable stability during a period of 30 days as well as a good agreement when implanted subcutaneously and compared with a commercial amperometric sensor (FreeStyle Navigator continuous sensor) during a 5 days period.

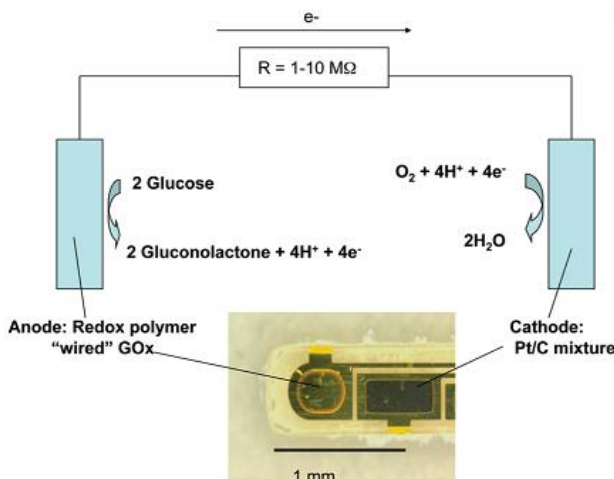


**Figure 3.11** Schematics of a self-powered amperometric glucose sensor with a picture of the actual device in the inset [24].

### 3.3 The enzymes for biocathodes: Multicopper oxidases (MCOs)

Multicopper oxidases belong to the family of enzymes that are able to catalyze the oxidation of a wide range of substrates (e.g. bilirubin, polyphenols, aminophenols, ascorbate etc. [42,84]) simultaneously with the four-electron reduction of oxygen (co-substrate).

The main structural characteristics of this protein family which is responsible for their catalytic activity is the existence of four copper ions (classified according to their spectroscopic and magnetic properties and which are named  $T_1$ ,  $T_2$  and  $T_3$ ) (**Figure 3.12a**).  $T_1$  (known as the blue copper site) is a mononuclear  $\text{Cu}^+$  ion that is positioned close to the edge of the protein shell ( $\sim 10 \text{ \AA}$  [85]) and therefore is responsible for DET communication between the protein and an electrode surface.  $T_1$  is normally coordinated by a set of amino-acids (for example, 1Cys2His1Met (*M. verrucaria* – BOD) or 1Cys2His1Phe/Leu (BODs obtained from *T. tsunodae* or *P. ostreatus* respectively) [86]) and is responsible for external electron transfer. Since the average distance between  $T_1$  and  $T_2/T_3$  redox sites is approximately  $13 \text{ \AA}$  an efficient electron-transfer is possible [49,87] as described above (**page 11**). The  $T_1$  site shuttles the electrons to the  $T_2/T_3$  sites, which are further engaged in oxygen reduction.

### 3 – Macroporous electrodes for the fabrication of a biocathode

During the four-electron oxygen reduction,  $T_2$  (coordinated with 2His1H<sub>2</sub>O/OH<sup>-</sup>) and  $T_3$  (coordinated with 3His residues and an OH<sup>-</sup> ionic bridge with other  $T_2$  copper ions) are operating simultaneously [88] as indicated in **Figure 3.12b**.

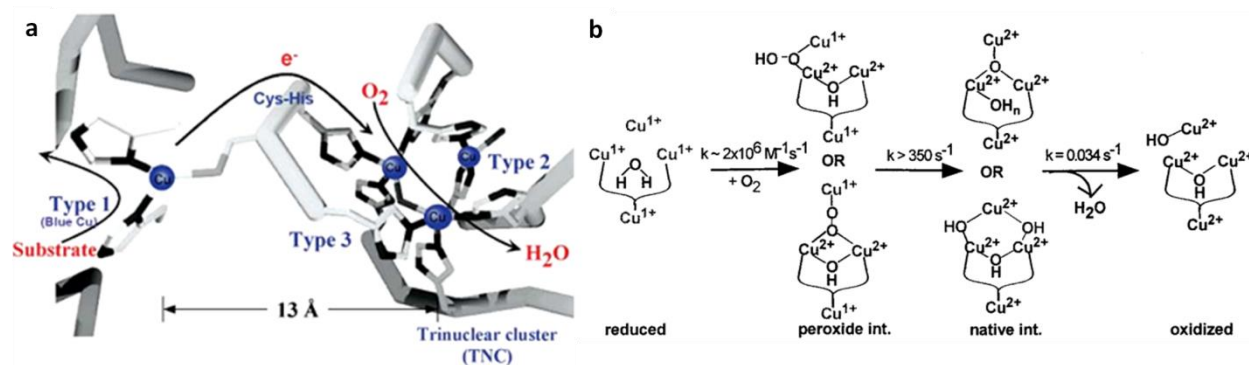
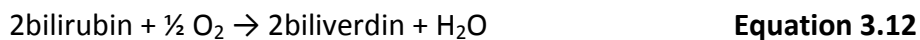


**Figure 3.12** (a) The structure of active sites of MCOs. The flow of substrates, products and electrons is indicated by the arrow [89]; (b) The molecular mechanism of four electron reduction of oxygen within the active site of MCOs. The reduction proceeds in two 2e<sup>-</sup> donating steps (the first step is much faster than the second one). In the first step, the oxygen is bound to the  $T_2/T_3$  site through the formation of intermediate peroxide. In the second step, an unstable oxide is formed by cleavage of an intermediate peroxide species. The oxides are immediately stabilized by protonation (possibly by -COOH groups of present amino-acids residues) and the hydroxyl bridges are formed in the  $T_2/T_3$  site. In the terminal stage the water molecules are released from the complex [87].

Some of the most utilized enzymes from the MCO family, which found wide applications in bioelectrochemical systems, are Laccase [62,81,90] and Bilirubin oxidase [56,74,75]. Laccase is a non-specific enzyme, capable of catalyzing the oxidation of different substrates (*e.g.* diphenols or aminophenols [84]) and bilirubin oxidase is engaged in the metabolism of Bilirubin (**Equation 3.12**). Based on this reaction, assays for the bilirubin level in the serum have been developed [91].



The main differences between Laccase and Bilirubin oxidase are the optimal operational conditions. While Laccase is able to operate under acidic conditions (citrate buffer, pH = 5 [92]) and shows high sensitivity to the presence of chloride ions (for example *C. hirsutus* laccase retained only 1% of its original catalytic activity in PBS compared to chloride free citrate buffer [93]), Bilirubin oxidase is known to tolerate much higher concentrations of chloride ions (0.14M NaCl) while operating under the physiological conditions (pH = 7.2) [75]. The latter characteristics makes BOD an enzyme of choice for the fabrication of miniaturized biofuel cells/biosensors that are expected to operate under the physiological conditions.

### 3 – Macroporous electrodes for the fabrication of a biocathode

Since the T<sub>1</sub> site is responsible for electrical “wiring” of the entire enzyme molecule to the electrode surface in case of DET or for the electron-exchange in case of MET, it is very important to know its redox potential. This determines the redox potential of electrode and an osmium redox polymer that has to be used (MET) or the electrode potential at which a cathode has to be polarized (DET). The redox potentials of T<sub>1</sub> and T<sub>2</sub>/T<sub>3</sub> site for some of the most utilized BODs are listed in **Table 3.4**.

Enzyme source	Molecular weight (kDa)	pH	Electrode material	E <sub>T1</sub> (mV) vs sat. Ag/AgCl	E <sub>T2/T3</sub> (mV) vs sat. Ag/AgCl	Reference
<i>Myrothecium verrucaria</i>	66	7.0	GCE/CNP*	501	201	[94,95]
<i>Trachoderma tsunodae</i>	64	7.4	SPGE	735	435	[85,95]
<i>Magnaporthe oryzae</i>	63.7	n.d.	n.d.	420	n.d.	[95]

**Table 3.4** The electrode potentials of BOD obtained from three different fungal sources. All redox potentials were calculated *versus* sat. Ag/AgCl reference electrode; GCE/CNP – glassy carbon electrode/carbon nano-powder, SPGE – spectroscopic pyrolytic graphite electrode, n.d. – not defined.

#### 3.4 Cylindrical macroporous electrodes for a BOD (fung. *Magnaporthe oryzae*) based biocathode

Regarding their high active surface areas and the variety of the materials that can be used for their synthesis (see **Chapter 2**), macroporous electrodes present promising candidates that can be used for applications in the field of bioelectrochemistry (biofuel cells and biosensors).

The four-electron reduction of oxygen to water under physiological conditions is still a challenging reaction since the final power output of most biofuel cells is still limited by the biocathode. Improvements of such systems can be obtained by optimizing the active surface area of electrodes as well as by improving the “wiring” of enzymes that are catalyzing the four-electron oxygen reduction [74]. This is especially important in conditions of low O<sub>2</sub> concentration such as in subcutaneous interstitial tissues where oxygen concentration is approximately only 0.2 mM [96].

MCOs/Os-redox polymers are systems of choice for the fabrication of oxygen-reducing biocathodes that are able to operate under the physiological conditions [97]. This is especially important for the elaboration of potentially implantable devices.

### 3 – Macroporous electrodes for the fabrication of a biocathode

---

As the long term goal of this project is to achieve implantable biofuel cells, based on tunable coaxial macroporous electrodes, our preliminary efforts to elaborate an oxygen-reducing biocathode will be discussed in this subchapter. Macroporous gold surfaces have already been reported as a material for Os-polymer/(cathode: BOD and anode: GOx) based glucose/oxygen biofuel cells [98] and a glucose biosensor based on DET [99].

As mentioned above, the final goal is the fabrication of a miniaturized biofuel cell (e.g. glucose/oxygen) using the fully integrated coaxial macroporous electrode architecture (**Chapter 2; Subchapter 2.4**) as an electrochemical platform.

Therefore, the appropriate procedure for the selective immobilization of enzymes and of corresponding Os-redox polymers (tailored for the chosen enzyme) on the surface of independently addressable electrodes is required. The procedure that will allow selective modification of each of the two independent coaxial electrodes needs to rely on electrochemical methods (e.g. electrodeposition or electrophoretic deposition). The possibility to electrically connect each of the two coaxial electrodes independently (one at a time) would allow their selective modification with different enzyme/Os-redox polymer systems.

For example, electrophoretic deposition of enzymes (DET) (or enzyme/redox-mediator (MET)) has been used for their immobilization on electrode surfaces and for the fabrication of a glucose/oxygen biofuel cell [100–102].

Another, simpler and more straightforward way to elaborate a biocathode/bioanode is based on electrochemical deposition of an enzyme and an Os-redox polymer. Briefly, the method is based on consecutive reduction of osmium sites within the polymer structure (in the present case  $\text{Os}^{2+/+}$ , **Figure 3.14b**) and substitution of the weakly bound chloride ligand by nitrogen-containing amino acid residues (histidine, lysine and arginine) that are naturally present in the protein structure (the ligand exchange upon reduction of a transition metal ion has already been reported for a diperchloratotris(bipyridine)nickel (III) complex). The ligand exchange step is followed by precipitation of the cross-linked enzyme/Os-polymer adduct at the electrode surface [103]. This strategy has been successfully demonstrated for coelectrodeposition of an Os-redox polymer (chlorobis(4,4'-dimethyl-2,2'-bipyridine) osmium(III) complex bounded to PAA/PVI copolymer) with several enzymes (GOX, soybean peroxidase (SBP) and laccase) on a GC electrode (at room temperature and PBS (pH = 7.2)). The result were electrocatalytic films that were selectively catalyzing the bio(electroreduction/oxidation) of corresponding substrates.

A similar mechanism is proposed for the coordinative cross-linking between neighboring Os-polymer chains, once the osmium site is in its reduced form.



### 3 – Macroporous electrodes for the fabrication of a biocathode

In this case, the cross-linking between polymer chains is based on the substitution of a labile bound chloro ligand with nonquaternized and chemically non-bound (no osmium-complex is bounded) pyridine or imidazole residues that are present in a polymer backbone structure as shown in **Figure 3.14b**. **Figure 3.13a** presents the electrochemical characterization of a cathodic Os-redox polymer that has been used in this project for (co)electrodeposition.

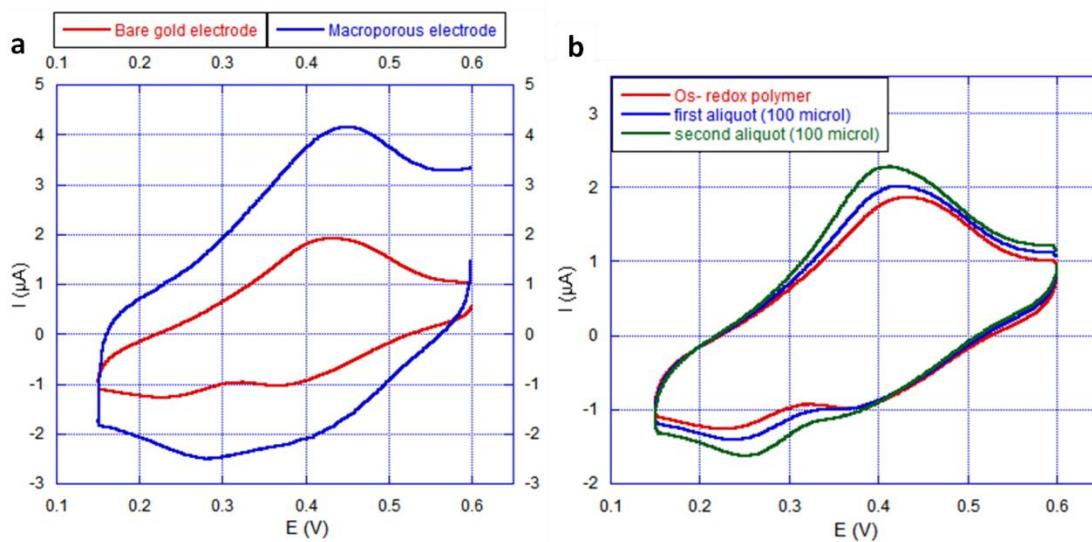


**Figure 3.13** (a) CVs of the cathodic Os-polymer ( $\text{PAA-PVI}[\text{Os}(4,4'\text{-dichloro-2,2'-bipyridine})_2\text{Cl}]^{+/2+}$  (with a molar ratio of vinylimidazol/acrylamide of 1:9,)) recorded at 50 mV/s at bare (red curve,  $S_{\text{act.}} = 0.12 \text{ cm}^2$ ) and macroporous (blue curve,  $S_{\text{act.}} = 0.52 \text{ cm}^2$ ) gold electrodes); (b) Electrochemical investigation of the origin of the peak that appears at 0.25V. An increase of the peak is observed upon addition of a saturated aqueous solution of the osmium-complex (chlorobis(4,4'-dichloro-2,2'-bipyridine)osmium (II)). All electrode potentials are given versus Ag/AgCl (3M NaCl) reference electrode.

As it can be seen from the CVs for the bare ( $\varnothing = 250 \mu\text{m}$ ) and macroporous gold electrodes (thickness = 3 half-layers,  $\varnothing_{\text{(pores)}} = 600 \text{ nm}$ ), the osmium redox polymer presents a reversible electrochemical system at 0.4 V vs. Ag/AgCl (3 M NaCl) with a peak-to-peak separation of approximately 60 mV, as theoretically expected for reversible systems [104]. In the voltammograms presented in **Figure 3.13a**, an additional peak in the range 0.25 V-0.3 V can be seen for both electrodes. This is ascribed to non-bound osmium complex that is present in the polymer due to insufficient post-synthetic purification of the product. The origin of this additional peak has been proven by addition of small aliquots of an aqueous solution of saturated osmium-complex. As it can be observed from the **Figure 3.13b**, this results in an increase of the peak intensity at 0.25 V.

In the first set of experiments, the possibility to deposit only Os-redox polymer at the surface of bare gold microwires and into the macroporous gold structure has been investigated. Prior to the electrodeposition step, the electrodes were immersed in the polymer solution ( $\gamma = 1.5 \text{ mg/ml}$  in MilliQ water) and left for 20 min to allow better penetration of the solution inside the



### 3 – Macroporous electrodes for the fabrication of a biocathode

pores. In the next step, the redox polymer has been electrodeposited by cycling the electrode potential in the potential window of 0.6 V-0.15 V (**Figure 3.14a** and **b**). It has been noticed that the peak-to-peak separation decreases during the electrodeposition. This can indicate the improvement of the electron-transfer rate constant [74] possibly due to a decrease in electron-hopping distance in between neighboring osmium sites upon consecutive cycles.

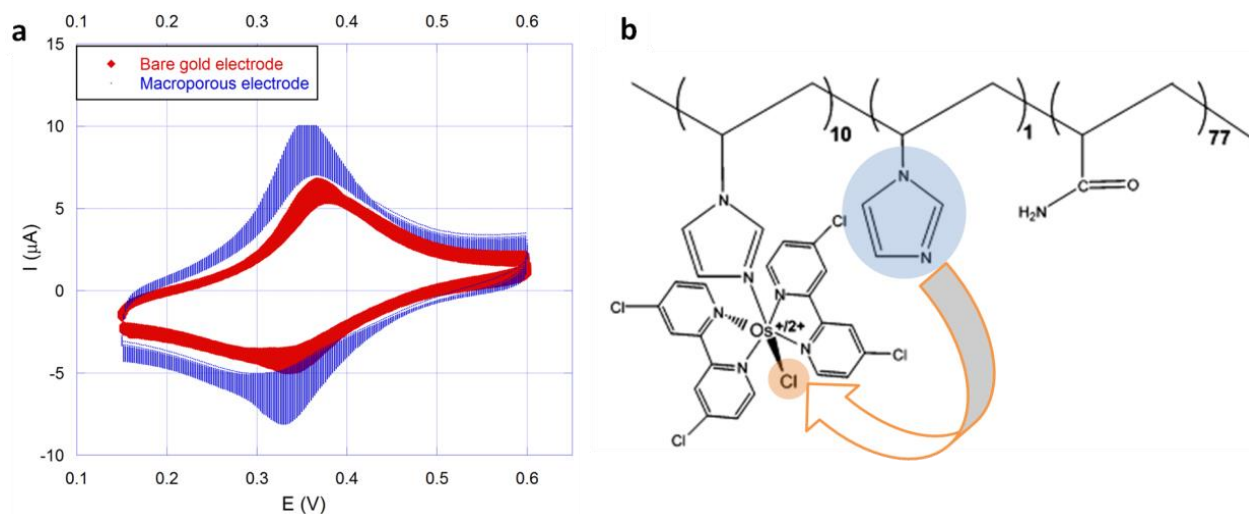


**Figure 3.14** (a) Electrochemical deposition of Os-redox polymer at bare (set of the red curves;  $S_{\text{act.}} = 0.12 \text{ cm}^2$ ) and macroporous (set of the blue curves;  $S_{\text{act.}} = 0.46 \text{ cm}^2$ ) electrodes by cycling the redox potential between 0.6 V-0.15 V at 50 mV/s in Os-polymer/MilliQ water solution ( $\gamma = 1.5 \text{ mg/ml}$ ) for 240 scans; (b) The mechanism of coordinative cross-linking between an imidazole ring and a reduced osmium center. As indicated by the arrow, the imidazole is substituting the chloride ligand once the osmium center is electro-reduced. All electrode potentials are given versus Ag/AgCl (3M NaCl) reference electrode.

The additional peak (**Figures 3.13a** and **b**) that has been observed in the CV of the polymer solution did not appear during the electrochemical characterization (**Figure 3.15a**) of the electrodeposited Os-polymer film, possibly due to its cross-linking to the imidazole ring that is present in the polymer structure. As it can be seen, two symmetric peaks appear around 0.35 V upon the oxidation/reduction of osmium sites as expected for surface adsorbed redox species. During the electrodeposition at the surface of bare gold electrodes, a continuous increase of the charge that corresponds to the amount of electrodeposited Os-polymer can be expected with an increasing number of electrodepositing cycles. In contrast to that, one might expect that a saturation level (with respect to the charge) should be reached once the pores are completely filled and the polymer growth continues only at the outmost pore layer. Taking into account geometric considerations (see the theoretical calculation below), it is also expected that the charge densities corresponding to the osmium content are in average higher for bare gold electrodes than for the macroporous ones in the case of thicker films and approximately the same for a very thin ones.

### 3 – Macroporous electrodes for the fabrication of a biocathode

According to the proposed calculation (see the inset below) the difference in charge densities between Os-polymer modified non-porous and porous electrodes seems to increase upon increasing the number of cycles. **Figure 3.15b** presents the evolution of charge densities for bare and macroporous gold electrodes. Besides the fact that the charge densities are higher for bare than for macroporous electrodes (see the proposed theoretical calculation at pages 83 and 84) it can be seen that their rather random distribution increases with polymer thickness. In contrast to bare gold electrodes, macroporous samples showed an almost linear dependence for low electrodeposition scans (82 to 160) and reached saturation for higher amounts of electrodeposited polymer (**Figure 3.15b**).

This suggests that the macroporous structure plays an important role in the structural control of electrodeposited polymer. Possible reasons for the random distribution of experimental data for non-porous gold electrodes could be the instability of the film (e.g. peeling), when it is directly brought in contact with the rinsing solvent (after the electrodeposition step the Os-polymer modified electrodes were kept in MilliQ water during 10 min in order to dissolve physisorbed polymer which would contribute to the total Os-charge) and the supporting electrolyte (100 mM PB, pH=7.2). In that sense, polymer that has been deposited within the pores would be protected since it is not directly exposed to the liquid medium (MilliQ water of PB solution) and is therefore able to give the signal that corresponds to the amount of electrodeposited Os-redox polymer without a random distribution of charge density. This can be further explained by swelling of the polymer film at the surface of non-porous electrodes due to the penetration of water molecules within its structure as a consequence of non-adjusted ionic strength of pure MilliQ water (similar to what has been observed for living cells when suspended in non-isotonic environment).

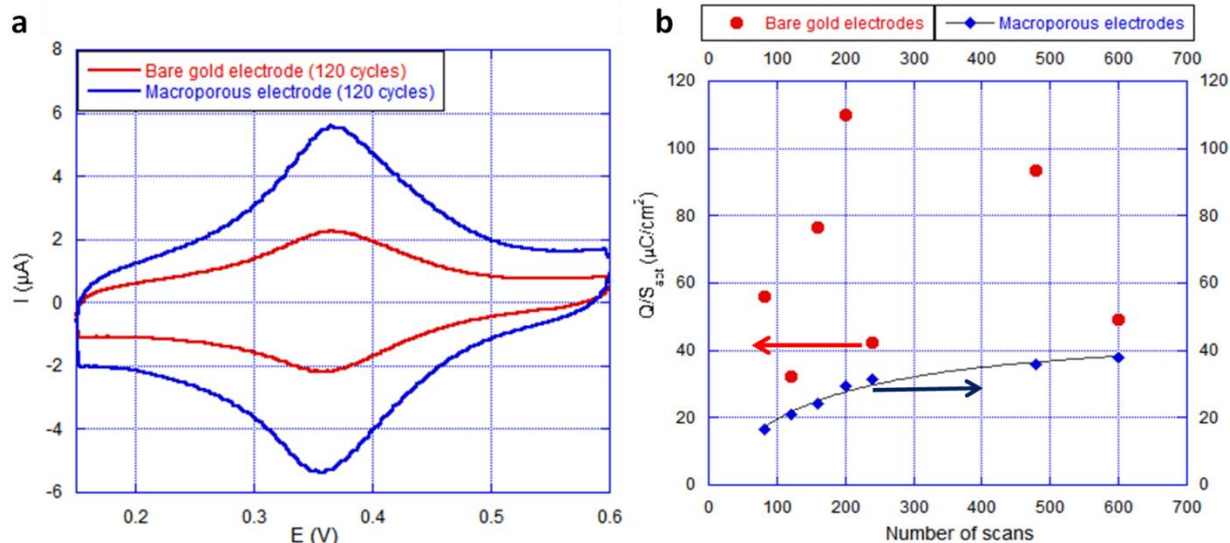
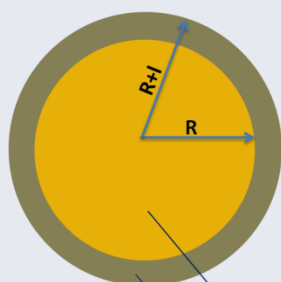


**Figure 3.15** (a) CVs of bare (red curve) and macroporous (blue curve) gold electrodes (recorded vs. Ag/AgCl (3M NaCl)) modified with Os-polymer during 120 cycles in phosphate buffer (PB, pH = 7.2) at 37.5 °C and a scan rate of 50 mV/s; (b) Charge densities as a function of number of scans for bare (red circles) and macroporous (blue rhomboids) electrodes. All electrode potentials are given versus Ag/AgCl (3M NaCl) reference electrode.

**Inset: Theoretical calculation of charge/surface ratio regarding the Os-polymer oxidation/reduction for bare and macroporous electrodes**  
(Geometric consideration)

**1. Calculation of n/S values for cylindrical bare gold electrode**



Cross section of gold microwire

Os-redox polymer film

For a cylindrical bare gold electrode of radius R it can be assumed that the length (L) is much bigger than the thickness of the Os-polymer film.

Assuming that the polymer film covers the entire wire (cylinder) the volume of the film (hollow cylinder) can be calculated as:

$$V = \pi(R + l)^2 L - \pi R^2 L \quad \text{Eq.1}$$

$$\Rightarrow V = \pi(2Rl + l^2)L \quad \text{Eq.2}$$

so it can be written:

$$V = 2\pi R L l \left(1 + \frac{l}{2R}\right) \quad \text{Eq.3}$$

The geometrical surface of a bare gold wire can be calculated as:

$$S = 2\pi R L \quad \text{Eq. 4}$$

As  $R \gg l \Rightarrow \frac{l}{R} \lll 1$  and it can be written (regarding the **Eq.3**) that:

$$V = 2\pi R L l \quad \text{Eq.5}$$

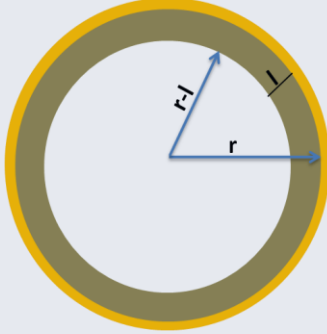
Knowing that the molar quantity is given as  $n = CV$  (where n- number of moles and C – molar concentration of osmium moieties within electrodeposited film), the osmium content within the electrodeposited film can be calculated as:

$$n = CV \Rightarrow n = CSl \quad \text{Eq. 6}$$

From the formulations mentioned above, it can be further concluded that:

$$\frac{n}{S} = Cl \quad \text{Eq. 7}$$

## 2. Calculation of n/S ratio for polymer layer of thickness $l$ within a pore of radius $r$



The volume of the surface layer of a single pore can be calculated as for any sphere as:

$$V = 4/3\pi(r^3 - (r - l)^3) \quad \text{Eq. 8}$$

$$\Rightarrow V = 4/3\pi(r^3 - r^3 + 3r^2l - 3rl^2 + l^3)$$

$$\Rightarrow V = 4/3\pi(3r^2l - 3rl^2 + l^3)$$

Now, let us consider three different situations:

### 2.1 The pore is modified with a very thin layer of polymer

Knowing that  $l \ll r$  (in other words  $l/r \ll 1$ ) the amount of osmium within the film can be calculated as:  $n = CV \Rightarrow n = C4\pi r^2 l$

Therefore it can be written that:

$$\frac{n}{S} = \frac{C4\pi r^2 l}{4\pi r^2} \Rightarrow \frac{n}{S} = Cl \quad \text{Eq. 9}$$

From the equation above one could expect that the charge per active surface area obtained during the oxidation/reduction of an Os-polymer film for macroporous electrodes should be approximately the same as for the bare one (Eq. 7).

### 2.2 The pore is modified with an Os-polymer layer of intermediate thickness

In this case we assume that  $l$  is not  $\ll r$  and therefore it can be written that:

$$n = CV \Rightarrow n = C4\pi r^2 l \left(1 - \frac{l}{r} + \frac{l^2}{3r^2}\right) \quad \text{Eq. 10}$$

In this situation the member in the bracket (Eq. 10) is not anymore negligible but it is still  $< 1$  and so:

$$\frac{n}{S} = Cl \left(1 - \frac{l}{r} + \frac{l^2}{3r^2}\right) < Cl \quad \text{Eq. 11}$$

This means that for an intermediate thickness of the Os-polymer film, the charge densities (that correspond to the surface concentration of osmium) will be smaller for a macroporous gold electrode compared to a bare one.

### 2.3 The pore volume is completely filled with Os-redox polymer ( $l = r$ )

Assuming now that  $l = r$ , the ratio  $\frac{n}{S}$  can be easily calculated by substituting  $l$  with  $r$  in the Eq. 10.

$$\frac{n}{S} = Cl \left( 1 - 1 + \frac{1}{3} \right) \Rightarrow \frac{n}{S} = \frac{Cl}{3} \quad \text{Eq. 12}$$

This calculation shows that the  $\frac{n}{S}$  ratio for a pore that is completely filled with polymer is 1/3 of the value that can be expected for a bare gold surface.

- Although the calculation above has been done for a single pore, the same conclusion can be made for a large number of pores that are present in a macroporous wire since the  $n/S$  ratio will scale with the number of pores.
- In other words, the curvature of the pores will result in the immobilization of relatively less and less active osmium sites when the polymer layer thickness in the pore is increasing (with respect to the total active surface area).

As already mentioned, different enzymes can be coelectrodeposited with the Os-redox polymer by considering the same mechanism as explained for electrodeposition of the polymer. To elaborate the biocathode, BOD (isolated from *Magnaporthe orizae*) has been coelectrodeposited with the cathodic redox polymer (**Figure 3.14b**). This BOD type was selected since it presents very efficient biocatalysis (compared to BOD/*M. verrucaria* and BOD/*T. tsunodae* that are frequently used) for the four-electron oxygen reduction as previously reported [74], and because of its ability to efficiently operate under physiological conditions (in contrast to Laccase (**Subchapter 3.3**)). **Figure 3.16** depicts the CVs recorded upon the coelectrodeposition of BOD and the Os-redox polymer that has been carried out under oxygen-free conditions. It was expected that during the coelectrodeposition a pair of symmetric peaks (that correspond to the oxidation and reduction of deposited Os-redox sites) would be observed. Instead of that, distortion of the peaks is noticed probably due to residual oxygen electrocatalysis that takes place under the chosen experimental conditions (potential window: 0.6 V-0.15 V vs. Ag/AgCl (3 M NaCl)). These oxygen traces in the solution can originate either from the atmosphere or from oxygen impurities that are present in argon (all solutions were bubbled with argon prior to the deposition step and argon was passed over the solution during the coelectrodeposition). Due to the fact that this phenomenon is not observed during the electrodeposition of the polymer alone and knowing that the system now contains the enzyme this conclusion seems reasonable. Also, this effect is more significant for macroporous electrodes than for the bare ones due to the increased active surface area.

### 3 – Macroporous electrodes for the fabrication of a biocathode

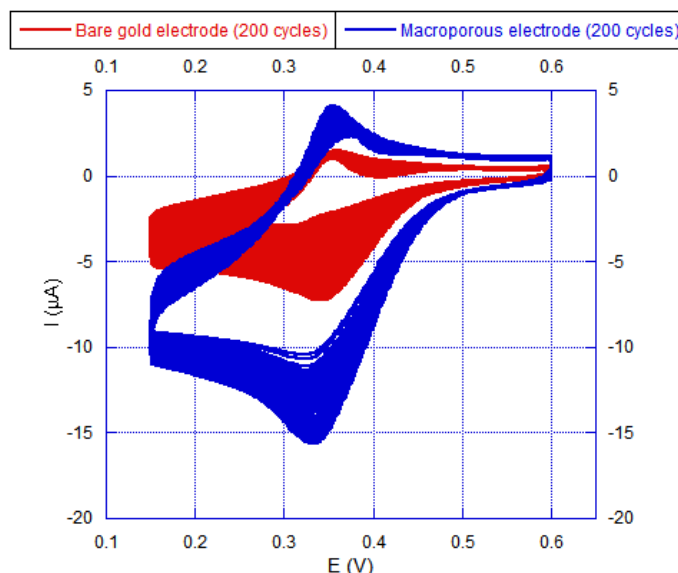


**Figure 3.16** CVs recorded at bare ( $S_{\text{act.}} = 0.23 \text{ cm}^2$ ) and macroporous electrodes ( $S_{\text{act.}} = 0.61 \text{ cm}^2$ ) during the coelectrodeposition of Os-redox polymer and BOD (*Magnaporthe orizae*) (68% wt. Os-polymer, 32% BOD) at 50 mV/s, pH=7.2 (100 mM PB), 37,5 °C for 200 consecutive cycles. Electrode potentials are given *versus* Ag/AgCl (3 M NaCl) reference electrode.

The electrocatalytic performances of the biocathode (with different amounts of electrodeposited BOD/Os-polymer) prepared in such a way were tested in oxygen saturated PB as depicted in **Figures 3.17 a** and **b**. As can be seen, the absolute electrocatalytic currents (**Figure 3.17a**) were, as expected, in all the cases higher for macroporous electrodes than for the bare ones. However, when looking at the trend of just the series of macroporous electrodes the absolute current of the electrode which has been modified with 500 cycles is smaller than the one obtained for 200 cycles. This can be explained by the fact that the first one had a smaller geometric surface area. In order to compare correctly the performance of all electrodes it is therefore necessary to calculate the catalytic current densities by taking into account the real active surface area (**Figure 3.17b**). In general, the catalytic current densities recorded for samples containing hydrogels with the same thickness (= same number of cycles) were higher for bare electrodes than for the macroporous ones as shown in **Figures 3.17b** and **3.18**. This can again be explained based on the same geometrical considerations that have been put forward for the case of electrodeposition of only Os-redox polymer (see the **geometric consideration present in the inset above**).

### 3 – Macroporous electrodes for the fabrication of a biocathode

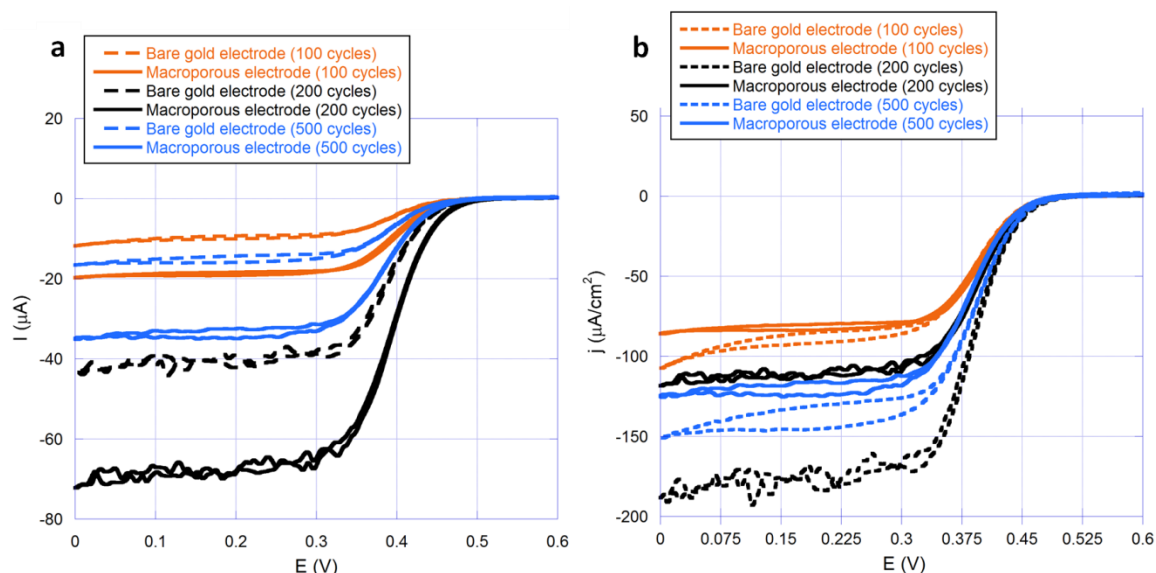


**Figure 3.17** Cyclic voltammograms of the bare and macroporous electrodes (vs. Ag/AgCl (3 M NaCl); current (a) and current densities (b) as a function of applied electrode potential) modified with different amounts of BOD/Os-redox polymer electrodeposit. The cyclic voltammograms have been recorded at 5 mV/s, in oxygen saturated 100 mM PB solution (pH = 7.2) at 37.5 °C. All electrode potentials are given *versus* Ag/AgCl (3M NaCl) reference electrode.

The dependence of catalytic current densities as a function of the number of electrodeposition cycles is depicted in the **Figure 3.18**. It can be seen that the values of current densities are increasing for macroporous electrodes, similar to what has been observed for electrodeposited Os-redox polymer (**Figure 3.15b**). In contrast to macroporous electrodes, once again, non-porous analogues show a rather erratic distribution of current densities upon increasing the number of coelectrodeposition cycles. As earlier mentioned, it is believed that the macroporous structure plays an important role in preserving the structural stability of the BOD/Os-polymer film in comparison to bare gold electrodes. Further, it has been noticed that the catalytic current densities reach a “saturation” level once the pores are filled with the deposit, as previously observed for the electrodeposition of a redox polymer alone (**Figure 3.15b**).



### 3 – Macroporous electrodes for the fabrication of a biocathode

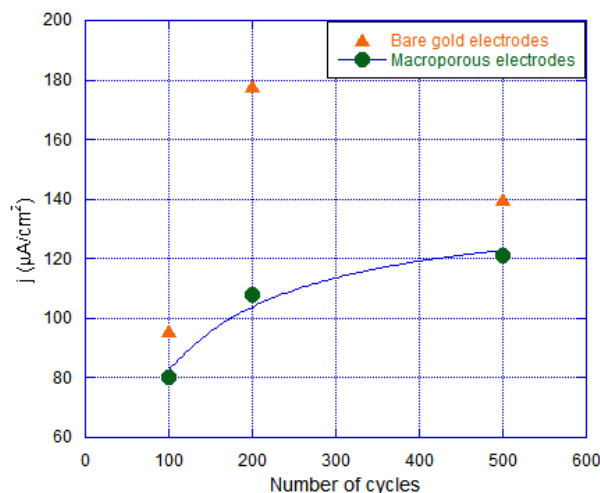


**Figure 3.18** Dependence of bioelectrocatalytic oxygen reduction current densities recorded for bare (orange triangles) and macroporous (green circles) electrodes. The samples were prepared by cycling the electrode potential 100, 200 and 500 times respectively for three different samples in a BOD/Os-redox polymer/MilliQ water mixture at 50 mV/s. During the cycling, an argon stream has been flowing over the electrochemical cell.

A short term stability test has been carried-out over 90 min under oxygen saturation. **Figure 3.19** depicts the decrease of catalytic currents for both electrodes (bare and macroporous samples) with a slightly faster rate (higher slope) for bare gold ( $ccd_{\text{(catalytic current decrease)}} = 59.6\%$ ) than for the macroporous one ( $ccd = 33.1\%$ ). This can be ascribed to the protective role of the macroporous structure regarding desorption and peeling off of the film due to the swelling in MilliQ water. This could play an important role in preserving the activity of BOD/Os-polymer film during its operation as a biocathode.

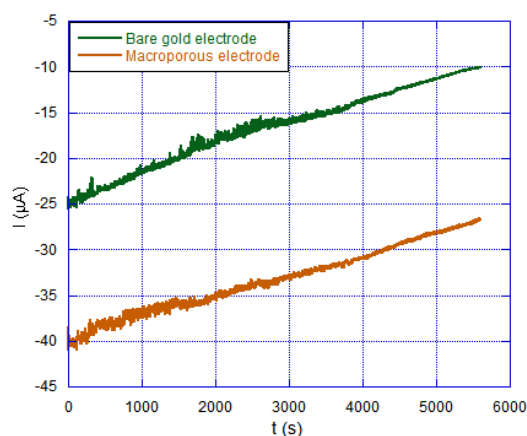


**Figure 3.19** Chronoamperometric curve for oxygen reduction recorded with a bare (green line,  $S_{\text{act}} = 0.23 \text{ cm}^2$ ) and a macroporous (orange curve,  $S_{\text{act}} = 0.61 \text{ cm}^2$ ) electrode in 100 mM PB solution at  $37.5^\circ \text{C}$  at a scan rate of  $5 \text{ mVs}^{-1}$ . Electrodes were polarized at  $+0.3 \text{ V}$  vs Ag/AgCl (3 M NaCl) for 93 min. Electrodes were prepared by BOD/Os-polymer deposition with 200 cycles.



### 3.5 Conclusions and perspectives

The results presented in this chapter confirm the feasibility of electrodeposition of Os-redox polymer and coelectrodeposition of BOD/Os-polymer using bare and macroporous gold electrodes. It has been shown that the “saturation” of macroporous gold electrodes with Os-polymer is reached at approximately 500 electrodeposition cycles. Above that point it can be assumed that the Os-redox polymer is deposited at the outmost layer of pores (similarly to the deposition of a polymer film at non-porous electrodes) although additional experiments are needed (e.g. environmental SEM) in order to confirm this assumption. In contrast to macroporous electrodes, the electrochemical characterization of the polymer film on bare gold electrodes showed a rather random behavior with respect to what could be expected for samples with increasing amounts of electrodeposited polymer. Macroporous electrodes allow immobilizing more polymer which is illustrated by higher absolute charge values when integrating the current-voltage curves. However in contrast to this, the charge densities obtained from the electrochemical characterization of Os-polymer modified electrodes were on average higher for bare gold electrodes in comparison with macroporous ones, which can be understood by taking into account geometric considerations. The possibility to coelectrodeposit BOD/Os-polymer has been demonstrated for both, bare and macroporous substrates. The dependence of catalytic current densities for O<sub>2</sub> reduction as a function of the electrodeposited BOD/Os-polymer shows an increase up to 500 cycles where “saturation” has been reached, similarly to what was also observed for electrodeposited redox polymer.

Our results suggest that coelectrodeposition of enzymes and corresponding Os-redox polymers present a promising strategy for immobilization of bioelectrocatalytic films on electrode surfaces. This method also offers the possibility for selective modification of the coaxial electrodes that we developed (see **Chapter 2**), with different enzyme/Os-redox polymers in an independent way. It should lead in the near future to the elaboration of the first coaxial and miniaturized glucose/O<sub>2</sub> biofuel cell.

## Literature

- [1] L. Carrette, K. A. Friedrich, U. Stimming, *Chemphyschem* 1 (2000) 162.
- [2] B. Demirel, P. Scherer, *Rev. Environ. Sci. Biotechnol.* 7 (2008) 173.
- [3] R.A. Bullen, T.C. Arnot, J.B. Lakeman, F.C. Walsh, *Biosens. Bioelectron.* 21 (2015) 2015.
- [4] M.G.K. J.H. Hirschenhofer, D.B. Stauffer, R.R. Engleman, *Fuel Cell Handbook* (fourth edition), Parsons Corporation, Morgantown - West Virginia (1998).
- [5] R. A. S. Luz, A.R. Pereira, J.C.P. De Souza, F.C.P.F. Sales, F.N. Crespilho, *ChemElectroChem*, (2014) 1751.
- [6] J. Larminie, A. Dicks, *Fuel Cell Systems Explained* (second edition), John Wiley & Sons, The Atrium Southern Gate - Chichester (West Sussex) - England (2003).
- [7] W.R.G.E. M.A., *Philos. Mag. Ser. 3* 14 (1839) 127.
- [8] S.M. Haile, *Acta Mater.* 51 (2003) 5981.
- [9] X. Ren, P. Zelenay, S. Thomas, J. Davey, S. Gottesfeld, *J. Power Sources* 86 (2000) 111.
- [10] J.R. Varcoe, R.C.T. Slade, *Fuel Cells* 5 (2005) 187.
- [11] M. A. Hickner, B.S. Pivovar, *Fuel Cells* 5 (2005) 213.
- [12] R.S. Jayashree, M. Mitchell, D. Natarajan, L.J. Markoski, P.J. A. Kenis, *Langmuir* 23 (2007) 6871.
- [13] F.R. Brushett, W.P. Zhou, R.S. Jayashree, P.J. A. Kenis, *J. Electrochem. Soc.* 156 (2009) B565.
- [14] X. Cheng, Z. Shi, N. Glass, L. Zhang, J. Zhang, D. Song, Z.S. Liu, H. Wang, J. Shen, *J. Power Sources* 165 (2007) 739.
- [15] E.H. Yu, K. Scott, *Energies* 3 (2010) 23.
- [16] K. Rabaey, W. Verstraete, *Trends Biotechnol.* 23 (2005) 291.
- [17] S.C. Barton, J. Gallaway, P. Atanasov, *Chem. Rev.* 104 (2004) 4867.
- [18] M.J. Cooney, V. Svoboda, C. Lau, G. Martin, S.D. Minter, *Energy Environ. Sci.* 1 (2008) 320.
- [19] D. Sokic-Lazic, S.D. Minter, *Biosens. Bioelectron.* 24 (2008) 939.
- [20] S. Xu, S.D. Minter, *ACS Catal.* 2 (2012) 91.
- [21] S.D. Minter, B.Y. Liaw, M.J. Cooney, *Curr. Opin. Biotechnol.* 18 (2007) 228.
- [22] A. Karajić, S. Reculosa, M. Heim, P. Garrigue, S. Ravaine, N. Mano, A. Kuhn, *Adv. Mater. Interfaces* 2 (2015) 1500192.
- [23] M. Southcott, K. MacVittie, J. Halámek, L. Halámková, W.D. Jemison, R. Lobel, E. Katz, *Phys. Chem. Chem. Phys.* 15 (2013) 6278.
- [24] Z. Liu, B. Cho, T. Ouyang, B. Feldman, *Anal. Chem.* 84 (2012) 3403.
- [25] D. Leech, P. Kavanagh, W. Schuhmann, *Electrochim. Acta* 84 (2012) 223.
- [26] J. A. Cracknell, K. A. Vincent, F. a. Armstrong, *Chem. Rev.* 108 (2008) 2439.
- [27] M.J. Eddowes, H.A.O. Hill, *J. Chem. Soc. Chem. Commun.* (1977) 771b.
- [28] P. Yeh, T. Kuwana, *Chem. Lett.* 6 (1977) 1145.
- [29] T. Zhong, Y. Qu, S. Huang, F. Li, *Microchim. Acta* 158 (2007) 291.
- [30] R. A. Marcus, *Angew. Chemie Int. Ed.* 32 (1993) 1111.
- [31] C. Leger, P. Bertrand, *Chem. Rev.* 108 (2008) 2379.
- [32] B. Durham, J.L. Fairris, M. McLean, F. Millett, J.R. Scott, S.G. Sligar, a Willie, *J. Bioenerg. Biomembr.* 27 (1995) 331.

- [33] Y. Zeng, R. Smith, P. Bai, M.Z. Bazant, J. Electroanal. Chem. 735 (2014) 77.
- [34] Philip Bartlett, ed., Bioelectrochemistry, Fundamentals, Experimental Techniques and Application, Wiley, The Atrium, Southern Gate, Chichester, West Sussex PO19 8SQ, England, 2008.
- [35] L.J.C. Jeuken, Biochim. Biophys. Acta - Bioenerg. 1604 (2003) 67.
- [36] M.J. Tarlov, N. Carolina, Society (1991) 1847.
- [37] K. Niki, J.R. Sprinkle, E. Margoliash, Bioelectrochemistry 55 (2002) 37.
- [38] Z. Qiang Feng, S. Imabayashi, T. Kakiuchi, K. Niki, J. Chem. Soc. Faraday Trans. 93 (1997) 1367.
- [39] Q. Chi, J. Zhang, J.E.T. Andersen, J. Ulstrup, J. Phys. Chem. B 105 (2001) 4669.
- [40] S. Song, R. A. Clark, E.F. Bowden, M.J. Tarlov, J. Phy. Chem. 97 (1993) 6564.
- [41] S. Shleev, A. Jarosz-Wilkolazka, A. Khalunina, O. Morozova, A. Yaropolov, T. Ruzgas, L. Gorton, Bioelectrochemistry 67 (2005) 115.
- [42] A. Christenson, N. Dimcheva, E.E. Ferapontova, L. Gorton, T. Ruzgas, L. Stoica, S. Shleev, A.I. Yaropolov, D. Haltrich, R.N.F. Thorneley, S.D. Aust, Electroanalysis 16 (2004) 1074.
- [43] E.E. Ferapontova, V.G. Grigorenko, A.M. Egorov, T. Borchers, T. Ruzgas, L. Gorton, Biosens. Bioelectron. 16 (2001) 147.
- [44] Y.T. Kong, M. Boopathi, Y.B. Shim, Biosens. Bioelectron. 19 (2003) 227.
- [45] L.H. Guo, H.A.O. Hill, G. a. Lawrance, G.S. Sanghera, D.J. Hopper, J. Electroanal. Chem. Interfacial Electrochem. 266 (1989) 379.
- [46] A. Ramanavicius, K. Habermuller, E. Csoregi, V. Laurinavicius, W. Schuhmann, Anal. Chem. 71 (1999) 3581.
- [47] a. Lindgren, L. Gorton, T. Ruzgas, U. Baminger, D. Haltrich, M. Schülein, J. Electroanal. Chem. 496 (2001) 76.
- [48] A. Lindgren, T. Larsson, T. Ruzgas, L. Gorton, J. Electroanal. Chem. 494 (2000) 105.
- [49] C.C. Page, C.C. Moser, X. Chen, P.L. Dutton, Nature 402 (1999) 47.
- [50] S. Zhao, K. Zhang, Y. Bai, W. Yang, C. Sun, Bioelectrochemistry 69 (2006) 158.
- [51] L. Wang, E. Wang, Electrochem. Commun. 6 (2004) 225.
- [52] D. Ivnitski, B. Branch, P. Atanassov, C. Apblett, Electrochem. Commun. 8 (2006) 1204.
- [53] A. Guiseppi-Elie, C. Lei, R.H. Baughman, Nanotechnology 13 (2002) 559.
- [54] C. Shan, H. Yang, J. Song, D. Han, A. Ivaska, L. Niu, Anal. Chem. 81 (2009) 2378.
- [55] V. Coman, R. Ludwig, W. Harreither, D. Haltrich, L. Gorton, T. Ruzgas, S. Shleev, Fuel Cells 10 (2010) 9.
- [56] A. De Poulpique, A. Ciaccafava, R. Gadiou, S. Gounel, M.T. Giudici-Orticoni, N. Mano, E. Lojou, Electrochem. Commun. 42 (2014) 72.
- [57] A. Zebda, C. Gondran, A. Le Goff, M. Holzinger, P. Cinquin, S. Cosnier, Nat. Commun. 2 (2011) 370.
- [58] A. Ramanavicius, A. Kausaite, A. Ramanaviciene, Biosens. Bioelectron. 20 (2005) 1962.
- [59] A. Heller, Phys. Chem. Chem. Phys. 6 (2004) 209.
- [60] N.L. Akers, C.M. Moore, S.D. Minter, Electrochim. Acta 50 (2005) 2521.
- [61] S. Rengaraj, V. Mani, P. Kavanagh, J. Rusling, D. Leech, Chem. Commun. 47 (2011) 11861.
- [62] S.C. Barton, H.H. Kim, G. Binyamin, Y. Zhang, A. Heller, J. Phys. Chem. B 105 (2001) 11917.

- [63] C. Qi-Jin, D. Shao-Jun, J. Mol. Catal. A Chem. 105 (1996) 193.
- [64] J. Moiroux, P.J. Elving, Anal. Chem. 50 (1978) 1056.
- [65] T.N. Rao, I. Yagi, T. Miwa, D.A. Tryk, A. Fujishima, Anal. Chem. 71 (1999) 2506.
- [66] G.T.R. Palmore, H. Bertschy, S.H. Bergens, G.M. Whitesides, J. Electroanal. Chem. 443 (1998) 155.
- [67] J. Kulys, G. Gleixner, W. Schuhmann, Electroanalysis 5 (1993) 201.
- [68] D. Zhou, H. Fang, Y. Wang, Anal. Chim. Acta 329 (1996) 41.
- [69] A. A. Karyakin, E.E. Karyakina, W. Schuhmann, H.L. Schmidt, Electroanalysis 11 (1999) 553.
- [70] H. Sakai, T. Nakagawa, Y. Tokita, T. Hatazawa, T. Ikeda, S. Tsujimura, K. Kano, Energy Environ. Sci. 2 (2009) 133.
- [71] E. Katz, I. Willner, A.B. Kotlyar, J. Electroanal. Chem. 479 (1999) 64.
- [72] A. Ciaccafava, P. Infossi, M. Ilbert, M. Guiral, S. Lecomte, M.T. Giudici-orticoni, E. Lojou, Angew. Chem. 51 (2012) 977.
- [73] A. Karyakin, E. Karyakina, H.L. Schmidt, Electroanalysis 11 (1998) 49.
- [74] M. Cadet, X. Brilland, S. Gounel, F. Louerat, N. Mano, ChemPhysChem 14 (2013) 2097.
- [75] N. Mano, F. Mao, A. Heller, (2003) 6588.
- [76] S. Boland, D. Leech, Analyst 137 (2012) 113.
- [77] F. Gao, L. Viry, M. Maugey, P. Poulin, N. Mano, Nat Commun 1 (2010) 2.
- [78] A. Heller, Curr. Opin. Chem. Biol. 10 (2006) 664.
- [79] N. Mano, J.L. Fernandez, Y. Kim, W. Shin, A.J. Bard, A. Heller, J. Am. Chem. Soc. 125 (2003) 15290.
- [80] F. Mao, N. Mano, A. Heller, J. Am. Chem. Soc. 125 (2003) 4951.
- [81] V. Soukharev, N. Mano, A. Heller, J. Am. Chem. Soc. 126 (2004) 8368.
- [82] A. Aoki, R. Rajagopalan, A. Heller, J. Phys. Chem. 99 (1995) 5102.
- [83] T. Chen, S.C. Barton, G. Binyamin, Z. Gao, Y. Zhang, H.H. Kim, a Heller, J. Am. Chem. Soc. 123 (2001) 8630.
- [84] I. Willner, Y. Yan, B. Willner, R. Tel-Vered, Fuel Cells 9 (2009) 7.
- [85] P. Ramírez, N. Mano, R. Andreu, T. Ruzgas, A. Heller, L. Gorton, S. Shleev, Biochim. Biophys. Acta - Bioenerg. 1777 (2008) 1364.
- [86] N. Mano, Appl. Microbiol. Biotechnol. 96 (2012) 301.
- [87] A. E. Palmer, S.K. Lee, E.I. Solomon, J. Am. Chem. Soc. 123 (2001) 6591.
- [88] T. Sakurai, K. Kataoka, Chem. Rec. 7 (2007) 220.
- [89] E.I. Solomon, A.J. Augustine, J. Yoon, Dalt. Trans. 9226 (2008) 3921.
- [90] F. Barrière, Y. Ferry, D. Rochefort, D. Leech, Electrochem. Commun. 6 (2004) 237.
- [91] A. Kosaka, C. Yamamoto, Y. Morishita, K. Nakane, Clin. Biochem. 20 (1987) 451.
- [92] S.C. Barton, H. H. Kim, G. Binyamin, Y. Zhang, A. Heller, J. Am. Chem. Soc. 123 (2001) 5802.
- [93] S.C. Barton, M. Pickard, R. Vazquez-Duhalt, A. Heller, Biosens. Bioelectron. 17 (2002) 1071.
- [94] S. Shleev, V. Andoralov, M. Falk, C.T. Reimann, T. Ruzgas, M. Srnec, U. Ryde, L. Rulíšek, Electroanalysis 24 (2012) 1524.
- [95] N. Mano, L. Edembe, Biosens. Bioelectron. 50 (2013) 478.
- [96] A. Heller, Anal. Bioanal. Chem. 385 (2006) 469.

- [97] N. Mano, H.H. Kim, Y. Zhang, A. Heller, J. Am. Chem. Soc. 124 (2002) 6480.
- [98] S. Boland, D. Leech, Analyst 137 (2012) 113.
- [99] M.T.Y. Paul, B. Kinkad, B.D. Gates, J. Electrochem. Soc. 161 (2013) B3103.
- [100] M. Ammam, J. Fransaer, Biotechnol. Bioeng. 109 (2012) 1601.
- [101] M. Ammam, Biosens. Bioelectron. 58 (2014) 121.
- [102] M. Ammam, J. Fransaer, Sensors Actuators B Chem. 160 (2011) 1063.
- [103] Z. Gao, G. Binyamin, H. H. Kim, S.C. Barton, Y. Zhang, A. Heller, Angew. Chemie Int. Ed. 41 (2002) 810.
- [104] A.J. Bard, L.R. Faulkner, Electrochemical methods - Fundamentals and Applications (second edition), John Wiley & Sons, Printed in the United States of America (2010).

---

*CHAPTER 4*

GUIDING PANCREATIC BETA-CELLS TO TARGETED  
ELECTRODES: TOWARD A WHOLE-CELL BIOSENSOR FOR  
DIABETES

#### 4 – Guiding pancreatic $\beta$ -cells to target electrodes: towards a whole-cell biosensor for diabetes

---

Regarding the reports of World Health Organization (WHO), non-communicable (chronic) diseases (NCDs) are the leading global causes of death, resulting in more deaths than all other causes combined [1]. Statistically, NCD were having the most intense strike at the world's low and middle-income population. In 2012, 68% of global reported deaths were directly caused by NCD, a broad spectrum of diseases which includes cardiovascular diseases, diabetes, cancer and chronic respiratory diseases. Certainly, a large percentage of them are preventable through the reduction of the four main risk factors: tobacco use, physical inactivity, excessive use of alcohol and unhealthy diets. **Figure 4.1** shows the proportions of deaths caused by NCD in 2012 in the population under the age of 70, by cause[1,2].

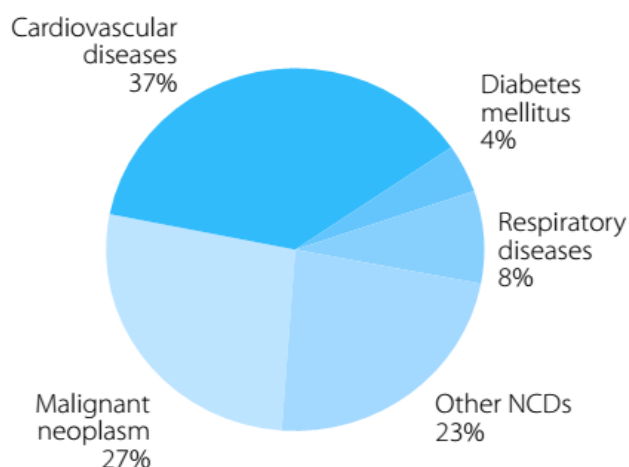


**Figure 4.1** Proportion of global deaths under the age 70 years, by cause of death, comparable estimates, 2012 (adapted from [2]).

Besides cardiovascular, chronic respiratory or digestive diseases and cancer that are together responsible for the highest percentage (96%) of NCD caused deaths, 4% are dedicated to diabetes and its related complications with an obvious worldwide growing population of the diabetes patients (**Figure 4.2**) [1–3].

Diabetes (*lat. Diabetes mellitus*) is a metabolic disorder of multiple etiologies. It is characterized by chronic hyperglycemia, with the disordered metabolism of carbohydrate, lipids and proteins. One of the main consequences related to diabetes is impaired ability of the body to produce and/or to respond to the pancreatic hormone insulin and therefore inability to react upon increased blood glucose level in order to maintain its homeostasis. This results in a long-term damage of various organs which has as a consequence renal and kidney failure, peripheral limb neuropathy, cardiac diseases and blindness [1,4].

#### 4 – Guiding pancreatic $\beta$ -cells to target electrodes: towards a whole-cell biosensor for diabetes

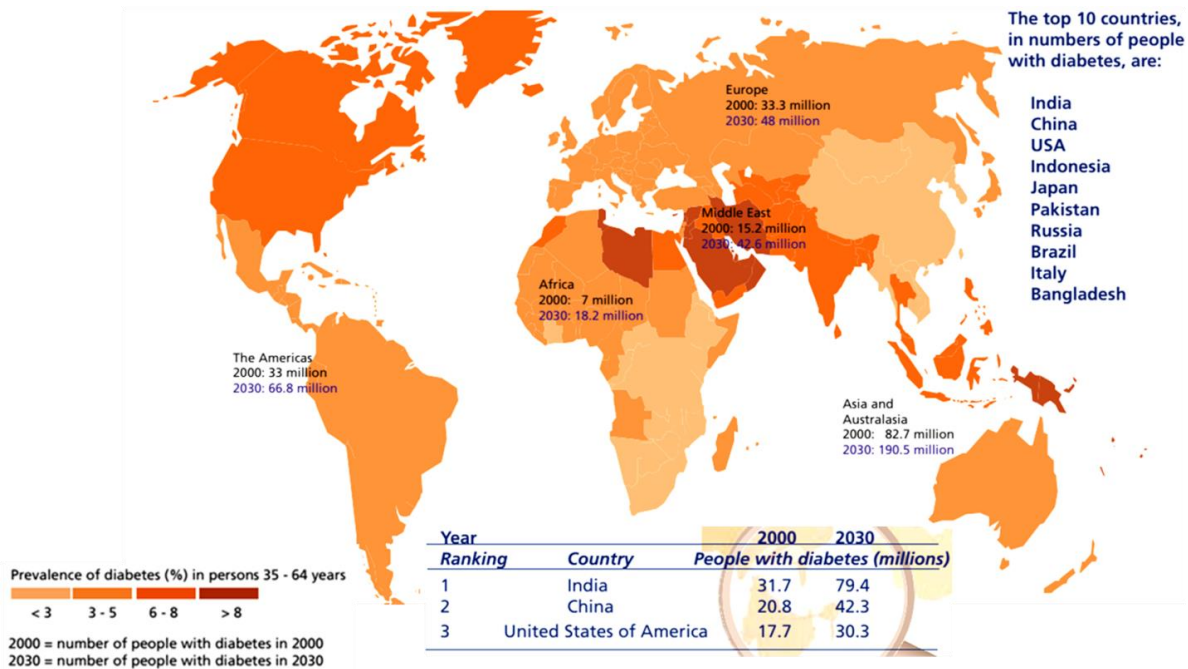


**Figure 4.2** The world map showing the prevalence of diabetes in the world with the predicted increase in diabetic population [3].

WHO has classified several types of diabetes:

- **Diabetes type 1** – insulin dependent type caused by autoimmune destruction of beta cells and consequently lack of insulin. It comprises 5-10% of the total diabetic population. Patients with this type are prone to ketoacidosis [4–6].
- **Diabetes type 2** – the most frequent type of diabetes (85-90% of all cases of diabetes) closely related to obesity. The main characteristics of this type is deficient insulin secretion and developed insulin resistance in target tissues [4,6].
- **Gestational diabetes** – specific type developed during pregnancy which may or may not disappear after that period [6,7].
- **Other specific types** – include a wide group of disorders with different etiologies such as: genetic defects of pancreatic cell function, genetic defects in insulin action, various diseases of exocrine pancreas that can damage its endocrine function, infections, genetic syndromes and drug- or chemically-induced diabetes [6].



### 4.1. Electrical activity of pancreatic $\beta$ -cells

The pancreas is a double functional organ that has both: a) an exocrine function responsible for the synthesis of digestive enzymes and b) an endocrine function through the synthesis of various hormones (**Table 4.1**) [8,9]. The later plays a key role in maintaining the appropriate level of nutrients, mainly through a negative feedback mechanism. The endocrine function arise from the activity of electrically excitable Langerhans islets (1-3 million dispersed through the pancreas) [4] which present an assembly of different electrogenic cells.

Type of the cell	Secreted hormone	Hormonal function
$\alpha$ -cells	glucagon	increase of blood glucose level during the hypoglycemia
$\beta$ -cells	insulin	decrease of blood glucose level during the hyperglycemia
$\delta$ -cells	somatostatin	inhibition of $\alpha$ - and $\beta$ -cell activity
PP-cells	pancreatic polypeptide	modulation of gastric acid secretion, gastrointestinal motility, gallbladder contraction etc.

**Table 4.1** Overview of the hormones synthesized by the cells of Langerhans islets with their main function [9,10].

The Langerhans islets (**Figure 4.3**) consist of insulin releasing  $\beta$ -cells which are the most abundant cell type (65-90%),  $\alpha$ -cells (15-20%) responsible for the synthesis of glucagon, somatostatin secreting  $\delta$ -cells (3-10%) and pancreatic peptide producing cells (1%) [8].

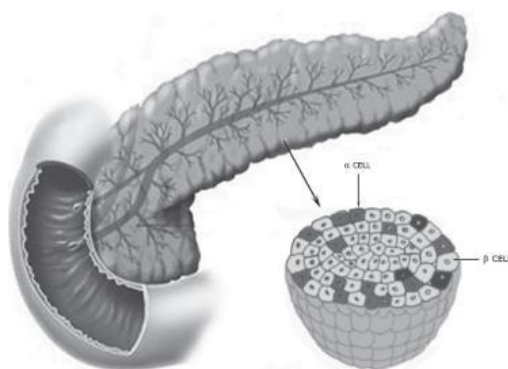


**Figure 4.3** Schematic representation of pancreas and the cellular structure of Langerhans islets [8].

Shaped through the evolution, pancreatic  $\beta$ -cells and therefore the Langerhans islets, present one of the best glucose sensors, which is adjusting insulin secretion and release to the prevalence of glucose into the blood.

#### 4 – Guiding pancreatic $\beta$ -cells to target electrodes: towards a whole-cell biosensor for diabetes

---

Beside glucose,  $\beta$ -cells are also capable of sensing other nutrients such as certain amino- and fatty acids [4]. Insulin is essentially important for glucose level homeostasis and it regulates glucose uptake by other cells (adipose and muscle cells) as well as glycogen breakdown through the process known as glycogenolysis [11]. Their sensing mechanism relies on their electrical activity [12,13] which is well known for some other electrogenic cell types (e.g. neurons and cardiac muscle cells) [14,15]. The generation of their electrical activity includes a close-loop mechanism and involves different voltage and ligand gated ion-channels (adenosine triphosphate (ATP)-dependent  $K^+$ -channels ( $K_{ATP}$ -channels), voltage gated  $Ca^{2+}$ -channels, Ca-dependent  $Ca^{2+}$  channels etc.) whose activity is narrowly linked to the metabolism of nutrients [16,17].

As soon as glucose enters the cell *via* glucose transporters (e.g. GLUT2 transporter) it undergoes further enzymatically catalyzed breakdown, well known as glycolysis. The whole glycolysis can be summarized by the **Equation 4.1**. Final products of glycolysis (ATP, NADH and pyruvate) are further involved in other metabolic pathways such as the tricarboxylic acid (TCA) cycle which takes place in mitochondria [11,18].



**Equation 4.1** The net reaction of glycolysis and formation of ATP and NADH ( $P_i$ – orthophosphate unit) [18].

At the physiological sub-threshold blood glucose level (< 7 mM) or in total absence of glucose, ATP- dependent  $K^+$  ion-channels are normally active and the efflux of potassium ions generates an excess of negative charge (i.e. the lack of positive charge). This has, as a consequence the negative “resting” membrane voltage (approximately -60 to -70 mV) of unstimulated  $\beta$ -cells [8,19].

The entry of nutrients (mainly glucose) inside the cells triggers the glucose breakdown as mentioned above. ATP synthesized during the glycolysis increases the ATP/ADP molar ratio which is of essential importance for the regulation of the  $K_{ATP}$ -channels [4,11]. Increase in ATP/ADP ratio in turn results in closure of  $K_{ATP}$ -channels, followed by membrane depolarization (reverse case compared to the resting stage of the mechanism) from its resting value (-70 mV) above the threshold of -55 mV [4,17]. The increase in transmembrane voltage (with a peak value at  $\approx$  -20 mV), leads to the activation of voltage gated  $Ca^{2+}$  ion channels, and in some animals voltage gated  $Na^+$  ion channels, which initiate series of action potentials (fast change of trans-membrane voltage that occurs in the millisecond range) [17]. The influx of calcium ions inside the cell activates release of insulin in the blood stream through exocytosis (energy consuming process) of insulin containing granules where the insulin is stored in the form of a zinc complex (**Figure 4.4**) [20].

#### 4 – Guiding pancreatic $\beta$ -cells to target electrodes: towards a whole-cell biosensor for diabetes

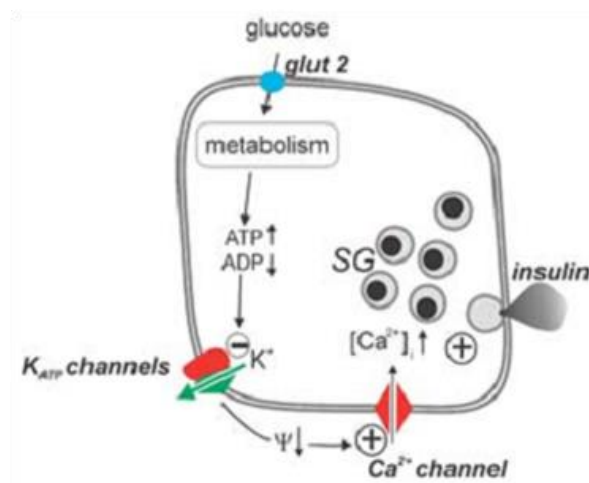


**Figure 4.4** Schematic representation of stimulated secretion of insulin in pancreatic  $\beta$ -cells. Abbreviations: Glut2 – glucose transporter;  $K_{ATP}$  – ATP dependent  $K^+$ -ion channels, SG – insulin containing secretory granules,  $\Psi$  – membrane potential,  $\uparrow\downarrow$  - increase or decrease of indicated parameter; +,- presents an stimulation or inhibition, respectively [20].

The mechanism of electrical response of beta cells is reflected in the large number of action potentials (i.e. bursting) that are superimposed onto its plateau value (active phase) with the repolarization phases in between two consecutive bursts (silent phase) as shown in **Figure 4.5**. Such a behavior of  $\beta$ -cells can be explained in a few steps. Once the voltage gated  $Ca^{2+}$ -channels are activated, the action potentials are triggered and the transmembrane potential increases until it reaches a peak at  $\approx -20$  mV. At that point, when the calcium inward currents are largest, the calcium-dependent inactivation of  $Ca^{2+}$ - channels takes place, and the depolarization is now counterbalanced by the activity of delayed rectifying  $K^+$ -ion channels (K-DR) whose activation starts at  $\approx -30$  mV and their activity increases linearly with depolarization. At the same time, another type of calcium - dependent  $K^+$ -channels (K-Ca channels) are activated and involved in the repolarization phase together with K-DR channels. The delayed outward currents ( $K^+$  current) activated during the depolarization steps become inactive at membrane voltages of  $\approx -40$  mV due to the complete closing of K-DR and K-Ca channels. The hyperpolarization phase which follows each spike arises from the fact that those channels are closing slowly during the repolarization which additionally adds some outward  $K^+$  current. In other words, every action potential (spike) is governed by the balance between inward calcium current and the delayed potassium outward current (K-DR and K-Ca). Similarly, the beginning and the end of each burst is dependent on the balance between inward calcium current and K-ATP dependent potassium outward current. One of the main characteristics of the bursts is that the duration as well as the inter-burst interval increases upon the increase of glucose concentration. It is worth mentioning that some hormones are capable of regulating the electrical activity of  $\beta$ -cells by playing a role either as potentiators of insulin release (glucagon, acetylcholine, vasopressin) or inhibitors (adrenalin, somatostatine, incretins) [4,17].

#### 4 – Guiding pancreatic $\beta$ -cells to target electrodes: towards a whole-cell biosensor for diabetes

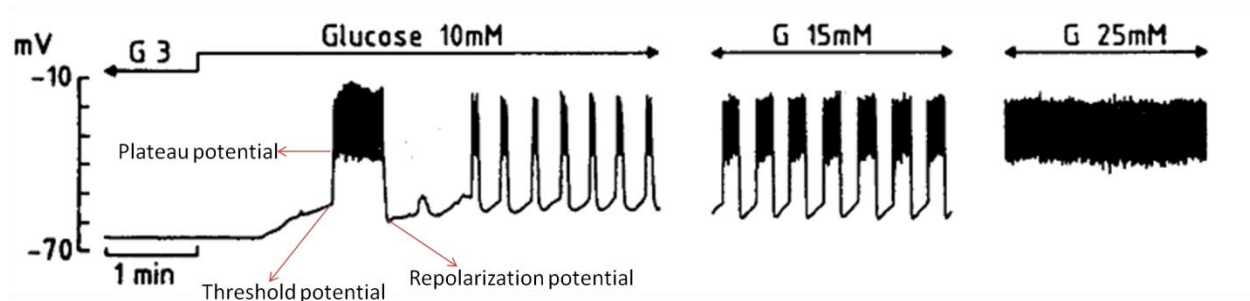


**Figure 4.5** Glucose induced electrical activity of pancreatic  $\beta$ -cells recorded by patch-clamp technique. At non-stimulatory glucose concentration G-3 (3 mM) no electrical activity is initiated and the membrane voltage is on its resting value. Increase of the glucose concentration triggers the depolarization with a characteristic plateau potential onto which the action potential spikes are superimposed. At the glucose concentrations above 20 mM, the electrical activity becomes continuous (adapted from [17]).

Consequently, the insulin secretion follows the electrical activity of  $\beta$ -cells and it occurs in a pulsed way (**Figure 4.6**).

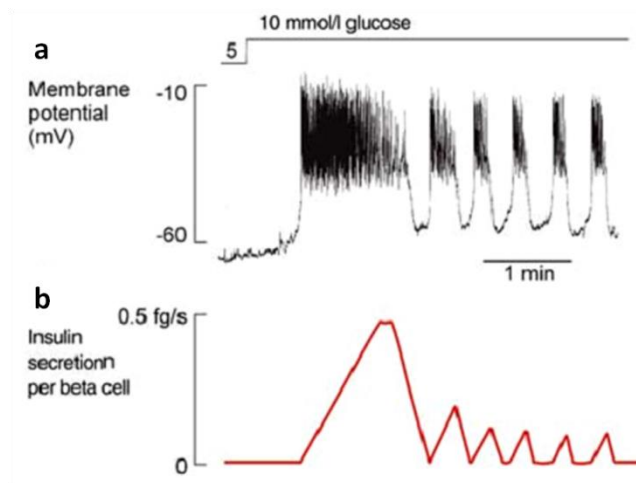


**Figure 4.6** Glucose- induced electrical activity of pancreatic  $\beta$ -cells (a) when glucose concentration is increased from 5mM to 10 mM (as indicated by staircase above (a)). The electrical activity of the cells is followed by a pulsed release of insulin into the blood stream (b).

Besides the traditional patch-clamp techniques [17], which have been used for decades in electrophysiology to perform intracellular investigations, microelectrode arrays (MEA) found their applications as an alternative way which allows extracellular recording of electrical activities of electrogenic cells or tissue slices.

#### 4 – Guiding pancreatic $\beta$ -cells to target electrodes: towards a whole-cell biosensor for diabetes

Compared to other techniques (i.e. patch-clamp technique), extracellular measurements have shown a few very important advantages: 1. the recording is not limited to one cell at a time. It is well suited for multi cell recordings in their native and intact form as well as tissue slices, 2. It allows long-term recordings, 3. Non-invasive and technically facile method [4,15,21].

The microelectrodes are capable to detect the changes in extracellular field potential which is caused by all the ionic flows across the cell membrane at a given moment. The record of the extracellular potential comprises all electrogenic cells which are positioned at the electrode surface and it decays with electrode-cell distance. As the number of cells, and thus the number of current point sources (ion channels) at the electrode surface is bigger, the recorded extracellular membrane potential increases as given by **Equation 4.1**. [14,22]:

$$V_e = \frac{1}{2\pi\sigma} \sum_{n=1}^N \frac{I_n}{r_n} \quad \text{Equation 4.1}$$

where:  $V_e$  is the extracellular membrane potential,  $r$  is the electrode-cell distance,  $I_n$  is the  $n^{\text{th}}$  individual point source (ion channel) current and  $\sigma$  is the conductivity of the medium.

**Figure 4.7** presents the comparison between intra- and extracellular recordings of electrical activity of Langerhans islets upon stimulation by 15 mM glucose. Two interesting features of extracellular recordings can be observed (**Figure 4.7a** and **b**): 1. The amplitude of recorded extracellular membrane potential is a few times higher for intracellular measurements. The same behavior was observed comparing with other electrogenic cells (i.e. neurons); 2. Extracellular recording of action potential showed negative deflection, in contrast to intracellular measurements [23].

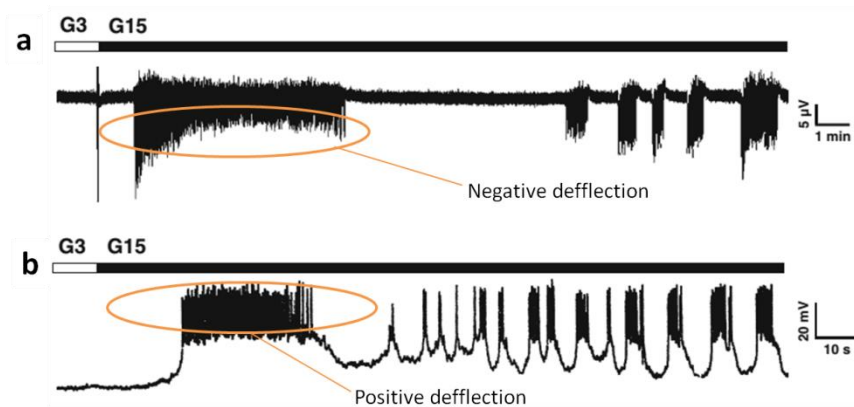


**Figure 4.7** Examples of extracellular (a) and intracellular (b) recordings of the membrane potential of pancreatic  $\beta$ -cells. The electrical activity (bursting) was induced by increasing the glucose concentration from 3mM to 15 mM.

## 4.2. Directed motion of charged objects in electric fields

During the years, different approaches have been developed regarding cell manipulation. Some of them are based on acoustic forces [24], common surface modifications using “adhesives” (such as proteins, poly-D-lysine, collagen etc.) [15,25], ultrasound [26], “optical-tweezers” [27,28] and electrical forces [28,29].

One of the most efficient methods that allow facile, precise and cheap manipulation of cells uses electrostatic forces. In general, methods based on electrical forces utilize the electrostatic interactions between charged objects (i.e. nanoparticles, cells) and a generated electric field. Those forces can be divided into two groups, which determine the final classification of available techniques as: 1. **Dielectrophoretic** or 2. **Electrophoretic**.

**Dielectrophoretic (DEP)** methods are based on the polarization of objects induced by non-uniform electric fields (**Figure 4.8a and b**). As a consequence, the non-uniform electric field forms a spatial gradient ( $\nabla E$ ) in which the particles with an induced charge are moving. The DEP force ( $F_{DEP}$ ) that governs the motion of the object is mainly dependent on its dipole moment ( $p$ ) and the intensity of the formed spatial gradient which can be quantitatively expressed as:  $F_{DEP} = \nabla E \cdot p$  (**Equation 4.1**) [30].

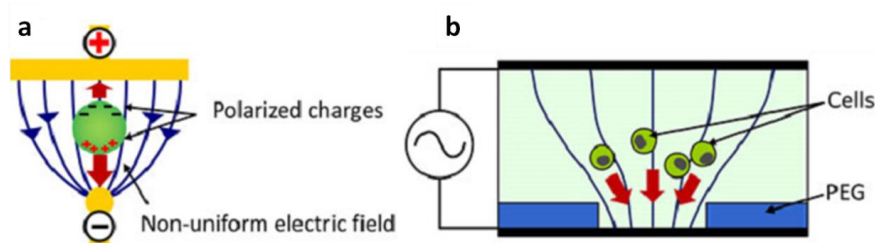


**Figure 4.8** (a) Schematic representation of the interaction between a non-uniform (positive DEP) electric field and a polarized particle. The polarized object moves towards the higher electric field region. (b) Representation of DEP patterning of an ITO array by means of cells motion in a non-uniform AC electric field [29].

To create non-uniform electric fields, alternating current (AC) is used rather than direct current (DC) in order to eliminate electrophoretic motion and to minimize electrochemical processes that occur at the electrode which could have an influence on maintaining the physiological conditions.

#### 4 – Guiding pancreatic $\beta$ -cells to target electrodes: towards a whole-cell biosensor for diabetes

---

The average DEP force in a linearly polarized sinusoidal field that acts upon a particle of given radius ( $r$ ) which is imposed by an AC field ( $E$ ) of angular frequency  $\omega$ , is given by **Equation 4.2**:

$$\langle F_{\text{DEP}} \rangle = 2\pi\epsilon_m r^3 \text{Re} [f_{\text{CM}}] \nabla |E(r)|^2 \quad \text{and} \quad f_{\text{CM}} = \frac{\epsilon_p^* - \epsilon_m^*}{\epsilon_p^* + 2\epsilon_m^*} \quad \text{Equation 4.2}$$

where,  $\epsilon_m$  is the electric permittivity of the medium, and  $\text{Re} [f_{\text{CM}}]$  is the real part of the Clausius – Mossoti (CM) factor. In the CM equation,  $\epsilon_p^*$  and  $\epsilon_m^*$  are complex permittivity of the particle and the medium, respectively, where each of them can be calculated as  $\epsilon^* = \epsilon - j \sigma / \omega$  ( $j = -1^{1/2}$  – imaginary unit,  $\sigma$  and  $\epsilon$  are conductivity and permittivity, respectively). Depending on  $\text{Re} [f_{\text{CM}}]$ , DEP can result either in motion of the particles up the field gradient (positive DEP) or in the opposite direction (negative DEP). If the particle (cell) is less polarizable than the medium then the  $\text{Re}[f_{\text{CM}}]$  will be positive and positive DEP will occur while for the inverse situation the particles will move down the electric field gradient [29,30].

In contrast to DEP, Electrophoresis arises from the interaction between the particle's inherent charge with a DC or AC generated field (**Figure 4.9**). The fact that the charged object can be easily moved towards the oppositely charged electrode, EP has found its application for the deposition of different materials such as colloidal crystals [31,32], nanosized zeolites [33], phosphor coating [34], biomaterials [35] etc.

Once the charged particles are dispersed in polar medium, the electrostatically directed adsorption of oppositely charged ions (counterions) takes place in order to counterbalance existing surface charge as shown in **Figure 4.9a**.

The region in the proximity of the particle's surface which, beside negatively charged counterions, contains also positive ions (surface-determining ions) is known as Stern layer. In the Stern layer, the concentration of counter ions and the electric potential decreases with the distance from the charged surface while the concentration of surface determining ions increases as a consequence of the electrostatic repulsion with the same sign charged surface. Outside this layer, the decrease in electric potential follows an exponential relation and at one point drops to zero. This point is marked as the border of the diffuse layer, which together with the Stern layer forms the total double layer (**Figures 4.9b** and **c**). When the electric field is applied, the motion of the particles towards the corresponding electrodes is associated with the motion of tightly bonded ions and solvent molecules. The plane which separates this tightly bonded layer from the bulk is called the slip (shear) plane. The electrical potential at the slip plane is known as zeta potential ( $\xi$ ) and it plays the most important role (beside viscosity) in the mobility of charged objects in an electric field [36,37].



#### 4 – Guiding pancreatic $\beta$ -cells to target electrodes: towards a whole-cell biosensor for diabetes

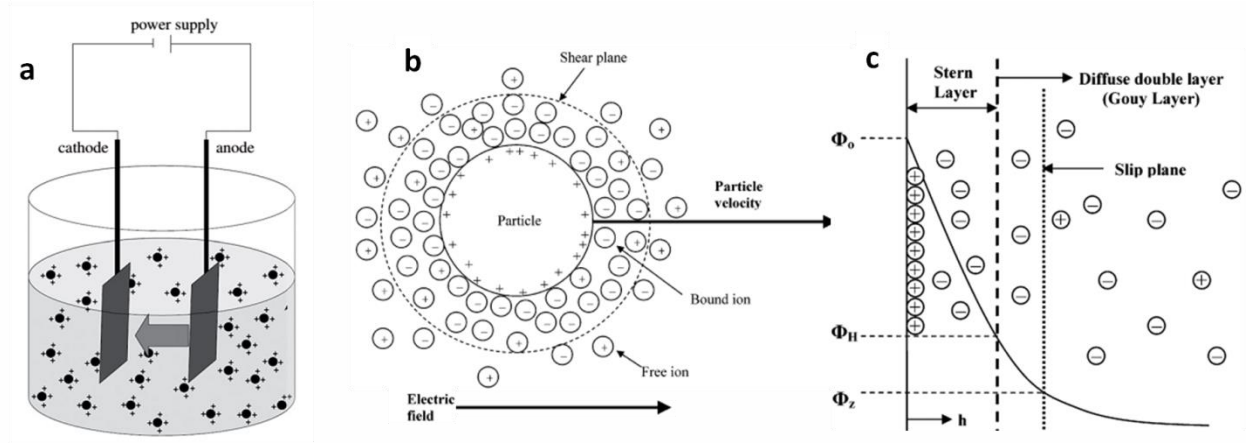


**Figure 4.9** (a) Schematic representation of the electrophoretic motion of positively charged particles in a DC electric field (adapted from [35]); (b) Structure of the electrical double layer around the positively charged particles with the demonstrated motion in the electric field; (c) Illustration of the electrical double layer and the variation of the electrical potential profile with the distance from the charged surface [36].

The parameters which have the greatest influence on the magnitude of zeta potential are: 1. ionic strength of the medium, 2. surface charge ( $Q$ ) and radius ( $r$ ) of particles, 3. dielectric constant of solvent ( $\epsilon$ ) and temperature ( $T$ ) as given by **Equation 4.3**.

$$\xi = \frac{Q}{4\pi\epsilon r(1+kr)}, \text{ and } k = \left( \frac{e^2 \sum n_i z_i^2}{\epsilon \epsilon_0 kT} \right)^{1/2} \quad \text{Equation 4.3}$$

where,  $\epsilon_0$  is dielectric constant of vacuum, Boltzmann's constant  $k$ , concentration  $n_i$  and charge of the ion  $z_i$  [36].

Another important parameter that has to be considered in order to quantitatively express the motion of charged objects in electric fields is their electrophoretic mobility. As shown by **Equation 4.4** electrophoretic mobility depends on zeta potential, the dielectric constant of the medium and its viscosity [36]:

$$\mu = \frac{2\epsilon_r \epsilon_0 \xi}{3\pi\eta} \quad \text{Equation 4.4}$$

Electrophoresis presents a useful method not only for deposition of different inorganic/organic materials but also for surface patterning with different cell types as well as for cell sorting. Cell motion upon an applied electric field arises from the fact that the cell membrane is anchored to and covered by glycocalyx (polyelectrolyte with a complex structure) [38]. Typically, glycocalyx is a dynamic network consisting of proteoglycans (conjugate of core protein on which a few glycosaminoglycan chains are linked), glycoproteins and glycosaminoglycans (**Figure 4.10**).



#### 4 – Guiding pancreatic $\beta$ -cells to target electrodes: towards a whole-cell biosensor for diabetes

---

Since it is a dynamic system, glycocalyx is in close interaction with its environment (i.e. blood). This has a great influence on its composition and thickness which on average scales from 7 nm (erythrocytes) to 30 nm (endothelial cells) in depth [38,39]. Due to the deprotonation of glycosaminoglycan residues at physiological pH, most of the cells exhibit negative charge and thus can be manipulated in electric fields [38,40].

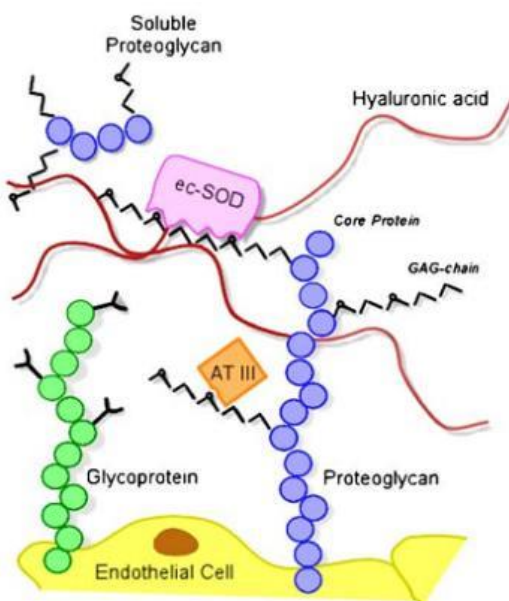


**Figure 4.10** Schematic representation of cellular (endothelial cells) glycocalyx where the proteoglycans with long unbranched glycosaminoglycan (GAG-chane) side-chaines and glycoproteins are bound to the cell membrane. Besides the bound components, the present glycocalyx contains some soluble components such as hyaluronic acid, soluble proteoglycans and various proteins (extracellular superoxide dismutase (ec-SOD) and antithrombin III (AT III)) [39].

#### 4.3. Guiding pancreatic $\beta$ -cells to target electrodes

*(Following results have been obtained through a collaboration with the group of Prof. Jochen Lang (CNRS – Institut de Chimie et Biologie des Membranes et des Nano-objets, Allée Geoffroy Saint-Hilaire, Pessac, France)*

As mentioned previously, MEAs present a very good alternative for recording extracellular electrical activity of pancreatic beta cells. They also present a candidate that can be used as a platform for the development of whole-cell based glucose biosensors [4,41] whose sensing properties rely on the glucose dependent electrical activity of beta-cells.

#### ***4 – Guiding pancreatic $\beta$ -cells to target electrodes: towards a whole-cell biosensor for diabetes***

---

The cells respond to glucose concentration fast which is manifested in a change of frequency of recorded signals [17,23]. Beside the robustness, the extracellular signals are not only dependent on glucose concentration, but also on other factors such as circulating hormones, lipids and certain amino-acids [41].

Compared to commercial biosensors, such multi-sensing properties of pancreatic beta cells already present the main advantage of whole-cell based biosensors. Besides that, this type of sensors can be used in the near future for rapid quality assessment of beta-cells prior to pancreatic islet transplantation.

The quality of the recorded extracellular signal and thus the sensor performances are mainly dependent on the number of cells at the electrode surface and the cell-electrode interaction. Keeping that in mind, as well as the fact that human islets are rare and valuable, the first step in developing an analytical platform based on the activity of beta-cells would be to decrease the number required for such a purpose. Therefore, a method allowing the manipulation of beta cells in a reproducible manner is necessary.

Taking advantage of the cell mobility in an applied electric field, electrophoresis presents a useful, fast and facile method which can be implemented in MEAs in order to direct the cells towards the surface of the microelectrodes.

Prior to the electrophoretic manipulation of model systems (polystyrene beads (PS)) and pancreatic beta cells, the optimal configuration for applying an electric field has to be determined. This can be done by modeling (using COMSOL Multiphysics software), based on solving the set of equations for a proposed electrode configuration in which the electric field is produced by applying an electric potential difference between microelectrodes. As can be seen from Figure 4.11, the present strategy is based on the use of oppositely polarized neighbouring electrodes. Regarding the map, the electric field steeply decays in the area between the electrodes with the same polarity (blue areas). Based on those results, it can be expected that the charged objects are moving faster closer to the electrode due to the attraction forces caused by the increasing electric field strength.

#### 4 – Guiding pancreatic $\beta$ -cells to target electrodes: towards a whole-cell biosensor for diabetes

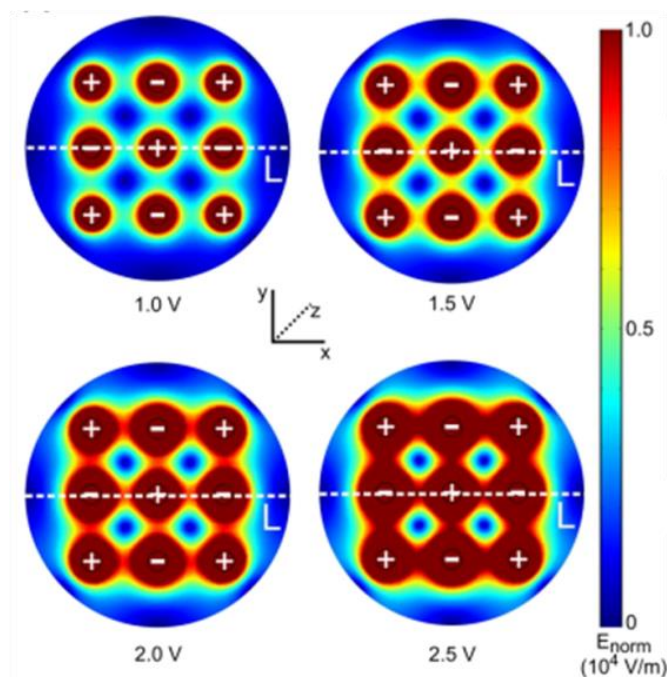


**Figure 4.11** The map of the electric field generated in a MEA system obtained by computational modeling. The application of different potentials (1.0 V, 1.5 V, 2.0 V and 2.5 V) between the neighboring electrodes leads to an increase of electric field between oppositely charged microelectrodes.

In order to demonstrate the effectiveness of the generated electric field with respect to the electrophoretic manipulation of charged objects, negatively charged PS beads ( $\phi = 10 \mu\text{m}$ ) suspended in low conductivity buffer (280 mOsm/l and a conductivity of  $0.01 \text{ mS cm}^{-1}$ ) have been loaded in a Pt-MEA chamber ( $d_{\text{microelectrodes}} = 30 \mu\text{m}$ ). The measurement of zeta potential (Zetasizer Nano ZS apparatus) presented in **Figure 4.12a**, showed that polystyrene beads are a good model system since they exhibit strong negative charge due to the sulfonate groups present on their surface [42]. By applying a potential of 2.5 V for 10 min the motion of PS beads was successfully directed towards the positively charged electrodes where the beads settled down.

#### 4 – Guiding pancreatic $\beta$ -cells to target electrodes: towards a whole-cell biosensor for diabetes

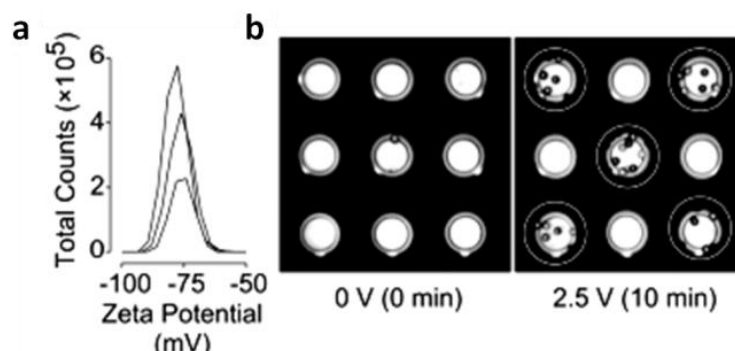


**Figure 4.12** (a) Measurement of zeta potential indicates strong negative surface charge ( $\xi = -76.6 \pm 1.5$  mV) of sulfonated PS beads. The measurement has been performed in a custom-designed low-conductivity buffer (5 mM HEPES (4-(2-hydroxyethyl)-1-piperazineethanesulfonic acid), 270 mM manitol and 5 mM glucose); (b) Comparative microscope images of a commercial platinum based MEA (MEA60-4Well-Pt (Qwane Biosciences SA, Lausanne, Switzerland),  $d_{\text{(electrode)}} = 40 \mu\text{m}$ ) at different times. By applying a potential difference of 2.5 V in between neighbouring micro-electrodes. The motion of suspended PS beads is directed towards the positively charged electrodes (indicated by white rings). After 10 min the PS beads are gathered on the positive electrodes and completely repelled from the negatively charged ones. The electrochemical system was consisting of alternating positively (working electrodes) and negatively (reference electrodes short-circuited with counter electrode) polarized micro-electrodes.

Similar to negatively charged PS beads,  $\beta$ -cells (clonal or original) as well as their clusters (i.e. Langerhans islets) are expected to show the same behavior due to the negatively charged glycocalyx present on the surface of their membrane. Due to the smaller value for the zeta potential of clonal INS832/13  $\beta$ -cells (**Figure 4.13a**) compared to PS beads ( $\xi = -76.6$  mV), it is reasonable to expect a smaller electrophoretic mobility once the electric field is applied. **Figure 4.13b** presents the time laps images showing the gradual migration of the cells towards positively polarized electrodes (labeled by white circles). The cells start to gather around the microelectrodes already 60 s after the exposure to the electric field generated by 1.5 V. It is obvious that cell clusters are formed on top of the electrode surface after 10 min.

#### 4 – Guiding pancreatic $\beta$ -cells to target electrodes: towards a whole-cell biosensor for diabetes

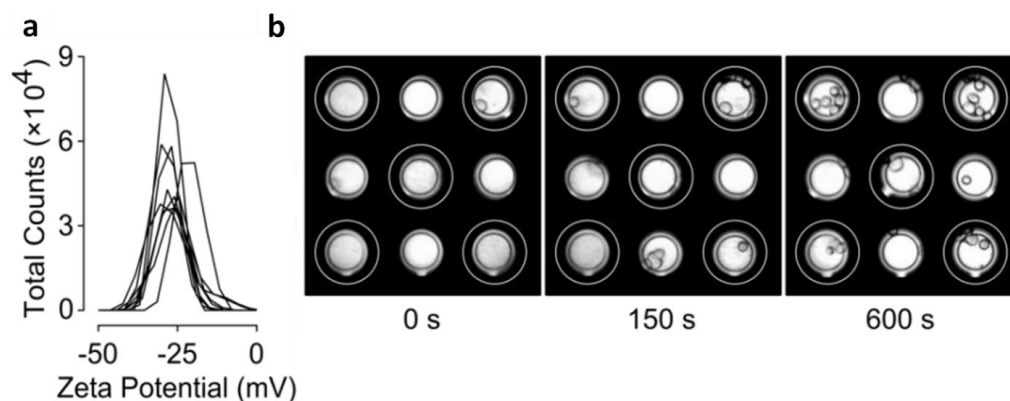


**Figure 4.13** (a) Measurement of zeta potential of clonal INS832/13  $\beta$ -cells show that the cells exhibit negative surface charge, expressed by the negative zeta potential of  $-27 \pm 1.4$  mV; (b) Time laps images showing the progressive electrophoretic migration of insulinoma (INS832/13)  $\beta$ -cells upon applying the electric field in between neighbouring Pt micro-electrodes ( $\varnothing = 40$   $\mu$ m). As expected, INS cells were migrating towards positively charged electrodes (indicated by white rings). The experiment has been performed in a custom-designed low-conductivity buffer by using a three electrode system that was consisting of alternating positively (working electrodes) and negatively (reference electrodes short-circuited with counter electrode) polarized micro-electrodes.

In order to determine the smallest electrode potential which is sufficient enough to induce migration of the cells towards positively charged electrodes, clonal INS832/13 cells were loaded in a MEA chamber, and different potentials (0 V, 1.0 V, 1.5 V, 2.0 V and 2.5 V) were applied for 10 min. **Figure 4.14a** depicts a gradual increase in number of cells that were attracted by the positively charged micro-electrodes as the imposed potential is increasing while at the same time being repelled from the negatively polarized ones. This trend can be better illustrated by plotting the number of cells at the electrode surface as a function of applied potential (**Figure 4.14b**).

As it can be seen from the number of cells counted on positively and negatively charged electrodes, the application of 1.0 V resulted in a two times higher number of cells at the positive electrodes compared to negative ones. A further increase of applied potential led to the increase of this ratio until 2.0 V where the negatively polarized electrodes became nearly bare.

#### 4 – Guiding pancreatic $\beta$ -cells to target electrodes: towards a whole-cell biosensor for diabetes

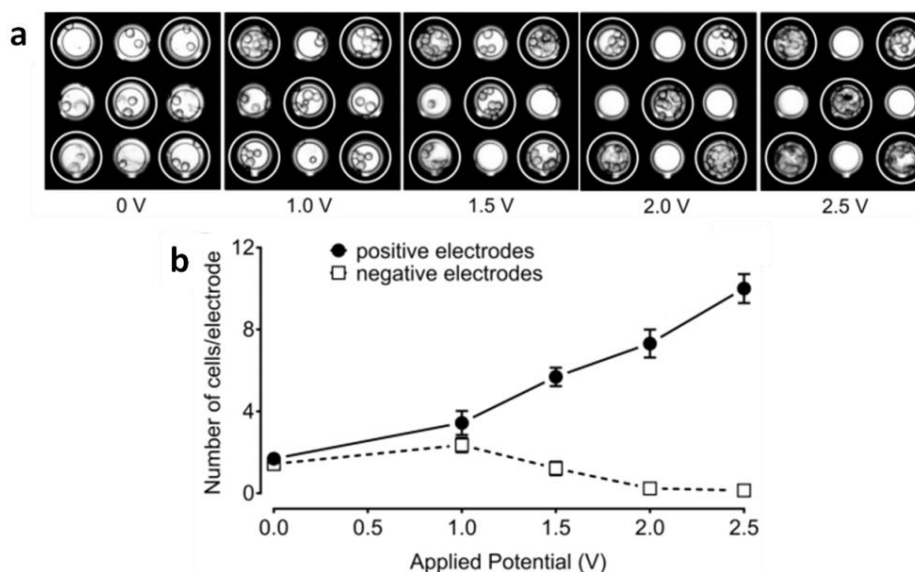


**Figure 4.14** (a) Microscopic images of a MEA ( $d_{\text{electrode}} = 40 \mu\text{m}$ ) with a loaded suspension of INS832/13 cells upon the gradual increase of applied electrode potential (0.0 V, 1.0 V, 1.5 V, 2.0 V and 2.5 V) where positively charged electrodes are indicated by white rings. Prior to application of the electric field INS832/13 cells have been suspended in low-conductivity buffer; (b) Graphical representation of number of INS832/13 cells at positively and negatively polarized electrodes for a given electrode potential.

Beside the fact that strong electric fields are necessary to induce efficient electrophoretic migration of the cells, it is nevertheless important to optimize the strength in order to prevent damage of the cells which would influence their viability and electrical activity. **Figures 4.15a** and **b** present inverted microscope images of INS832/13 (positioned around the microelectrodes) cultured for 3 days in culturing medium (CMRL1066 culturing medium - Invitrogen), after potentials of 1.5 V and 2.0 V were applied for 10 min. It can be seen that cells exposed to 1.5 V kept their intact (stretched) morphology which was observed for the control probe (at 0 V). This indicates that the cell membrane and thus the cell viability are not damaged by the applied electric field. However, it is notable that 2.0 V was detrimental for the cells, causing membrane blebbing, decreasing the adherence of the cells and their proliferation rate.

#### 4 – Guiding pancreatic $\beta$ -cells to target electrodes: towards a whole-cell biosensor for diabetes

---

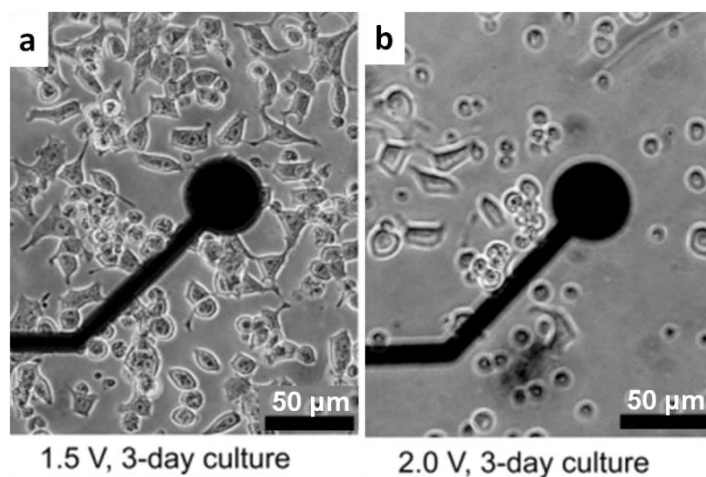


**Figure 4.15** An inverse microscope image of INS832/13 cells obtained after 3 days of culturing in 11 mM glucose solution as described in Ref. [43]. The cells were exposed to 1.5 V (a) and 2.0 V (b) for 10 minutes.

The electrophoretic migration presents a possibility not only for surface patterning with single  $\beta$ -cells but also it can be applied to bigger systems such as cell-assemblies that comprise other pancreatic cell types. The Langerhans islets are known to be less robust systems, more sensitive to the stress compared to  $\beta$ -cells, and therefore the applied electric field may have a big influence on their behavior and integrity. The semi-natural assembly of endocrinal pancreatic cells (i.e. dissociated islets) presents a good alternative to whole islets and it can be used for studying their electrophoretic behavior in a MEA system. Dissociated murine islets dispersed in low conductivity buffer were loaded in a MEA chamber and different potentials were applied to generate an electric field. **Figure 4.16** illustrates the MEA after applying 0 V, 1.0 V, 1.5 V and 2.0 V for 10 min. Similar to INS cells, in the absence of electric field between neighboring electrodes, the surface coverage of all electrodes was comparable as graphically shown in **Figure 4.16b**. Upon application of 1.0 V, cell coverage of positively polarized electrodes increased by a factor 2.66 and continued to increase at a rate of 2 dissociated islets per electrode per V when the potential was further increased. In the case of the negatively charged electrodes the rate of decrease was -0.2 dissociated islets per electrode per V.

As additional proof of principle, dissociated murine islets were loaded into a MEA chamber and potential of 2 V was applied. Once the dissociated islets were aligned with an electrode surface (approximately 1 min.) the polarity of the electrodes was reversed. As it can be expected, most of “pseudo” islets migrated in the opposite direction which proves that the presence cells on the electrode surface was due to the applied electric field (**Figure 4.16c**).



#### 4 – Guiding pancreatic $\beta$ -cells to target electrodes: towards a whole-cell biosensor for diabetes

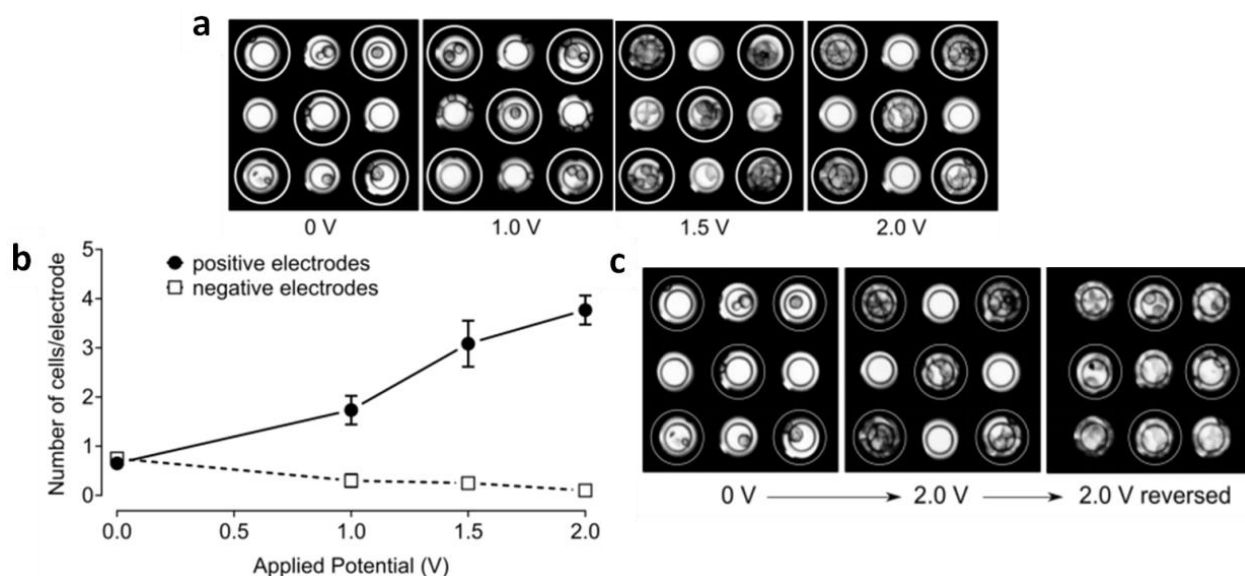


Figure 4.16 (a) Microscope images of MEAs ( $d_{\text{(electrode)}} = 30 \mu\text{m}$ ) covered by dissociated murine islet cells, recorded after the electrodes were polarized at different potentials for 10 min: 0 V, 1.0 V, 1.5 V and 2.0 V. Positively charged electrodes are indicated by white circles. The electrophoretic migration of mouse islet cells was performed in a low conductivity buffer.; (b) Graphical representation of the number of dissociated islets that are covering the microelectrodes upon the application of increasing potential; (c) Reversibility of electrophoretic migration of dissociated murine islets once the polarity of the electrodes is reversed.

Besides the microscopic imaging of cells that have been electrophoretically deposited (**Figure 4.15**) onto the surface of targeted micro-electrodes, another technique is required in order to test cell viability in a more quantitative way. This can be done by recording electrical activity of beta cells after the application of electric field. Affected by an increase in glucose concentration, beta cells are exhibiting their normal electrical activity which is characterized by a low-frequency signal, termed as a slow potentials [21]. Slow potentials are an integral part of the electrical signal of beta cells and can be isolated by using appropriate band-pass filter (0.2-2 Hz). **Figure 4.17a** depicts a record of electrical activity (slow potentials) of murine islet  $\beta$ -cells that have been electrophoretically deposited on an electrode surface by applying 1 V for 3 min. In the following step, cells (control group and electrophoretically treated) were cultured on the MEA for 3 days and their slow-wave potentials were recorded. This cell culture period was sufficient to ensure good cell adhesion and gap-junction formation between neighboring  $\beta$ -cells. The latter one arises from a linkage formation between the cells, just like in the case of intact islets [21]. It can be observed that the slow potentials have small amplitude or are totally absent ( $0.018 \pm 0.005$  Hz) when the cells are stimulated by 3 mM glucose (**Figure 4.17a**) solution and quickly raised ( $0.360 \pm 0.015$  Hz) when 15 mM glucose (**Figure 4.17b**) was used as a stimulus. Those values did not significantly differ from the control experiment ( $f_{(3\text{mM})} = 0.016 \pm 0.005$  Hz and  $f_{(15\text{mM})} = 0.369 \pm 0.015$  Hz) and therefore it can be concluded that the cells retained their viability and thus their discriminatory response to the change of glucose concentration.



#### 4 – Guiding pancreatic $\beta$ -cells to target electrodes: towards a whole-cell biosensor for diabetes

In addition, the influence of the stress hormone adrenaline (5  $\mu$ M) and the antidiabetic sulphonyl urea glibenclamide (100 nM) was examined. As it can be seen from **Figure 4.17c** and **d**, the addition of adrenaline suppressed the slow potentials, while the glibenclamide showed the opposite effect, as it has already been reported by other authors [21]. This is an additional proof that the  $\beta$ -cells did not lose their ability to react to the presence of drugs and hormones. This imposes the conclusion that electrophoresis under moderate conditions does not affect their viability and sensing properties. This is confirmed by the comparison of the slow wave frequency of the treated cells with the control population (**Figure 4.17e**).

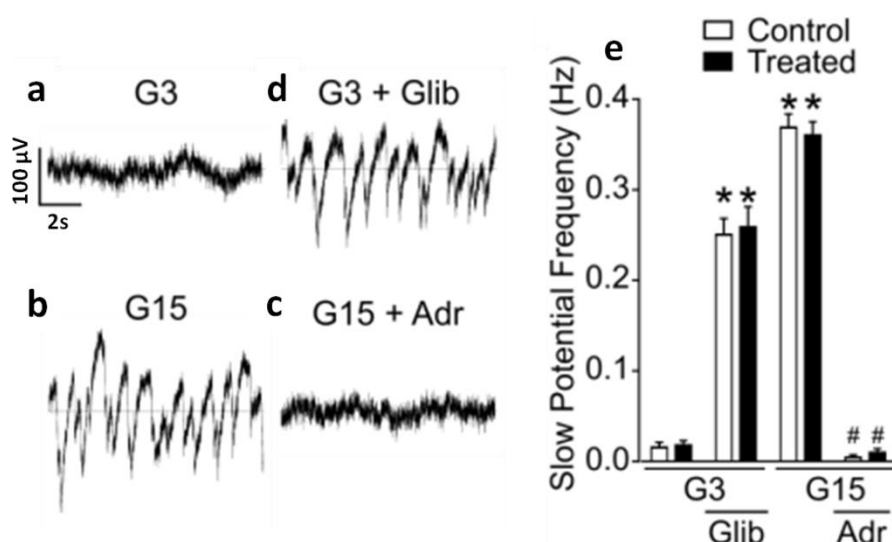


**Figure 4.17** Electrical activity of control and electrophoretically treated murine islet  $\beta$ -cells after 3 days of culturing on a MEA. (a) Slow-wave potential records in 3 mM (G3) glucose and subsequent stimulation with glibenclamide (d); (b) electrical activity in 15 mM (G15) glucose solution with an abolished electrical activity caused by adding adrenaline (c); (e) Graphical representation of the dependence of slow potential frequency for control (white bars,  $n=29$  electrodes) and electrophoresed cells (black bars,  $n=24$  electrodes) on changes in the cell environment (different glucose concentration and addition of glibenclamide (Glib) and adrenaline (Adr)). Simultaneous analog data were acquired at 10 kHz per electrode using a MEA1060-InvBC-Standard amplifier (Multichannel Systems; gain: 1100; analog filter: 0.1–3000 Hz). Recordings of extracellular membrane potentials have been performed at 37 °C in a physiological buffer containing: 135 mM NaCl, 4.8 mM KCl, 1.2 mM  $MgCl_2$ , 1.2 or 1.8 mM  $CaCl_2$ , 10 mM HEPES and glucose as indicated (pH of 7.4 has been adjusted with NaOH).

The possibility of electrophoretic manipulation of whole Langerhans islets has been investigated. However, under the same applied voltages that have been used to manipulate the  $\beta$ -cells, no significant motion of islets was observed. This is probably due to the fact that the islets are assemblies of 1000-3000 cells [4] and consequently this increase in size changes drastically the electrophoretic mobility.

## **Literature**

- [1] A. Alwan, Global Status Report on Noncommunicable Diseases, World Health Organization, Geneva (Switzerland), 2010.
- [2] Shanthi Mendis, Global Status Report On Noncommunicable Diseases 2014, World Health Organization, Geneva, 2014.
- [3] World Health Organisation, Diabetes Action Now: An Initiative of the World Health Organization and the International Diabetes Federation, World Health Organization, Geneva, 2004.
- [4] M. Raoux, G. Bontorin, Y. Bornat, J. Lang, S. Renaud, Biohybrid Systems: Nerves, Interfaces, and Machines (first edition), Wiley-VCH, Berlin, 2011.
- [5] Nch, Type 1 Diabetes Diagnosis and Management of Type 1 and Young People, NICE, 2009.
- [6] World Health Organization - Department of Noncommunicable Disease Surveillance, (1999).
- [7] N.C.C. for W. and C. Health, Diabetes in Pregnancy: Management of Diabetes and Its Complications from Preconception to the Postnatal Period, RCOG Press at the Royal College of Obstetricians and Gynaecologists, London, 2008.
- [8] M. Skelin, M. Rupnik, A. Cencic, ALTEX 27 (2010) 105.
- [9] J. Gromada, I. Franklin, C.B. Wollheim, Endocr. Rev. 28 (2007) 84.
- [10] S. Barg, J. Galvanovskis, S.O. Göpel, P. Rorsman, L. Eliasson, Diabetes 49 (2000) 1500.
- [11] P.E. MacDonald, J.W. Joseph, P. Rorsman, Philos. Trans. R. Soc. London B Biol. Sci. 360 (2005) 2211.
- [12] P.M. Dean, E.K. Matthews, Nature 219 (1968) 389.
- [13] H.P. Meissner, H. Schmelz, Pflügers Arch. 351 (1974) 195.
- [14] M.E.J. Obien, K. Deligkaris, T. Bullmann, D.J. Bakkum, U. Frey, Front. Neurosci. 8 (2015) 1.
- [15] I.L. Jones, P. Livi, M.K. Lewandowska, M. Fiscella, B. Roscic, A. Hierlemann, Anal. Bioanal. Chem. 399 (2011) 2313.
- [16] a S. Rajan, L. Aguilar-Bryan, D. a Nelson, G.C. Yaney, W.H. Hsu, D.L. Kunze, a E. Boyd, Diabetes Care 13 (1990) 340.
- [17] F.M. Ashcroft, P. Rorsman, Prog. Biophys. Mol. Biol. 54 (1989) 87.
- [18] J. Berg, J. Tymoczko, L. Stryer, Biochemistry, 5<sup>th</sup> edition, W. H. Freeman and Company and Sumanas Inc., New York, 2002.
- [19] P. Rorsman, Diabetologia 40 (1997) 487.
- [20] P. Rorsman, E. Renström, Diabetologia 46 (2003) 1029.
- [21] F. Lebreton, A. Pirog, I. Belouah, D. Bosco, T. Berney, P. Meda, Y. Bornat, B. Catargi, S. Renaud, M. Raoux, J. Lang, Diabetologia, 58 (2015) 1291.
- [22] G. Buzsáki, C.A. Anastassiou, C. Koch, Nat Rev Neurosci 13 (2012) 407.
- [23] T. Pfeiffer, U. Kraushaar, M. Düfer, S. Schönecker, D. Haspel, E. Günther, G. Drews, P. Krippeit-Drews, Pflügers Arch. Eur. J. Physiol. 462 (2011) 835.
- [24] T. Franke, S. Braunmüller, L. Schmid, A. Wixforth, D.A. Weitz, Lab Chip 10 (2010) 789.
- [25] P.C. Gach, P.J. Attayek, R.L. Whittlesey, J.J. Yeh, N.L. Allbritton, Biosens. Bioelectron. 54 (2014) 476.

#### ***4 – Guiding pancreatic $\beta$ -cells to target electrodes: towards a whole-cell biosensor for diabetes***

---

- [26] H. Mulvana, S. Cochran, M. Hill, *Adv. Drug Deliv. Rev.* 65 (2013) 1600.
- [27] M.M. Wang, E. Tu, D.E. Raymond, J.M. Yang, H. Zhang, N. Hagen, B. Dees, E.M. Mercer, A.H. Forster, I. Kariv, P.J. Marchand, W.F. Butler, *Nat Biotech* 23 (2005) 83.
- [28] M. Ozkan, T. Pisanic, J. Scheel, C. Barlow, S. Esener, S.N. Bhatia, *Langmuir* 19 (2003) 1532.
- [29] H. Tsutsui, E. Yu, S. Marquina, B. Valamehr, I. Wong, H. Wu, C.-M. Ho, *Ann. Biomed. Eng.* 38 (2010) 3777.
- [30] J. Voldman, *Annu. Rev. Biomed. Eng.* 8 (2006) 425.
- [31] R.C. Hayward, D.A. Saville, I.A. Aksay, *Nature* 404 (2000) 56.
- [32] M. Holgado, F. García-Santamaría, A. Blanco, M. Ibisate, A. Cintas, H. Míguez, C.J. Serna, C. Molpeceres, J. Requena, A. Mifsud, F. Meseguer, C. López, *Langmuir* 15 (1999) 4701.
- [33] W. Shan, *Microporous Mesoporous Mater.* 69 (2004) 35.
- [34] J. Yum, S.-Y. Seo, S. Lee, Y.-E. Sung, *J. Electrochem. Soc.* 150 (2003) H47.
- [35] A.R. Boccaccini, S. Keim, R. Ma, Y. Li, I. Zhitomirsky, *J. R. Soc. Interface* 7 (2010) S581.
- [36] Cao, J. *Phys. Chem. B* 108 (2004) 19921.
- [37] M. Ammam, *Biosens. Bioelectron.* 58 (2014) 121.
- [38] J.N. Mehrishi, J. Bauer, *Electrophoresis* 23 (2002) 1984.
- [39] S. Reitsma, D. Slaaf, H. Vink, M.M.J. van Zandvoort, M.A. oude Egbrink, *Pflügers Arch. - Eur. J. Physiol.* 454 (2007) 345.
- [40] M.P.I. Vandamme, J. Tiglias, N. Nemat, B.N. Preston, *Anal. Biochem.* 223 (1994) 62.
- [41] Y. Bornat, M. Raoux, Y. Boutaib, F. Morin, G. Charpentier, J. Lang, S. Renaud, *Electronic Design, Test and Application, 2010. DELTA '10. Fifth IEEE International Symposium*, (2010) 233
- [42] C. Burkhardt, K. Fuchsberger, W. Nisch, M. Stelzle, *Lithography (edited by Michael Wang), InTech - Croatia*, (2010) 629.
- [43] M. Dubois, P. Vacher, B. Roger, D. Huyghe, B. Vandewalle, J. Kerr-Conte, F. Pattou, N. Moustaid-Moussa, J. Lang, *Endocrinology* 148 (2007) 1605.

---

## EXPERIMENTAL SECTION

## Colloidal crystals: Assembly and characterization

### 1. Synthesis and covalent modification of silica particles

Silica nanoparticles have been synthesized using the well-known Stöber method based on a hydrolysis of tetraethylorthosilicate (TEOS; Sigma-Aldrich) in basic solution and polycondensation of the formed silicate acid.

The synthesized silica nanoparticles have been covalently functionalized using a coupling reaction with 3-aminopropyltriethoxysilane (APTES; 99.5% wt., Sigma-Aldrich).

#### 1.1 Synthesis of silica nanoparticles

The synthesis of silica beads has been performed in a two-step procedure at room temperature by controlled addition of TEOS-absolute ethanol (Sigma-Aldrich) mixture (i.e. synthesis mixture), using a single-syringe pump system, into a three-necked flask that contained an absolute ethanol-water-ammonia (25% wt.) solution (i.e. hydrolyzing solution). The set-up was equipped with a magnetic stirrer and a refrigerator.

#### First step – synthesis of 300 nm silica “seeds”

Silica seeds were prepared by adding TEOS directly in the hydrolyzing solution. The experimental conditions are listed in **Table 1**:

Data	Value
<b>V ( TEOS)</b>	10 ml
Hydrolyzing solution:	
<b>V (ammonia)</b>	30 ml
<b>V (abs. ethanol)</b>	200 ml
<b>V (water)</b>	50 ml
<b>Speed of addition of the solution</b>	TEOS was added at once in the hydrolyzing solution
<b>Time of synthesis</b>	2 h 30 min.
<b>Speed of mixing</b>	300 rpm
<b>Final diameter of synthesized silica nanoparticles</b>	300 nm (the diameter of colloidal particles has been measured by SEM)

**Table 2.** Experimental condition for the synthesis of 300 nm silica “seeds” (first step).

### **Second step – synthesis of 600 nm silica particles from 300 nm silica “seeds”**

The pre-synthesized 300 nm silica beads were used as seeds for the synthesis of 600 nm silica particles (second step). Experimental conditions are shown in **Table 2**. The excess of ammonia present in the suspension of 300 nm seeds was sufficient enough to hydrolyze the TEOS that has been added in the second step of synthesis.

Data	Value
<b>V (suspension of 300 nm silica beads)</b>	181 ml
Synthesis solution:	
<b>V (TEOS)</b>	45 ml
<b>V(abs. ethanol)</b>	45 ml
Hydrolyzing solution:	181 ml of the suspension of 300 nm silica seeds
<b>Speed of addition of the solution</b>	8 ml/h
<b>Time of synthesis after the synthesis solution was added</b>	12h
<b>Speed of mixing</b>	300 rpm
<b>Final diameter of synthesized silica particles</b>	600 nm (the diameter of colloidal particles has been measured by SEM)

**Table 3.** Experimental condition for the synthesis of 600 nm silica particles from 300 nm silica “seeds”.

### **1.2 Covalent functionalization of silica nanoparticles**

The surface of silica particles has been covalently modified with APTES.

The amount of added APTES was 10 times larger than the calculated value in order to ensure a good surface coverage of the silica beads.

APTES was added to the original post synthetic mixture that contains the silica nanoparticles. The mixture was stirred over night and heated the next day at 80 °C for 1h to ensure a good covalent binding of APTES.

Calculation of the sufficient amount of APTES is based on the geometrical consideration that 2 APTES molecules cover 1 nm<sup>2</sup> of the surface of silica particles and that the density of silica beads is 2.2 g/cm<sup>3</sup>.

**Calculation of the amount of APTES that has to be added for the covalent functionalization of the entire silica particle surface:**

$$\rho \text{ (silica)} = 2.2 \text{ g/cm}^3$$

$$d \text{ (one sphere)} = 600 \text{ nm}$$

$$V \text{ (one sphere)} = \frac{4}{3}r^3\pi$$

$$m \text{ (one sphere)} = V \cdot \rho$$

$$\text{Number of spheres per gram of silica} = \frac{1 \text{ g}}{m \text{ (one sphere)}}$$

$$\text{Area of one sphere} = 4r^2\pi$$

$$\text{Surface area per gram of silica spheres} = \text{Area of one sphere} \cdot \text{Number of spheres per gram of silica}$$

$$\text{Number of APTES molecules} = \text{Surface area per gram of silica spheres [nm]} \cdot 2 \text{ molecules per nm}$$

$$n(\text{APTES}) = N/N_A$$

$$V(\text{APTES}) = 10 \cdot [n \cdot M(\text{APTES}) / \rho(\text{APTES})]$$

**1.3 Purification of covalently modified silica nanoparticles**

Functionalized silica nanobeads were purified by rinsing with MilliQ water 10 times. Each rinsing cycle is followed by centrifugation in order to separate the supernatant from the bulk. Additionally, beads were purified using dialysis (Cellu Sep, membrane T1, Nominal MWCO: 3500) against MilliQ water in three separate segments. During the first two dialysis cycles MilliQ water was changed after 2 h, while for the last one the dialysis was carried-out over night.

**Fabrication of colloidal-crystal template**

Colloidal crystal templates have been prepared using the Langmuir-Blodgett technique based on the assembly of covalently functionalized silica nanoparticles at an air/water interface.

**1.4 Cleaning of silica nanoparticles**

Silica nanoparticles ( $d = 600 \text{ nm}$ ), used for the synthesis of the Langmuir film, were previously sonicated for 10 minutes in order to avoid aggregation. In the following step, silica beads were washed 5 times with absolute ethanol and centrifuged each time to separate the supernatant from the nanoparticle deposit.

Between two consecutive washing steps, silica nanoparticles were sonicated for a few minutes in order to enhance the washing procedure and disperse them in the bulk.

### **1.5 Resuspension of silica nanoparticles**

After completion of the washing procedure, silica nanoparticles were redispersed in an ethanol-chloroform mixture (20% v/v - 80% v/v respectively). The solvents were added separately. The redispersion of silica beads after adding each solvent was followed by 5 min of sonication. Freshly prepared suspensions of silica nanoparticles were immediately used for the preparation of the Langmuir-Blodgett film.

### **1.6 Preparation of Langmuir- Blodgett (LB) films**

The compression of a monolayer of nanoparticles has been carried out on LB trough (NIMA, type: 622).

The Teflon-coated surface of the apparatus as well as the surface of the moveable barriers was cleaned with dichloromethane.

The apparatus was filled with MilliQ water and dust contaminations were sucked-out by a water pump. The suspension of silica nanoparticles was added onto the pre-cleaned water surface drop by drop with an interval of a few seconds between two consecutive additions.

The substrates to be modified were attached to the dipping mechanism of the LB trough.

Parameter	Value
<b>Targeted surface tension</b>	8 mN/m
<b>Speed up</b>	1 mm/min
<b>Speed down</b>	63 mm/min
<b>Barrier speed</b>	29 cm <sup>2</sup> /min
<b>Programmed number of layers</b>	30

**Table 4.** Parameters for the compression of a 600 nm silica based Langmuir film.



## **Development of coaxial macroporous electrode architectures by infiltration of colloidal crystals**

The device consisted of two cylindrical macroporous electrodes - the inner (macroporous gold microwire) and outer (mechanically stabilized macroporous film) electrodes. Both electrodes were prepared independently and the final device (which comprises both electrodes) was assembled in the last step of the fabrication.

### **2. Preparation of inner electrode and outer electrodes (procedure based on the glass capillary approach)**

#### **2.1 Preparation of the samples**

A gold microwire ( $d = 250\ \mu\text{m}$ , AlfaAesar, purity 99.9%) was cut into 5 cm long pieces that were straighten by slight rolling between two microscope glass slides.

TLC glass capillaries (HIRCHMANN® LABORGERATE) were cut into 7 cm long pieces.

##### **2.1.1 Cleaning and hydrophilisation of the samples**

In order to clean and hydrophilize the samples, gold microwires were immersed into “Piranha” solution (prepared by mixing concentrated sulfuric acid (98% wt., Sigma Aldrich) with concentrated Hydrogen peroxide (30% wt., Sigma Aldrich) in volumetric ratio 75% v/v-25% v/v. ) two times for 10 minutes and subsequently rinsed with MilliQ water.

Additionally, cleaned gold microwires were hydrophilized using UV/O<sub>3</sub> cleaner (UVOCS®, PA - USA) for 20 min just before deposition of the silica particles (see subsection 4.3.).

Prior to the “Piranha” treatments, glass capillaries were degreased by 15 min sonication in chloroform.

After the cleaning step, samples have been rinsed with MilliQ water a few times and dried with compressed air.

## 2.2 Electroless metallization of glass capillaries

The degreased and pre-cleaned glass capillaries have to be metalized by a thin silver coating. The metallization is based on the well known reduction of diamminesilver(I) ions by glucose in the presence of anionic surfactant (sodium-dodecylsulphonate (SDS)).

The composition and the procedure for the preparation of diamminesilver(I) reagent (i.e. Tollens' reagent) is given in **Table 1**.

Compound	Concentration	Volume/Mass
Silver-nitrate (AlfaAesar®)	0.1M	70 ml
Sodium-hydroxide (Sigma-Aldrich)	1M	Added in drops into silver-nitrate until the precipitation of Ag <sub>2</sub> O occurred
Ammonia (Acros)	25 % wt.	Added in drops until the Ag <sub>2</sub> O was completely dissolved
SDS (Sigma-Aldrich)	Added as solid for a final concentration of 20 mM*	520 mg
Glucose (Sigma-Aldrich)	20 % wt.	20 ml

\*The first three compounds were mixed as described, and SDS was added to the pre-measured 70 ml of the obtained mixture. After adding SDS the mixture was stirred until the SDS was completely dissolved.

**Table 1.** Composition of the solution used for electroless silver metallization of glass capillaries. The components used for the preparation of Tollens' reagent are denoted in blue color.

The glass capillaries were immersed in Tollens' solution which was pre-heated up to 70 °C. In the following step, the glucose solution was added at once and both components were shortly mixed by magnet stirrer.

After 3 min the metallization was complete and the metalized glass capillaries were firmly rinsed with MilliQ water.

Metalized glass capillaries were used straight away for the deposition of silica particles by the Langmuir-Blodgett technique.

## **2.3 Preparation of the inner electrode**

The inner macroporous electrode has been prepared by potentiostatic electrodeposition of gold using a commercially available gold electroplating solution (ECF63, Metalor).

The electrodeposition was performed in a conventional three-electrode system, consisting of working (colloidal-crystal modified gold microwire that was connected to the potentiostat by means of copper tape), reference (Ag/AgCl (3M NaCl)) and cylindrical counter (Pt) electrodes. The gold electrodeposition was performed at an electrode potential of -0.66 V vs Ag/AgCl (3M NaCl).

The length of the colloidal-crystal template immersed into the electroplating solution was dependent on the quality of the template along the wire.

The precise positioning of the sample inside the electrochemical cell has been accomplished by a micro-positioning system built on purpose.

### **2.3.1 Electrical addressing of the inner electrode**

The inner electrode was electrically addressed by means of copper tape (3M<sup>TM</sup>, Austin - Texas) that was used to connect the silica-template covered gold microwire to the potentiostat during the electrodeposition of gold (as described above in subsection 2.3.).

## **2.4 Preparation of the outer electrode**

The colloidal crystal assembled on the surface of the metalized glass capillary, served as a template for the electrodeposition of gold.

Prior to the electrodeposition of gold, the thin silver layer was stabilized by a short (3 min) potentiostatic electrodeposition of a nickel layer. The nickel layer was electrodeposited using a commercially available nickel electroplating solution (semi-bright nickel solution, AlfaAesar<sup>®</sup>) at -0.9 V vs. Ag/AgCl (3 M NaCl).

After the electrodeposition of the nickel layer, the gold/silica composite structure was obtained by electrodeposition of gold (ECF63, Metalor) at -0.75 V vs Ag/AgCl (3 M NaCl) through the silica based template until the desired number of layers was infiltrated.

#### **2.4.1 Electrical addressing of the outer electrode**

The outer electrode was electrically addressed by means of a gold microwire (50  $\mu\text{m}$ ). The gold microwire was attached on the surface of outer electrode with a droplet of conductive silver paint (Agar silver paint, Agar). In the following step the structure was heated by an air-gun in order to harden the paint quickly by evaporating the solvent.

#### **2.5 Etching of silver and nickel layers**

Silver and nickel layers were removed by etching in 24% wt. nitric-acid (Sigma Aldrich) over night. This step facilitates the subsequent etching of the glass capillary since once the underlying silver/nickel layer (that may act as a protective shell) is removed, the glass capillary is easily accessible to hydrofluoric acid.

#### **2.6 Sealing of the assembled structure**

After the inner and the outer electrode were assembled into a device, the whole structure was sealed at its extremities by using a two-component epoxy glue (Quick Set Epoxy Adhesive, RS).

#### **2.7 Etching of silica nanoparticles and glass capillary**

Once the full structure is assembled and the two-component epoxy glue is completely cured, the assembled device is etched with concentrated (48% wt.) HF (Sigma Aldrich) for 5-6 hours. During the etching, the silica beads were removed in the first few seconds while the etching of the glass capillary required a longer time (5-6 h).

The final macroporous coaxial double electrode device was kept in MilliQ water.

#### **2.8 Preparation of coaxial and macroporous two-electrode electrochemical cell**

The fabrication of coaxial macroporous gold electrodes with cylindrical geometry can be summarized in three different steps (see **Chapter 2**):

- (a) Electrodeposition of alternating metal layers
- (b) Etching of the spacer metal layer with nitric acid
- (c) Stabilisation of the structure and prevention of short circuits
- (d) Electrochemical characterisation of the structure

### **2.8.1 Electrodeposition of alternating metal layers**

Electrodeposition of alternating gold-nickel-gold (Au-Ni-Au) metal layers throughout the colloidal-crystal template consisting of 600 nm silica nanoparticles have been performed successively using commercially available non-cyanide electroplating solutions ECF63 (Metalor, gold solution,  $\gamma(\text{Au}) = 10 \text{ g/l}$ ) and semibright nickel solution (AlfaAesar®).

Electrodeposition was performed at a constant electrode potential using chronoamperometry. The experimental conditions for electrodeposition of alternating metal layers are given below.

#### **Electrodeposition of the gold**

$E = -0.66 \text{ V}$  (1<sup>st</sup> Au layer) or  $-0.75 \text{ V}$  (2<sup>nd</sup> Au layer) vs. Ag/AgCl (3 M NaCl)

#### **Electrodeposition of the nickel**

$E = -0.85 \text{ V}$  vs Ag/AgCl (3 M NaCl)

For the electrodeposition of metal layers a three electrode system consisting of a working electrode (colloidal crystal template on gold microwire), reference electrode (sat. Ag/AgCl) and counter electrode (Pt cylinder) has been used.

The length of the colloidal-crystal template immersed into the electroplating solution was dependent on the quality of the template along the wire.

For the precise positioning of the sample inside the electrochemical cell a micropositioner built on purpose has been used.

### **2.8.2 Etching of the nickel layer**

The sandwiched nickel layer was etched with 30% nitric acid for 20 hours at ambient temperature over a period of three days.

In the next step, samples were washed with MilliQ water to remove dissolved nickel and nitric acid. The set-up was equipped with a stirrer to improve the etching process.

### **2.8.3 Stabilisation of the coaxial structure**

Stabilization of the coaxial structure and prevention of short circuit between the two porous coaxial gold layers has been achieved by the insertion of small drops of nail varnish diluted with absolute acetone (Sigma-Aldrich) (1:1) at the extremities of the wire (at the end and just below the point where the silver paint droplet was deposited). The total length of the sample (the part that remained uncoated by varnish) was 2-3 mm.

In addition, the structure is dried with a hot air stream to prevent lateral diffusion of the diluted nail varnish and clogging of the channel between two electrodes.

The procedure was repeated twice to ensure a stable space separation between the two independent macroporous gold electrodes.

### **2.8.4 Dissolution of silica nanobeads**

Silica nanoparticles have been removed from the composite metal-silica structure by etching the samples with 5% hydrofluoric acid for 10 min.

In the next step, samples were dipped in MilliQ water to remove HF solution that could remain into the structure.

Samples were then dried at room temperature and used for electrochemical characterization.

## **2.9 Electrochemical characterization**

Final confirmation of the existence and geometric stability of the coaxial macroporous system with two independently addressable electrodes was obtained by cyclic voltammetry (CV).

A CV record was performed using a three electrode system of working electrode (coaxial sample), reference electrode (sat. Ag/AgCl; BASi, Inc.) and counter electrode (hollow Pt cylinder).

### Experimental section

Experimental conditions are given in the table below:

Parameter	Value
<b>Scan rate</b>	100 mV/s
<b>Potential window</b>	0 V to 1.6 V
<b>Supporting electrolyte</b>	0.1 M sulphuric acid (Sigma-Aldrich)
<b>Deaeration of the electrolyte</b>	Solution was purged with pure argon for 10 min.

In order to connect the two macroporous coaxial electrodes to the system separately, an external electrical connection was established by attaching a thin gold wire (d=50  $\mu\text{m}$ , AlfaAesar®) with a conductive silver paint to the surface of the outer porous gold electrode while the inner porous electrode had already a direct contact to the bare gold wire used for the fabrication of colloidal-crystal template.

The electrode potential was cycled several times during the experiment until the current reached a constant value.

## 3. Macroporous electrodes for the fabrication of a biocathode

### 3.1 Cleaning of the bare and macroporous gold electrodes prior to the electrochemical characterization

Bare and macroporous gold microwires have been cleaned in “Piranha” solution (75% v/v of 96% sulfuric acid and 25% v/v of 30% wt. hydrogen-peroxide), prior to the electrochemical characterization. In the following step, the samples were washed in MilliQ water for 10 min and immediately used for the determination of their active surface area.

All chemicals used were purchased from Sigma-Aldrich, Germany.

### 3.2 Electrochemical determination of the electroactive surface area

The electroactive surface area of bare and macroporous gold electrodes has been determined as described in Chapter 2 (section 2.3). Once the electrodes were immersed in deaerated (argon has been purged for 10 min) 0.1 M sulfuric acid (Sigma-Aldrich, Germany) the electrode potential has been cycled between 0 V-1.5 V until the cathodic peak stopped changing.

All electrochemical experiments were carried out with a bipotentiostat (CH Instruments, model CHI 842B, Austin, TX, USA). All electrochemical measurements have been done in a conventional three electrode system consisted of working electrode, counter electrode (Pt wire) and a reference electrode (Ag/AgCl (3 M NaCl; BASi, Inc)).

### 3.3 Preparation of BOD and polymer solutions and (co)electrodeposition

BOD (*Magnaporthe orizae*) and Os-redox polymer (PAA-PVI-Os[4,4'-Dichloro-2,2'-Pipyridine)2Cl]<sup>2+/-</sup> used in the experiments were obtained from Dr. N. Mano (CRPP, University of Bordeaux).

#### 3.3.1 Preparation of Os-polymer solution and electrodeposition of the polymer

Osmium polymer solutions ( $\gamma = 1.5$  mg/ml) have been prepared by diluting the stock solution ( $\gamma = 10$  mg/ml) with MilliQ water. The electrodeposition of Os-redox polymer has been carried out by cycling the electrode potential between 0.6 V-0.15 V (at 50 mV/s) for a desired number of scans. Prior to the electrodeposition step, the macroporous electrodes were kept in the polymer solution for 20 min in order to ensure complete penetration of the solution into the porous system. After the electrodeposition was finished, the electrodes (bare and macroporous) were kept in MilliQ water for 10 min in order to remove physisorbed polymer that could interfere with the electrodeposited one.

When not used, polymer stock solutions were kept in the fridge at 4 °C.

#### 3.3.2 Preparation of the BOD/Os-polymer mixture and their coelectrodeposition

The solutions of osmium redox polymer (0.5 mg/ml) and BOD (0.5 mg/ml) have been prepared by diluting their stock solutions (10 mg/ml and 64.15 mg/ml respectively) with deaerated (Ar was purged for 30 min.) MilliQ water.

The solution that has been used for coelectrodeposition was prepared by mixing 480  $\mu$ l of the BOD solution with 1020  $\mu$ l of the polymer solution. The final weight ratio of the polymer and the enzyme was 2.125.

Enzyme stock solutions were kept in the fridge at - 81 °C to preserve the enzyme activity.

Prior to coelectrodeposition, macroporous electrodes were left in the solution for 20 min in order to ensure better penetration of the mixture into the pores.

Coelectrodeposition has been performed with a three-electrode system in the potential window from 0.6 V to 0.15 V at 50 mV/s.



During the coelectrodeposition, a slight stream of Argon was flown over the setup in order to prevent oxygen absorption from the atmosphere. Once the coelectrodeposition was finished the electrodes were dipped in deaerated MilliQ water for 10 min.

Finally a “curing” step of the coelectrodeposited film has been performed at 4 °C for at least 4 h.

### **3.3.3 Testing of the Os-polymer and BOD/Os-polymer modified electrodes**

The testing of the modified electrodes has been done in both, deaerated and oxygen saturated 100 mM phosphate buffer solution (PB, pH= 7.2).

Os-polymer modified electrodes were tested in deaerated PB solution by cycling the electrode potential at 50 mV/s from 0.6 V to 0.15 V.

BOD/Os-polymer modified electrodes were tested in oxygen saturated PB solution (oxygen was intensively purged for 30 min.) in the potential window from 0.6 V to 0.15 V at a scan rate of 5 mV/s at 37.5 °C.

### **3.4 Stability test of BOD/Os-polymer modified electrodes**

Short term stability tests have been carried out by chronoamperometry. Electrodes were polarized at +0.3 V for 90 min in oxygen saturated PB in a thermostated electrochemical cell (at 37.5 °C). During the experiment an oxygen stream was flown over the PB surface to maintain the oxygen saturation level.

## **Guiding pancreatic $\beta$ -cells to target electrodes in a whole-cell biosensor for diabetes**

### **4.1. Preparation of low-conductivity buffer**

The conductivity of the incubating solution was reduced by decreasing the concentration of ions in the solution and substituting them with nonionic solutes to maintain an osmotic pressure suitable for biological cells (270–300 mOsmL<sup>-1</sup>). Mannitol was selected to balance the osmolarity because it does not affect glucose-induced insulin secretion. Therefore, a custom buffer composed of 5 mM HEPES (4-(2-hydroxyethyl)-1-piperazineethanesulfonic acid), 270 mM mannitol, and 5 mM glucose was formulated. The osmolarity of the solution was measured using an automatic MicroOsmometer Type 15 (Löser Messtechnik, Berlin, Germany).

The pH of the solution was determined using a 0.1% bromothymolsulfone phthalein (BTB) solution in 20% ethanol. The conductivity of the solution as well as the zeta potential of the polystyrene spheres and INS832/13 cells was measured using a disposable, capillary folded chamber and a Zetasizer Nano ZS apparatus (Malvern Instruments Ltd, Worcestershire, UK).

### **4.2 Micro-electrode arrays (MEAs)**

Studies were performed with two types of MEAs (Qwane Biosciences SA, Lausanne, Switzerland): MEA60-4Well-Pt for polystyrene spheres or clonal INS832/13  $\beta$ -cells, and MEA60-100-30-Pt for mouse or human islet cells. MEA60-4Well-Pt consists of 4 cylindrical Plexiglas chambers (6 mm diameter, 8 mm height), each housing 15 recording electrodes (30  $\mu$ m in diameter and spaced 100  $\mu$ m apart) and one internal reference electrode. MEA60-100-30-Pt consists of one cylindrical glass chamber (24 mm diameter, 6 mm height) housing 59 recording electrodes (40  $\mu$ m in diameter and spaced 200  $\mu$ m apart) arranged in an 8 $\times$ 8 matrix without corner electrodes and one internal reference electrode. The substrate material was glass and the insulation material was SU-8 epoxy (5  $\mu$ m thick). The MEA surface was rendered hydrophilic by plasma treatment with air at 9.83 W L<sup>-1</sup> for 2 min; it was prepared for cell culture by coating with Matrigel (2%, v/v, BD Biosciences, San Diego, CA, USA).

### **4.3 Spatial manipulation by electrophoresis**

An electric field was produced by applying an electric potential difference between neighboring electrodes. The electric potential was generated using an EmStat 3 potentiostat (PalmSens BV, Utrecht, Netherlands) with the working electrode being at a positive potential and the counter electrode short circuited with the reference electrode being at a negative potential. The electrophoresis of negatively charged round particles was investigated using uniform dyed polystyrene microspheres (IJPIJS/2% DVB) of 10  $\mu$ m diameter (Bangs Laboratories Inc., Fishers, IN, USA). Time-lapse images and videos were acquired using a Leica DFC295 digital camera mounted on a Leica MSV266 stereoscopic microscope and the Leica Application Suite (LAS) v4.3.0 (Leica, Heerbrugg, Switzerland). The efficacy of the treatment was determined by counting the number of cells on each electrode before and immediately after application of the potential. After 3-day culture, cell viability was quantified with the LIVE/DEAD Cell Imaging Kit (Life Technologies, Eugene, OR, USA), which produces green fluorescence for living cells (ex/em 488 nm/515 nm) and red fluorescence for dead cells (ex/em 570 nm/602 nm).

### ***Experimental section***

---

The kit was used according to the manufacturer's protocol recommending incubation of cells in equal volumes of cell culture medium and 2 × stock solutions for 15 min at 20 °C. The fluorescence was visualized by using FITC and TRITC filters.

---

## CONCLUSIONS AND PERSPECTIVES

## **Conclusion and perspectives**

In the present work, we describe a new straightforward way to elaborate a miniaturized coaxial double electrode electrochemical cell using two different strategies. The fabrication procedure exploits the hard template synthesis of macroporous materials which were used as building elements for designing the final cell architecture. Macroporous electrodes are selected as the best choice due to their high active surface area and the variety of materials that can be used for their fabrication. The route for their synthesis is based on the potentiostatic deposition of electro-conductive materials through a silica based colloidal crystal template. The Langmuir-Blodgett (LB) technique has been selected as the best choice for assembling a silica based template allowing a perfect control of the spatial arrangement of submicron particle layers and the absence of cracks in the structures. This is one of the most important prerequisites that determine the quality of the final macroporous material.

The first strategy for the fabrication of a miniaturized electrochemical cell is based on the potentiostatic electrodeposition of gold-nickel-gold metal layers through the silica particle based template. Once the nickel layer is dissolved, the obtained structure is stabilized by incorporation of spots of diluted nail varnish. In the next step the electrodes are independently addressed and the structural stability is investigated by cyclic voltammetry in acidic medium (0.5 M sulfuric acid). The electrochemical stability test of the structure is based on determining the active surface area of the gold electrodes calculated from the gold-oxide stripping peak. The difference in charge (that is related to the gold-oxide stripping peak) for each independently addressed coaxial macroporous electrode with different active surface area indicates the absence of electrical short-circuits. In control experiments, the two electrodes were externally short-circuited and their common stripping-peak charge has been obtained. This result additionally confirmed the structural stability. The electrochemical functionality of the fabricated miniaturized electrochemical cell was demonstrated by cyclo-voltammetric investigation of oxygen reduction (in oxygen saturated sulfuric acid solution ( $C=50\text{ mM}$ )) at each macroporous gold electrode. Although one could expect certain limitations with respect to oxygen diffusion and electrolyte penetration towards the inner electrode (due to the fact that the inner electrode is surrounded by the outer one), the obtained results clearly demonstrate the possibility to reduce oxygen at the surface of the inner electrode.

The second alternative and complementary strategy for the fabrication of coaxial and macroporous double electrochemical cells relies on assembling the final architecture from two independently prepared and electrochemically addressed cylindrical macroporous electrodes. The fabrication procedure for the outer cylindrical macroporous electrode is based on electrodeposition of gold through the silica colloidal template (also prepared by LB technique) that has been synthesized at the surface of a silver coated glass capillary. Once the inner macroporous electrode is introduced into the cavity of the macroporous gold-glass capillary electrode, the structure is sealed by epoxy glue and glass/silica beads are chemically etched by 48% HF. Like in the case of the architecture prepared by the first strategy, the electrochemical characterization and functionality of these structures were confirmed.

The essential difference between these two approaches is the possibility to vary the inter-electrode distance and that way the volume of the electrolyte that can be stored within the electrochemical cell. While the first strategy offers the possibility to fabricate architectures with an inter-electrode separation of tens of micrometers (due to technical limitations of the LB technique), the second alternative approach allows values that are in the range of hundreds of microns. This may have significant advantages for some applications even though this architecture is geometrically much bigger and the fabrication procedure is less elegant in comparison with the first one.

Further work in this area should be focused on the improvement of mechanical stability of the electrochemical cells which is one of the main prerequisites prior to their utilization for the fabrication of eventually implantable devices such as biofuel cells and biosensors. Further, the present strategies open the possibility for the fabrication of more complex structures such as three-electrode systems that could be used in both aqueous and non-aqueous media. This could be done by introducing a macroporous silver layer during the electrodeposition of a silver/nickel-gold-nickel-gold sequence (**Figure 1**). After dissolution of the nickel layer and an appropriate stabilization of so obtained architecture, macroporous silver could be used as a pseudo-reference electrode. Since the electrochemically active volume of the obtained miniaturized electrochemical cells is in the range of 0.1  $\mu\text{l}$  (with the possibility to further decrease this value) this would allow electrochemical/electroanalytical investigations in a very small volume of redox active species if the sample availability is the limiting factor.

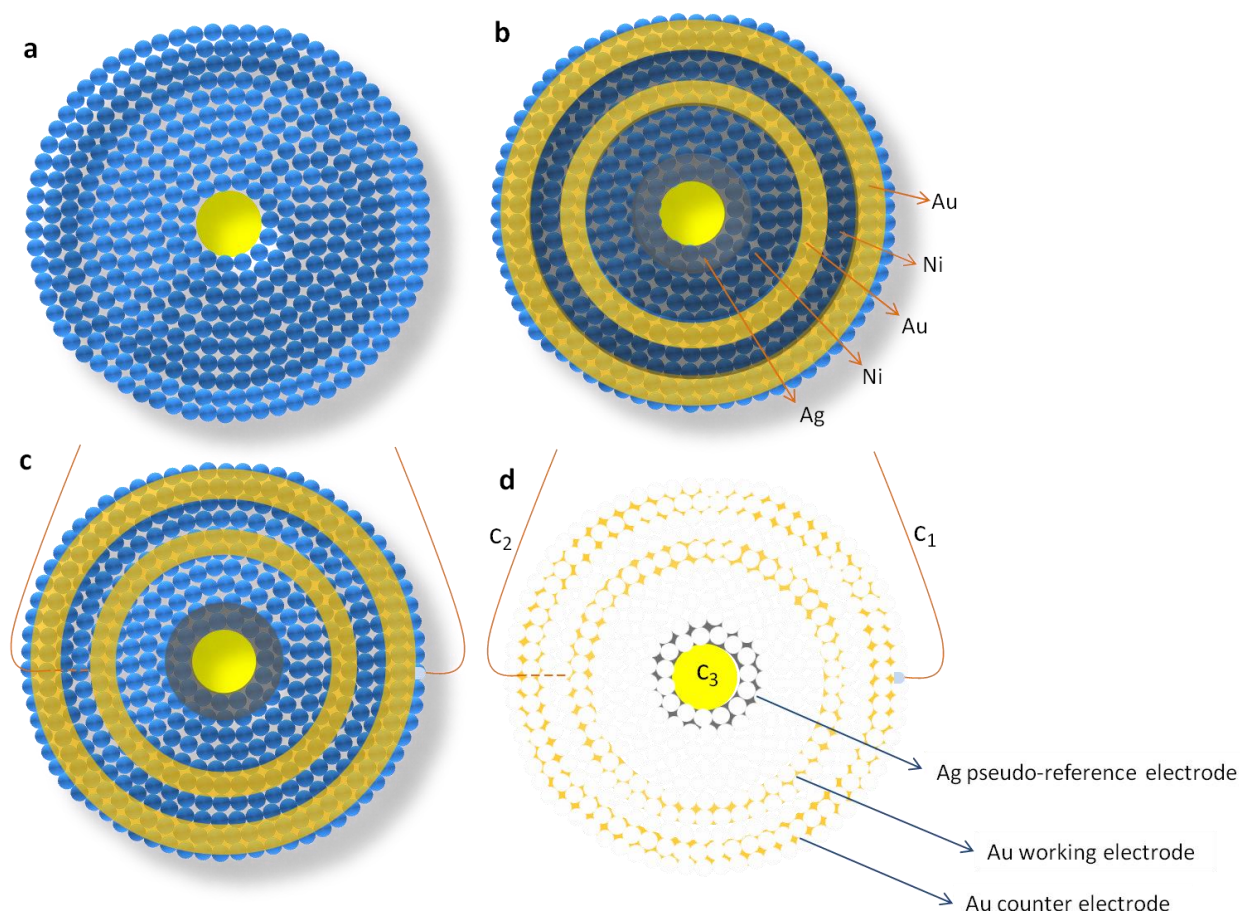


**Figure 1.** Schematic of the main steps for the fabrication of a miniaturized triple-electrode electrochemical cell. The synthesis can be carried out by potentiostatic electrodeposition of alternating silver-nickel-gold-nickel-gold layers (**b**) into a cylindrical silica based colloidal crystal template (**a**). After the chemical etching of the nickel layers (**c**) a structural stabilization of the final architecture through incorporation of spots of non-conductive elements (e.g. diluted nail varnish) is obtained (**d**) before dissolution of the silica nanoparticles with hydrofluoric acid. Each cylindrical gold electrode is independently addressed by means of a thin gold wire (connections  $C_1$  and  $C_2$  in figure **d**) while the connection of the silver layer is established directly *via* the gold microwire ( $C_3$ ) that served as a support (during the synthesis of the initial colloidal crystal).

One of the final long term goals of this work is to use the miniaturized two-electrode electrochemical cell (mentioned above) for the fabrication of miniaturized glucose/oxygen biofuel cells. Macroporous electrodes were selected as one of the best candidates that could be used to increase the electrochemical performances (power output) of a fuel/oxygen biofuel cell due to their high surface area.

The advantage of increased active surface area can be exploited in systems where the oxygen concentration is very low (e.g. subcutaneous oxygen concentration is 0.2 mM) and therefore limits the efficiency of actual biofuel cells. Further, the power output of such a biofuel cell can be increased by enhancing the interfacial electron transfer between the enzyme and the electrode surface. This can be done by using the appropriate redox mediator such as an osmium redox-polymer that has been used in this work. We have demonstrated the possibility to use the obtained macroporous electrodes for electrochemically assisted deposition of Os-redox polymer and coelectrodeposition of bioelectrocatalytically active BOD/Os-redox polymer adducts. The obtained results show the possibility to electrodeposit a redox polymer and an enzyme/redox-polymer adduct within the porous structure using cyclic voltammetry. The electrochemical characterization of so obtained electro-deposits shows that the saturation of the macroporous structure with the deposit is reached at approximately 500 electrodeposition cycles for the deposition of Os-polymer. After this value, further film growth is preferentially occurring at the outmost pore layers. Similar to those results, the saturation of the bioelectrocatalytic current for BOD catalyzed oxygen reduction reached its saturation level at approximately the same number of coelectrodeposition cycles as previously observed for electrodeposition of only Os-polymer.

Also, the more reproducible behavior of modified macroporous gold electrodes (compared to the erratic one for bare gold electrodes) suggests the protective role of the macroporous structure. Future work in this part of the project should be focused on the fabrication of a glucose oxidizing bioanode (e.g. glucose oxidase based bioanode) which includes the optimization of the conditions for electro-assisted deposition of the corresponding Os-redox polymer and a GOx/Os-polymer cross-linked structure. This would be the first step prior to the fabrication of a full miniaturized glucose/oxygen biofuel cell. This can be achieved by independent deposition of GOx/Os-polymer I and BOD/Os-polymer II adducts on each of the miniaturized macroporous gold electrodes thanks to the possibility to establish their independent connection to the potentiostat. During this process it is likely that the enzyme and the redox polymer also spontaneously get physisorbed at the non-corresponding electrode (e.g. adsorption of GOx and Os-polymer at the surface of the outer during the electrochemical deposition of GOx/Os-polymer at the surface of the inner one). This problem could be partially solved by keeping the electrode architecture after the electrodeposition of each enzyme/polymer adduct in a flow of phosphate buffer. This should result in the desorption of physisorbed species.



Finally we have demonstrated the development of a whole cell based glucose biosensor that relies its sensing properties on the electrophysiological response of pancreatic beta cells. Beta cells have been selected as best candidates for such a purpose due to their quick response (series of action potentials that can be measured externally) to any change of glucose concentration (and some other metabolites) in their environment. We have demonstrated a quick non-invasive way to guide living beta cells electrophoretically towards targeted micro-electrodes (using commercial micro-electrode arrays (MEA)) and increase in that way the performance of the future sensor (as the quality of the measured extracellular electric signals depends on close cell-electrode interaction). The results show that the viability of beta cells and dissociated islets (smaller clusters of beta cell obtained by partial dissociation of original pancreatic islets) was preserved after the application of electric field for guiding the cells in the MEA device. This has been confirmed by microscopy (the morphology of the viable cells was preserved in the proximity of the micro-electrodes) and by measuring the extracellular electric activity of mouse islet beta cells upon increase of glucose concentration. Future work in this field should be directed towards improving the contact between beta cells and the surface of micro-electrodes. One of the possible ways to accomplish this is based on the formation of artificial microscopic metal "bowls" at the surface of microelectrodes. This could be done by formation of silica or polystyrene colloidal crystals (using beads with diameters bigger than the size of cells) at the surface of the electrode and subsequent electrodeposition of an electroconductive material (e.g. gold or platinum).

### Résumé

Dans le cadre de cette thèse, notre principal sujet d'étude a été la mise en place de nouvelles voies de fabrication d'électrodes miniatures structurées qui pourraient trouver des applications dans des domaines liés à l'électrochimie tels que des batteries, des biocapteurs et éventuellement des piles à biocombustible implantables.

Dans la première partie de ce manuscrit (chapitre 1), nous nous sommes attachés à expliciter les principes de base de la physique des systèmes colloïdaux auto-assemblés ainsi qu'à décrire les différentes méthodes permettant la formation de cristaux colloïdaux. Nous nous sommes plus particulièrement intéressés à la technique de Langmuir-Blodgett que nous avons utilisée au cours de ce travail pour élaborer des matériaux sacrificiels à base de particules de silice. Celle-ci a en effet été sélectionnée comme une méthode de choix permettant un bon contrôle de l'arrangement spatial des billes formant ces matériaux qui ne présentent aucune fissure et dont l'épaisseur est bien définie. Ces propriétés sont déterminantes pour l'obtention de matériaux macroporeux, répliques inverses de l'assemblage initial, obtenues par une méthode décrite dans le chapitre suivant.

Dans le Chapitre 2, nous décrivons deux stratégies d'élaboration d'une cellule électrochimique constituée de deux électrodes coaxiales miniaturisées. Celles-ci mettent en jeu des matériaux macroporeux semblables à ceux décrits précédemment et qui sont assemblés pour obtenir l'architecture finale souhaitée. Notre choix s'est porté sur des électrodes macroporeuses en raison de leur surface active élevée, mais également pour la grande variété de matériaux dont elles peuvent être constituées, tout matériau pouvant être formé par électrodéposition potentiostatique au sein d'un cristal colloïdal de silice étant un candidat possible.

La première stratégie utilisée pour la mise au point d'une telle cellule électrochimique exploite l'électrodéposition à potentiel constant de couches alternées d'or, de nickel et d'or dans la matrice à base de silice colloïdale.

## Résumé

---

Après dissolution de la couche intermédiaire de nickel, la structure est stabilisée mécaniquement par le biais de l'incorporation de gouttes de vernis dilué. Les deux électrodes en or sont ensuite connectées électriquement et la stabilité de la structure est évaluée par voltampérométrie cyclique en milieu acide (acide sulfurique 0,5 M) qui permet de mesurer la surface électroactive de chaque électrode à partir de l'aire du pic de réduction caractéristique des oxydes d'or. En effet, une différence dans la valeur de la charge – proportionnelle à l'aire de ce pic – mesurée pour chaque électrode connectée individuellement est la preuve d'une absence de court-circuit entre les deux compartiments macroporeux. Lorsque ceux-ci sont mis délibérément en court-circuit, la charge globale mesurée correspond bien à la somme des charges des électrodes considérées séparément, preuve supplémentaire de la stabilité de la structure.

Par ailleurs, nous avons vérifié le fonctionnement de la cellule électrochimique ainsi élaborée grâce à des mesures de réduction de l'oxygène dans des solutions acides ( $\text{H}_2\text{SO}_4$  0,05M) préalablement saturées en  $\text{O}_2$ . En dépit des limitations que l'on peut attendre en termes de diffusion et de pénétration de l'électrolyte vers elle, les résultats ont clairement mis en évidence qu'il était possible de réduire l'oxygène à la surface de l'électrode centrale bien que celle-ci soit entourée par une électrode externe d'une plus grande épaisseur. Les densités de courant mesurées après avoir normalisé l'intensité du courant par l'aire géométrique de l'électrode interne étaient supérieures à celles mesurées pour l'électrode externe, ce qui suggère une sous-estimation de l'aire de l'électrode interne imputable à cette vitesse de pénétration de l'électrolyte qui serait plus lente.

La seconde stratégie adoptée a consisté à préparer séparément deux électrodes cylindriques macroporeuses puis à les assembler dans un deuxième temps pour former le dispositif final. Ici, l'électrode externe est élaborée par électrodéposition d'or dans un assemblage colloïdal déposé par la technique de Langmuir-Blodgett sur un capillaire de verre recouvert d'une fine couche d'argent. Une électrode macroporeuse simple est ensuite introduite dans le canal du capillaire avant que la structure ne soit scellée à ses extrémités avec une colle époxy. Après dissolution simultanée du capillaire en verre et des billes de silice par de l'acide fluorhydrique concentré, la caractérisation et la preuve de fonctionnalité du dispositif sont apportées par des mesures électrochimiques semblables à celles décrites précédemment.

Entre ces deux approches, la différence essentielle réside dans la possibilité d'ajuster la distance inter-électrodes et donc de faire varier le volume de l'électrolyte stocké dans la cellule électrochimique. Si la première permet de réduire cette distance à quelques dizaines de micromètres, la seconde permet d'accéder facilement à des distances de plusieurs centaines de microns qu'il serait difficile d'atteindre par la technique de Langmuir-Blodgett. Bien qu'un peu moins élégant dans son concept et en dépit du volume global plus imposant du dispositif obtenu par cette seconde approche, celle-ci peut toutefois être utile dans certaines applications.

L'un des objectifs à long terme de ce travail est l'utilisation de la cellule électrochimique à deux électrodes miniaturisée (mentionnée ci-dessus) pour la fabrication de biopiles glucose/oxygène miniaturisées. Les résultats obtenus en ce sens font l'objet du Chapitre 3.

Du fait de leur aire surfacique élevée, les électrodes macroporeuses comptent parmi les meilleurs candidats pouvant être utilisés dans le but d'augmenter les performances électrochimiques (puissance de sortie) d'une biopile à combustible/oxygène. Les avantages de cette aire surfacique active accrue peuvent être exploités dans des systèmes où la concentration d'oxygène est très faible (la concentration d'oxygène sous-cutanée est par exemple de 0,2 mM), et limite par conséquent l'efficacité des biopiles à combustible actuelles. Par ailleurs, la puissance de sortie d'une telle biopile à combustible peut être augmentée en améliorant le transfert d'électron interfacial entre l'enzyme et la surface de l'électrode. Ceci peut être réalisé en utilisant un médiateur rédox approprié, comme le polymère rédox qui a été utilisé dans ce travail. Les électrodes macroporeuses obtenues ici ont pu être utilisées pour la déposition électrochimique d'un polymère rédox d'osmium, mais également pour la co-électrodéposition d'un adduit formé du polymère rédox d'osmium et d'une bilirubine oxydase (BOD), qui s'est montré actif pour la bioélectrocatalyse.

Les résultats obtenus montrent qu'il est possible d'utiliser la voltammétrie cyclique pour déposer dans la structure poreuse un polymère rédox, ou un adduit enzyme/ polymère rédox. La caractérisation électrochimique des électro-dépôts ainsi obtenus montre que la saturation de la structure macroporeuse par le dépôt est atteinte après environ 500 cycles d'électro-dépôt pour le polymère rédox à base d'osmium. Au-delà de cette valeur, la croissance ultérieure du film a lieu de façon préférentielle au niveau des couches de pores extérieures, ce qui par conséquent ne tire pas profit de l'importance de l'aire surfacique active du système macroporeux. De manière similaire, le courant bioélectrocatalytique de réduction de l'oxygène

catalysée par la BOD atteint sa saturation aux alentours du 500<sup>ième</sup> cycle de co-électrodépôt, comme cela avait été observée auparavant pour l'électrodépôt du polymère d'osmium seul. De plus, les densités de charges correspondant à l'oxydation/réduction du polymère d'osmium déposé électrochimiquement, ainsi que les courants enregistrés pour la réduction bio-électrocatalytique du dioxygène par les films formés par l'adduit BOD/polymère d'osmium, se sont révélés plus faibles dans le cas des électrodes d'or macroporeux que ce qui avait été observé dans le cas d'une électrode d'or plane. Ceci a été expliqué dans le modèle théorique proposé par des considérations géométriques (voir Chapitre 3).

D'un autre côté, le rôle protecteur de la structure macroporeuse est suggéré par le comportement plus reproductible des électrodes macroporeuses modifiées (en comparaison du caractère aléatoire observé pour les électrodes d'or planes) en ce qui concerne les densités de courant enregistrées pour la réaction de réduction bio-électrocatalytique du dioxygène.

Enfin, nous avons décrit au Chapitre 4 le développement d'un biocapteur à glucose à cellules entières, dont les propriétés de détection reposent sur le comportement électrophysiologique des cellules bêta pancréatiques. Les cellules bêta ont été sélectionnées pour cet objectif à cause de leur réponse rapide à tout changement de la concentration de glucose (et de certains autres métabolites comme certains acides aminés, hormones ou lipides) dans leur environnement. Cette réponse s'exprime comme des séries de potentiels d'action qui peuvent être mesurés à l'extérieur de la cellule grâce à des ensembles de micro-électrodes (micro-electrode array, MEA). Nous avons développé un moyen rapide et non-invasif de guider électrophorétiquement des cellules bêta vivantes vers des micro-électrodes ciblées, en utilisant le motif de potentiel d'électrode généré par des ensembles de micro-électrodes commerciaux. Nous voulions augmenter de cette manière les performances du futur capteur (la qualité des signaux électriques extracellulaires mesurés dépend d'interactions rapprochées entre les cellules et l'électrode). Les résultats montrent que la viabilité des cellules bêta et des « îlots » dissociés (plus petits amas de cellules bêta obtenus par dissociation enzymatique partielle des îlots pancréatiques originaux) était préservé après application du champ électrique optimisé, généré au sein du dispositif MEA pour guider les cellules vers les micro-électrodes ciblées. Ceci a été confirmé par microscopie (la morphologie des cellules vivantes était préservée à proximité des micro-électrodes), et en mesurant l'activité électrique extracellulaire de cellules bêta de souris en réponse à une augmentation de la concentration de glucose.

## Résumé

---

De plus, le potentiel de membrane extracellulaire a montré une altération lors de l'addition de composés (glibenclamide et adrénaline) qui peuvent provoquer l'ouverture ou la fermeture de canaux ioniques spécifiques et par conséquent changer l'intensité du potentiel de membrane généré.